

Fabrication and applications of AuAg alloy metasurfaces and hybrid metal dielectric nanoantennas

Présentée le 3 août 2021

Faculté des sciences et techniques de l'ingénieur
Laboratoire de nanophotonique et métrologie
Programme doctoral en photonique

pour l'obtention du grade de Docteur ès Sciences

par

Debdatta RAY

Acceptée sur proposition du jury

Prof. L. Thévenaz, président du jury
Prof. O. Martin, directeur de thèse
Prof. D. A. Stemmer, rapporteur
Dr Y. Ekinici, rapporteur
Dr Z. Benes, rapporteur

Acknowledgements

The long journey of my PhD would not have been complete without the help of numerous people around me. In this thesis I would like to take this opportunity to acknowledge their help and efforts for making the journey of my PhD successful. I would like to start by thanking my supervisor, Prof. Olivier J.F. Martin, without whom the journey would not have commenced. Prof. Martin has done true justice to the word "supervisor". He has motivated me during trying times, encouraged me when results were few, taught me how to ask the correct questions and guided me towards solutions. This thesis would not have taken shape without his constant help and guidance. Next I would like to thank Dr, Christian Santschi. The success of the nanofabrication projects shown throughout the thesis would not have been possible without his tireless co-operation and excellent feedback. I would also like to take this opportunity to thank all the CMi staff, for training me on the machines and answering my never ending questions. Following, I would like to thank my collaborators Prof. Hatice Altug and Dordaneh Etezadi for their co-operation. I would also like to thank my fellow co-authors- T.V. Raziman, Madasamy Thangamuthu, Hsiang-Chu Wang, Jeonghyeon Kim and Andrei Kiselev for their support and co-operation in the several projects. I would like to acknowledge the help given to me by my senior colleagues Xialong Wang and Gabriel Bernasconi during my PhD. Finally, I would also like to thank my other lab members- Karim Achouri, Mintae Chung, Siarhei Zavatski and Marco Riccardi for the numerous discussions that propelled me to work better. Here I would also like to thank my jury members Prof. Luc Thévenaz, Dr. Benes Zdenek, Prof. Andreas Stemmer and Prof. Yasin Ekinici for agreeing to review my thesis. Finally, I would like to thank my close family members and friends for providing me with the much needed support.

Abstract

The most prevalent materials used in the field of plasmonics are Au and Ag. However, for the past few years, the plasmonic community has also been looking for alternative materials that have lower losses than Au and higher stability than Ag. This thesis is an attempt to provide some nanotechnological solutions in that direction. In this thesis, I have experimentally demonstrated plasmonic nanostructures and metasurfaces with other alternative materials like AuAg alloys and hybrid metal-dielectric nanoantennas: Al disk stacked on top of Si cylinder. The development of new processes for the incorporation of novel materials for the fabrication of nanostructures requires rigorous optimization procedures which have been detailed in the greater part of the thesis. In the first part of the thesis, I describe the development of a novel low-temperature alloying process for fabricating AuAg alloyed nanostructures. With this process, nanostructures of varying stoichiometries were fabricated by annealing a bilayer of Au and Ag, the relative thickness of the bilayer determined the composition. The process made possible to perfectly retain the shape of the nanostructures after annealing, without the use of insulating material like SiO₂ as a protective cover. Further, it only required a single annealing step after the completion of fabrication by conventional lithography and enabled the fabrication on the same substrate of alloyed nanostructures with different stoichiometries, unlocking an additional degree of freedom for nanostructure design. I extended this versatile and cost-effective technique successfully to the fabrication of complex 4-rod Fano resonant nanostructures and to binary plasmonic metahologram and metalenses. The metasurfaces were built from similar shape nanostructures with the different phase responses provided by a variation of composition (Au_{0.2}Ag_{0.8} and Au_{0.8}Ag_{0.2}) rather than the conventionally used variation in geometrical parameters. This technique paves the way for fabricating plasmonic metasurfaces with meta-atoms varying in both geometry and composition. In the second part of the thesis I investigate the effect of introducing dielectric to metal nanostructures. In order to do this analysis, I use a hybrid metal-dielectric nanoantenna with stacked geometry comprising of a metal disk on a Si cylinder. I perform a systematic study showing the evolution of the multipoles along with the spectra for this hybrid metal-dielectric nanoantenna as its dimensions are varied one by one. I broaden the analysis to demonstrate the "magnetic light" at energies above 1 eV by varying the height of the Ag on the Si cylinder and below 1 eV by introducing insulating spacing between them. The appearance of the anapole state is also explored along with some exceptionally narrow spectral features by varying the radius of the Ag disk. This geometry has also been fabricated using Al as the metal which also acted as an etching mask, simplifying the fabrication process and Si as the dielectric, together with

Acknowledgements

a SiO₂ spacer. These nanostructures have been used for bulk refractive index sensing with glucose solution showing a sensitivity of 208 nm/RIU, which has been further improved to 245 nm/RIU by under etching the SiO₂ spacer. I believe the nanotechnological processes developed in this thesis will facilitate the fabrication of metasurfaces with these alternative materials resulting in new and superior performances.

Résumé

Les matériaux les plus utilisés en plasmonique sont l'Au et l'Ag. Ces dernières années, des activités de recherche importants ont émergé pour utiliser d'autres matériaux, avec par exemple des pertes plus petites qu'Au, ou une meilleure stabilité chimique qu'Ag. Cette thèse apporte des solutions technologiques à cette quête. Dans ce travail, j'ai réalisé expérimentalement des nanostructures et des métasurfaces plasmoniques en utilisant des matériaux alternatifs, tels des alliages AuAg ou des structures hybrides combinant un métal avec un diélectrique. Le développement de technologies originales qui incorporent de nouveaux matériaux pour la fabrication de nanostructures requiert une optimisation rigoureuse des différentes étapes de fabrication et forme la part majeure de cette thèse. Dans la première partie, je décris un processus de recuit à basse température pour des nanostructures en AuAg, qui permet de fabriquer des nanostructures de différentes stœchiométrie en faisant un recuit d'une bicouche d'Au et d'Ag, dont les épaisseurs relatives déterminent la stœchiométrie finale. Cette recette permet que les nanostructures gardent leur forme après le recuit, sans qu'il soit nécessaire de les protéger avec un matériau isolant comme du SiO₂. De plus, elle ne nécessite qu'un seul recuit après toutes les autres étapes de fabrication par lithographie et permet de créer sur le même substrat des structures en alliages avec des stœchiométries différentes, ouvrant de nouvelles possibilités pour la conception de systèmes complexes. J'utilise cette méthode polyvalente et économique pour fabriquer des systèmes à 4 nano-barres supportant des résonances de Fano, ainsi que des méta-hologrammes et des méta-lentilles. Ces métasurfaces sont construites avec des nanostructures de même forme mais de compositions différentes : (Au_{0.2}Ag_{0.8} et Au_{0.8}Ag_{0.2}) , au lieu de l'approche traditionnelle qui consiste à varier les paramètres géométriques pour contrôler la réponse des nanostructures. Cette nouvelle technologie offre de nouveaux degrés de liberté pour concevoir des métasurfaces construites avec des méta-atomes dont non seulement la géométrie varie, mais aussi la stœchiométrie. Dans la seconde partie de la thèse, j'étudie l'effet d'un diélectrique sur une structure métallique. Pour cela, j'analyse une nano-antenne hybride métal-diélectrique composée d'un disque métallique sur un cylindre en Si. Une étude systématique de l'évolution des modes multipolaires et des spectres optiques de cette nano-antenne en fonction des différents paramètres géométriques est conduite. Je démontre l'existence de "lumière magnétique" à des énergies supérieures à 1 eV - en variant l'épaisseur du métal - et inférieures à 1 eV - en introduisant un espace diélectrique entre le métal et le Si. Un état anapolaire ainsi que des résonances spectrales extrêmement étroites sont aussi mis en évidence. Cette géométrie hybride est fabriquée en utilisant Si comme diélectrique Al comme disque métallique; ce dernier servant à la fois de

Acknowledgements

structure plasmonique et de masque pour l'attaque sèche, simplifiant ainsi le processus de fabrication. Un espaceur en SiO_2 permet de contrôler le couplage électromagnétique entre les deux parties. Ces structures sont utilisées pour détecter les variations d'indice de réfraction de solutions de glucose, avec une sensibilité de 208 nm/RIU. Cette dernière atteint même 245 nm/RIU lorsque l'espaceur est diminué pour favoriser l'accès au champ optique. Les nanotechnologies développées dans cette thèse vont permettre la fabrication de métasurfaces complexes utilisant ces matériaux alternatifs et présentant des performances nouvelles et supérieures.

Contents

Acknowledgements	iii
Abstract (English/Français)	v
List of figures	xi
List of tables	xxiv
1 Introduction	1
1.1 Thesis objectives	2
1.2 Thesis organization	2
I Alloy nanostructures: New Fabrication techniques and their application	5
2 Importance and relevance of alloy in nanophotonics	7
2.1 Introduction	7
2.2 Understanding AuAg alloys	8
2.3 Existing methods of fabrication	12
2.3.1 Chemical synthesis	12
2.3.2 Annealing Au@Ag core-shell nanostructures covered with SiO ₂ to form AuAg alloy	15
2.3.3 Green synthesis	16
2.3.4 Galvanic replacement	16
2.3.5 Laser ablation	24
2.3.6 Miscellaneous techniques of fabrication	25
2.4 Applications of AuAg alloys	26
2.4.1 Biosensors	26
2.4.2 SERS	29
2.4.3 Stability of alloys	36
2.4.4 Photocatalysis	36
2.4.5 Photocurrent	40
2.4.6 Photothermal	42
2.4.7 Miscellaneous applications	42
2.5 Conclusion	44
	ix

3	Developing new technology for fabricating alloy nanostructure	45
3.1	Introduction	45
3.2	Fabrication of AuAg alloy thin films with low temperature annealing method . .	46
3.2.1	Recipe	46
3.2.2	Studies of AuAg alloy ($\text{Au}_{0.2}\text{Ag}_{0.8}$, $\text{Au}_{0.5}\text{Ag}_{0.5}$, $\text{Au}_{0.8}\text{Ag}_{0.2}$) thin films with optimized recipe	52
3.2.3	Challenges with $\text{Au}_{0.8}\text{Ag}_{0.2}$ thin films on 4-inch wafers	55
3.2.4	Long term stability studies	56
3.3	Fabrication of alloyed nanostructures with the optimised recipe	60
3.3.1	Fabrication of alloyed nanorods and nanotriangles ($\text{Au}_{0.2}\text{Ag}_{0.8}$)	60
3.3.2	Fabrication and measurements of alloyed Fano resonance structures . .	60
3.4	Conclusion	61
4	Optical applications of AuAg alloys	65
4.1	Applications in optics: Alloyed metasurface with $\text{Au}_{0.2}\text{Ag}_{0.8}$ and $\text{Au}_{0.8}\text{Ag}_{0.2}$ alloys	65
4.1.1	3 level alignment for the binary metasurface	66
4.1.2	Fabrication of alloyed metasurfaces: Holograms and Fresnel Zone Plate	69
4.2	Applications in Chemistry: Generation of hot electron with $\text{Au}_{0.5}\text{Ag}_{0.5}$ alloys . .	73
4.2.1	Motivation	73
4.2.2	Fabrication	75
4.2.3	Characterization	76
4.2.4	Detection of Hot electrons	77
4.3	Outlook	84
4.3.1	Broadband absorption	84
II	Hybrid nanoantenna : Theory, Fabrication and application	87
5	Hybrid Nanoantenna	89
5.1	Introduction	89
5.2	Nanofabrication	90
5.3	Multipole analysis	92
5.4	Experiments	94
5.5	Nanoantenna with an undercut	96
5.6	Conclusions	100
6	Theory of hybrid nanoantenna	103
6.1	Introduction	103
6.2	Results and discussion	105
6.2.1	Response of the dielectric cylinder	106
6.2.2	Influence of the metal disk	108
6.2.3	Coupling between the dielectric cylinder and the metal disk	111
6.3	Conclusion	113

7 Conclusion and Outlook	115
Bibliography	153
Curriculum Vitae	155

List of Figures

- 2.1 (a) Bulk phase diagram of the AuAg alloy. Reproduced with permission from [114]. Copyright 2016, American Chemical Society. (b)-(c) n and k values of AuAg thin films of various compositions computed from experimentally obtained ellipsometric data. (b)-(c) Reproduced with permission from [261]. Copyright 2014, OSA. (d) Molecular orbital energies of the Au₂, AuAg and Ag₂. The occupied electrons are shown in circles while the value in parenthesis is the number of degenerate states of the d-orbital type molecular orbitals. Reproduced with permission from [177]. Copyright 2003, American Chemical Society. (e) TEM HAADF scans of the Ag@Au core-shell cluster as a function of temperature (upper row) and Au@Ag core-shell cluster scanned at the same temperature (bottom row). With increasing temperature the core-shell boundaries starts to blur out. (e) Reproduced with permission from [174]. Copyright 2018, The Royal Society of Chemistry. (f)-(i) HAADF STEM images along with EDX maps showing the different stages of evolution of the dimer during laser welding. The schematic of each stage is given below the SEM and EDX images. (f)-(i) Reproduced with permission from [395]. Copyright 2018, The Royal Society of Chemistry. 9
- 2.2 (a) Schematic showing the configuration used for acquiring EELS data in (b). The electron beam is traversing the center of the particle. (b) The EELS spectra obtained for AuAg alloyed disk for various composition with the configuration described in (a). (a)-(b) Reproduced with permission from [141]. Copyright 2019, American Chemical Society. (c) Structural sketches of the nanostructures mentioned outside each box. Inset shows the vial containing the nanoparticle solution. (d) Corresponding HAADF STEM images of the geometries shown in (c). (e) Corresponding EELS maps showing the evolution of the LSPR spectra of the nanoparticles. (c)-(e) Reproduced with permission from [97]. Copyright 2016, American Chemical Society. 11

2.3	(a) HAADF-STEM and EDX maps of the nanoparticles sampled at different times of the synthesis. Reproduced with permission from [28]. Copyright 2019, John Wiley & Sons, Ltd. (b) Schematic showing the fabrication of the AuAgQC by the QC-QC interaction. (c) Picosecond resolved fluorescence transients of AuQC, AgQC, AuAgQC.(b)-(c) Reproduced with permission from [228]. Copyright 2012, The Royal Society Of Chemistry. (d) Schematic of the fabrication of Folic acid modified dendrimer-stabilized AuAg alloy nanoparticles (e) Comparison of X-Ray attenuation intensity between Omnipaque and the before said AuAg alloy nanoparticles. (d)-(e) Reproduced with permission from [196]. Copyright 2013, The Royal Society Of Chemistry.	14
2.4	(a) Schematic of the process showing how AuAg alloyed nanorods coated with SiO ₂ are fabricated by annealing. (b)-(d) TEM images of the same nanostructures annealed at different temperature. SERS spectra of the R6G adsorbed on (e) AuAg alloyed nanorods (f) Au@Ag core shell nanorods before and after etching in NH ₄ OH and H ₂ O ₂ . Reproduced with permission from [240]. Copyright 2019, , Chinese Laser Press.	17
2.5	(a) Schematic diagram showing the stages of a conventional galvanic reaction between HAuCl ₄ and Ag nanocube (both in 3D and in cross sectional view). Reproduced with permission from [333]. Copyright 2004, American Chemical Society.(b) Schematic diagram showing galvanic replacement reaction with Ag nanocubes and AuCl ₂ ⁻ (both in 3D and in cross sectional view). Reproduced with permission from [51]. Copyright 2010, Elsevier. (c)-(h) TEM images of different stages for galvanic replacement reaction between Ag nanowire and HAuCl ₄ following the same steps shown in (a). TEM image of a (c) Ag nanowire and (d)-(h) for various volumes of 1 mM of HAuCl ₄ . (d) 0.3 (e)0.6 (f)1.5 (g)2.3 (h) 3.0 ml. The inset in (c) is the the TEM image of the microtomed sample of silver nanowires, while the insets in (e)-(h) are their corresponding SEM images. (c)-(h) Reproduced with permission from [333]. Copyright 2004, American Chemical Society. (i) Schematic of the one step process showing AuAg alloy nanowrapper with Ag nanocube as a sacrificial template. (j) Large area (k) locally magnified (l) high-magnification SEM image. (m) HAADF-STEM characterization along with EDS maps of the nanowrapper (n) Schematic of the working principle using the “nanowrapper” as a cargo carrier and releasing of the DNA- capped nanospheres. (i)-(n) Reproduced with permission from [207]. Copyright 2018, American Chemical Society.	19

- 2.6 (a) Schematic of the fabrication of the AuAg nanorod with gaps with a gap in the middle. (b) HRTEM image of the AuAg nanostructure with a nanogap inside. (c) Raman Spectra of CV (10^{-6} M) on the substrate with AuAg alloy with gap. The control sample with only nanorod without CV. The incident laser is 633 nm. (a)-(c) Reproduced with permission from [65]. Copyright 2019, Elsevier. (d) Schematic of the fabrication process to form the hollow nanorice. SEM and TEM image (in the inset) of the (e) Ag nanorice (f) AuAg hollow nanorice. (d)-(f) Reproduced with permission from [407]. Copyright 2017, MDPI. Synthesis of different type of AuAg holey nanoplates. (g) Ag nanoplates (h)-(i) Holey AuAg nanoplate as an intermediate and nanoframes, as the final product, formed by galvanic replacement reaction of HAuCl_4 and Ag nanoplates. (j)-(k) Holey nanoplates as an intermediate as final product formed by galvanic replacement between Ag nanoplate and $\text{Na}_3\text{Au}(\text{SO}_3)_2$. (g)-(k) Reproduced with permission from [382]. Copyright 2016, The Royal Society Of Chemistry (l) Schematic showing how a single Ag nanoplate can be evolved to numerous AuAg alloyed nanoplates (m) SEM image of the Ag nanoplate (n)-(p) The TEM image of the various evolved AuAg nanoplates shown in the schematic in (l). (q) Extinction spectrum of the various nanoplates evolved from the Ag nanoplate. (r) Change in temperature of the AuAg alloy nanoplates and (s) nanorings after being irradiated by 808 nm NIR laser. (l)-(s) Reproduced with permission from [270]. Copyright 2016, Springer. 21
- 2.7 (a) Schematic of the steps of the fabrication of Ag@AuAg nanorattle. (b) Fluorescence images of calcein Am (green, live cells) and red fluorescence dye (red, dead cells) contained MDA-MB-231 cells after laser irradiation. (c) Rise of temperature of the nanoparticle solution as a function of laser power. (d) Cell viability of MDA-MB-231 cells treated with nanorattles and 808 nm laser irradiation with various laser powers. (a)-(d) Reproduced with permission from [399]. Copyright 2017, John Wiley & Sons, Ltd. TEM images of Ag@AuAg alloy core frame nanocubes are etching with 3% aqueous H_2O_2 . The samples were prepared by co-titrating various combinations of AgNO_3 (0.3 mM) and HAuCl_4 (0.1 mM) (e) 0.2 (f) 0.4 (g) 0.8 (h) 1.5 ml for each precursor. (i) Scheme showing top 3 competing equations involved in the co-titration process. The bottom schematic shows the transformation of the Ag nanocubes into three types of Ag@AuAg core frame nanocubes by increasing the volume of the co-titrated precursors, followed by etching of the Ag. (j) SERS spectra of the 1,4-BDT adsorbed on the Ag@AuAg core frame nanocubes at an excitation wavelength of 785 nm. (e)-(j) Reproduced with permission from [331]. Copyright 2015, The Royal Society of Chemistry. (k) In-situ testing of tensile strength of the $\text{Au}_{30}\text{Ag}_{70}$ alloy nanowire. Reproduced with permission from [155]. Copyright 2020, Elsevier. 23

- 2.8 (a) Specificity of the AuAg nanoparticle solution towards ClO^- . The specificity is monitored using the absorption intensity at 410 nm. The inset shows the schematic representation of the working principle of sensing ClO^- using AuAg alloy nanoparticles. Reproduced with permission from [305]. Copyright 2017, The Royal Society of Chemistry. (b) Scheme showing how the in situ sensing is done with AuAg nanoboxes using cyanide etching. The results obtained from Hela cell and the Zebrafish using the same principle is also shown. Reproduced with permission from [371]. Copyright 2017, American Chemical Society. Experimental results obtained for three compositions of 60 nm nanoparticles (Au, Ag and $\text{Au}_{50}\text{Ag}_{50}$) (c) dark field microscopy images (d) Intensity and (e) colour image reconstructed from hyper spectral data obtained by the hyperspectral 2D scan performed with 100 \times immersion oil objective, 200 nm displacement steps, 3 s time constant and 100 μm spectrometer slit. (f) Darkfield imaging of MDA-MB-231 cells incubated with Au, Ag and AuAg nanoparticles for atleast an hour. (c)-(f) Reproduced with permission from [260]. Copyright 2014, The Royal Society of Chemistry. (g) The response of the hollow AuAg nanoparticles (HGN) fabricated on inkjet substrate towards 20 g of salmon spiked with putrescine (PT) an biogenic amine found in spoiled foods. (0-2000 ppm). The background response from the blank sample has always been subtracted. Reproduced with permission from [350]. Copyright 2017, American Chemical Society. (h) Linear dependence of $\Delta\lambda_R$ for various concentration of aqueous sodium chloride. (i) Schematic of the SPR sensor using wavelength interrogation technique implemented with Kretschmann configuration. (h)-(i) Reproduced with permission from [405]. Copyright 2020, Elsevier. 27
- 2.9 SEM images of the porous striped AuAg alloy nanowires for various etching conditions defined by variation in the concentration of HNO_3 (a) $\text{Au}_{30}\text{s}-30\text{s}-\text{HNO}_3$ (0%) (b) $\text{Au}_{30}\text{s}-\text{Ag}_{30}\text{s}-\text{HNO}_3$ (20%) (c) $\text{Au}_{30}\text{s}-\text{Ag}_{30}\text{s}-\text{HNO}_3$ (25%) (d) $\text{Au}_{30}\text{s}-\text{Ag}_{30}\text{s}-\text{HNO}_3$ (30%) (e) Schematic of dealloying of stripped AuAg alloy nanowires. (f) TEM images of $\text{Au}_{30}\text{s}-\text{Ag}_{30}\text{s}-\text{HNO}_3$ (25%) (g) Schematic of the fabrication procedure of AuAg alloy nanowires using the template based electrochemical deposition process. (h) Raman mapping image of 4-MBA functionalized porous stripped AuAg alloy nanowires. (a)-(h) Reproduced with permission from [298]. Copyright 2020, Elsevier. (j) FESEM image of the bowl like pore array composed of hollow AuAg alloy nanoparticles. (k) Shows an zoomed image of the same (l) SERS spectra of 10^{-5} melamine aqueous solution on these nanostructures. (j)-(l) Reproduced with permission from [241]. Copyright 2019, Elsevier. 31

- 2.10 (a) Paper based plasmonic alloy stripes (b) EDS mapping of the various alloy composition on the paper substrate. (c) Fluorescence enhancement from FITC, R6G and CR depending on the resonance wavelength of individual composition. (d) Chromatographic MEF. The dye mixture of TB, SO and CR was separated using the paper substrate and selectively detected. (e) SERS spectra of $\text{Au}_{0.12}\text{Ag}_{0.88}$ showing picomolar detection for folic acid. Reproduced with permission from [256]. Copyright 2018, American Chemical Society. 33
- 2.11 (a) Schematic of the fabrication procedure of Au decorated AuAg alloy tubes. (b) STEM image of 9 ± 2 PEI capped Au nanoparticles (c) SEM image of the Ag nanowires with an average diameter of 167 ± 6 nm and a length of $40\ \mu\text{m}$. (d) SEM image of the AuAg nanotubes with an average external diameter of 215 ± 29 nm. (e) SEM image of the Au decorated AuAg tubes. (f) In situ SERS monitoring of the catalytic reduction of 4-NTP initiated by the NaBH_4 on Au decorated AuAg tubes (g) Time dependent SERS spectra showing the disappearance of 4-NTP and evolution of 4-ATP. (a)-(g) Reproduced with permission from [15]. Copyright 2018, Elsevier. (h) Scheme showing how simultaneous detection of sPD-1, SPD-L1 and sEGFR can be done. The output is a Raman spectra showing simultaneous detection of sPD-1, SPD-L1 and sEGFR in human serum. They were added to human serum in the concentrations 1 ng/ml, 0.1 ng/ml and 10 ng/ml. The 1585^{-1} , 1335^{-1} and $1376\ \text{cm}^{-1}$ shows the presence of sPD-1, SPD-L1 and sEGFR. Reproduced with permission from [186]. Copyright 2018, American Chemical Society. 35
- 2.12 (a) Dark field image of the AuAg-mTNF-H . Inset shows the area used for EDS mapping. (b)-(e) EDS mapping of the elements (a)-(e) Reproduced with permission from [41]. Copyright 2019, American Chemical Society. (f) Cyclic Voltammetry data showing difference in methanol oxidation using Au@Ag core shell and Au core AuAg alloy shell nanoparticles fabricated with the citrate method. Reproduced with permission from [246]. Copyright 2018, American Chemical Society. (g) HAADF-STEM images of $\text{Au}_{0.4}\text{Ag}_{0.6}/\text{ZIS}$ (h) H_2 production rate of the several nanostructures. (g)-(h) Reproduced with permission from [13]. Copyright 2020, Elsevier. 37

2.13	(a) Rate of yield of the nanostructures over different photocatalysts during CO ₂ reduction with H ₂ (b) Selectivity of CO and CH ₄ for corresponding samples. (a)-(b) Reproduced with permission from [337]. Copyright 2017, Elsevier. (c) Schematic of the working principle of the sandwich n-Cu ₂ O/AuAg/p-Cu ₂ O structure. (d) Cross-sectional view. Inset shows the top view of the sandwich structure showing AuAg alloy nanoparticles on p-Cu ₂ O (e) Incident photon to current conversion efficiency (IPCE) characteristics at 0.7 V _{RHE} . (c)-(e) Reproduced with permission from [192]. Copyright 2019, American Chemical Society. (f) Formation of colony of E.coli on the different nanostructures (g) Efficiency for killing of bacteria in dark and sunlight. Data shown as mean ± standard deviation. (h) Photothermal efficiencies of the nanostructures when exposed to sunlight. (i) Effect of the temperature (40°C-49°C) on E.coli killing efficiency. (f)-(i) Reproduced with permission from [379]. Copyright 2019, The Royal Society of Chemistry.	41
2.14	(a) Temperature rise from the initial temperature ($\Delta T = T(t) - T_0$) at the center of tumor ($r=0$) for monolayer graphene coated AuAg HNS with varying composition of alloy, as a function of the laser irradiation time t . Here the incident intensity is 0.3 W/cm ² with 4×10^9 particles/ml. Inset shows the schematic of the graphene coated AuAg alloy hollow nanoshell. Reproduced with permission from [83]. Copyright 2019, American Chemical Society. (b) Schematic of the colorimetric sensing with HRP-AuAg hybrid nanocage with Ag inside. TEM images of the HRP-AuAg hybrid cages (c) before and (d) after reaction with 1 mM H ₂ O ₂ in CA/SC buffer, pH 4.0 for 10 minutes in room temperature. (e) Schematic of the glucose sensing with GO _x and HRP-AuAg hybrid cages. (b)-(e) Reproduced with permission from [377]. Copyright 2019, The Royal Society Of Chemistry. (f) Schematic of the repeated liftoff process used for fabrication of plasmonic colour filter. (g) The dark field microscopic image of the plasmonic colour filter made of 10 nm of Au, Au ₇₀ Ag ₃₀ , Au ₃₀ Ag ₇₀ , and Ag. (f)-(g) Reproduced with permission from [134]. Copyright 2019, Nature Publishing Group. (h) AuAg nanoparticles along the long-axis (on-axis) and along short axis (off-axis) of the microtube. Raw trajectories are shown in light green while the median filtered traces are shown in green. Insets show the distribution of step sizes of the kinesin-1 head at 1 mM ATP Reproduced with permission from [14]. Copyright 2019, American Chemical Society.	43
3.1	The schematic of the 2 media model	47
3.2	SEM images of 150 nm Au _{0.2} Ag _{0.8} films annealed at (a) 450°C for 1 h without preheating and adhesion layer, (b) 450°C for 1 h with preheating and adhesion layer, (c) 150°C for 1 h and then at 450°C for 1 h without preheating and adhesion layer. Inset show zoomed in images of the same.	49

3.3	SEM images of $\text{Au}_{0.2}\text{Ag}_{0.8}$ nanorods of length 100 nm and width 50 nm (a) not annealed (b) annealed at 450°C for 1 h (c) XPS analysis of 150 nm thin films of $\text{Au}_{0.2}\text{Ag}_{0.8}$ annealed at 450°C for 1 h. The dashed black line shows the beginning of the substrate and the shaded purple part denotes the depth inside the substrate.	50
3.4	SEM images of 150 nm $\text{Au}_{0.2}\text{Ag}_{0.8}$ films (without preheating and adhesion layer) annealed at (a) 300°C for 2 h (b) 300°C for 5 h. Inset shows zoomed in images of the same.	51
3.5	XPS measurements for an $\text{Au}_{0.2}\text{Ag}_{0.8}$ films annealed for 300°C for (a) 2 hours (b) 5 hours	51
3.6	XPS measurements for an $\text{Au}_{0.2}\text{Ag}_{0.8}$ films (a) annealed for 300°C for 8 hours (b) not annealed.	51
3.7	(a) Process flow for fabricating thin films with a specific stoichiometry; yellow denotes Au and grey denotes Ag. (b) SEM image of a double-layer film for $\text{Au}_{0.2}\text{Ag}_{0.8}$ before annealing. (c) SEM image of the same film after annealing. The insets in (b) and (c) show a magnified view. (d) Superimposed EDX maps for Au, Ag and Ti. (e) XPS analysis of the $\text{Au}_{0.2}\text{Ag}_{0.8}$ alloy, demonstrating a homogeneous alloy over the entire 150 nm depth. (f) Experimentally obtained ellipsometric data for pure Au, $\text{Au}_{0.2}\text{Ag}_{0.8}$, $\text{Au}_{0.5}\text{Ag}_{0.5}$ and pure Ag.	53
3.8	$\text{Au}_{0.5}\text{Ag}_{0.5}$ and $\text{Au}_{0.8}\text{Ag}_{0.2}$ thin films (a-b) SEM images. Inset shows magnified view. (c-d) Superposed EDX maps of Au, Ag and Ti. (e-f) XPS analysis of the annealed films showing homogeneous alloy.	54
3.9	Ellipsometry carried out at 9 points of a 4-inch wafer of 150 nm thick (a) $\text{Au}_{0.8}\text{Ag}_{0.2}$ composition (bi-layer) annealed at 300°C for 8 h and 450°C for 30 min (b) $\text{Au}_{0.8}\text{Ag}_{0.2}$ composition (tri-layer,) annealed at 300°C for 8 h and 450°C for 2 h and 30 min.	55
3.10	Comparison of permittivity between values obtained from Rioux model and that measured using ellipsometry	57
3.11	SEM images of 150 nm AuAg thin film alloys taken right after annealing (on float glass substrate) and after 4-5 months after annealing (on Si substrate)	58
3.12	SEM images of 150 nm $\text{Au}_{0.8}\text{Ag}_{0.2}$ thin film (a) not annealed after deposition (on float glass substrate) (b) annealed at 300°C for 8 h and 450°C for 30 min (on float glass substrate). SEM images of 150 nm $\text{Au}_{0.8}\text{Ag}_{0.2}$ thin film after 4.5 months (c) not annealed (on Si substrate) (d) annealed at 300°C for 8 h and 450°C for 60 min (on Si substrate).	59
3.13	Fabrication and optical characterization of alloyed nanostructures. (a) Process flow. SEM images of an array of $\text{Au}_{0.2}\text{Ag}_{0.8}$. The colour code is same as Fig. 3.7a. (b) 400 nm × 50 nm rods and (c) 260 nm equilateral triangles before (top row), after (middle row) low temp annealing at 300°C for 8 hours followed by 450°C for 30 min, as well as (bottom row) high temp. annealing at 800°C for 3 hours. The insets show a single nanostructure from the corresponding array.	61
3.14	EDX images of the nanotriangle showing distribution of Au, Ag and superimposed image of Au and Ag distribution.	62

3.15	Fabrication and optical characterization of Fano resonant structures. (a) SEM images of a $\text{Au}_{0.8}\text{Ag}_{0.2}$ 4-rod Fano-resonant structure before and after low. temp annealing. (b) Calculated and (c) measured optical spectra of the Fano-resonant structures with different stoichiometries. Measurements of the Fano resonant structures were performed by Jeonghyeon Kim.	63
3.16	The scatterings of the Fano resonant structures at different alloy compositions were imaged using an inverted optical microscope. The dark-field imaging was realized with a 45-degree glass plate with a circular mirror at the center, which reflected the incident light from a halogen lamp (grey columns) and transmitted the high-angle component of the back-scattered light from the sample (yellow columns). Once confirmed at the imaging CMOS camera, the same scattered signal was sent to a spectrometer, and the scattering spectrum for a single nanostructure was measured. Figure from Jeonghyeon Kim.	64
4.1	Figure shows a representative wafer map with alignment markers used for fabricating binary metasurfaces. The white dashed square shows the prealignment marker. It consists of an array (29×29) of squares of side $10\mu\text{m}$. There are 8 such arrays. During each exposure one of these arrays are used for alignment. The 5 black cross shows the region of global marker while the green crosses shows the local alignment markers. Both the global markers and local markers consists of an array (3×3) of squares of side $10\mu\text{m}$ each. During each exposure, one of these squares are used as markers. The number of global markers is constant while local markers used are at the edges of each 1 cm chip. This array of 3×3 is present at the edges of each 1 cm square (marked in the figure). However, with each job the position of the chips vary, hence varying the number and the positions of the local markers.	67
4.2	SEM image of array of (a) nanodisks (b) nanorods (c) nanotriangles with bad alignment. The scale bar in (b) shows that the successive layer is misaligned by 500-600 nm.	68
4.3	The figure shows the schematic of the 3 step e-beam alignment process used for fabrication of alloyed binary metasurfaces. The numbers in bold in the left denotes the exposure number.	69

4.4	Alloyed metasurfaces. (a) Simulated reflectance and phase for alloyed meta-atoms with different stoichiometries. The inset shows the meta-atom composed of an alloyed disc with diameter $d = 110$ nm, height $h = 50$ nm, positioned atop an Al mirror with a SiO_2 spacer of thickness $t = 100$ nm. The period is $p = 300$ nm. (b) Simulated and measured reflectance spectra for different disc stoichiometries. (a-b) Simulations and measurements done by Hsiang-Chu Wang. (c) SEM image of the hologram device and its optical projection under (d) horizontally and (e) vertically polarized light. (f) SEM image of the FZP with focal length $f = 400$ μm and $\text{NA} = 0.35$. (g) Intensity distribution at the focal plane and (h) normalized intensity profile at the centre of the focal spot. The insets in panels (c) and (f) emphasize with colours the two different stoichiometries used for the meta-atoms. (d-e,g-h) Measurements done by Hsiang-Chu Wang.	70
4.5	(a) Optical setup for measuring reflectance. A silver (Ag) mirror is utilized as reference. The sample is illuminated with a Fianium supercontinuum white light source. A linear polarizer is also applied. Spectra are measured with the spectrometer at the 3 rd image plane. (b) Optical setup for measuring metahologram. The focal spot is captured at the 2 nd Fourier plane. The focal spot can be distinguished from the normal reflection with the sample tilt few degrees. The normal reflection is blocked in the 1 st Fourier plane. Figures taken from Hsiang-Chu Wang.	71
4.6	Optical setup for measuring metalens. The focal spot is captured at the 2 nd Fourier plane. The focal spot can be distinguished from the normal reflection with the sample tilt few degrees. The normal reflection is blocked in the 1 st Fourier plane. Figure taken from Hsiang-Chu Wang.	72
4.7	The schematic shows how hot electrons are excited on a metal- TiO_2 interface. (a) shows the band diagram of a bare TiO_2 substrate. The blue line shows the Fermi energy level (b) shows a Au- TiO_2 interface. The distribution of the hot electrons and holes in the non-equilibrium condition is shown. The TiO_2 bends to have a continuous Fermi energy level across the interface. (c) shows the AuAg alloy- TiO_2 interface. (b-c) The x-axis on the right of the metal- TiO_2 indicates the distance x from the interface into TiO_2 , while the x-axis on the left of the interface denotes the carrier excitation rate. Schematic adapted from [336] while the carrier excitation rate profile is adapted from [24].	75
4.8	Schematic of the steps of fabrication for AuAgNPs- TiO_2	76
4.9	SEM images on nanoparticles on fused silica substrates (a) AuNPs (b) AgNPs (c) AuAgNPs (d) EDX images showing presence of both Au and Ag homogeneously in the nanoparticle	77
4.10	Particle size distributions for (a) AuNPs, (b) AgNPs, and (c) AuAgNPs on fused silica substrates corresponding to Fig. 4.9	78

List of Figures

4.11 Optical characterization. (a) Absorption spectra of the bare AuNPs, AgNPs, and AuAgNPs. (b) Absorption spectra of the AuNPs-TiO ₂ , AgNPs-TiO ₂ , and AuAgNPs-TiO ₂ . Absorption spectra were plotted by 1-Reflection-Transmission. Measurements performed by Dr. Madasamy Thangamuthu.	79
4.12 Schematic drawing of the (a) 3 electrode system. Adapted from [390] (b) electrochemical photocurrent measurement setup. Figure from Dr. Madasamy Thangamuthu.	79
4.13 Electrochemical photocurrent responses of the electrodes measured in the 0.1 M KNO ₃ solution containing 10% ethanol under $\lambda=620\pm40$ nm (a, b and e) narrow-band irradiation with a 1mW cm^{-2} power. (a) Photocurrent responses of the bare AuNPs, AgNPs, and AuAgNPs. (b) Photocurrent responses of the TiO ₂ , AuNPs-TiO ₂ , AgNPs-TiO ₂ , and AuAgNPs-TiO ₂ . (c) Photocurrent changes (ΔI) of the TiO ₂ , AuNPs-TiO ₂ , AgNPs-TiO ₂ , and AuAgNPs-TiO ₂ . (d) Photocurrent response of the AuNPs-TiO ₂ measured under $\lambda=385\pm20$ nm irradiation. (e) Photocurrent response of the AuNPs-TiO ₂ measured under $\lambda=620\pm40$ nm irradiation. (f) The hot electron extraction rate (right side) and the IPCE of the AuNPs-TiO ₂ , AgNPs-TiO ₂ , and AuAgNPs-TiO ₂ (left side). Measurements performed by Dr. Madasamy Thangamuthu.	81
4.14 (a) The photocurrent responses (ΔI) observed for TiO ₂ under various excitation energies showing that the defect sites were not linear (b) The stability of nanoparticles integrated TiO ₂ electrodes observed in terms of the photocurrent responses (ΔI) observed for Day 1 and Day 30. Measurements performed by Dr. Madasamy Thangamuthu.	82
4.15 SEM images of nanoparticles fabricated on ITO substrates for photochemical measurements (a) Au (b) Ag (c) AuAgNPs.	83
4.16 (a) General schematic of the process for fabrication of broadband absorber system with metal mirror. SEM image of the (b) Al ₂₀₀ -TiO ₂ -AuNPs (c) W ₅₀ -TiO ₂ -AuNPs (d) W ₂₀₀ -TiO ₂ -AuNPs on fused silica substrates.	86
5.1 (a) Geometry of the hybrid metal-dielectric nanoantenna. k denotes the propagation direction of the incident wave, whereas E denotes the direction of the electric field. SEM images of the nanoantenna array with a period of 670 nm: (b) top view and (c) 52° tilt; the inset shows the cross-section, made by Focussed Ion Beam (FIB) etching, of a single nanoantenna. (d) Process flow for the fabrication of the hybrid nanoantenna	91

5.2	Multipole decomposition using vector spherical harmonics for a single (a) 60 nm thick Al disk (b) 220 nm thick Si cylinder (c) hybrid nanoantenna comprising these two elements with a 75 nm thick air spacer. ED, MD, EQ and MQ denote the electric dipole, the magnetic dipole, the electric quadrupole and the magnetic quadrupole, respectively. (d) Contribution of the different multipoles from the Al disk and the Si cylinder to that of the hybrid nanostructure. The red curves in (a)-(d) represent the scattering cross-section of the nanostructure, which is equal to the sum of all the multipoles considered. The individual multipoles in (c) are decomposed in (d) where the contributions from the Al disk and the Si cylinder are plotted separately.	93
5.3	Simulations for (a) a 60 nm thick Al disk (b) a 220 nm thick Si cylinder, and (c) the hybrid nanoantenna comprising these two elements with a 75 nm thick air spacer, for four different background refractive indices corresponding to different mass percentages of glucose in the solution. The evolution of 1 (panel a), 4 (panel b) or 5 (panel c) spectral features as a function of the background is indicated with color dots and corresponds to the values reported in Table 5.1.	95
5.4	Experimental results for bulk refractive index sensing performed with the hybrid nanoantenna with four different glucose solution as background. The red dashed curve show the calculation for an air background ($n=1$), scaled to the same magnitude as the experimental data.	97
5.5	(a) Geometry of the hybrid nanoantenna with 50 nm undercut in SiO_2 . Surface plots of electric field amplitude enhancement (the amplitude of the incident field is 1) in the yz plane for a periodic array of hybrid nanoantennas (b) with and (c) without a 50 nm undercut in the SiO_2 . The outline of the nanoantenna is indicated in black. (d) Top view SEM image of the hybrid nanoantenna array with a period of 670 nm. (e) SEM image of the hybrid nanoantenna array imaged at a tilt of 52° to evidence the undercut in the SiO_2 spacer. The inset shows the cross-section made by FIB for a single nanoantenna. (f) Experimental transmittance for bulk refractive index sensing performed with hybrid nanoantenna with a 50 nm undercut in the SiO_2 for four different background conditions.	98
5.6	Distribution of $ E $ field: (a) $ E_x $ (b) $ E_y $ and (c) $ E_z $ for the nanoantenna with undercut shown in Figure 5.5b, at $z=256$ nm and across y . The shaded region shows the region inside the dielectric spacer.	99
6.1	Scattering cross section (SCS) and its decomposition into Cartesian multipoles: electric dipole (ED), magnetic dipole (MD) and electric quadrupole (EQ). (a) Constant height $H = 220$ nm and varying radius R , (b) constant radius $R = 235$ nm and varying height H , (c) varying height H and radius R . All dimensions are in nm and the orange dashed line traces the position of the anapole state. . . .	107
6.2	Resonance peak positions of the ED and MD varying with the change in dimensions. The circles refer to peaks at lower energy while the diamonds refer to peaks at higher energy.	108

List of Figures

- 6.3 SCS and its Cartesian multipoles decomposition for a Si cylinder ($R = 235$ nm, $H = 220$ nm) covered with an Ag disk of varying thicknesses t . Note that for $t = 15$ nm, the SCS at 1.11 eV is solely defined by the MD. All dimensions are in nm. 109
- 6.4 SCS and its Cartesian multipoles decomposition for a Si cylinder ($R = 235$ nm, $H = 220$ nm) covered with a $t = 60$ nm thick Ag disk of varying radii r . All dimensions are in nm. 111
- 6.5 SCS and its Cartesian multipoles decomposition for a Si cylinder ($R = 235$ nm, $H = 220$ nm) covered with an Ag disk ($t = 60$ nm, $r = 235$ nm) placed at a spacing distance δ . The first two panels show the response for the individual cylinder and disk. 112

List of Tables

5.1	Sensitivity values for a single nanoantenna computed from Fig. 5.3a-c	96
5.2	Sensitivity values obtained from the experiment and corresponding spectral range.	96
5.3	Sensitivity values obtained from the experiment and corresponding spectral range for nanoantennas with 50 nm undercut.	100
6.1	The spectral changes due to changes in the Si cylinder radius R and height H , the metal disk thickness t and radius r , or the spacing distance δ . The symbols indicate: \leftarrow = redshift, \rightarrow = blueshift, \uparrow = increase, \downarrow = decrease, \times = no significant change.	113

1 Introduction

The field of plasmonics relies on the interaction of an incident electric field with noble metal nanostructures, which exhibit a strong electric field enhancement due to resonant oscillations of the free electrons [369, 229, 213]. This ability of the metal nanoparticles to confine light at subwavelength scales is key to the success of plasmonics [213, 300], which has gained tremendous success in biosensing [220, 363, 262], surface enhanced Raman spectroscopy (SERS) [211, 142] and metal enhanced fluorescence [56]. Thanks to the technological advancement in nanofabrication tools that enables large area fabrication, in recent times it has also shown promising potential in demonstrating metaholograms [63] and metasurfaces with sophisticated functionalities, e.g. generation of vortex beams [223, 221], spatial separation of left and right circularly polarized beams [304], to name a few. In all these cases, Gold (Au) has been the material of choice over Silver (Ag) due to its superior stability, in spite of its higher losses. However, with the progress of the field, in recent times there has been a search for alternative materials to extend the limits of current applications. The community is looking for materials with lower losses than Au and higher stability than Ag, as well as for those that can exploit the plasmon resonances over the entire visible and near infrared spectrum [384, 234, 310]. In this thesis, I contribute to this search by providing fabrication techniques for nanostructures with alternative materials, AuAg alloys of varying stoichiometries and metal-dielectric hybrid nanoantenna with a geometry where the metal is stacked on top of the dielectric.

AuAg alloys have been widely used for a long time [254] in several applications like SERS [142], photocatalysis [147], dye-sensitized solar cells [287], etc. AuAg alloys are more stable than pure Ag [84] and are capable of tuning the plasmon resonance between that of pure Au and Ag [261]. One of the oldest publications on AuAg alloys dates back to 1886 [291] followed by numerous publications over the years [87, 26, 214]. However, in all these cases the alloys are fabricated using bottom-up approaches [101]. Since the plasmonic response relies on the precise shape of the nanostructure, top-down approaches like e-beam lithography, focussed ion beam milling (FIB) providing high degree of control and uniformity over the geometry, are preferred over bottom-up approaches where the level of control is lower. This dearth of top-down nanofabrication processes has motivated me to develop a low temperature

alloying technique for AuAg alloyed nanostructures of various stoichiometries using top-down nanofabrication processes.

In addition to pure plasmonic nanostructures, hybrid metal-dielectric nanostructures have recently come up as a promising system that can circumvent the drawbacks of both metal - high losses - and dielectric - low electric field enhancement [182]. Due to the presence of dielectric, these nanostructures support higher order multipoles, which can be tailored for highly directional radiation [293, 116, 126] making them excellent candidates for fluorescence enhancement [64, 330, 327, 328]. Hybrid nanoantennas have also been used in subtractive colour filtering [408], and in non-linear applications like efficient generation of second [100] and third harmonics [309]. Intrigued by such unique properties, I have demonstrated such an hybrid metal-dielectric nanoantenna with stacked geometry (metal on top of dielectric) for bulk refractive index sensing.

1.1 Thesis objectives

The objective of this thesis is to develop nanofabrication techniques and procedures using top-down techniques like e-beam lithography, to fabricate nanostructures with alternative materials. With this objective in mind, two main techniques have been investigated. One pertaining to the development of a low temperature alloying process for fabricating AuAg alloyed nanostructures, while the second one is the fabrication of hybrid nanoantennas containing both metal and dielectric. On the way to these development, efforts have also been made to understand the underlying working principles by undertaking a detailed and systematic analysis of the optical response of the nanostructures. Finally, different experimental applications of the fabricated nanostructures are demonstrated in fields such as meta-holograms, absorption or refractive index sensing.

1.2 Thesis organization

The thesis has been divided into two main parts. Part I details the fabrication of AuAg alloyed nanostructures and metasurfaces. This part is divided into three chapters. Chapter 2 gives a detailed review of the existing literature on AuAg alloys showing the importance and relevance of these alloys in nanophotonics. In Chapter 3, I detail the steps taken to develop a novel low temperature alloying process for fabricating AuAg nanostructures. It is followed by Chapter 4, which describes several applications performed with these AuAg alloys. Part II of the thesis deals with the work undertaken with hybrid metal-dielectric nanoantennas. This part is divided into two chapters. In Chapter 5, I describe the fabrication of hybrid nanoantennas with stacked geometry and its application in bulk refractive index sensing. Chapter 6 reports a systematic study undertaken to understand the effects of geometrical parameters on the spectra of the hybrid metal-dielectric nanoantenna. Finally, I conclude the thesis in Chapter 7 along with a brief outlook of some future works that can be undertaken with the processes

developed in this thesis.

Alloy nanostructures: New Fabrication techniques and their application

Part I

2 Importance and relevance of alloy in nanophotonics

In this Part I talk about how I have developed a new technology based on low temperature annealing for fabricating AuAg alloyed nanostructures. I apply this recipe to fabricate AuAg alloyed metasurfaces. I also undertake photoelectrochemical applications with AuAg alloys. Before I describe the technology developed and the applications undertaken it is essential to understand the importance of alloys in plasmonics. In this chapter I present a review showing the progress of the AuAg alloys with the help of literature obtained till date. I believe that this chapter will provide a sound background about the importance of alloys and the works done so far. This will also help the readers to understand later how our work on AuAg alloys is different from the existing literature. My contributions were performing the literature survey, organizing the relevant articles and writing the review manuscript presented in this chapter. Parts of this chapter will be published in scientific literature [278].

2.1 Introduction

Historians consider alloy a revolutionary discovery, so much so that they make it the basis for dividing the chronology of human history. The start of the Bronze Age at 300 B.C. marked a new era in human civilization. From that day onwards mankind has been using metals and alloys. With time the association with alloys have strengthened leading to invention of alloys like invar and steel that have changed the course of human history. Among all the alloys available to mankind the gold-silver alloy or “electrum”, known from the beginning of 3rd millennium B.C. [114], deserves a special mention here. With time it’s usage has evolved, from jewellery to coins for financial transactions in the old days to more modern applications like porcelain fusing [250] and coloured alloys [54]. To the author’s knowledge, one of the oldest publication in modern times talking about alloys is by Robert-Austen, in 1886 [291], where he talks about the colours imparted by alloys and metals. The advent of nanotechnology introduced a new branch of physics called plasmonics, which initially investigated the properties of pure noble metals, mainly gold and silver in nanoscale – the former due to its lack of reactivity and the later due to its low losses. But as every penny has two sides, so has the noble metals: Au has high losses while Ag is toxic for human applications. An increasing demand for plasmonic

applications and the need for customized optical properties have prompted a search for other plasmonic materials. This led scientists to use alloys [291, 219, 283], a mixture of two known metals resulting in a completely new material.

Gold and silver alloys have been one of the most widely used since they can be easily alloyed due to similar properties. They are both face-centred lattice, their melting points are close enough (1064°C for Au and 961.8°C for Ag) and their atomic radius is similar (both 144 pm), thus making them very much miscible with each other as shown in the solidus-liquidus curve in Fig. 2.1a. In this review, we focus only on alloys of Au and Ag in the perspective of nanotechnology. This choice is dictated by the prominent role both metals and their combinations occupy in current research and the ensuing rapidly rising body of scientific publications in chemistry and physics. There exist reviews talking about properties of noble metal alloys in general [87, 26, 101], their various fabrication methods [214, 51, 52, 366, 424, 414, 92] along with specific applications like electrochemical energy [406], photocatalysis [147], chemiluminescence [135, 274], dye-sensitized solar cells [287], and Surface Enhanced Raman Spectroscopy (SERS) [142]. The review is organized into 3 major sections. In the first section gives a brief introduction about alloys, their properties and advantages. This will help the reader appreciate the importance of alloys in nanotechnology and plasmonics. The next section describes the different fabrication methods used till date to produce alloyed nanoparticles. Finally, various applications of alloyed nanoparticles in nanotechnology are described. Before we proceed further it should be noted that throughout the entire text we refer the gold silver alloy as AuAg.

2.2 Understanding AuAg alloys

The concept of alloying demands our attention and appreciation as it can change the material parameters and thus the permittivity by tuning its composition [106, 261], a property unavailable by changing the dimensions of a nanostructure alone, as shown in Fig. 2.1b-c. The permittivity of a metal is a crucial parameter in understanding its losses and resonance frequencies, which becomes a decisive factor while choosing them for various applications. There are several models available to compute the permittivity of an alloy [261, 288], of which the one proposed by Rioux *et al* [288] is widely used. Here they use the parameters of three reference composition Au, Ag and $\text{Au}_{0.5}\text{Ag}_{0.5}$ to predict the permittivity of other compositions. The change in the permittivity due to alloying stems from the manipulation of the band diagram, which can be calculated either by density functional theory (DFT) [340, 180, 177, 236, 105, 146], the most widely known, or by other new upcoming methods [419, 124]. These techniques give a theoretical understanding as to how the bands of two pure metals hybridise resulting into new energy levels as shown graphically in Fig. 2.1d [177, 146]. They also provide insights as to how the arrangements of the atoms influence the band structure. Shayegi *et al.* [306] and Gong *et al.* [105] have experimentally verified these calculated band diagrams using longitudinal photodissociation spectroscopy [306] and X-Ray photoelectron spectroscopy (XPS) [105], respectively. Manipulation of the band diagram also leads to the change in the

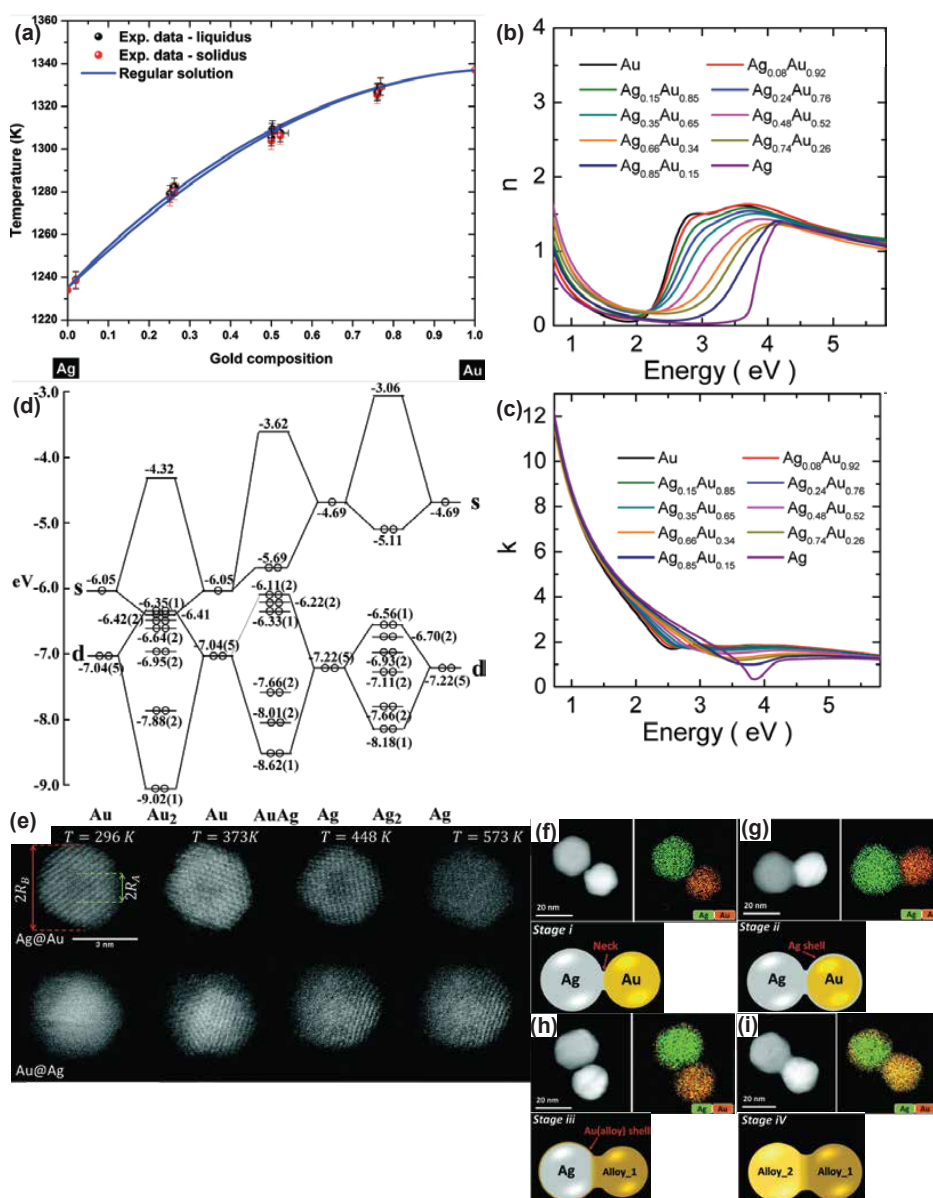


Figure 2.1 – (a) Bulk phase diagram of the AuAg alloy. Reproduced with permission from [114]. Copyright 2016, American Chemical Society. (b)-(c) n and k values of AuAg thin films of various compositions computed from experimentally obtained ellipsometric data. (b)-(c) Reproduced with permission from [261]. Copyright 2014, OSA. (d) Molecular orbital energies of the Au_2 , AuAg and Ag_2 . The occupied electrons are shown in circles while the value in parenthesis is the number of degenerate states of the d-orbital type molecular orbitals. Reproduced with permission from [177]. Copyright 2003, American Chemical Society. (e) TEM HAADF scans of the Ag@Au core-shell cluster as a function of temperature (upper row) and Au@Ag core-shell cluster scanned at the same temperature (bottom row). With increasing temperature the core-shell boundaries starts to blur out. (e) Reproduced with permission from [174]. Copyright 2018, The Royal Society of Chemistry. (f)-(i) HAADF STEM images along with EDX maps showing the different stages of evolution of the dimer during laser welding. The schematic of each stage is given below the SEM and EDX images. (f)-(i) Reproduced with permission from [395]. Copyright 2018, The Royal Society of Chemistry.

dispersion properties as can be seen for alloyed thin films of various compositions [105, 204]. Consequently, the reflection [106, 204] and transmission [106] varies for different compositions of the thin films. Like pure metal films, alloyed films also support surface plasmon resonances which can be used for sensing [405] or for calculating the binary diffusion constant in metal nanoalloy films [258].

The vast majority of literature available on AuAg alloys is based on nanostructures rather than thin films, since they can be used for applications that rely on the highly localized electric field around the nanoparticle. The variation of the spectra of the alloyed nanoparticles for different compositions has been theoretically calculated by several scientists using the boundary element method [97, 269], the discrete dipole approximation¹, [179, 387, 19] and multisphere T-matrix models [317]. Debela *et al.* have proposed a new model using quasistatic theory to compute resonance spectra of nanoparticles with Au_{0.5}Ag_{0.5} core, SiO₂ cover and Ag shell [61]. To distinguish between core-shell and alloyed nanoparticles the Vegard rule can be used [317]. The size effect of the nanoparticles on parameters like melting temperature, melting enthalpy and interaction parameters at both the solid and liquid phases have been calculated using a nanothermodynamic approach by Guisbiers *et al.* [114]. Experimental verification of optical spectra variation, with changing composition of the alloyed nanoparticles has been shown with UV-Vis spectrometer [387, 168, 104, 39].

Apart from the conventional methods, the advances in nanotechnology now provide insights into the nanoparticles at an atomic scale. Gottlieb *et al.* have shown an extremely precise way of fabrication of 25 atom AuAg alloy nanoparticles [111]. The number of atoms were precisely maintained with matrix-assisted laser desorption ionization mass spectroscopy (MALDI-MS). In situ heating capacity inside the transmission electron microscope (TEM) has given the opportunity to see the dynamics of alloying at nanoscale, either by heating an AuAg core shell nanoparticle [174] on a heatable carbon grid as shown in Fig. 2.1e, or by laser induced interwelding of a Au-Ag dimer [395] in a ultrafast transmission electron microscope (UTEM), as shown in Fig. 2.1f-i. More advanced experimental demonstrations providing in-depth knowledge of the near-field of the nanostructures have also been performed. The near-field of the particle has been probed with the near-field scanning optical microscope (NSOM) [104]. A variation of the spectra at nanoscale for different compositions has been shown by probing Au-Ag alloy clusters of various sizes with scanning tunneling microscope (STM) [22], while the spectral variation for a single alloyed nanobox has been measured using single-particle spectroscopy. Electron energy loss spectroscopy (EELS) in TEM is another well-known technique for near-field imaging of plasmonic excitations over large frequency ranges and with nanometric spatial resolution. This technique has been used to see the modes in the plasmonic structure [97] and how they vary with changes in composition [97, 388, 141] as shown in Fig. 2.2.

We hope that we have been able to provide the readers with theoretical understanding about the alloys and have also convinced them about their importance. With this we continue to the next section where we describe the different fabrication methods for fabricating alloyed

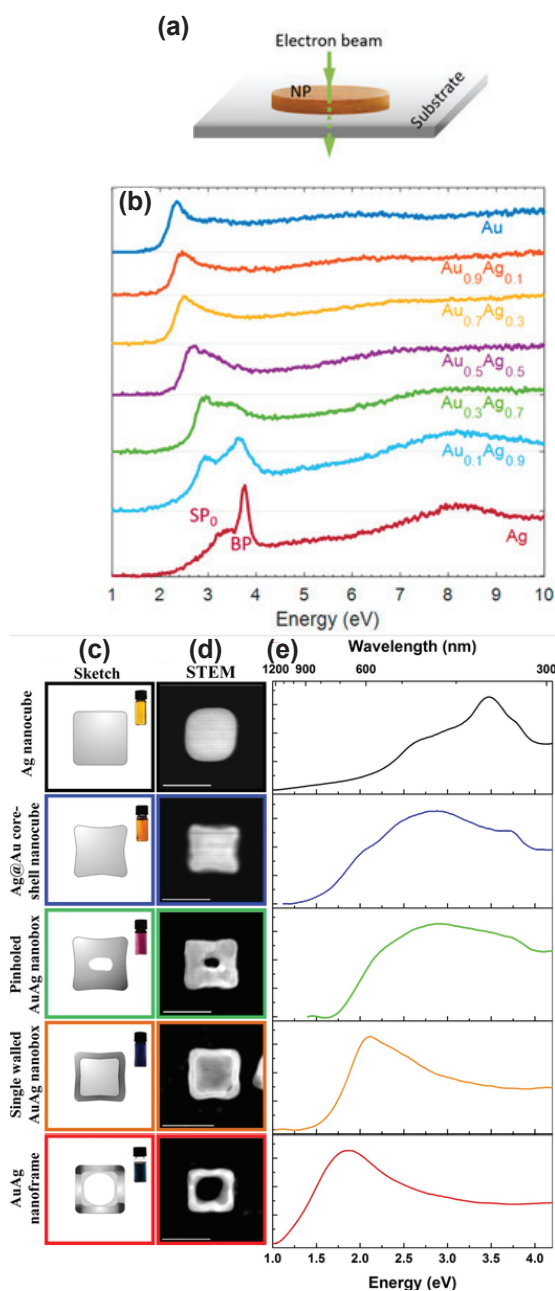


Figure 2.2 – (a) Schematic showing the configuration used for acquiring EELS data in (b). The electron beam is traversing the center of the particle. (b) The EELS spectra obtained for AuAg alloyed disk for various composition with the configuration described in (a). (a)-(b) Reproduced with permission from [141]. Copyright 2019, American Chemical Society. (c) Structural sketches of the nanostructures mentioned outside each box. Inset shows the vial containing the nanoparticle solution. (d) Corresponding HAADF STEM images of the geometries shown in (c). (e) Corresponding EELS maps showing the evolution of the LSPR spectra of the nanoparticles. (c)-(e) Reproduced with permission from [97]. Copyright 2016, American Chemical Society.

nanoparticles.

2.3 Existing methods of fabrication

Equipped with an understanding about the basics of an alloy, let us now take a closer look at the several fabrication techniques used for fabricating AuAg alloys. To the author's knowledge, almost all alloyed nanoparticles reported in the literature are fabricated using bottom-up fabrication procedures of which solution phase synthesis is the most widely used technique followed by laser ablation. Top-down fabrication techniques like ebeam-lithography forming periodic structures has been used only by a handful of papers as reported in later sections. Apart from using these conventional techniques there are several novel techniques that have been reported in the literature. To accommodate for all these fabrication techniques mentioned before, we have divided the available literatures into six main subsections. The first four subsections report solution-based fabrication techniques while the latter two report techniques involving laser ablation and all other miscellaneous techniques, respectively.

2.3.1 Chemical synthesis

One of the most used method for fabricating alloyed nanoparticles is the reduction of the metal salts in a suitable solvent with various reducing agents [101, 52, 366, 349]. One of the oldest literature available on nanosynthesis of alloy is by Papavassiliou *et al.* where the AuAg colloids were fabricated by passing an AC signal through an AuAg cover at the end of the Pt electrode [254]. Depending upon the shape, composition and morphology of the desired product, various solvents and reducing agents have been used in the literature till date. Moreover, additional control over the fabrication process can be achieved by controlling other parameters like pressure, temperature, etc. González *et al.* have provided insights into the most commonly used method of AuAg alloy formation by doing a time-resolved study of the formation of the alloy by monitoring the UV-Vis spectra [292]. The investigation was done during boiling of AgNO₃ and HAuCl₄ in the presence of sodium citrate. This study has shown that the gold and silver particles nucleate separately but the lattice arrangement eventually leads to the formation of alloy nanoparticles with expected composition. Blommaerts *et al.* have studied the formation of Au-Ag alloy by reduction of AgNO₃ and HAuCl₄ in the presence of sodium citrate in further details [28] as shown in Fig. 2.3a. They have performed EDX measurements for samples taken after 4, 7, 10, 13 and 16 min after the reaction started. The EDX plot shown in Fig. 2.3a indicates that in the initial phase of synthesis it forms an homogeneous alloy whereas as time progresses it forms more like a core-shell particle with an Au enriched core and Ag enriched shell. Moreover, they have also shown that in reality the final nanoparticles have a radially varying composition of the alloy, instead of the common belief that it forms an homogeneous alloy of a single composition. Finally they have concluded that the spectral broadening of nanoparticles can be attributed more to this varying composition rather than particle size distribution. Nanoparticles prepared by this conventional method

also showed multiple twins and stacking faults, as reported by Link *et al.* [193]. The effects of temperature, pH, time of addition of reducing agent and ratio of Au and Ag on the size of the alloy nanoparticles has also been studied by Shaikh *et al.* [303]. The alloy nanoparticles fabricated by them were used for antibacterial studies against *Escherichia coli* and *Staphylococcus aureus*. Those prepared at lower temperatures of 60°C to 70°C are more active against *E. coli* while those fabricated in 80°C to 90°C are more active against *S. aureus*. The effects of Ar or O₂ gas on the morphology of the AuAg nanoparticles has also been studied [10]. Under Ar gas bubbling, the main products produced after heating for 10 min were polygonal Au core Ag-rich AuAg alloy shell particles and spherical Ag-rich AuAg alloy particles. They were modified to larger excentered Au@AuAg particles with an average diameter of 340 ± 106 nm after further heating for 20-50 min. On the contrary, under O₂ gas bubbling, major products after heating for 10 min were Au@Ag core-shell particles having a thin Ag shell, large Au-rich AuAg alloy particles and many small spherical Ag particles with an average diameter of 4 ± 2 nm. After further heating for 20-50 min, the Au@Ag particles fuse and aggregate to form spherical Au-rich AuAg alloy particles with an average diameter of 259 ± 37 nm.

Varying mole fractions of HAuCl₄ and AgNO₃ can also be reduced by sodium borohydride (NaBH₄) in the presence of sodium citrate as a capping agent [215]. NaBH₄ can also double as a reducing agent to synthesize AuAg alloys [102]. The use of NaBH₄ makes the process fast and eliminates the need for a second stabilizer like sodium citrate or high temperature. Here the temperature of the NaBH₄ solution and the order in which the Au and Ag salts are added decides the final structure. Ethylene glycol (EG) has also been used both as reducing agent and solvent to prepare AuAg nanoparticles. 2-hydroxy-2-propyl radical generated by photochemical cleavage of Irgacure-2959 (I-2959) can also be used as a reducing agent, to reduce HAuCl₄ and AgNO₃ in aqueous surfactant solution [107]. The surfactant used determines the nanoparticle architecture. When sodium dodecyl sulfate (SDS) is used as the surfactant, it promotes the formation of AuAg alloy nanoparticles, while the use of hexadecyltrimethyl ammonium chloride (CTAC) promotes formation of Au (core) and Ag (shell) nanoparticles. Ramirez *et al.* have shown the fabrication of AuAg nanoparticles by only using sodium citrate as the reducing agent without using any other protective or capping agent [318]. The metal concentration used here was very low, around 1.32×10^{-3} mM.

One pot synthesis of oleylamine coated monodisperse AuAg nanoparticles can be fabricated by simultaneous reduction of Au and Ag salts in organic solution [365]. The precursor ratio and the growth time decides the composition of the alloy. Oleylamine and octadecene has also been used as reductant and surfactant to form AuAg alloy by reducing AgNO₃ and HAuCl₄. Reducing and stabilizing agents like sucrose, ascorbic acid and rosalite, which are also low toxic and stable compounds can also be used to fabricate AuAg nanoalloys [32]. Trioctylphosphine (TOP), oleic acid (OAc) and oleylamine (OAm) have been used as stabilizing agents for fabrication of large area AuAg alloy nanoparticles via hot organic media [44]. During the synthesis, complexation between TOP and metal precursors are found, which slows down the rate of nucleation and leads to growth of large size AuAg nanoalloys. Crespo *et al.* have fabricated monodisperse Au-Ag alloy nanoparticles of different compositions through a mild

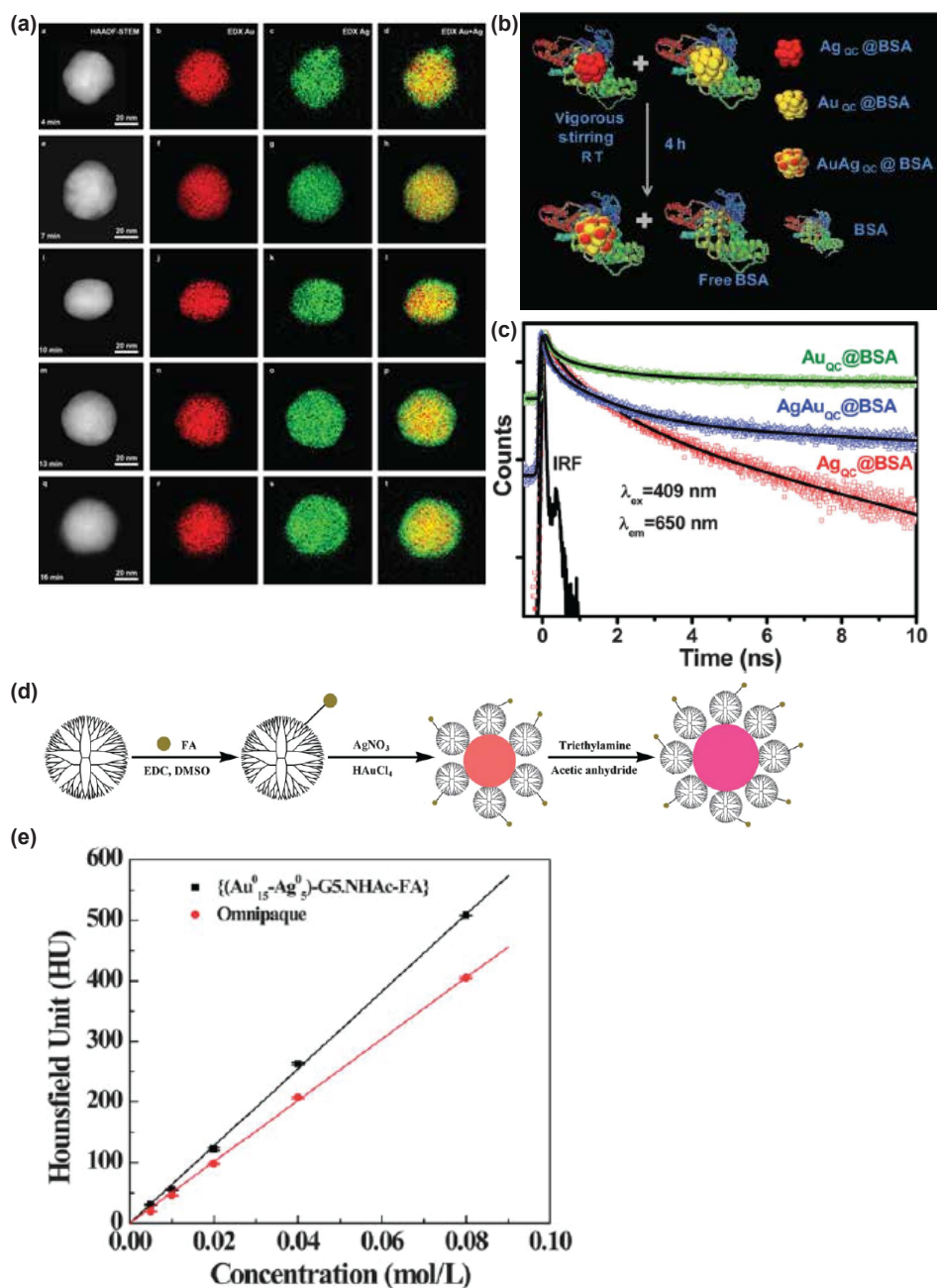


Figure 2.3 – (a) HAADF-STEM and EDX maps of the nanoparticles sampled at different times of the synthesis. Reproduced with permission from [28]. Copyright 2019, John Wiley & Sons, Ltd. (b) Schematic showing the fabrication of the AuAgQC by the QC-QC interaction. (c) Picosecond resolved fluorescence transients of AuQC, AgQC, AuAgQC.(b)-(c) Reproduced with permission from [228]. Copyright 2012, The Royal Society Of Chemistry. (d) Schematic of the fabrication of Folic acid modified dendrimer-stabilized AuAg alloy nanoparticles (e) Comparison of X-Ray attenuation intensity between Omnipaue and the before said AuAg alloy nanoparticles. (d)-(e) Reproduced with permission from [196]. Copyright 2013, The Royal Society Of Chemistry.

decomposition of the bimetallic precursor $[\text{Au}_2\text{Ag}_2(\text{C}_6\text{F}_5)_4(\text{OET}_2)_2]_n$ in an organic solvent using hexadecylamine (HDA) as a stabilizing ligand [53]. The alloy composition can be tuned by various combinations of the amount of HDA with solvents of different boiling points.

In the dendrimer mediated synthesis of AuAg alloys, the use of other reducing agents has been precluded by the use of amine terminated generation of 5 poly(amidoamine) dendrimers as stabilizers [197]. Keeping the total metal atom/dendrimer molar ratio constant, with the variation of Au content the alloy nanoparticles change from sphere to curved nanowires. Liu *et al.* have used folic acid (FA) modified amine terminated generation 5 poly (amido amine) dendrimers ($\text{G5.NH}_2\text{-FA}$) as the stabilizers in the fabrication of their FA modified dendrimer-stabilized Au-Ag alloy nanoparticles [196]. These dendrimer stabilized nanoparticle performed as superior CT contrast agent as compared to the conventional iodine-based agent named Omnipaque. The schematic of the fabrication process and their performance as compared to superior CT contrast agent are shown in Fig. 2.3d-e.

Apart from using several types of reducing and stabilizing agents to reduce the metal salts to form nanoalloys, there are also other existing methods to perform solution based synthesis of AuAg nanoalloys. Mohanty *et al.* have reported the synthesis of luminescent AuAg alloy quantum clusters of various composition in bovine serum albumin (BSA) for the first time [228] as shown in Fig. 2.3b-c. The unique properties of protein BSA, their foaming ability and zwitterionic character at the protein isoelectric point have also been used by Singh *et al.* to fabricate AuAg alloy nanoparticles [315]. The BSA coats and stabilizes the nanoparticles, thus eliminating the need of any additional stabilizer.

AuAg nanorods and nanowires are fabricated by rapidly diffusing Ag into preformed Au nanorods [117]. By varying the molar ratio of AgCl/Au nanorod seeds to different kinds of AuAg alloy nanostructures- AuAg nanowires and $\text{Ag}_{33}\text{Au}_{67}$ nanorods are fabricated. AuAg alloy with prismatic structures can be prepared at room temperature in aqueous solution by photoinduced conversion of spherical Au-Ag alloy nanoparticles [153]. Lesser known techniques like microwave heating can be used to fabricate AuAg alloy nanoparticles in ethylene glycol and glycerol in presence of PVP [259].

2.3.2 Annealing Au@Ag core-shell nanostructures covered with SiO_2 to form AuAg alloy

Till now we have seen how researchers have fabricated AuAg alloyed nanoparticles by use of chemical reagents. However, instead of fabricating AuAg alloys directly, many authors have resorted to heating a AuAg core-shell nanoparticle to form an alloyed nanostructure. Au@Ag core shell nanoparticles prepared through chemical synthesis have been in vogue for a long time [52]. These nanoparticles can then be covered in SiO_2 as an additional step and annealed at high temperatures to form alloyed nanoparticles. The SiO_2 covering serves multiple purposes. It prevents aggregation of nanoparticles during annealing and helps retaining the shape of the nanostructure [11]. This SiO_2 shell can then be etched away at

later stages [199, 417, 18, 240]. This technique is very useful to fabricate alloyed nanorods. Albrecht *et al.* have achieved an alloyed nanorod by annealing an Au@Ag core-shell nanorod geometry at 450°C in N₂ atmosphere to prevent oxidation of Ag [11]. Similar results can be obtained by heating the silica covered core-shell with a xenon lamp of 300 W [38]. Ni *et al.* have also shown that the homogeneous alloying can be attained at 450°C, while the shape can be retained upto 600°C [240] as shown in Fig. 2.4a-d. The silica covered Au-Ag nanorod core-shell geometry can also withstand higher temperatures e.g. 800°C for 3 h in Ar atmosphere [18]. Other geometries like nanocubes annealed at 700°C for 2 h [417] and nanospheres annealed at 950°C [199] has been obtained similarly. Further modifications had been done on the latter two nanostructures, where Ag has been selectively leached or dealloyed to result in a sponge like geometry which is ideal for SERS application [199, 417].

Shore *et al.* have fabricated AuAg nanoparticles by heating Au@Ag core-shell particles at 250°C without SiO₂ covering [312]. They have also shown that after making the Au core, the particles can be simultaneously annealed while making the Ag shell, to form AuAg alloy nanoparticles.

2.3.3 Green synthesis

In recent times there has been an effort to use biosynthesizers instead of chemical reagents to make the fabrication environment-friendly and reduce the amount of toxic waste. Emam *et al.* have synthesized AuAg alloyed nanoparticles with a resonant wavelength of 480-495 nm by using Arabic gum as the biosynthesizer [74]. It reduced metal ions to nanosized crystals and acted as crystal growth modifier to the so-called nanocomposite. The alloyed nanoparticles can also be fabricated using xylanases of *Aspergillus niger* L3 (NE), and *Trichoderma longibrachiatum* (TE) produced through the valorisation of corn-cob [73] or using cell-free extract of *Bacillus safenis* LAU13 strain [249]. The resultant nanoparticles show a plethora of virtues like excellent antibacterial and antifungal growth, catalytic degradation of dyes like malachite green and methylene blue, along with excellent antioxidant, anticoagulant and thrombolytic activities. Other biosynthesizer used for the green synthesis of AuAg nanoparticles include the extract of Chinese wolfberry fruit [326] and soluble starch [325]. The finished product acts as photocatalysts to reduce 4-nitrophenol. Nanoparticles showing enhanced electrocatalytic performance towards methanol oxidation can be fabricated using non-toxic milk thistle, *Silybum marianum*, by successive reduction [110]. Philip *et al.* has used *Volvariella volvacea*, a naturally occurring mushroom extract, both as reducing and protecting agent to fabricate AuAg alloyed nanoparticles [264]. AuAg nanoalloys showing better antipathogenic reactions can be prepared by using hydroxythyl cellulose as a superior, reducible, non-toxic, biodegradable polymer [5].

2.3.4 Galvanic replacement

Another prominent solution phase synthesis to produce AuAg alloyed nanostructures is galvanic replacement. A galvanic replacement reaction occurs when atoms of one metal with

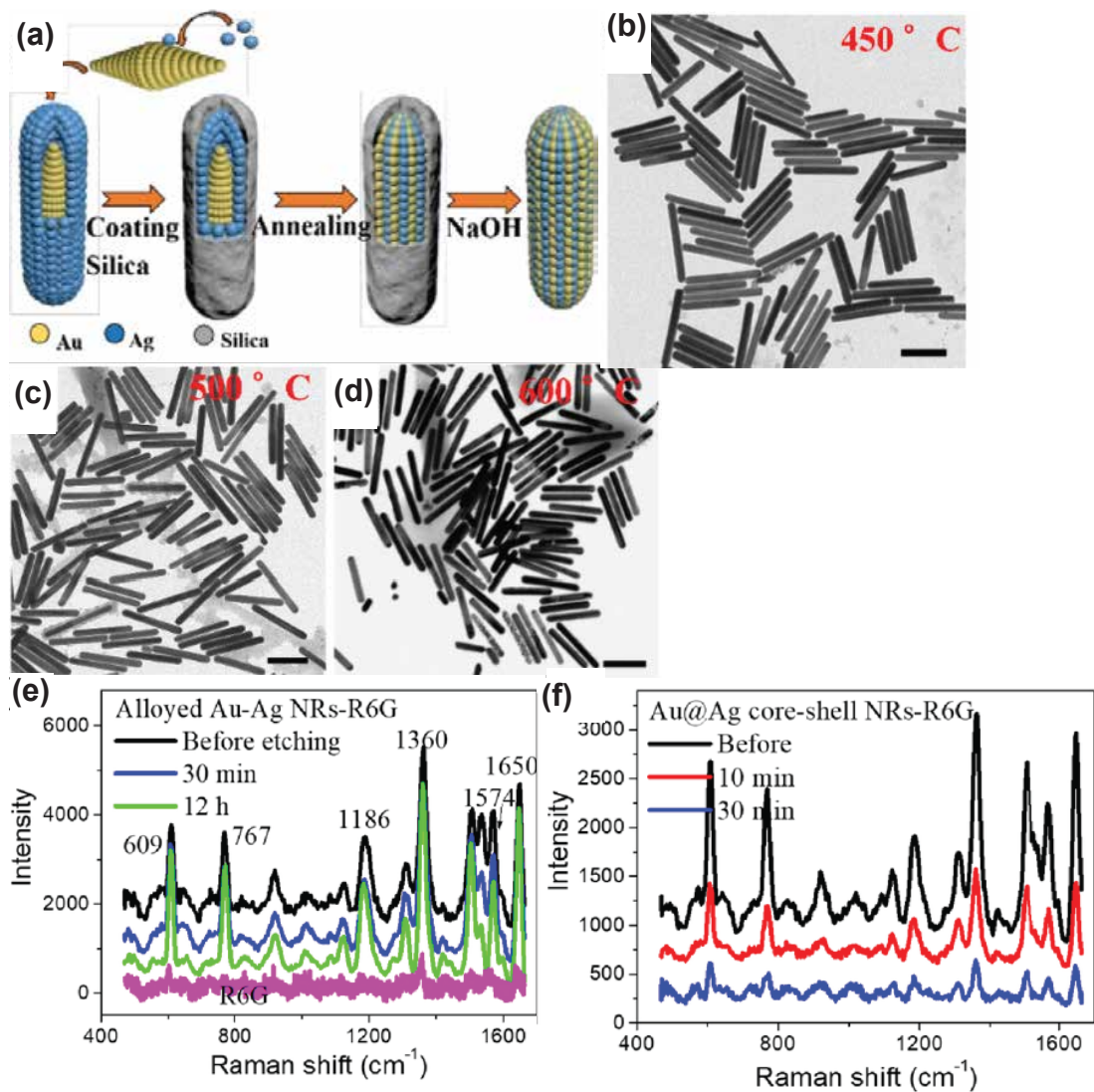
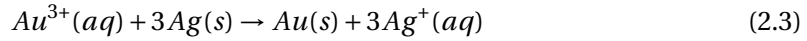


Figure 2.4 – (a) Schematic of the process showing how AuAg alloyed nanorods coated with SiO_2 are fabricated by annealing. (b)-(d) TEM images of the same nanostructures annealed at different temperature. SERS spectra of the R6G adsorbed on (e) AuAg alloyed nanorods (f) Au@Ag core shell nanorods before and after etching in NH_4OH and H_2O_2 . Reproduced with permission from [240]. Copyright 2019, , Chinese Laser Press.

lower electrochemical potential react with ions of another metal having a higher electrochemical potential in solution phase [51]. In that case, the metal gets oxidised and dissolves into the solution while the metal ion gets reduced and gets deposited in the solution. In our case Ag gets oxidised as its electrochemical potential is 0.80 vs S.H.E (Standard Hydrogen Electrode) which is lower than Au that gets reduced (electrochemical potential 1.50 vs S.H.E). The equations describing a typical galvanic replacement reaction with HAuCl_4 and Ag template is shown in Eqs. 2.1- 2.3:



Combined equation:



It is possible to produce alloyed AuAg nanostructures using a galvanic reaction since they are easy to alloy. Au diffuses into Ag as the reaction progresses producing alloyed nanostructures. In other cases where the interdiffusion of metals does not occur easily, core-shell nanostructures are formed. The ability to fabricate hollow nanostructures sets galvanic apart from other solution phase reactions [101, 51, 366, 424, 92, 67, 389, 185]. These hollow structures are ideal for the analyte to access the enhanced electric field and are thus used extensively in plasmonic application like SERS and biosensors as will be shown in the Sec. 2.4.2 and 2.4.1 subsequently. Galvanic replacement reaction shares a lot of similarity with the seeded growth technique. In both the cases you would need a template to start with. But in a seeded growth technique the template is not oxidised as is done in galvanic replacement [366]. It only strictly acts as the seed on which the secondary metal grows. As for the galvanic replacement, the final shape and the crystallinity of the nanoporous structure is similar to the template, only the dimension of the resultant structure is slightly larger. The steps of a typical galvanic reaction between Ag nanocube as a template and HAuCl_4 (both in 3D and in cross sectional view) is shown in Fig. 2.5a. As described in Eq. 2.3 for every 3 atoms of Ag one Au atom gets deposited. In the initial steps, as Ag is dissolved from the Ag nanocube in the solution, Au gets deposited, forming a thin shell and a pit from which Ag is dissolved as shown in step (A) of Fig. 2.5a. As the reaction progresses, the shell becomes slightly thicker and the pit widens, creating a hollow structure shown in step (B) of Fig. 2.5a. At this stage since Au and Ag can be easily alloyed due to their similar lattice parameters, the shell resembles an AuAg alloy as seen in step (B) of Fig. 2.5a. This alloying process can be modelled by Fick's second law of diffusion [101].

$$C_x = C_s - C_s \text{erf}\left[\frac{x}{2\sqrt{Dt}}\right] \quad (2.4)$$

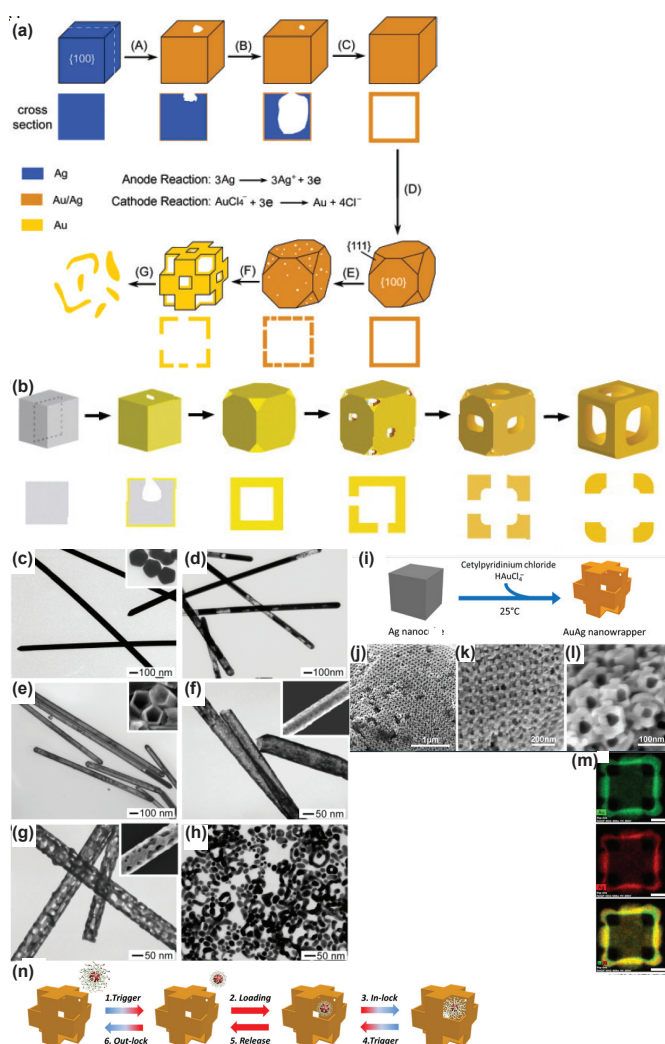


Figure 2.5 – (a) Schematic diagram showing the stages of a conventional galvanic reaction between HAuCl_4 and Ag nanocube (both in 3D and in cross sectional view). Reproduced with permission from [333]. Copyright 2004, American Chemical Society. (b) Schematic diagram showing galvanic replacement reaction with Ag nanocubes and AuCl_2^- (both in 3D and in cross sectional view). Reproduced with permission from [51]. Copyright 2010, Elsevier. (c)-(h) TEM images of different stages for galvanic replacement reaction between Ag nanowire and HAuCl_4 following the same steps shown in (a). TEM image of a (c) Ag nanowire and (d)-(h) for various volumes of 1 mM of HAuCl_4 . (d) 0.3 (e) 0.6 (f) 1.5 (g) 2.3 (h) 3.0 ml. The inset in (c) is the TEM image of the microtomed sample of silver nanowires, while the insets in (e)-(h) are their corresponding SEM images. (c)-(h) Reproduced with permission from [333]. Copyright 2004, American Chemical Society. (i) Schematic of the one step process showing AuAg alloy nanowrapper with Ag nanocube as a sacrificial template. (j) Large area (k) locally magnified (l) high-magnification SEM image. (m) HAADF-STEM characterization along with EDS maps of the nanowrapper (n) Schematic of the working principle using the "nanowrapper" as a cargo carrier and releasing of the DNA- capped nanospheres. (i)-(n) Reproduced with permission from [207]. Copyright 2018, American Chemical Society.

where D is the interdiffusion coefficient of the two metals, C_x is the atomic concentration of metal N as a function of time t at a distance of x from the M/N interface. C_s is the initial metal N at the M/N interface. The diffusion constant is a strong function of temperature. As the temperature increases the diffusion constant increases, increasing the rate of alloying and galvanic replacement [101]. Finally, a hollow nanostructure with an outer AuAg alloyed shell is produced as shown in step (C) of Fig. 2.5a. Until now the sharp edges at the nanocube were retained. If the reaction progresses, i.e. as additional HAuCl_4 is added, then Ag from the shell is selectively dissolved, which is called dealloying and gives rise to nanoporous structures. Moreover, as 3 Ag atoms dissolve to deposit one Au atom, more vacancies are created. In order to incorporate those vacancies at these points, the edges of the cube are reconstructed as shown in step (D) and (E) in Fig. 2.5a. On continued addition of HAuCl_4 all the Ag gets dissolved leaving pure Au nanoporous structures as shown in step (F) of Fig. 2.5a. With further addition of HAuCl_4 the structure collapses [333] as shown in step (G) of Fig. 2.5a.

It is worthwhile to note that if, instead of HAuCl_4 , AuCl was used, the final products would be very different, as can be seen in Fig. 2.5b [51]. The main difference between an Au(III) and Au(I) is that for the latter, one Au atom gets deposited for each dissolved Ag atom. The reaction with Au(I) gives rise to thicker alloyed shells, the pit from where the Ag disappears goes away faster than Au (I) and the tapering of the geometry occurs at an earlier stage than Au(III) [51], as can be seen in Fig. 2.5b. The traditional Ag nanocube template-based galvanic reaction can be modified to generate a “nanowrapper” type geometry instead of a nanoshell [207]. Here the surfactant cetylpyridinium chloride plays a crucial role in achieving openings at the corner of the cube and the cubic shape in one step. The schematic of the process is shown in Fig. 2.5i while the EDX mapping and HAADF STEM images are shown in Fig. 2.5m and Fig. 2.5j-l, respectively. These nanostructures show significant potential for ‘loading’ and ‘unloading’ of nanoscale cargo like the DNA coated nanoparticles shown in Fig. 2.5n. Until now we have only explained galvanic reactions with commonly used Ag nanocube as template. However, depending on the desired geometry, many other templates can also be used.

Rehn *et al.* have used Ag spheres as a template to finally fabricate smooth alloyed nanoshells with resonance wavelength tunable from 494 nm to 567 nm [285]. Daniel *et al.* have used a co-reduction assisted galvanic replacement reaction to form hollow nanostructures with smooth shells [273]. Here they have used hydrolysis of the Au precursor by varying the time and pH of the solution to control the previously mentioned technique. The degree of hydrolysis determines how smooth the cells are.

Galvanic replacement reactions performed with Ag nanorods and HAuCl_4 can give rise to a hollow nanorod [65], and a nanoporous nanorod [333]. Figure 2.5c-h reproduces the SEM images of the nanoporous nanorod taken at different stages of galvanic replacement reaction. Figure 2.6a-b shows the schematic of the fabrication of hollow alloyed nanorods and their corresponding TEM images. More complicated geometries like hollow AuAg nanorice, starting with Ag nanorice as template [407] shown in Fig. 2.6d-f, AuAg nanostars with Ag nanostars as template [96], and holey AuAg alloy nanoparticles with Ag nanoplates as templates [382]

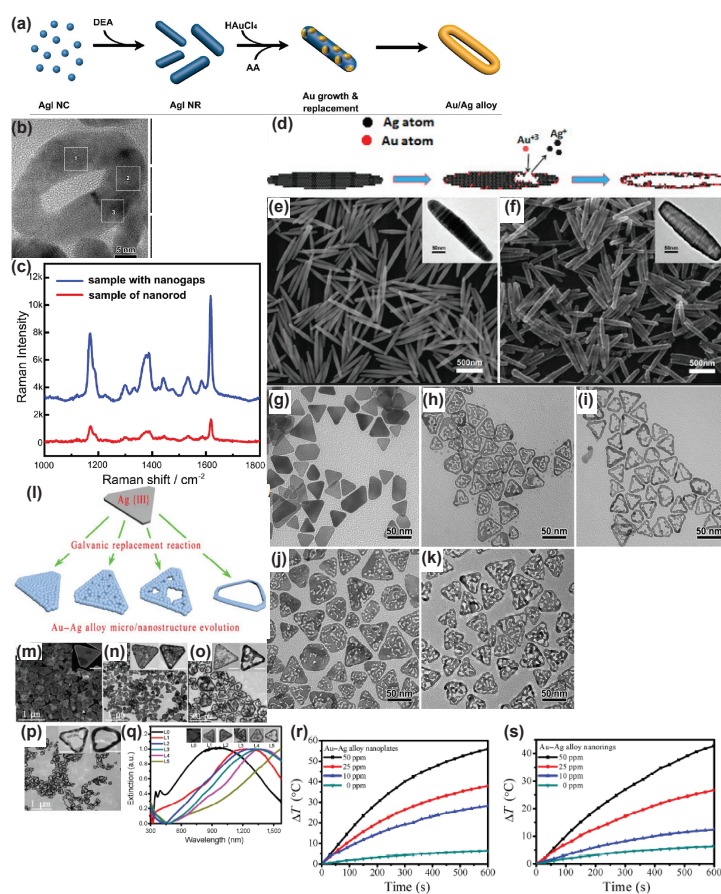


Figure 2.6 – (a) Schematic of the fabrication of the AuAg nanorod with gaps with a gap in the middle. (b) HRTEM image of the AuAg nanostructure with a nanogap inside. (c) Raman Spectra of CV (10^{-6} M) on the substrate with AuAg alloy with gap. The control sample with only nanorod without CV. The incident laser is 633 nm. (a)-(c) Reproduced with permission from [65]. Copyright 2019, Elsevier. (d) Schematic of the fabrication process to form the hollow nanorice. SEM and TEM image (in the inset) of the (e) Ag nanorice (f) AuAg hollow nanorice. (d)-(f) Reproduced with permission from [407]. Copyright 2017, MDPI. Synthesis of different type of AuAg holey nanoplates. (g) Ag nanoplates (h)-(i) Holey AuAg nanoplate as an intermediate and nanoframes, as the final product, formed by galvanic replacement reaction of HAuCl₄ and Ag nanoplates. (j)-(k) Holey nanoplates as an intermediate as final product formed by galvanic replacement between Ag nanoplate and Na₃Au(SO₃)₂. (g)-(k) Reproduced with permission from [382]. Copyright 2016, The Royal Society Of Chemistry (l) Schematic showing how a single Ag nanoplate can be evolved to numerous AuAg alloyed nanoplates (m) SEM image of the Ag nanoplate (n)-(p) The TEM image of the various evolved AuAg nanoplates shown in the schematic in (l). (q) Extinction spectrum of the various nanoplates evolved from the Ag nanoplate. (r) Change in temperature of the AuAg alloy nanoplates and (s) nanorings after being irradiated by 808 nm NIR laser. (l)-(s) Reproduced with permission from [270]. Copyright 2016, Springer.

shown in Fig. 2.6g-k can also be fabricated using a galvanic replacement reaction. Qian *et al.* have explained all the geometries e.g. nanorings, holey nanoplates and other intermediate geometries that can be obtained by galvanic replacement reactions of Ag nanoplates [270], Fig. 2.6l-q.

Multiple galvanic replacement reactions can be performed in series to form multiwalled nanostructures and nanorattles [332]. Using this technique Yang *et al.* have made an unique geometry: a Au@AuAg alloy nanorattle of 15 nm in size and a wall thickness of 2.5 nm [399] shown in Fig. 2.7a. In order to fabricate these nanostructures they have first fabricated a Au@Ag nanocubes via seed mediated growth followed by a thin shell deposition of Au, being reduced by ascorbic acid in alkaline conditions. Finally, in the last step, a galvanic replacement reaction ensued between Ag and HAuCl_4 to result in the Au@AuAg alloy nanorattle. The deposition of an Au thin shell in the second step, preceding the galvanic reaction, increases the robustness to the thin shells formed as end product.

Several parameters in the traditional galvanic replacement can be modified to form unique geometries. The temperature of a galvanic replacement reaction can be modified to form a desired morphology. Jang *et al.* has shown a low temperature mediated (at 4°C) partially inhibited galvanic reaction followed by etching of excess Ag in H_2O_2 to form a porous nanostructure [136]. Here they have started with a polyvinylpyrrolidone (PVP) coated Ag nanoparticle as a template that prevents expansion of the nanostructure and also provides mechanical support, thus preventing it from collapsing. The low temperature galvanic reaction leads to deposition of AgCl on the reactive sites as the reaction continues, thus inhibiting the further galvanic replacement process. This gives rise to clustered nanostructures on the Ag surface, which occur due to this low temperature process. After the completion of the galvanic reaction, the excess silver is etched, leaving a clustered nanoporous surface that can be used in chemo-thermo-gene-multitherapy. Nanoporous AuAg alloyed disks can also be fabricated by continuous dealloying of a AuAg alloyed solid disks [17]. Here, periodic AuAg alloyed disks are fabricated by ebeam lithography and successive deposition of 4 nm Au and 13 nm Ag for 4 times. The disks are annealed at 400°C for 30 mins to form an alloy. They are then dealloyed in nitric acid at 70°C nitric acid for 1 min to form a nanoporous structure.

Some authors have also proposed alternative routes of synthesis to stop the galvanic replacement reaction. Sun *et al.* have proposed a mechanism that puts the galvanic reaction backward [331] shown in Fig. 2.7e-i. Here they have performed a co-titration of AgNO_3 and HAuCl_4 in the presence of ascorbic acid and PVP in an aqueous solution of Ag nanocubes. The amount of AgNO_3 is made very high ($\text{AgNO}_3:\text{HAuCl}_4$ at a molar ratio of 3 and above) such that it puts the galvanic reaction at a backfoot, and performs a reduction by ascorbic acid of both Ag and Au ions to Ag and Au atoms, respectively. The reaction pathway resembles seed-mediated growth where Au and Ag atoms get deposited at the corners of the Ag nanocubes to perform the Au@AuAg alloyed nanocubes. Yang *et al.* have done a further analysis of this galvanic replacement reaction between Ag nanocubes and HAuCl_4 in the presence of ascorbic acid [403]. The presence of the ascorbic acid deviates the reaction from the traditional galvanic

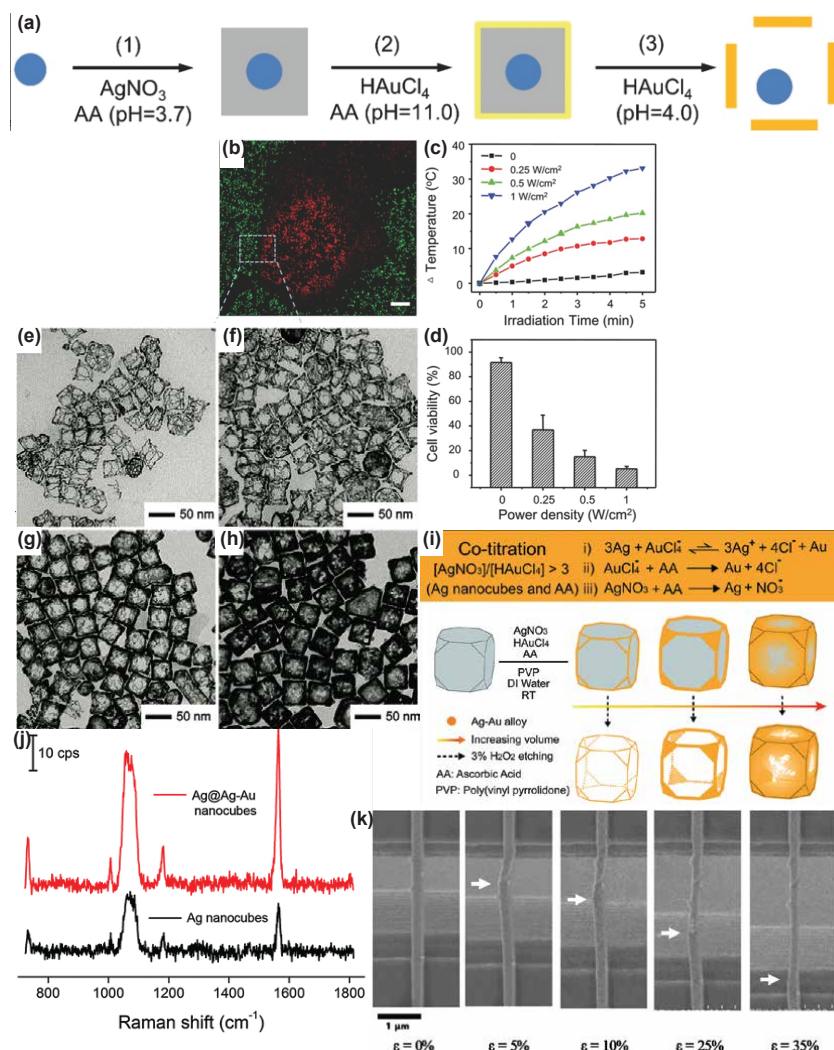


Figure 2.7 – (a) Schematic of the steps of the fabrication of Ag@AuAg nanorattle. (b) Florescence images of calcein Am (green, live cells) and red fluorescence dye (red, dead cells) contained MDA-MB-231 cells after laser irradiation. (c) Rise of temperature of the nanoparticle solution as a function of laser power. (d) Cell viability of MDA-MB-231 cells treated with nanorattles and 808 nm laser irradiation with various laser powers. (e)-(d) Reproduced with permission from [399]. Copyright 2017, John Wiley & Sons, Ltd. TEM images of Ag@AuAg alloy core frame nanocubes are etching with 3% aqueous H₂O₂. The samples were prepared by co-titrating various combinations of AgNO₃ (0.3 mM) and H₂AuCl₄ (0.1 mM) (e) 0.2 (f) 0.4 (g) 0.8 (h) 1.5 ml for each precursor. (i) Scheme showing top 3 competing equations involved in the co-titration process. The bottom schematic shows the transformation of the Ag nanocubes into three types of Ag@AuAg core frame nanocubes by increasing the volume of the co-titrated precursors, followed by etching of the Ag. (j) SERS spectra of the 1,4-BDT adsorbed on the Ag@AuAg core frame nanocubes at an excitation wavelength of 785 nm. (e)-(j) Reproduced with permission from [331]. Copyright 2015, The Royal Society of Chemistry. (k) In-situ testing of tensile strength of the Au₃₀Ag₇₀ alloy nanowire. Reproduced with permission from [155]. Copyright 2020, Elsevier.

replacement reaction, as in this case Ag^+ ions are reduced to Ag atoms as well. This reduction of Ag^+ ions does not occur in conventional galvanic replacement reactions. These Ag atoms along with Au gets deposited on the corners and edges of the Ag nanocubes. The amount of ascorbic acid decides the morphology of the structure. With the increase in the amount of ascorbic acid, the percentage of Ag increases as well, giving rise to AuAg hollow nanostructures with higher Ag content. Paramanik *et al.* have also proposed an anti-galvanic way to fabricate highly luminescent AuAg bimetallic alloy clusters [255].

A unique way of alloying-dealloying AuAg nanoparticles prepared by sol-gel techniques is reported by Paramanik *et al.* [267]. With the rise in temperature from 50°C to 400°C the Ag in the alloy gets oxidised thus red shifting the spectra towards pure Au. However, this phenomenon can be reverted back i.e. “realloying” can be ensued in the presence of trace amount of H_2 . Nishi *et al.* have shown a unique way of dealloying using a photochemical method to make nanoporous structures [243]. In this method, the scientists have fabricated AuAg nanoparticles on TiO_2 thin films. This configuration, when irradiated with light under water, leads to plasmon-induced charge separation at the alloy- TiO_2 interface. This causes dissolution of Ag from the alloy, creating nanopores. The rate of dissolution of Ag is controlled by the incident wavelength, thus causing different pore and ligament size.

2.3.5 Laser ablation

So far, we have discussed fabrication techniques involving chemicals only. Now we turn our attention to other existing techniques that do not require the use of chemicals. Laser ablation of targets to make small alloyed nanoparticles is one such widely used technique [414]. It has been shown in the literature that laser ablation produces both core-shells and nanoalloys, the latter being produced with higher ablation time [314]. A number of parameters control the final morphology of the alloyed nanoparticles. Nikov *et al.* [242] and Nastulyavichus *et al.* [235] have done a detailed study on the effect of the laser fluence, the wavelength and the film thickness on the size distribution and optical properties of the nanoparticles that are fabricated by nanosecond laser ablation on Au-Ag bimetallic films in double-distilled water. Nikov *et al.* have observed that spherical nanoparticles of 3-8 nm were fabricated for all wavelengths, whereas particles with larger diameters were only fabricated with $\lambda = 1064$ nm. They have also studied the effect of the laser fluence: a network of nanowires is formed for lower values whereas spherical nanoparticles are formed at higher values. Further effects of laser parameters and type of irradiated target on the final morphology and resonant wavelength of the nanostructure have also been studied [263, 167]. Scientists have shown that irradiating a mixture of Au and Ag^+ ions with a laser at 532 nm favours the formation of spherical alloy nanoparticles, whereas, on the other hand, if a mixture of Au and Ag nanoparticles is irradiated with a laser of wavelength 532 nm and 355 nm respectively, it produces nanoalloys with sintered structures [263]. They have further concluded that the morphology of the obtained nanoalloys depends not only on the laser wavelength but is also a strong concentration of the nanoparticles in the initial mixture. With increasing concentration, large scale interlinked networks are observed

upon laser irradiation. Another method of fabricating AuAg alloyed nanoparticles with laser is by laser-induced heating of Au@Ag core-shell geometries. Hodak *et al.* have shown that in the case of nanosecond excitation, alloying and reshaping from faceted and irregular particles into smooth spheres occurs at absorbed energies of 5-6mJ/pulse. Whereas for higher energies > 10 mJ/pulse fragmentation takes place. On the other hand, in the case of picosecond excitation (30 ps laser excitation) the thresholds for alloying/reshaping and fragmentation are lower: 1 and 4mJ/pulse respectively [128]. Densely packed Au-Ag nanoparticle thin film with a mean radius of 20-40 nm and a packing density of 10^{10} - 10^{11} particles/cm² can be fabricated by sequential ablation of pure Au and Ag targets [361]. Illumination with pulsed laser can be used to dewet an Au/Ag bilayer film to form nanoparticles [248]. The pulsed laser beam can be further modulated by transmitting through a mask [248]. When it falls on a surface, this spatially modulated beam, patterns the surface, thus creating the replica of the mask. Silica coated AuAg alloy nanoparticles can also be fabricated by a 3-step laser ablation technique, where a Si target immersed in water is ablated for a few minutes, followed by the addition of AgNO₃ and HAuCl₄, and laser ablation respectively [108].

2.3.6 Miscellaneous techniques of fabrication

Apart from the conventional, well-established techniques used to fabricate alloys, there are several unconventional and upcoming methods of fabrication, which deserve a mention. Kim *et al.* have fabricated defect free single-crystalline Au₃₀Ag₇₀ nanowires exhibiting high strength and deformability by topotaxial growth, Fig. 2.7k. The critical dimension at which these nanowires show superplastic deformation at $\lambda = 333$ nm, is two times higher than Au nanowires. Their value of stacking fault is 21mJ/m² as opposed to 31mJ/m² for pure Au nanowires [155]. Sakono *et al.* have fabricated AuAg alloy composite nanoparticles in the vapour phase using the evaporation/condensation method [296]. The alloy nanodots are fabricated by dewetting a bilayer of Au/Ag at 350°C-450°C for 5 h. Shin-ichi *et al.* have demonstrated a unique photochemical method for fabrication of AuAg alloy@AgBr crystal [236, 311]. They have explored two ways of achieving it. In the first case AgNO₃ is added dropwise to a KBr and HAuBr₄ solution. UV light is shone on this mixture, which results in AuAg alloy nanoparticles [311]. In the second method, an Au doped AgBr nanoparticle is formed on the mesoporous TiO₂ by successive ionic layer adsorption and reaction [236]. It is followed by UV radiation on the sample in methanol, yielding Au_xAg_{1-x} alloy particles of around 5 nm in the interior of AgBr. Periodic, well-controlled AuAg nanoparticles can be made by successive magnetron sputtering of Au and Ag on a substrate coated with polystyrene beads [413]. The deposition of Au is followed by annealing at 1000°C for 2 h. In the next step, Ag is also deposited and the film is then finally annealed at 750°C for 2 h. Self-organized fcc-AuAg (001) alloy nanodots can be fabricated by dewetting a bilayer of Au/Ag at 350°C-450°C for 5 h on an MgO substrate [144]. Co-sputtering or co-deposition of Au and Ag is a widely used technique to form an alloy. Several scientists have used this technique to form alloyed nanoparticles on different substrates. AuAg films have been deposited by RF reactive magnetron co-sputtering technique. The film can later be annealed at 400°C, 600°C and 800°C to form nanoparticles

[297]. With increasing temperature, the optical absorption peak redshifts from $\lambda = 400$ to 450 nm, the particle size decreases and the surface concentration increases. Nishijima *et al.* have talked about nanostructures fabricated by e-beam and alloy deposited by co-deposition [245]. AuAg nanostructures have also been fabricated by annealing bilayers of Au and Ag at 500°C for 24 h in a reducing atmosphere (4% H₂ in Ar) [247]. Here the nanostructures are defined by hole-mask lithography technique [342]. Gholamali *et al.* have demonstrated the redshift of the LSPR peak with the increase in AuAg alloy embedded in a diamond-like carbon film obtained by co-deposition of RF sputtering and RFPECVD methods with acetylene gas and AuAg target [98]. AuAg nanoparticles of various compositions can be formed by double target sputtering into the liquid [239]. Beyene *et al.* have shown fabrication of homogeneous AuAg alloy by vapour phase co-deposition technique in a Teflon AF matrix [25], which forms a polymer-metal nanocomposite. In this case, the Au_{0.5}Ag_{0.5} composition shows the least damping.

2.4 Applications of AuAg alloys

Having gained a detailed understanding of several techniques used for fabrication of alloyed nanoparticles, we now describe different applications where these nanoparticles are used. We have accommodated the large number of applications using AuAg alloy into 6 main subsections. Among these the first two subsections talk about the most established applications of plasmonic nanoparticles: Biosensors and surface enhanced Raman spectroscopy (SERS) while the next three are more recent ones: photocatalysis, photocurrent and photothermal. Finally, a miscellaneous subsection describes some of the unconventional and latest applications. We have also paid special attention in discussing the stability of the AuAg alloys. Before we proceed, it is worthwhile mentioning here that many of the literature mentioned in the fabrication section also demonstrate various applications and are also referenced here.

Biosensing and SERS are the two major applications that have immensely benefitted from the field of plasmonics [101, 142] and from its nanotechnology advances.

2.4.1 Biosensors

The interaction of analytes with metal nanoparticles providing high field enhancement leads to high sensitivity, high figure of merit and lower limit of detection (LoD) for the sensor. The lower toxicity [320], higher stability and the absence of any surface oxide has made Au the material of choice for biosensing. Recently, in order to take advantages of the low losses of Ag compared to Au, AuAg alloys have emerged for applications in biosensing. The use of alloys enables tuning the resonances by varying the stoichiometry, while having lower losses than pure Au and lower toxicity and higher stability than pure Ag.

Recently there has been quite a few publications using biosensors to detect heavy metals and poisons in food and water, thus leading to easier ways of maintaining a better quality of

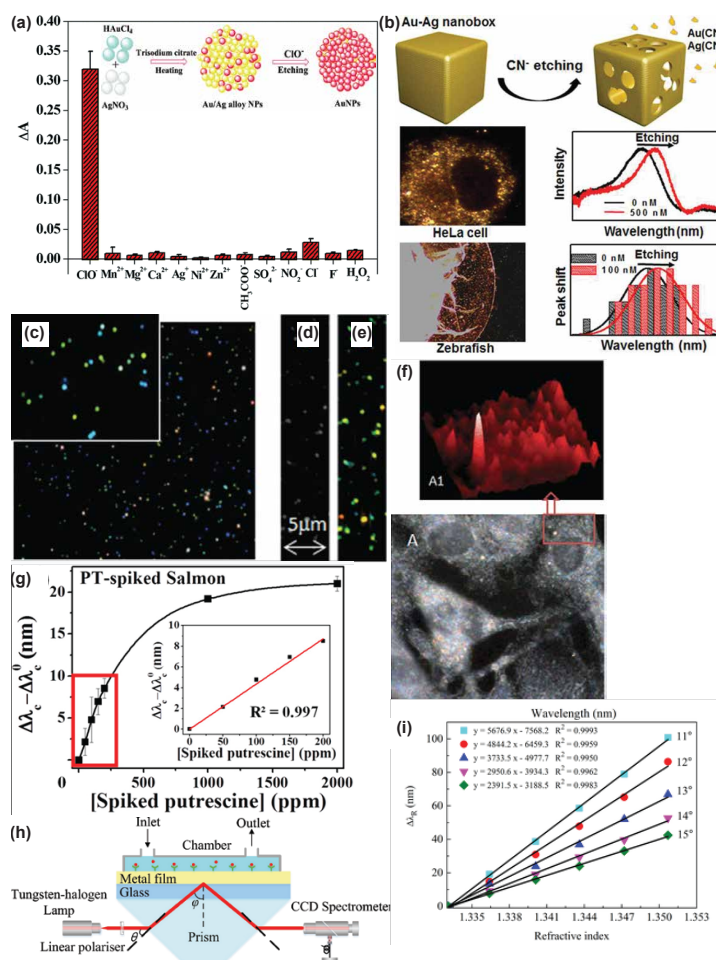


Figure 2.8 – (a) Specificity of the AuAg nanoparticle solution towards ClO^- . The specificity is monitored using the absorption intensity at 410 nm. The inset shows the schematic representation of the working principle of sensing ClO^- using AuAg alloy nanoparticles. Reproduced with permission from [305]. Copyright 2017, The Royal Society of Chemistry. (b) Scheme showing how the in situ sensing is done with AuAg nanoboxes using cyanide etching. The results obtained from HeLa cell and the Zebrafish using the same principle is also shown. Reproduced with permission from [371]. Copyright 2017, American Chemical Society. Experimental results obtained for three compositions of 60 nm nanoparticles (Au, Ag and $\text{Au}_{50}\text{Ag}_{50}$) (c) dark field microscopy images (d) Intensity and (e) colour image reconstructed from hyper spectral data obtained by the hyperspectral 2D scan performed with 100 \times immersion oil objective, 200 nm displacement steps, 3 s time constant and 100 μm spectrometer slit. (f) Darkfield imaging of MDA-MB-231 cells incubated with Au, Ag and AuAg nanoparticles for at least an hour. (c)-(f) Reproduced with permission from [260]. Copyright 2014, The Royal Society of Chemistry. (g) The response of the hollow AuAg nanoparticles (HGN) fabricated on inkjet substrate towards 20 g of salmon spiked with putrescine (PT) an biogenic amine found in spoiled foods. (0-2000 ppm). The background response from the blank sample has always been subtracted. Reproduced with permission from [350]. Copyright 2017, American Chemical Society. (h) Linear dependence of $\Delta\lambda_R$ for various concentration of aqueous sodium chloride. (i) Schematic of the SPR sensor using wavelength interrogation technique implemented with Kretschmann configuration. (h)-(i) Reproduced with permission from [405]. Copyright 2020, Elsevier.

life. Wang *et al.* have used the spectral shift caused by the etching of AuAg nanoboxes in the presence of cyanide as shown in Fig. 2.8b, as an indicator for the amount of cyanide present in the system [371]. Their early experiments conducted in Hela cells and in vivo Zebra fish embryos have resulted in a LoD of 1 nM, which is much lower than the acceptable limit by WHO. A similar approach has been taken to sense hypochlorite in tap water samples [305], Fig. 2.8a, and chlorine in a bleach solution and tap water samples [227]. In the former case, the spectra changes colour from yellow to purple, as it starts to etch the AuAg nanoparticles surface [305]. The LoD achieved is as low as $0.30 \times 10^{-6} \text{ mol dm}^{-3}$. In the latter case, the sensing has been done by AuAg alloy and fluorescent carbon nanodots (C-dots) [227]. Chlorine etches the Ag in the AuAg alloy, causing a distinct change in colour and intensity of the LSPR spectrum. The C-dots benefit from this lowering of LSPR intensity and thus gives an unperturbed fluorescent enhancement, thus providing an LoD for the colorimetric and fluorimetric sensing as $6.2 \times 10^{-7} \text{ M}$ and $5.1 \times 10^{-7} \text{ M}$, respectively. Hg(II) ions in drinking water, environment and food samples were detected by a plasmonic sensor based on the AuAg NPs/PVA (polyvinyl alcohol)/ITO probe with an LoD of 0.01 ppb [339]. A chitosan/AuAg alloy nanocomposite has also been used for colorimetric Hg sensor with a detection limit of $5 \times 10^{-8} \text{ M}$ [71]. The cytotoxicity demonstrated by these nanocomposites towards breast cancer cell lines (MCF-7) is also higher than that of just Au, Ag or chitosan alone. AuAg nanoparticles on Cu_2O nanocubes have shown high selectivity and efficiency towards detection of a non-enzymatic hydrogen peroxide (H_2O_2) [184]. The LoD achieved is $1.30 \mu\text{M}$ with a sensitivity of $4.16 \mu\text{A cm}^{-2} \text{ mM}^{-1}$.

The biosensor community makes a constant endeavour to cater to a wider audience which also includes people with limited financial competences. Recently, in order to reduce the price of the sensors, paper-based sensing has been proposed as a possible alternative. Tseng *et al.* have used paper-based plasmonic gas sensors containing AuAg hollow nanoparticles to successfully detect the freshness of salmon [350] as shown in Fig. 2.8g. The nanoparticles are fabricated with commercial inkjet substrates and sense volatile biogenic amines (BA) like putrescine released from spoiled food. The use of paper substrates makes the sensor effective, eco-friendly and very selective to BA vapours.

Multiplexing plasmonic sensors is a simple yet effective way of simultaneous detection of various pathogens. Multiplexed plasmonic sensors made of Ag nanocubes, AuAg alloy nanoparticles and Au/Ag nanocages are used to detect rabbit antichickens, anti-rat and anti mouse antibodies simultaneously [253].

Biosensing with alloy nanoparticles coupled with a fluorescent dye as markers has also been demonstrated. AuAg alloyed nanoparticles conjugated with L-glutathione-capped CdSeS alloyed quantum dots acting as fluorescent markers, and functionalized with 3-mercaptopropionic acid (MPA) are used as a sensor for detecting ZIKA virus RNA [4], with a LoD of detection of 1.7 copies/ml. AuAg nanoparticles marked with fluorescent dyes are also used as contrast agent for multiplexed cell-imaging applications. Tu *et al.* have used AuAg alloy core or Ag core and SiO_2 shell nanoparticles with fluorescent dye fluorescein isothiocyanate (FITC) or rhodamine B isothiocyanate (RBITC) embedded in the shell to fabricate 4 different contrast

agents: Ag@SiO₂-FTIC, Ag@SiO₂-RBITC, AuAg alloy@SiO₂-FTIC, AuAg alloy@SiO₂-RBITC [351]. They have been successfully used to demonstrate fluorescence imaging in fixed retinal cells.

Alloy nanoparticles formed by annealing a double layer of Au and Ag at 550°C for 3 h under Argon atmosphere and functionalized with aminosilanes can sense picomolar concentrations of human IgG with a dynamic range of 0.89 to 1000 pM [272]. AuAg alloy semi nanoshell arrays fabricated by a combination of nanosphere lithography, reactive-ion etching and magnetron co-sputtering of the Au and Ag target can demonstrate label free biosensing with biotin-streptavidin complex [294]. The reactive ion etching decides the gap between adjacent nanostructure in the array. An etching time of 8 min increases the gap while a lower etching time of 3 min decreases the gap, leading to an LoD of 10⁻¹⁰ M and 10⁻¹¹ M and sensitivity of 385 nm/RIU and 405 nm/RIU. Sensing of biotin-streptavidin complex bound to a substrate made of AuAg alloyed disks has also been done with RGB colorimetric sensors [225]. This technique avoids the use of a spectrometer, as the detection can be done with a smartphone, camera and white light, thus reducing the complexity immensely.

Sensing with alloy has conquered boundaries and has set new precedents. For example, Patskovsky *et al.* have performed hyperspectral reflected light microscopy with 60 nm AuAg alloy nanoparticles used as chromatic biomarkers in cancer cells [260] as shown in Fig. 2.8c-f. They have multiplexed the Au, Ag and AuAg (50:50) NPs as biological chromatic markers for biomedical diagnostics and optical biosensing. This proposed microscopic method can be utilized in NP imaging as well as in highly diffusive medium like a cellular environment.

Apart from LSPR sensing with AuAg alloy nanoparticles, biosensing with AuAg alloyed thin films has also been done recently [190]. Immunodetection of highly carcinogenic benzo[a]pyrene (BaP) in water with an LoD of 0.01 µg.L⁻¹ was performed with a hue based sensor functionalized with a monoclonal antibody. Surface plasmon resonance imaging (SPRi) with an AuAg alloy thin film based on this hue based enhanced sensitivity shows a sensitivity of 29879/RIU measured by the ratio of changes in hue over the refractive index change of the background, which is 8 times higher than that obtained with a gold layer. AuAg alloy thin film has also been used as a SPR sensor to detect cancer antigen CA125 by wavelength interrogation sandwich immunoassay. The sensor with AuAg alloy is 2.25 times more sensitive than that with Au layer only [405] as shown in Fig. 2.8h-i.

Original geometries, such as a SPR based fibre optic sensor coated with AuAg alloy nanoparticles forming a thin film, have also been proposed to increase the detection efficiency and detection accuracy [170].

2.4.2 SERS

After biosensing, the next most used application with AuAg alloys has been SERS, where detailed chemical information is obtained about the molecule that is adsorbed on the plasmonic surface. The high field enhancement obtained from the metal amplifies the chemical

information of the molecules, thus enabling detection of chemicals in extremely diluted concentrations, down to even single molecule detection.

Several types of metal nanostructures have been used in the literature for SERS of which those with nanoporous architectures have been proved to be the most effective. Apart from having high field enhancement at the edges of the nanostructure, these nanoporous structures have additional pockets of high field enhancement in the pores. Thus the adsorbed molecule on these nanostructures have multiple exposures to enhanced electric field, as compared to solid nanostructures leading to high SERS signal. In most of these cases these hollow or nanoporous structures have been fabricated by a galvanic replacement reaction. Nanoporous AuAg shells fabricated this way work as excellent SERS substrates for p-nitrothiophenol [400]. These nanostructures have also performed a reduction of p-nitothiophenol to 4,4'-dimercapto-azobenzene at ambient temperature. This catalysis is 79 to 123 times faster than pure on Au nanoparticles and 2 to 3 times faster for Ag nanoparticles. These nanostructures were fabricated with conventional galvanic replacement reaction between Ag colloid as the template and HAuCl_4 . Hollow Au-Ag nanostructures prepared by complementing the galvanic replacement reaction between Ag nanocubes and HAuCl_4 with co-reduction with ascorbic acid was used for SERS of 1,4-benzenedithiol(1,4-BDT) [403]. At $\lambda = 785$ nm these nanostructures show 15 times and 33 times more SERS signal than pure Ag nanocubes and AuAg nanocubes prepared only by galvanic reaction. Trace detection of thiam with a detection limit of 10^{-12} M using SERS was performed with AuAg alloyed microcages fabricated with a simple NaBH_4 -cooperative galvanic replacement reaction [375]. This process enables tuning the composition of the alloy and hence the LSPR peak of the nanocage to a great degree of accuracy. AuAg alloyed hollow nanocubes obtained by galvanic replacement with Ag nanocube as template demonstrate higher SERS signal for 4-aminothiophenol (4-ATP) molecules [115]. SERS detection of 4-aminophenol (4-ATP) with a detection limit as low as 10^{-10} M has been obtained with periodic porous AuAg alloyed nanodisk using stepwise metal-deposition on polystyrene beads, subsequent annealing followed by dealloying [416]. The periodicity is determined by the size of the beads while the dealloying determines the size of the interconnected ligands in a porous nanostructure. 4-ATP has also been detected with an enhancement factor of around 10^8 and an LOD of 10^{-10} M on AuAg porous nanocubes [417]. SERS of CV performed on ring shaped AuAg alloy nanostructure [65] as shown in Fig. 2.6c and porous AuAg alloyed nanosphere [199] can detect concentrations as low as 10^{-6} M.

Geometries where metal nanoparticles are decorated on a metal crystal are challenging in fabrication but are ideal for SERS. Such a structure has been fabricated by Fan *et al.* where AuAg alloy nanoislands are formed on a Au crystal, and has shown high SERS enhancement for Crystal Violet (CV) [81]. Fluorescent AuAg alloy nanoclusters with blue luminescence showed an enhancement of SERS spectra by 1.44×10^6 for methylene blue dye (MB) [255].

SERS spectra of trace amount of hexachlorocyclohexane (HCH), both γ and α variety, with a LOD of 1.5 ppb is achieved with a unique core-shell geometry [423]. Here the core is not a conventional sphere, but rather an urchin like structure while the shell is a zeolite imidazole

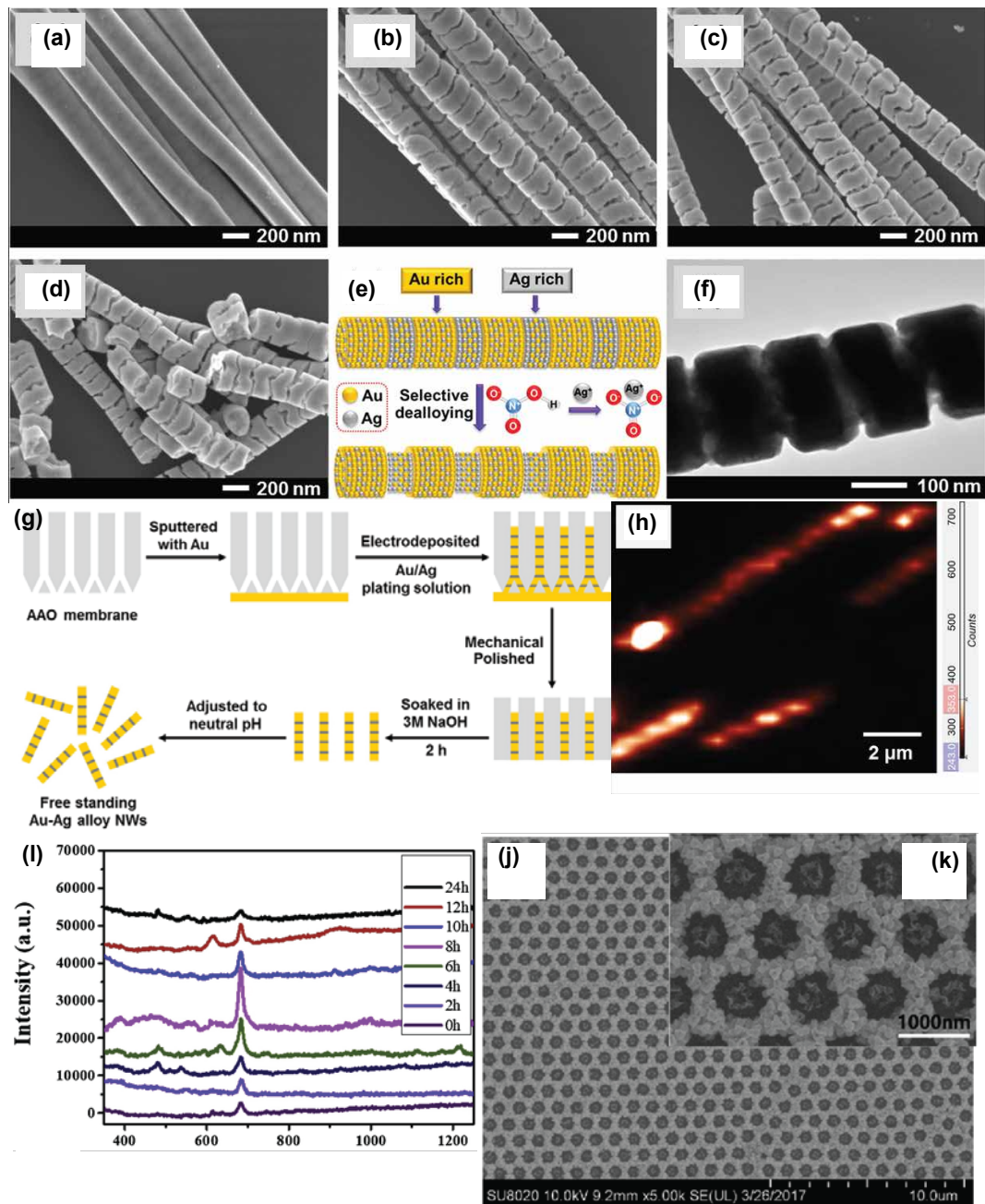


Figure 2.9 – SEM images of the porous striped AuAg alloy nanowires for various etching conditions defined by variation in the concentration of HNO₃ (a) Au₃₀s-30s-HNO₃ (0%) (b) Au₃₀s-Ag₃₀s-HNO₃ (20%) (c) Au₃₀s-Ag₃₀s-HNO₃ (25%) (d) Au₃₀s-Ag₃₀s-HNO₃ (30%) (e) Schematic of dealloying of stripped AuAg alloy nanowires. (f) TEM images of Au₃₀s-Ag₃₀s-HNO₃ (25%) (g) Schematic of the fabrication procedure of AuAg alloy nanowires using the template based electrochemical deposition process. (h) Raman mapping image of 4-MBA functionalized porous stripped AuAg alloy nanowires. (a)-(h) Reproduced with permission from [298]. Copyright 2020, Elsevier. (j) FESEM image of the bowl like pore array composed of hollow AuAg alloy nanoparticles. (k) Shows an zoomed image of the same (l) SERS spectra of 10⁻⁵ melamine aqueous solution on these nanostructures. (j)-(l) Reproduced with permission from [241]. Copyright 2019, Elsevier.

framework (ZIF-8). The total size of the structure is about 100 nm and the nanoporous ZIF-8 shell can be varied in thickness from 10 to 40 nm, depending on the concentration of hexadecyltrimethyl ammonium bromide (CTAB) in the solution. They can also be used for SERS detection of small volatile molecules. Other types of core-shell geometries with hollow AuAg alloy as a core Ag as a shell is used for SERS detection of 4-mercaptothiophenol with a LOD of 1 attomolar [140]. The hollow core is fabricated through a direct one-pot synthesis using Tween 80 micelles, as a soft template.

A complicated and unique nanostructure of stripes (S) and porous striped (PS) AuAg alloy nanowires has been used for demonstration of SERS of β -hydroxybutyric acid for the very first time [298] as shown in Fig. 2.9a-h. The LoD of these nanostructures is 11 nM. SERS of other known compounds like 4-mercaptobenzoic acid has also been performed with these structures. The S type nanowires were fabricated using anodic aluminium template based electrodeposition, whereas an additional step of dealloying forms the PS based nanowires. These rough and porous nanostructures create excellent hotspots for SERS. SERS of milk contaminated with melamine added intentionally has been performed in real time [241] as shown in Fig. 2.9l. The SERS substrate is a bowl like pore array composed of AuAg alloy nanoparticles as shown in Fig. 2.9j-k. The achieved LoD is 0.1 ppm, which is 10 times lower than the tolerance limit in infant milk imposed by FDA in USA and 1.5 times lower than the strictest standard in the world [241].

SERS of Rhodamine 6G and $(\text{Bu}_4\text{N})_2[\text{Ru}(\text{dcbpyH})_2-(\text{NCS})_2]$ performed on AuAg nanosponges is 25 times and 7 times higher, respectively, than solid AuAg alloy nanoparticles [222]. SERS along with fluorescent enhancement with Rhodamine 6G (R6G) has been demonstrated with Au-Ag alloy nanocluster as core and SiO_2 as a shell [410]. The best result is obtained with a 8 nm of SiO_2 shell. SERS of Rhodamine 6G is also performed by AuAg alloy nanoparticles fabricated by sequential laser ablation of a AuAg alloy film [361] and by AuAg hollow nanorice [407]. The latter nanostructure can also perform single molecule detection of p,p'-dimercaptoazobenzene (DMAB).

Advanced multifunctional substrates performing SERS and other detection like fluorescence or photocatalytic reactions have been reported in the literatures. SERS of picomolar concentration of Folic acid as cancer biomarkers and adenine were done on AuAg nanoparticles fabricated on low cost paper substrates by concurrent deposition of Au and Ag below 100°C [256]. This substrate was used for multifunctional purposes as shown in Fig. 2.10a-e. By changing the composition of the alloy the resonance of the nanoparticle varied, leading to metal enhanced fluorescence (MEF). MEF was achieved for three types of fluorescent dyes-FITC, R6G and Congo Red (CR) shown in Fig. 2.10c. Chromatographic MEF of safranin O (SO), toluidine blue (TB) and CR was also performed on the similar substrate shown in Fig. 2.10d. Kang *et al.* have also performed metal enhanced fluorescence with SERS with AuAg nanoparticles by dewetting a 14 nm film at 700°C [145]. The best response for SERS of benzenethiol as well as fluorescence was achieved for the $\text{Au}_{0.5}\text{Ag}_{0.5}$ alloy composition. Variation of SERS intensity due to variation in the composition has also been reported by Chaffin *et al.* [40].

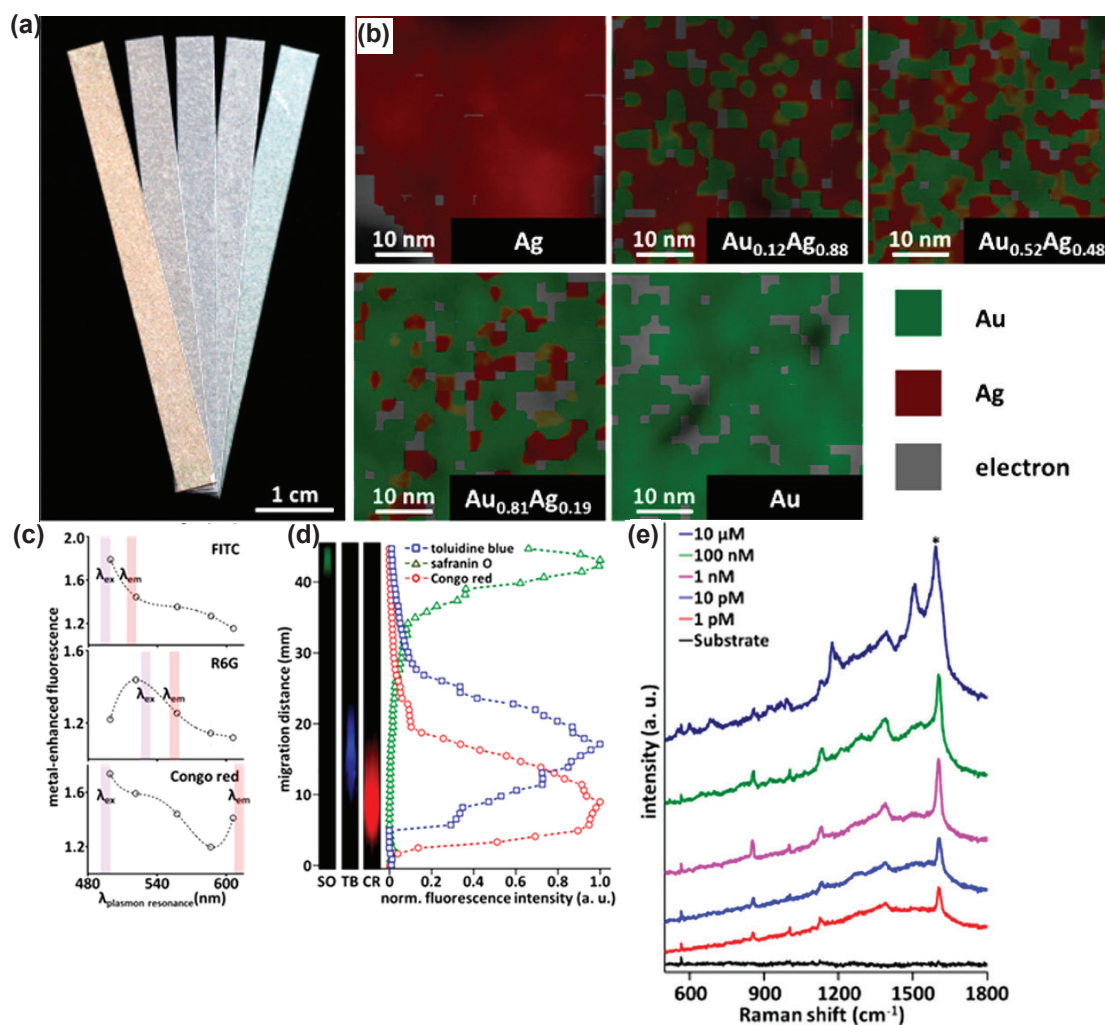


Figure 2.10 – (a) Paper based plasmonic alloy stripes (b) EDS mapping of the various alloy composition on the paper substrate. (c) Fluorescence enhancement from FITC, R6G and CR depending on the resonance wavelength of individual composition. (d) Chromatographic MEF. The dye mixture of TB, SO and CR was separated using the paper substrate and selectively detected. (e) SERS spectra of $\text{Au}_{0.12}\text{Ag}_{0.88}$ showing picomolar detection for folic acid. Reproduced with permission from [256]. Copyright 2018, American Chemical Society.

Fan *et al.* [80] have shown that for positively charged SERS probe, Oxazine 720 and Nile Blue A, the alloy with higher content of Au is better while the reverse is true for negatively charged SERS probe HTP and thiophenol [80]. Bifunctional substrates performing photocatalytic reactions and SERS of 4-nitrothiophenol have also been reported by Ankudze *et al.* [15] shown in Fig. 2.11a-g. Here the substrate is made of gold nanoparticle covered with AuAg nanotubes. The photocatalytic reaction converts 4-nitrothiophenol to 4-aminothiophenol. Han *et al.* have demonstrated a unique concept, where the change in the SERS signal was used to monitor the catalytic activity of the AuAg alloy for the reduction of 4-nitrothiophenol (4-NTP) by sodium borohydride (NaBH_4) to 4-ATP [119]. This work has potential applications in sewage treatment. A highly sensitive, low cost, multiplexed SERS platform was made to detect a panel of soluble cancer protein biomarkers: soluble programmed death-1 (sPD-1), soluble programmed death-ligand 1 (sPD-L1) and soluble epidermal growth factor receptor (SEGFR) in human serum [186]. The schematic of the working mechanism along with the multiplexed Raman signal is shown in Fig. 2.11h. AuAg alloyed nanoboxes were used as SERS substrate in this case, making the LoDs of the system as 6.17 pg/ml, 0.68 pg/ml and 69.86 pg/ml, respectively.

SERS activity of 1,4-benzene dithiol (BDT) has been demonstrated with alloy made by an antisolvent method using β -D-glucose as a reducing agent and soluble starch as the protecting agent [6]. Complicated geometries like Au core@AuAg alloy spine nanostructures (LoD 100 pM) were used for SERS experiments with malachite green in presence of a large number of interfering ions [42].

Low cytotoxicity of AuAg alloy nanoparticles have been used for demonstrating for the first time a biocompatible ratiometric SERS sensor to detect intra cellular endonuclease activity as well as endonuclease in living cells [313]. For the ratiometric sensor, alloy nanoparticles functionalized with 4-thiophenylacetylene (TPA) served as the reference as its SERS at 1983 cm^{-1} remains intact. Another set of alloy nanoparticles functionalized with single stranded DNA (ssDNA) carrying 3-[4-(phenylethynyl)benzylthio]propanoic acid (PEB) acted as the endonuclease responsive SERS signalling molecule. In the presence of endonuclease, the ssDNA is cleaved releasing the PEB molecules from the particle surface. This decreased the SERS signal at 2215 cm^{-1} . The ratio of intensities (I_{1983}/I_{2215}) gave a detection limit as low as 0.056 unit/ml. These alloy nanoparticles were AuAg core shell nanoparticles covered with SiO_2 , followed by annealing at 900°C and stripping of SiO_2 . SERS of benzidine has been shown by nanoparticles fabricated on similar lines i.e. by annealing of an AuAg core shell nanoparticle coated with SiO_2 annealed at 930°C [93].

AuAg alloy nanoparticles has been used as the label in sandwiched immunoassay used for detection of alpha-fetoprotein, which is critical for liver cancer [95]. The SERS substrate is an Ag/AgBr hybrid structure. LoD is as low as 1.86 fg/ml and has a broad dynamic range from 2 fg/ml to $0.8\mu\text{g/ml}$. AuAg nanohybrid system has been used as a bifunctional substrate to perform surface enhanced infrared measurements (SEIRA) on bromophenol and photocatalysis of 4-nitro-aniline (4-NA) to p-phenylenediamine (p-PDA) [360].

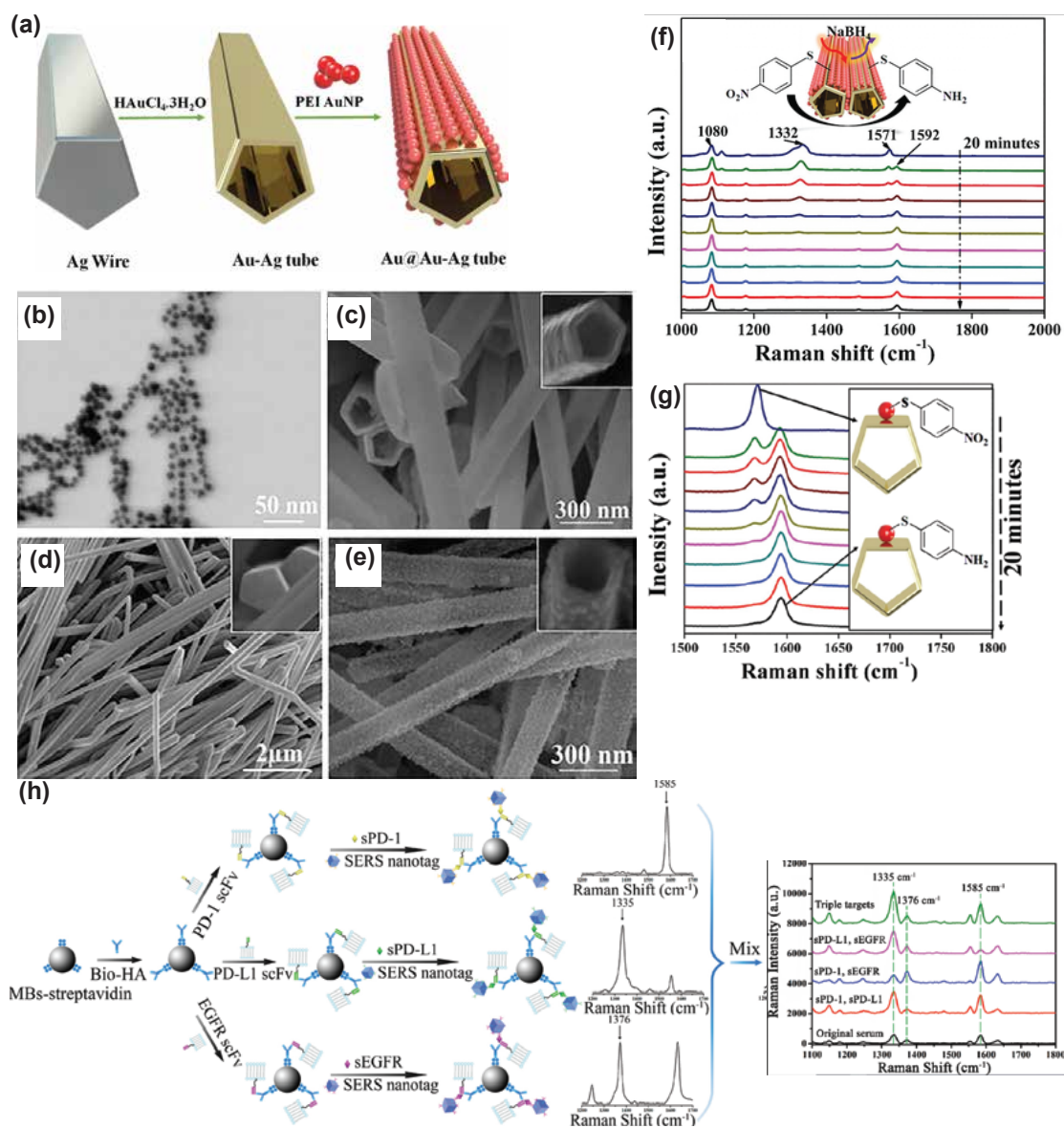


Figure 2.11 – (a) Schematic of the fabrication procedure of Au decorated AuAg alloy tubes. (b) STEM image of 9 ± 2 PEI capped Au nanoparticles (c) SEM image of the Ag nanowires with an average diameter of 167 ± 6 nm and a length of $40 \mu\text{m}$. (d) SEM image of the AuAg nanotubes with an average external diameter of 215 ± 29 nm. (e) SEM image of the Au decorated AuAg tubes. (f) In situ SERS monitoring of the catalytic reduction of 4-NTP initiated by the NaBH_4 on Au decorated AuAg tubes (g) Time dependent SERS spectra showing the disappearance of 4-NTP and evolution of 4-ATP. (a)-(g) Reproduced with permission from [15]. Copyright 2018, Elsevier. (h) Scheme showing how simultaneous detection of SPD-1, SPD-L1 and sEGFR can be done. The output is a Raman spectra showing simultaneous detection of SPD-1, SPD-L1 and sEGFR in human serum. They were added to human serum in the concentrations 1 ng/ml, 0.1 ng/ml and 10 ng/ml. The 1585^{-1} , 1335^{-1} and 1376 cm^{-1} shows the presence of SPD-1, SPD-L1 and sEGFR. Reproduced with permission from [186]. Copyright 2018, American Chemical Society.

Chen *et al.* have demonstrated a novel way of Raman characterization of commonly used Raman dyes, which are also fluorescent molecules [46]. The fluorescent molecule Alexa Fluor 488 is used in this work. They have achieved their goal by using a novel substrate mode of $\text{Au}_{0.7}\text{Ag}_{0.3}$ alloy nanoparticles adsorbed on an amine functionalized graphene oxide (FGO) on a SiO_2 substrate. The FGO quenches the fluorescence, whereas the alloy enhances the Raman signal leading to a Raman signal to fluorescent background intensity as high as 1.6. This technique would also be beneficial to Resonance Raman Spectroscopy which suffers from large fluorescence background signal.

Recently theoretical studies on SERS trying to provide insights on the SERS mechanism from the atomic scale are also coming up. Takenaka *et al.* have made an effort to understand the dynamics of SERS spectra of 2,2'-Bipyridyl adsorbed on AuAg nanoparticles by theoretically analysing how the surface of the alloy nanoparticles enhances the electric field. They have also calculated different binding energies and bond length of nanoalloys and also performed quantum chemical simulations for the same [338]. Their work shows that DFT studies trying to replicate experimental SERS spectra provide significant insights as to how the material parameter and roughness along with hotspots affect the spectra.

2.4.3 Stability of alloys

As had been mentioned previously, AuAg alloys are more stable than pure Ag, thus facilitating experiments to be carried over in much harsher conditions. Before moving on to the other application subsections, we would like to briefly discuss the literatures that has demonstrated the stability of AuAg alloys experimentally. The superior stability of the alloys as opposed to Au@Ag core shell nanostructures has been experimentally demonstrated by observing the SERS signal and the UV-Vis spectra from the alloyed nanostructures, over a period of several hours (even days), after being immersed in etchant NH_4OH and H_2O_2 [18, 240, 38, 93]. The alloys performed much better than Au@Ag core shell structures with degradation of the spectra after 12 h of immersion in the solution as opposed to 30 min for the core shell geometry [240]. Guo *et al.* [115] and Kang *et al.* [145] have shown that when exposed to ambient conditions, the alloys perform better than pure metals. Their spectral intensity remains unchanged over several weeks as opposed to that of pure Ag, whose intensity diminishes remarkably within the first week itself. Figure 2.4e-f shows the SERS spectra of the alloyed and the core shell nanorods for Rh6G adsorbed on their surface, before and after being immersed in the etching solution of NH_4OH and H_2O_2 .

2.4.4 Photocatalysis

Metal nanoparticles especially Au nanoparticles combined with semiconductors like TiO_2 have already been investigated in the context of photocatalytic applications. These metal nanoparticles form a Schottky barrier at the metal-semiconductor interface and electrons can be transferred from the metal into the conduction band of the semiconductor when they

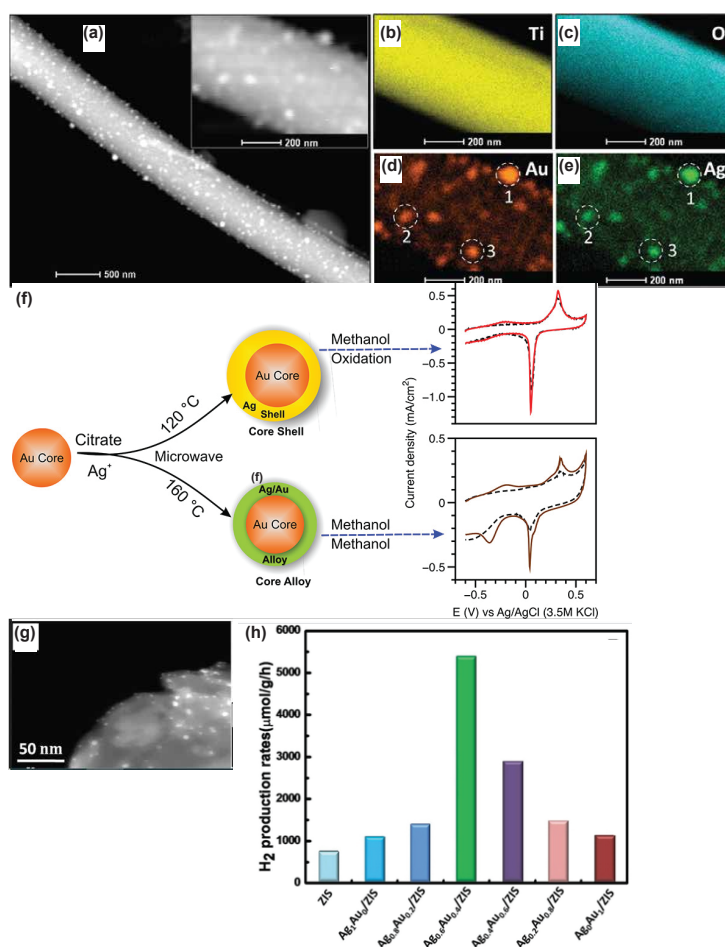


Figure 2.12 – (a) Dark field image of the AuAg-mTNF-H . Inset shows the area used for EDS mapping. (b)-(e) EDS mapping of the elements (a)-(e) Reproduced with permission from [41]. Copyright 2019, American Chemical Society. (f) Cyclic Voltammety data showing difference in methanol oxidation using Au@Ag core shell and Au core AuAg alloy shell nanoparticles fabricated with the citrate method. Reproduced with permission from [246]. Copyright 2018, American Chemical Society. (g) HAADF-STEM images of Au_{0.4}Ag_{0.6}/ZIS (h) H₂ production rate of the several nanostructures. (g)-(h) Reproduced with permission from [13]. Copyright 2020, Elsevier.

are resonantly excited. These highly energetic electrons in the non-equilibrium are called hot electrons and can reduce molecules adsorbed on the semiconductor surface while the molecules adsorbed on the surface of the metal get oxidised [154]. These photocatalytic reactions depend upon resonantly exciting the metal and also occur below the bandgap energy of the semiconducting material. Metal resonances vary as a function of size, shape, surrounding material and composition, thus providing the opportunity to tailor photocatalytic applications at the desired wavelength. Apart from the tuning of resonant wavelength, changing the metal composition also alters the Schottky barrier height, thus affecting the efficiency of the electron extraction [356]. Therefore, using AuAg alloys is highly attractive to enhance photocatalytic reactions, since it reduces the Schottky barrier bandgap, compared to pure Au. Tailoring the Schottky barrier modulates the number of electrons injected into the semiconductor, which in turn alters the photocatalytic efficiency. In this case, it increases the number of hot electrons injected into TiO_2 as compared to pure Au, thus enhancing the photocurrent [244] and the photocatalytic activity. In contrast, photocatalytic enhancement arising at the wavelength above the bandgap energy of the metal-semiconductor complex is mainly dominated by near-field effects and hot electrons play only a minor role in such systems [343].

Researchers have demonstrated enhanced photocatalytic activities using alloy-semiconductor configurations. Enhanced water splitting for H_2 production ($516 \mu\text{mol h}^{-1} \text{g}^{-1}$) and methylene blue decomposition ($0.027 / \text{min}$) under simulated solar light irradiation have been demonstrated [41] using mesoporous TiO_2 nanofibers covered with AuAg nanoparticles as shown in Fig. 2.12a-e. In addition, H_2 production using a cost-effective graphene sensitized with AgAu alloy, fabricated using green synthesis methods, has further been reported [216]. AuAg structures provide an enhanced rate of H_2 evolution that is 1.4 times faster than the Au-graphene and 2 times better than the Ag-graphene systems. A 3-dimensional $\text{Ag}_x\text{Au}_{1-x}/\text{ZnIn}_2\text{S}_4$ system produces 7.1 times more H_2 than that with only ZnIn_2S_4 system [13] shown in Fig. 2.12g. The H_2 production rate for various metal compositions are also shown in Fig. 2.12h. CO_2 reduction to CO catalysed by TiO_2 nanowires capped with AuAg alloy nanoparticles has also been reported. This structure outperforms the Au/ TiO_2 , Ag/ TiO_2 , bare TiO_2 and TiO_2 nanoparticles by 1.72, 1.84, 72.5 and 201 times, respectively [337] as shown in Fig. 2.13a-b.

AuAg alloy nanoparticles supported on titania exhibit superior methanol conversion and selectivity towards methyl formate for selective oxidation of methanol under atmospheric conditions and UV irradiation in the $15\text{-}45^\circ\text{C}$ range [118]. The highest methanol conversion to methyl formate achieved in such a configuration is around 90%, and the highest selectivity reached towards methyl formate is 85%. The performance of carbon-supported AuAg nanoparticles, which are either core-shell or core-alloy nanostructures, for methanol oxidation reaction in alkaline solution has also been studied [246] as shown in Fig. 2.12f.

Photocatalysts with alloyed nanoparticles are used in photodegradation, a process where photocatalysts help degrade dyes, waste and pollutants. The process can be briefly described as follows: the photocatalyst absorbs the energy from the incident light and gets excited creating electron hole pairs. The electron and the holes move to the conduction band and the

valence band, respectively. These excited catalysts are unstable and can easily hydrolyze or oxidise, producing hydroxyl or superoxide radicals that have the ability to break down the dyes and the pollutants.

Photodegradation of Rh6G is performed by an AuAg alloy@TiO₂@Fe₃O₄ nanoparticles system [12], with 4 times more photocatalytic activity under xenon lamp irradiation. With such a configuration, degradation of organic pollutant in wastewater originating from a textile factory in Zanjan, Iran, has been demonstrated. AuAg alloys on graphitic carbon nitride with varying ratios of Au/Ag have been used to measure the photocatalytic activity of the AuAg/g-C₃N₄ exposed to natural sunlight and artificial visible light [103]. The AuAg alloy modified g-C₃N₄ shows a higher photocatalytic activity for the decolourization of Rhodamine B in the visible range, as compared to the bare g-C₃N₄.

Zn-Cr layered hydroxide/graphene oxide nanocomposites modified with AuAg metal particles showed 2.5 times better photocatalytic performance to convert benzyl alcohol to benzaldehyde and nitrobenzene to aniline, as compared to similar geometry without alloy nanoparticles [295].

Core-shell geometries with Au core-alloy shell have shown the highest catalytic activity in reducing 4-nitroaniline in the presence of sodium borohydride [335]. Photo-impregnated Au_{0.3}Ag_{0.7} alloy nanoparticles, with a surface plasmon resonance at $\lambda = 490$ nm, on commercially available TiO₂ source P90 also act as a photocatalyst for the degradation of stearic acid. Since the intensity of the solar spectrum is also maximum at 490 nm, these nanoparticles exhibit enhanced photocatalytic activity under sunlight irradiation [359].

Silicon nanowire arrays modified with AuAg alloy nanoparticles act as a photoinduced antibacterial material [379]. Due to photothermal and photocatalytic effects, these nanostructures decimate bacteria (*E.coli* MG1655) under sunlight irradiation with high efficiency in a few minutes, as shown in Fig. 2.13f-i. These nanostructures can be “recycled” without loss of this bactericidal effect. This work will be instrumental in preparing nanomaterials for novel antibacterial agents.

AuAg nanoparticles of various shapes and sizes have been used extensively to perform photocatalytic activity to reduce 4-Nitrophenol [153, 326, 325, 121]. AuAg nanoparticles prepared on mesoporous aluminosilicate (MCM) shows high catalytic activity towards oxidation of CO [198]. At very low temperatures of -23.15°C, this system with alloy nanoparticles (Au:Ag molar ratio of 3:1) shows a catalytic activity as compared to no activity from the Au@MCM or Ag@MCM system. Feng *et al.* have shown how oxidation of p-aminothiophenol to p,p'-dimercaptoazobenzene varies with variation of the alloy composition of AuAg [370], with Au_{0.19}Ag_{0.81} nanoparticles exhibiting the highest activity.

Recently multifunctional substrates performing various functions are very much in vogue. Bifunctional substrates with AuAg nanoparticles are used for SERS as well as reduction of 4-nitro-aniline (4-NA) to p-phenylenediamine (p-PDA) [360] and conversion of 4-nitrothiophenol

to 4-aminothiophenol [15]. In the latter case the SERS spectra were monitored during the catalytic reaction showing the evolution of new bonds.

In addition to photocatalysis, alloys also enhance the electrocatalytic oxygen reduction in a Nafion-matrix/graphitic carbon nitride (g-C₃N₄)/ AuAg nanoparticles system as compared to their pure metal counterparts [268]. Manivannan *et al.* have shown electrocatalytic effects of AuAg alloyed nanodots [217]: 1-3 nm-sized AuAg alloy nanodots, synthesized by a green seedless one-step synthesis method and embedded in an amine-functionalized silicate sol-gel matrix, demonstrate sensing and electrochemical reduction of nitrobenzene, an environmental pollutant [217].

2.4.5 Photocurrent

Changing the alloy particles not only tunes the resonance frequency but also tunes the absorption of the nanoparticle. This property of alloys is used in plasmonic solar cells, where the use of alloy nanoparticles enhance the absorption of the incident illumination, which in turn increases the power conversion efficiency. The alloy nanoparticles are embedded in solar cells in various layers, depending upon the configuration used. Xu *et al.* have shown that Au_{0.37}Ag_{0.623} nanoparticles incorporated into organic solar cells fabricated by co-evaporation and thermal annealing increase the electron conversion efficiency to 3.03%, which is an enhancement of 19% over solar cells without nanoparticles [393]. AuAg alloy sandwiched in between n-Cu₂O and p-Cu₂O (n-Cu₂O/AuAg alloy/p-Cu₂O) can also be used for solar energy harvesting [192], as shown in Fig. 2.13c-e. AuAg@AuAg core shell alloy nanocrystals fabricated into PEDOT:PSS layer of p-i-n perovskite solar cells have a power conversion efficiency of 16.76% which is an enhancement of 28% compared to the non-doped ones [334]. N719 dye doped AuAg alloy nanoparticles were incorporated into porous TiO₂ films to make dye sensitized solar cells [7]. These showed a power conversion efficiency of 5.81% which is 8.4% and 52.1% higher than those with Au or without any plasmonic nanoparticles, respectively. 1% of large sized Au₁₁Ag₈₉ nanoalloys when incorporated into the active layer of a polymer solar cell, promotes a power conversion efficiency of 4.73%, which outperforms the device without metal nanoparticles [44]. This alloy doped solar cell has enhanced short-circuit current density J_{SC}, open circuit voltage (V_{OC}), fill factor (FF) and incident photon-to-current efficiency (IPCE). All these enhancements in turn enhance the power conversion efficiency (PCE) by 31% as compared to the reference device.

Apart from using simple nanoparticle geometries, complicated geometries like AuAg alloyed nanoprisms coated with SiO₂ in a quasi 2D perovskite photodetector [137] or dye sensitized solar cells with alloyed popcorn nanoparticles [394] have also been used in solar cells. In the latter case, a white diffuse reflection film is added on the exterior of the counter electrode [394]. This geometry along with alloy popcorn nanoparticles enhances the power conversion efficiency to 32% as compared to those without the nanoparticles.

Not only solar cells but also light emitting diodes benefit from the AuAg alloy nanoparticles.

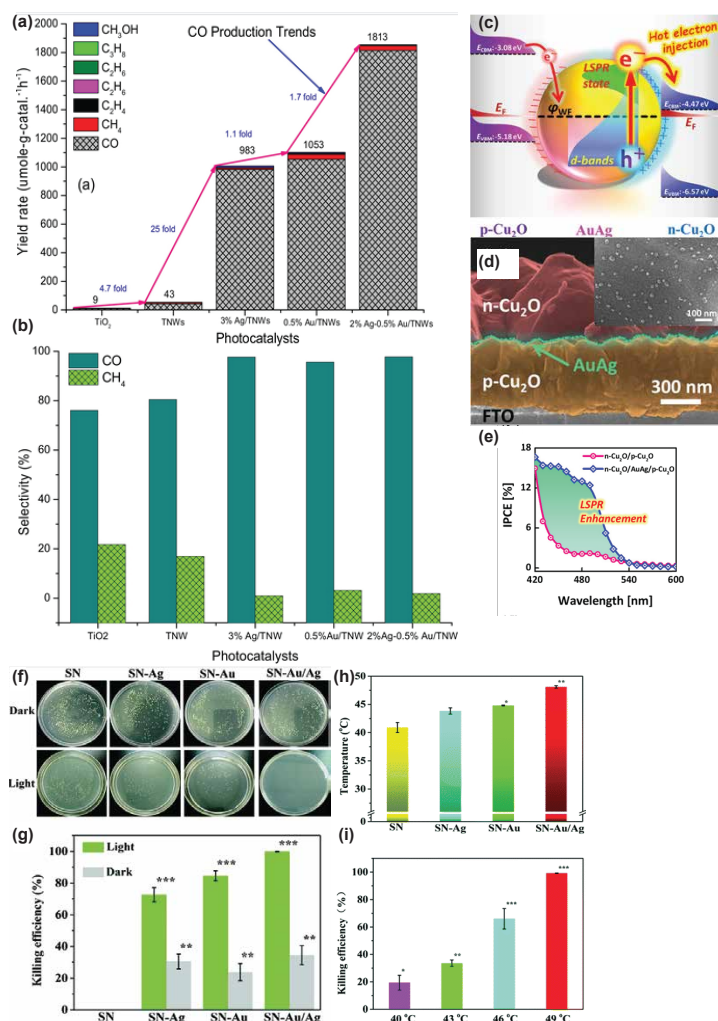


Figure 2.13 – (a) Rate of yield of the nanostructures over different photocatalysts during CO₂ reduction with H₂ (b) Selectivity of CO and CH₄ for corresponding samples. (a)-(b) Reproduced with permission from [337]. Copyright 2017, Elsevier. (c) Schematic of the working principle of the sandwich n-Cu₂O/AuAg/p-Cu₂O structure. (d) Cross-sectional view. Inset shows the top view of the sandwich structure showing AuAg alloy nanoparticles on p-Cu₂O (e) Incident photon to current conversion efficiency (IPCE) characteristics at 0.7 V_{RHE}. (c)-(e) Reproduced with permission from [192]. Copyright 2019, American Chemical Society. (f) Formation of colony of E.coli on the different nanostructures (g) Efficiency for killing of bacteria in dark and sunlight. Data shown as mean ± standard deviation. (h) Photothermal efficiencies of the nanostructures when exposed to sunlight. (i) Effect of the temperature (40°C-49°C) on E.coli killing efficiency. (f)-(i) Reproduced with permission from [379]. Copyright 2019, The Royal Society of Chemistry.

Zhang *et al.* demonstrate an increase in the 25% luminescence efficiency by tuning the alloy composition and the size [420].

2.4.6 Photothermal

Metal nanoparticles are extremely versatile for photothermal applications, of which, due to their absorption properties, AuAg nanoparticles are particularly appropriate. Farokhnezhad *et al.* conducted a detailed theoretical analysis to probe the potential of graphene coated AuAg hollow nanoshells for photothermal therapy for treating tumour [83] as shown in Fig. 2.14a. The resonant wavelength of these structures can be tuned to the desired frequency windows, appropriate for biological tissues, by changing the alloy composition, thickness of the shell and their inner radius. Au@AuAg alloy geometry have been used as efficient photothermal agents for MDA-MB-231 cancer cells; they kill the cells effectively with laser irradiation [399] as shown in Fig. 2.7b-d. Zhu *et al.* have demonstrated photothermal properties of alloy nanoparticles decorating carbon nanomaterials and mesoporous carbon. In their first work, they investigated an arrangement consisting of ZIF-8-derived nitrogen doped graphitic polyhedrons (ZNG's) and AuAg alloy nanoparticles where the nanoparticles were loaded onto the ZNG carrier using an impregnation reduction method [425]. Compared to bare Au and Ag nanoparticles, the photothermal conversion efficiency has been improved by a few percents. In their second work, AuAg alloy nanoparticles on mesoporous carbon enhanced the photothermal efficiency by up to 5% [426]. AuAg alloy nanoplates also show photothermal conversion efficiency as high as 78.5% [270] as shown in Fig. 2.6r-s. Jang *et al.* have demonstrated superior chemo-thermo-gene multi-therapy with clustered AuAg nanoporous particles showing enhanced photothermal conversion of near-infrared light [136].

2.4.7 Miscellaneous applications

Apart from the conventional applications previously mentioned, there are several new and unconventional upcoming applications that rely on AuAg alloys. The tuning of resonance spectra of the alloy by tuning the composition can be used to generate colours [60]. Progressive H_2O_2 etching of Ag from a horseradish peroxidase (HRP) functionalized AuAg hybrid nanocage causes an evolution of the colours denoting the change in amount of Ag in the nanostructure [377], as shown in Fig. 2.14b-e. The AuAg hybrid nanocages have been prepared by galvanic replacement reaction between citrate capped Ag nanospheres and $HAuCl_4$. These structures have also been used for colorimetric sensing of glucose in human serum samples. In this case, glucose oxidase (GO_x) introduced along with glucose, catalyses the oxidation of glucose and generates H_2O_2 that starts etching of Ag as described before. Coloured nailpolish with $Au_{0.5}Ag_{0.5}$ [175] and colour filters [134] (shown in Fig. 2.14f-g) have also been demonstrated. In the latter case they have made a mosaic with 7 compositions: Au, $Au_{10}Ag_{90}$, $Au_{30}Ag_{70}$, $Au_{50}Ag_{50}$, $Au_{70}Ag_{30}$, $Au_{90}Ag_{10}$ and pure Ag performed through successive ebeam lithographies. Parra-Barranco *et al.* have shown fabrication of large area substrates with varying colours in x- and y-polarizations along with varying composition of the alloy [257]. The AuAg alloy

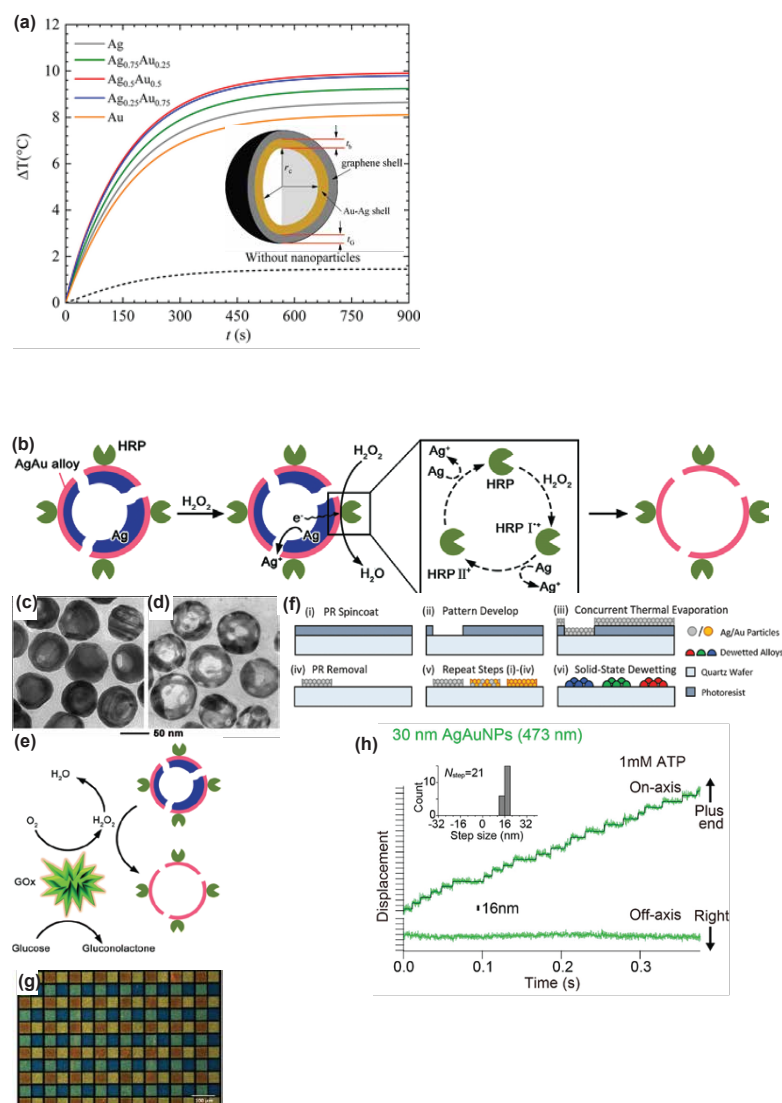


Figure 2.14 – (a) Temperature rise from the initial temperature ($\Delta T = T(t) - T_0$) at the center of tumor ($r=0$) for monolayer graphene coated AuAg HNS with varying composition of alloy, as a function of the laser irradiation time t . Here the incident intensity is 0.3 W/cm^2 with 4×10^9 particles/ml. Inset shows the schematic of the graphene coated AuAg alloy hollow nanoshell. Reproduced with permission from [83]. Copyright 2019, American Chemical Society. (b) Schematic of the colorimetric sensing with HRP-AuAg hybrid nanocage with Ag inside. TEM images of the HRP-AuAg hybrid cages (c) before and (d) after reaction with 1 mM H_2O_2 in CA/SC buffer, pH 4.0 for 10 minutes in room temperature. (e) Schematic of the glucose sensing with GO_x and HRP-AuAg hybrid cages. (b)-(e) Reproduced with permission from [377]. Copyright 2019, The Royal Society Of Chemistry. (f) Schematic of the repeated liftoff process used for fabrication of plasmonic colour filter. (g) The dark field microscopic image of the plasmonic colour filter made of 10 nm of Au, $\text{Au}_{70}\text{Ag}_{30}$, $\text{Au}_{30}\text{Ag}_{70}$, and Ag. (f)-(g) Reproduced with permission from [134]. Copyright 2019, Nature Publishing Group. (h) AuAg nanoparticles along the long-axis (on-axis) and along short axis (off-axis) of the microtube. Raw trajectories are shown in light green while the median filtered traces are shown in green. Insets show the distribution of step sizes of the kinesin-1 head at 1 mM ATP. Reproduced with permission from [14]. Copyright 2019, American Chemical Society.

nanoparticles are fabricated on open voids found in thin films deposited by oblique angle deposition. Chiral AuAg alloyed nanoparticles have been fabricated in the presence of D/L pencillamine (D/L pen) [381]. These nanoparticles can be used for colorimetric detection of various chiral enantiomers. AuAg alloy nanotubes show excellent chiral detection of amino acids [195]. Au, Ag and AuAg alloy nanoparticles have been used for multicolour precise high speed tracking of biomolecules e.g. diffusional motions of phospholipids in a supported membrane and motions of kinesins in steps along microtubes with a localization precision of 2 nm [14], as shown in Fig. 2.14h. Hatef *et al.* have theoretically calculated that AuAg alloys can be used as photoacoustic agent that show superior photoacoustic signal as compared to pure Au and Ag [123].

2.5 Conclusion

I believe that this literature review has given a bird's eye view on the AuAg alloys providing details on the underlying theory, different methods of fabrication and applications. This work would help the readers to have an wholesome in-depth understanding of the current advances in the field of AuAg alloys in nanophotonics and thus would benefit them enormously in their scientific progress.

3 Developing new technology for fabricating alloy nanostructure

After providing an in-depth literature review on the importance and relevance of alloys in nanophotonics, I devote this chapter to the detailed description of a novel low temperature alloying process developed by me for fabricating AuAg alloyed nanostructures retaining their shape after annealing. Parts of this chapter were submitted in [280]. My contributions were the development of the low temperature alloying recipe and fabrication and imaging of all the samples shown in this chapter. The simulations of the Fano resonant structures were also performed by me. The XPS measurements are done by Pierre Mettraux. The measurements of the alloyed Fano resonant structures shown in Sec. 3.3.2 is carried out by Jeonghyeon Kim. Parts of this chapter has been submitted for publication [280].

3.1 Introduction

Every nanotechnology is indissociable from the materials it uses. Conversely, the materials involved often determine and limit the possible technological choices and the potential applications that can be envisioned. This is true for many different scientific fields, from energy [88, 208] to chemistry [122, 36], semiconductors [109, 373, 194], medicine [75, 319] or even food industry [383]. Plasmonics – the resonant optical interaction of light with free electrons in metals – also strongly relies on the utilization of specific materials, viz. coinage metals with a very high free electron density [21].

Thanks to its electronic properties, ease for fabrication and chemical stability, Au is the most widely used coinage metal for plasmonic applications. Its dielectric function $\epsilon(\lambda)$, where λ is the wavelength of light, produces a plasmon resonance in the long-wavelength range of the visible spectrum. Other metals, like Al and Ag, have plasmon resonances towards shorter wavelengths, but are more difficult for nanotechnology [344]. While the real part of $\epsilon(\lambda)$ determines the wavelength at which the plasmon resonance occurs, its imaginary part controls the plasmon resonance strength [162]. Since a decade, there has been a surge of research for alternative materials to Au, Ag and Al, in order to exploit plasmon resonances over the entire visible and near infrared spectrum [384, 234, 310].

In addition to pure materials, heterogeneous combinations of metals such as core-shell particles [415] and alloys [26] have also been proposed. Especially AuAg alloys as described in detail in Chapter 2, have demonstrated extremely interesting properties in terms of dielectric function tunability and chemical stability [403, 84]. Moreover, AuAg alloy very well thanks to their similar lattice constants [59] and a very simple binary phase diagram [114].

Existing techniques for the fabrication of AuAg alloys include laser ablation [178], co-reduction of AuAg salts [87, 101], co-deposition [25, 104], annealing at very high temperatures of Au-Ag core-shell nanoparticles with [11, 199, 417] and without [312] SiO₂ coating. All those bottom-up techniques provide limited control of the nanoparticles shape, as well as its reproducibility. In contrast, top-down fabrication techniques, such as e-beam lithography (EBL), are remarkably versatile and provide reliable control over the shape and size of individual nanoparticles [47]. Since the size of targeted nanostructures is typically in the range of a few tens to hundreds of nm, metal depositions are carried out using directional e-beam evaporation rather than isotropic co-sputtering to ensure reliable lift-off performances. Alloys have been deposited either by alloyed targets [245], which is costly since each composition requires a different target; or by alternating deposition of thin Au and Ag layers with subsequent annealing at high temperature, resulting in nanostructures that do not retain the original shape [392]. This represents a very severe limitation since the shape of plasmonic nanostructures determines their optical properties [162]. This warrants a need for cost-effective techniques for the stable fabrication of alloyed nanostructures with well-controlled sizes and shapes.

Here, I address this challenge and propose an original process for fabricating alloyed nanostructures. The method is based on the deposition of a bilayer of Au and Ag with subsequent annealing at low temperature at 300°C, far below the melting points of the individual metals. Thanks to the low temperature, the shape of the nanoparticles is retained after annealing. To demonstrate and verify that homogeneous alloys can be fabricated by this low temperature process, I first fabricate thin films of AuAg alloys and confirm their homogeneity by X-ray photoelectron spectroscopy (XPS) and energy-dispersive X-ray spectroscopy (EDX). Ellipsometric studies demonstrate the variation of the permittivity across different compositions. This technique is then applied to fabricate different alloyed nanostructures that perfectly retain their shape after low temperature annealing. Optical measurements demonstrate that the dielectric function of these nanostructures is tuned by varying the alloy's composition.

3.2 Fabrication of AuAg alloy thin films with low temperature annealing method

3.2.1 Recipe

Every new technology demands rigorous optimizations, and ours was no exception. Before I proceed to the next sections talking about alloy nanostructures, I want to elaborate in detail the challenges that I had faced on our way to developing a new recipe and the solutions

3.2. Fabrication of AuAg alloy thin films with low temperature annealing method

implemented to overcome them all. To start with let us talk about some steps that I have followed throughout this optimization process in order to get the best results.

1. I had started the development process by depositing a bilayer of Au and Ag of total thickness of 150 nm. I started optimization with thin films, to ensure continuous metal films crucial for reliable XPS analysis throughout the depth of the film to confirm the formation of an alloy. Since the size of XPS beam is several microns large (100 μm) it is not possible to perform XPS analysis on nanostructures, hence, I started with thin films and proceeded to use the optimized recipe for fabrication of nanostructures. The relative thickness for Au and Ag depends on the composition e.g.(30 nm Au and 120 nm Ag for $\text{Au}_{0.2}\text{Ag}_{0.8}$, 75 nm each for $\text{Au}_{0.5}\text{Ag}_{0.5}$ and 120 nm Au and 30 nm Ag for $\text{Au}_{0.8}\text{Ag}_{0.2}$). I had chosen this thickness, since 150 nm can be considered as opaque and therefore carrying out ellipsometry the bulk calculation model in WinElli II for calculating the refractive index can be used [344]. Figure 3.1 show the schematic of the 2 medium model on which the bulk calculation model of WinElli II is based. Since the thickness of the metal film is 150 nm and as mentioned opaque, I can ignore the effects of the substrate. Equation. 3.1 shows the corresponding equation, based on Frenel's equations, to measure the refractive index ($\epsilon_s = n - ik$) of the desired material. The parameter ρ in Eq.(3.1) is shown by Eq. (3.2), where Ψ and Δ are the parameters obtained from ellipsometry and ϕ_0 is the angle of reflectance.

$$\epsilon_s = \sin^2 \phi_0 + \sin^2 \phi_0 \tan^2 \phi_0 \frac{(1 - \rho)^2}{(1 + \rho)^2} \quad (3.1)$$

$$\rho = \tan \Psi e^{i\Delta} \quad (3.2)$$

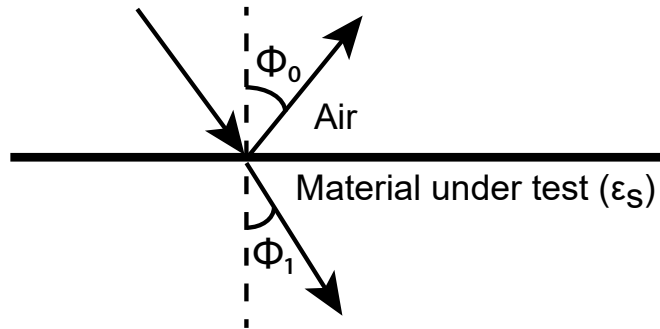


Figure 3.1 – The schematic of the 2 media model

2. XPS and Scanning electron microscope (SEM) images were obtained from the thin films fabricated on float glass. Since ellipsometric results are influenced by roughness of the film, 4-inch Si wafers with smooth polished surfaces were used as substrates for thin film deposition to ensure smoother films for ellipsometry. The alloy nanostructures shown in Sec. 3.3 were also fabricated on float glass.

3. Since the aim of this work, was to use this recipe for fabrication of alloyed nanostructures by liftoff method, the deposition for thin films, was also carried out in the ebeam evaporator (LAB600H), used for liftoff, with a source to substrate distance of 1010 mm. Indeed, such a long distance produces a more collimated beam of atoms, which is important for liftoff.
4. Ag nanostructures are difficult to fabricate since Ag nanostructures are strongly affected by the humidity more than Au and lose their shape [376]. Since our alloy included Ag the wafer was kept in the nitrogen chamber before and after fabrication (Sato Keiryoki MFG CO. LTD) [376]. In the nitrogen chamber there is always a steady N₂ flow of @4.25 Nl/min. Leaving the wafer in the chamber for a few days to a few weeks prior to the fabrication helped getting rid of some percentage of water molecules from the bulk substrate. More importantly it changes the morphology of the surface and reduces surface diffusion. The surface becomes more hydrophobic and remains dry after exposure to ambient conditions whereas if tried to remove by excessive heating the surface becomes rather hydrophilic. This step gave the Ag a much drier substrate to be deposited on and thus prevented forming islands when heated. The water from the surface is easier to remove and can be done by preheating the wafer at 180°C, as is done before depositing the e-beam resist. The pumping in LAB 600H to reach a desired vacuum before deposition, can also remove surface water to a certain extent. However none of these techniques can reduce the percentage of water molecules inside the bulk of the substrate, hence the need of the nitrogen chamber. After fabrication I also kept the wafers back in the nitrogen chamber which helped retaining the shape of Ag and AuAg alloy nanostructures, before annealing them to form an alloy. Ag is slightly soluble in water and therefore prone to surface dissolution in the presence of surface adsorbed H₂O. The dried substrate reduces this process from taking place and thus helps to retain the shape of the nanostructure [376]. However, I had annealed them within a few days after being kept in the nitrogen chamber to take advantage of the "unstable" configuration for annealing at lower temperatures. This is explained in more details in the later half of Sec. 3.2.2. In the subsection 3.2.4 I also explain in details the effects on the thin film associated with prolonged exposure in the nitrogen chamber.

For all the recipe optimizations I had chosen the composition Au_{0.2}Ag_{0.8} initially. Reaching the final recipe, I applied it to other two compositions Au_{0.5}Ag_{0.5} and Au_{0.8}Ag_{0.2} and confirmed that they were also well alloyed using the optimised parameters.

In order to start optimizing the recipe for annealing, I started by annealing the 150 nm thin films on 4-inch wafers at 450°C for 1 hour (temp. rose @10°C/min) under N₂ atmosphere in an oven (Neytech Qex Vacuum Porcelain furnace) since the float glass substrate could only withstand up to 550°C. However, without 2 nm of Ti adhesion layer, the film had small islands (around 1.5 to 2 μm large) after annealing as shown in Fig. 3.2a. Intending to decrease the islands in the film, I modified the recipe, and first heated the sample to 150°C (temp. rose @ 5°C/min) and kept the temperature for 1 hour, then the temperature was increased to 450°C

3.2. Fabrication of AuAg alloy thin films with low temperature annealing method

(temp. rose @5°C/min) and again kept for 1 hour. The idea behind the additional step of heating at 150°C was the decrease of surface dewetting to reduce the formation of islands and to favor, rearrangement of metal atoms in a more stable configuration with no islands. Unfortunately, the result was worse than before and larger islands were formed (Fig. 3.2c) showing that at 150°C surface diffusion is dominant compared to rearrangement of the metal. In order to decrease the islands, I preheated the fresh wafer at 450°C for 3 hours before the deposition of the metal. This along with addition of the 2 nm Ti as the adhesion layer did decrease the formation of islands, but did not remove them completely, as shown in Fig. 3.2b. Those results clearly show the impact of adsorbed H₂O on surface diffusion. XPS analysis of these wafers revealed a very homogeneous alloy, and Ti had diffused very little into the film, thus, retaining the purity of the AuAg alloy as shown in Fig. 3.3c. In a subsequent step this recipe was applied to plasmonic nanostructures. To our disappointment nanorods of 100 nm length and 50 nm width and thickness (Fig. 3.3a) did not keep their shape and transformed into oblate spheroids as shown in Fig. 3.3b. Thus, further optimization is required since high temperature annealing did not serve for our purpose (thin films with islands and destroyed nanostructures). Consequently, I decided to lower the annealing temperature.

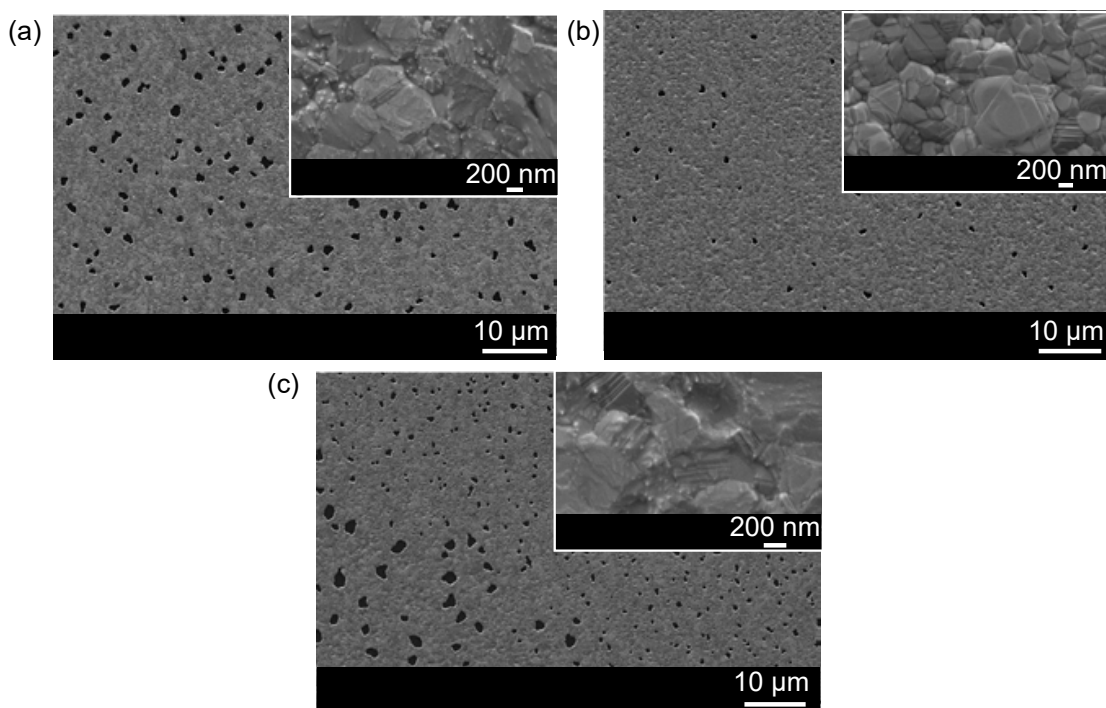


Figure 3.2 – SEM images of 150 nm Au_{0.2}Ag_{0.8} films annealed at (a) 450°C for 1 h without preheating and adhesion layer, (b) 450°C for 1 h with preheating and adhesion layer, (c) 150°C for 1 h and then at 450°C for 1 h without preheating and adhesion layer. Inset show zoomed in images of the same.

I endeavored further at lower temperature. I reduced the annealing temperature to 300°C (temp rose @10°C/min) and also increased the time of annealing to 2 h resulting in very nice

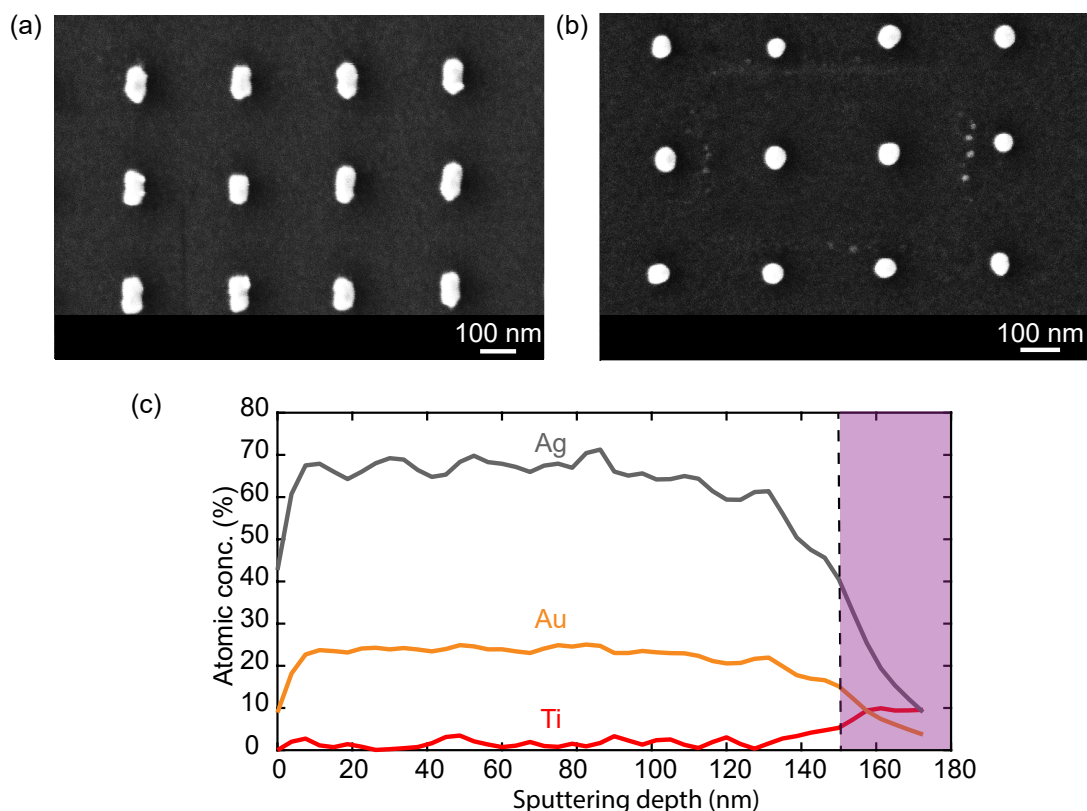


Figure 3.3 – SEM images of $\text{Au}_{0.2}\text{Ag}_{0.8}$ nanorods of length 100 nm and width 50 nm (a) not annealed (b) annealed at 450°C for 1 h (c) XPS analysis of 150 nm thin films of $\text{Au}_{0.2}\text{Ag}_{0.8}$ annealed at 450°C for 1 h. The dashed black line shows the beginning of the substrate and the shaded purple part denotes the depth inside the substrate.

uniform films without any islands even without preheating and adhesion layer as shown in Fig. 3.4a. Unfortunately, XPS results showed an incomplete annealing of the film (Fig. 3.5a). Preheating the fresh wafer before deposition had given us encouraging results for fabrication of thin films, especially with 450°C (Fig. 3.2b). However, parallel tests with nanostructures showed that preheating had buckled the float glass wafer to such an extent that the variation of height across the wafer exceeded the threshold value of 50 μm needed to perform accurate e-beam lithography. The electron beam became highly defocussed and thus only wrote the markers which are several microns large but failed to write the nanostructures. To overcome the problem, I also tried to preheat the wafer at 450°C in two intervals each for 1 hour 30 mins. After the first interval the wafer was taken out and its side was flipped. It was done to ensure that both sides of the wafer experience the same temperature variations. I believed that it would compensate for the height variations and the buckling. But unfortunately, it failed too. Since I already had encouraging results from 300°C for 2 h (Fig. 3.4a) without preheating, I continued without preheating the fresh wafer and directly proceeded to deposition, both for thin films and for nanostructures to maintain the continuity.

3.2. Fabrication of AuAg alloy thin films with low temperature annealing method

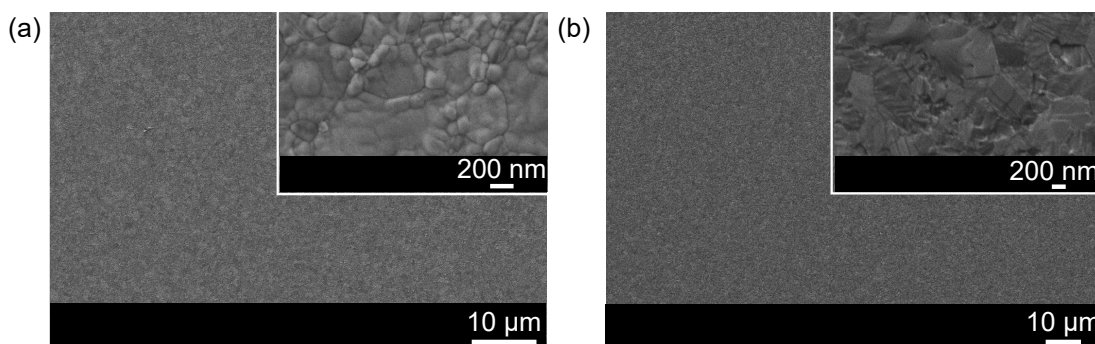


Figure 3.4 – SEM images of 150 nm $\text{Au}_{0.2}\text{Ag}_{0.8}$ films (without preheating and adhesion layer) annealed at (a) 300°C for 2 h (b) 300°C for 5 h. Inset shows zoomed in images of the same.

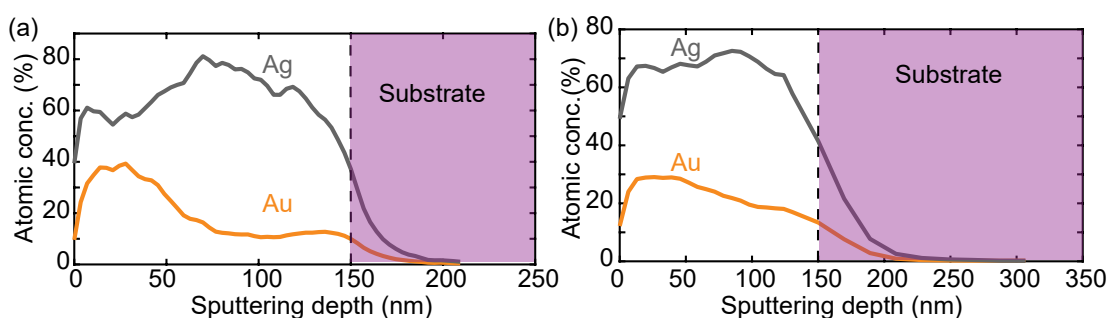


Figure 3.5 – XPS measurements for an $\text{Au}_{0.2}\text{Ag}_{0.8}$ films annealed for 300°C for (a) 2 hours (b) 5 hours

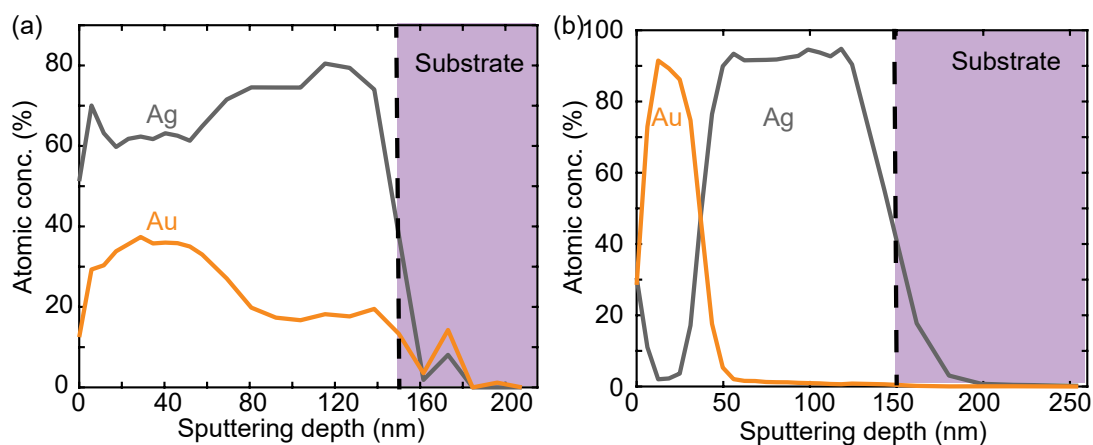


Figure 3.6 – XPS measurements for an $\text{Au}_{0.2}\text{Ag}_{0.8}$ films (a) annealed for 300°C for 8 hours (b) not annealed.

Next, by keeping the temperature constant to 300°C (temp. rose @10°C/min), I increased the time to 5 hours. Here also I had nice films even without Ti as adhesive layer as shown in Fig. 3.4b. However, XPS results showed a better annealing compared to Fig. 3.5a, the

distribution was still not homogeneous throughout the entire thickness of the metal layer (Fig. 3.5b). Finally, I increased the time to 8 hours keeping all other parameters constant and for better nanostructures and enhanced adhesion I used 2 nm of Ti as adhesion layer for both the thin films and nanostructures. The XPS results for 150 nm thin film heated at 300°C for 8 hours are shown in Fig. 3.6a. It shows that it is better alloyed than 300°C for 5 hours (Fig. 3.5b) but still not alloyed homogeneously. Finally I modified the recipe to anneal at 300°C for 8 hours and at 450°C for 30 mins. This additional heating step at 450°C for 30 min resulted in forming a homogeneous alloy as shown in Fig. 3.7e. In contrast, XPS analysis of films carried out prior to annealing distinctly shows the bilayer of Ag and Au, Fig. 3.6b.

3.2.2 Studies of AuAg alloy ($\text{Au}_{0.2}\text{Ag}_{0.8}$, $\text{Au}_{0.5}\text{Ag}_{0.5}$, $\text{Au}_{0.8}\text{Ag}_{0.2}$) thin films with optimized recipe

Figure 3.7a shows the schematic of fabrication of thin films using the low temperature annealing method. Figures 3.7b and 3.7c show SEM images for this double layer film before and after annealing (300°C for 8 hours followed by 30 min at 450°C), with insets providing magnified views. It can be clearly seen that the film has lost its grainy appearance and reorganized into a more crystalline configuration during the annealing process [376, 173]. EDX maps of all elements of interest are superimposed in Fig. 3.7d, revealing a homogeneous distribution of Au and Ag.

The alloying conditions have a huge impact on the material parameters of the film. Since the method of low temperature alloying is new and different from the traditional alloying temperatures, I also wanted to measure the refractive index of the films with ellipsometry. The incident angle was chosen as 75°C and measurements were performed at 9 points across the wafer to analyse the homogeneity of the film across the wafer. As discussed in Sec. 3.2.1 the bulk calculation model of WinElli II was used to extract the parameters. For $\text{Au}_{0.2}\text{Ag}_{0.8}$ I got similar values across the 9 points showing that the annealed film is homogeneous. Since this annealing temperature has given a homogeneous alloy, both vertically and spatially across the 4-inch wafer, as confirmed by XPS (Fig. 3.7e), EDX (Fig. 3.7d) and ellipsometry respectively, I applied this final recipe to investigate alloyed plasmonic nanostructures in Sec. 3.3.

I then applied these conditions on the other compositions as well i.e on $\text{Au}_{0.5}\text{Ag}_{0.5}$ and $\text{Au}_{0.8}\text{Ag}_{0.2}$. For $\text{Au}_{0.5}\text{Ag}_{0.5}$ the films were successfully alloyed as verified by XPS measurements (Fig. 3.8e). Figure 3.8a shows the SEM image of the film after being annealed whereas, Fig. 3.8c shows the superposed EDX maps showing a homogeneous distribution of the metals. Moreover the ellipsometric measurements over all the 9 points were similar thus showing the homogeneity of the films. In Fig. 3.7f the average value measured over 9 points during ellipsometry for Au, $\text{Au}_{0.5}\text{Ag}_{0.5}$, $\text{Au}_{0.2}\text{Ag}_{0.8}$ and Ag are shown [281]. It can be seen that the real part of the dielectric function for both alloys lies between pure Au and pure Ag. This modification of ϵ_{real} with change in composition leads to variations of the plasma frequency as well [141]. The imaginary part, however, is more complicated since it reflects the material losses and can

3.2. Fabrication of AuAg alloy thin films with low temperature annealing method

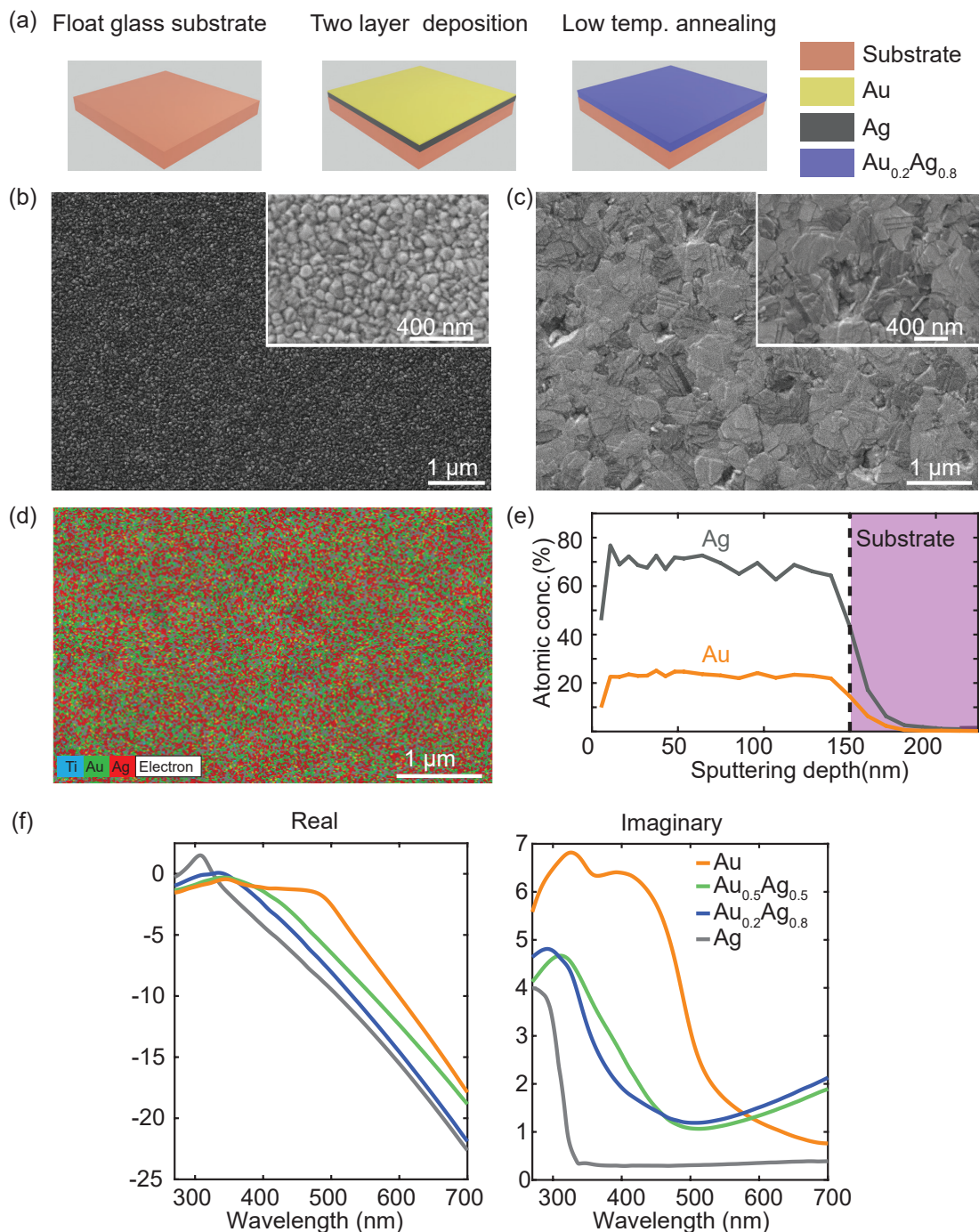


Figure 3.7 – (a) Process flow for fabricating thin films with a specific stoichiometry; yellow denotes Au and grey denotes Ag. (b) SEM image of a double-layer film for $\text{Au}_{0.2}\text{Ag}_{0.8}$ before annealing. (c) SEM image of the same film after annealing. The insets in (b) and (c) show a magnified view. (d) Superimposed EDX maps for Au, Ag and Ti. (e) XPS analysis of the $\text{Au}_{0.2}\text{Ag}_{0.8}$ alloy, demonstrating a homogeneous alloy over the entire 150 nm depth. (f) Experimentally obtained ellipsometric data for pure Au, $\text{Au}_{0.2}\text{Ag}_{0.8}$, $\text{Au}_{0.5}\text{Ag}_{0.5}$ and pure Ag.

be affected by various factors such as grain boundaries and defect sites [131, 308].

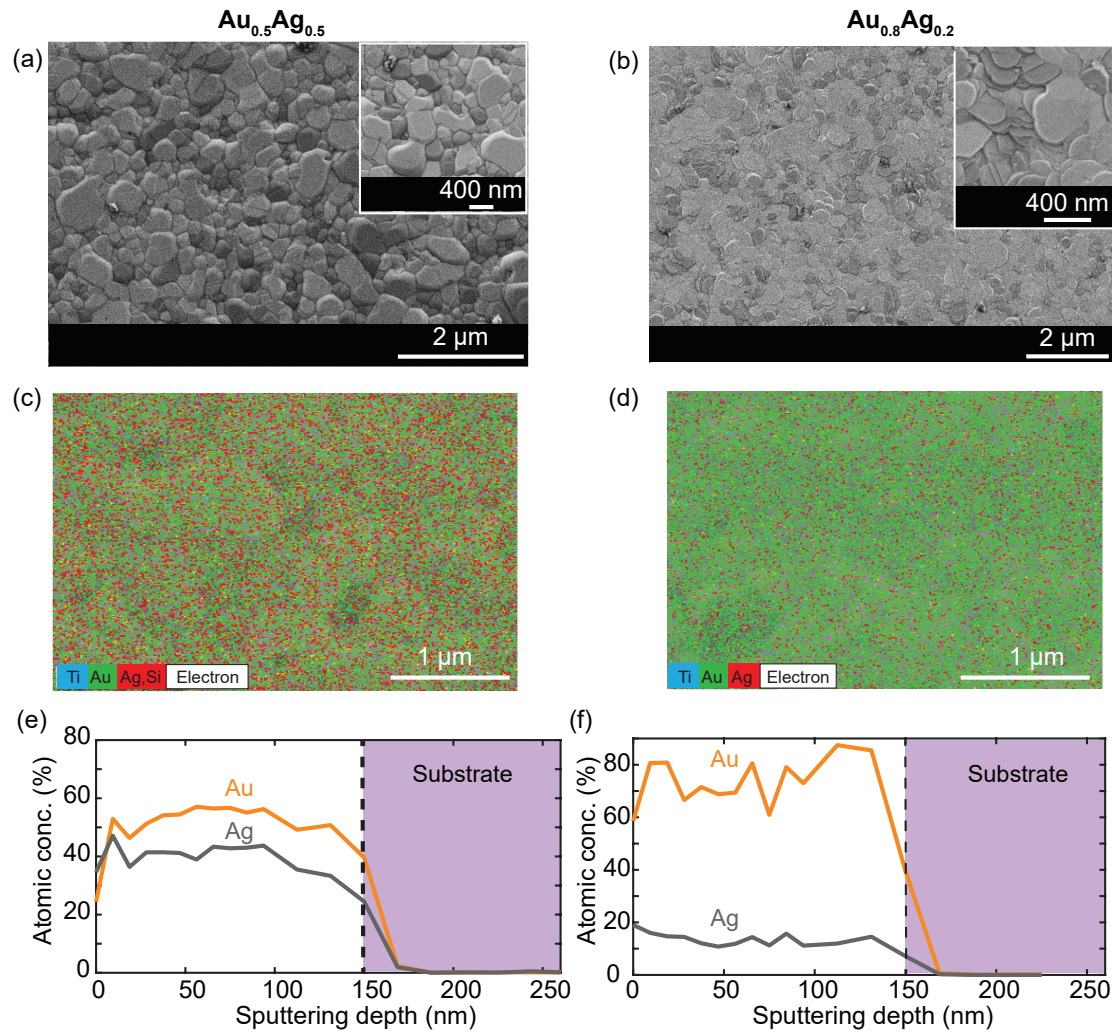


Figure 3.8 – $\text{Au}_{0.5}\text{Ag}_{0.5}$ and $\text{Au}_{0.8}\text{Ag}_{0.2}$ thin films (a-b) SEM images. Inset shows magnified view. (c-d) Superposed EDX maps of Au, Ag and Ti. (e-f) XPS analysis of the annealed films showing homogeneous alloy.

Before I proceed to more results, I would like to briefly discuss the conditions that make alloying at low temperature successful. Homogeneously alloyed samples at 300°C – which is well below the Tamman temperature of Au and Ag [16] – require the annealing to be performed within a few days after metal deposition. The deposition of the metal film, leaves it in an unstable morphology due to the presence of high relative humidity and the film remains in this state for a couple of days after the deposition [376]. Since the film is not yet well-ordered, it takes less thermal energy for the Au and Ag atoms to diffuse. Thus, the onset of the diffusion occurs at lower temperatures, which makes it possible to completely alloy thin films at a temperature of 300°C. On the other hand, I have observed that it was not possible to anneal at low temperature bilayer Au-Ag films that were kept in a nitrogen atmosphere (Saito Keiryoki

3.2. Fabrication of AuAg alloy thin films with low temperature annealing method

MFG. CO. LTD) for more than a week before annealing. The effects of leaving the sample long term in the N₂ chamber has been explained in more details in Sec. 3.2.4.

3.2.3 Challenges with Au_{0.8}Ag_{0.2} thin films on 4-inch wafers

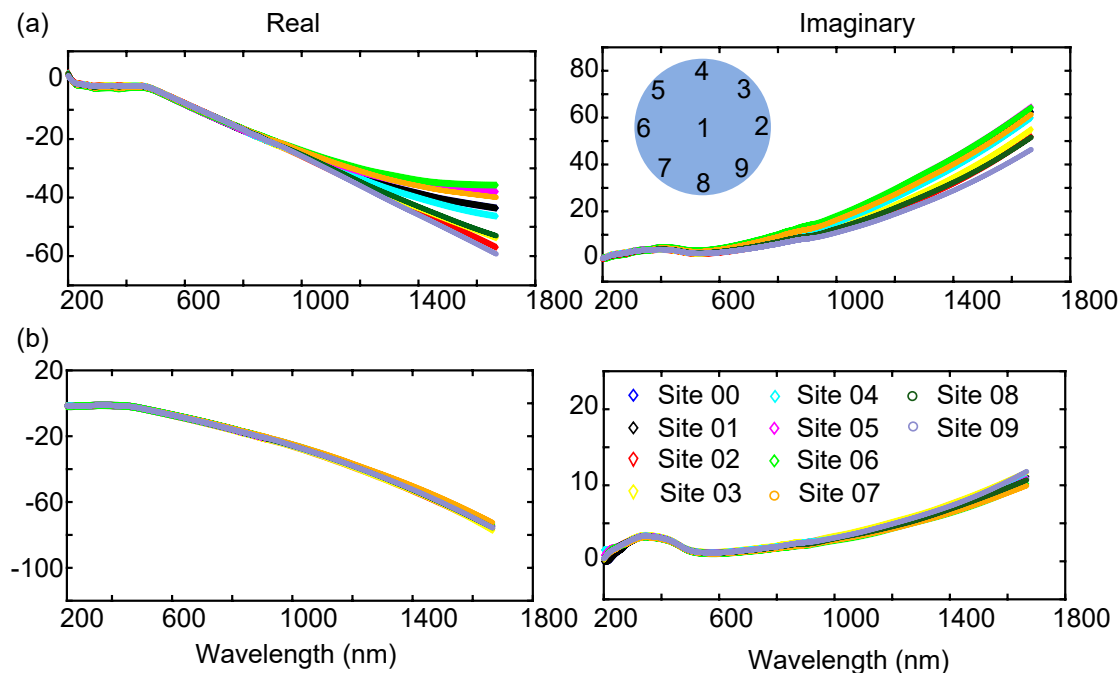


Figure 3.9 – Ellipsometry carried out at 9 points of a 4-inch wafer of 150 nm thick (a) Au_{0.8}Ag_{0.2} composition (bi-layer) annealed at 300°C for 8 h and 450°C for 30 min (b) Au_{0.8}Ag_{0.2} composition (tri-layer,) annealed at 300°C for 8 h and 450°C for 2 h and 30 min.

The optimized recipe of low temperature alloying (300°C for 8 h and 450°C for 30 min) worked very well for the Au_{0.2}Ag_{0.8} and Au_{0.5}Ag_{0.5} thin films deposited on 4 inch wafer. However the Au_{0.8}Ag_{0.2} thin films proved to be an exception. As for Au_{0.8}Ag_{0.2}, after annealing even though the film was homogeneously alloyed, as shown by XPS (Fig. 3.8f) and EDX (Fig. 3.8d), I did not obtain similar results over the 9 points in the wafer during ellipsometry showing that the annealed film was not homogeneous across the 4-inch wafer (Fig. 3.9a). This called for some additional optimization steps.

The fact that XPS results showed that the film is homogeneously alloyed while the ellipsometric data across the 9 points of the wafer exhibit different results at each point indicates that this discrepancy arose from annealing 4-inch wafer for ellipsometric study as compared to annealing 1 cm chips for XPS. 300°C is a relatively low temperature which gives just enough energy to the Au and Ag atoms to expedite their diffusion process and form an homogeneous alloy. I believe that across the 4-inch wafer there was temperature variations due to which there is inhomogeneous alloying across the wafer. This effect is more pronounced in the Au_{0.8}Ag_{0.2} composition since a thicker film of Au (120 nm) needs to diffuse into Ag (30 nm) and

diffusion of Au into Ag is slower than diffusion of Ag in Au [45]. Since temperature influences the rate of diffusion, the variation of temperature across the wafer lead to inhomogeneous alloying with pronounced effect in the ellipsometry. For the XPS, since the beam is only 100 μm large and sample is examined at one site, a chip less than 1 cm was annealed. The annealing conditions are good enough to produce spatially homogeneous films across such small chips.

Having identified the problem successfully, I decided to solve it. However again it should be noted here that this solution was not necessary for fabricating $\text{Au}_{0.8}\text{Ag}_{0.2}$ nanostructures as both XPS and EDX results showed that the $\text{Au}_{0.8}\text{Ag}_{0.2}$ alloyed film was homogeneous both vertically and spatially and our nanostructures are only a few hundreds of nm large. However, since I aimed at a recipe that can be also used for fabrication of wafer scale thin films I continued our research.

To facilitate diffusion I deposited three layers of Au and Ag in a sandwich structure i.e. 60 nm of Au-30 nm of Ag-60 nm of Au. It was also annealed at 300°C for 8 hours and 450°C for 30 mins which did not provide the desired results. It was then annealed at 300°C for 8 hour and at 450°C for 2 h 30 min leading to similar results across all the 9 points showing that the film has now been homogeneously alloyed, (Fig. 3.9b). In Fig. 3.10 I provide the permittivity of all the composition including $\text{Au}_{0.8}\text{Ag}_{0.2}$ (data taken as the average data from ellipsometric measurements of Fig. 3.9b) and a comparison with the Rioux model [288], a theoretical model used extensively in the literature to predict the behaviour of alloys. The permittivity of Au, $\text{Au}_{0.2}\text{Ag}_{0.8}$, $\text{Au}_{0.5}\text{Ag}_{0.5}$ and Ag agrees very well with the model of Rioux. *et al.* [288]. The experimental data also agree well with the experimental values reported by Rodriguez. *et al.* [261]. The ϵ_{imag} obtained by measuring our $\text{Au}_{0.8}\text{Ag}_{0.2}$ film shows that the film has lesser absorption in 700-1200 nm than that predicted by the Rioux model. Overall, the agreement with the Rioux model is very good. In the later sections for fabrication of AuAg alloyed nanostructures, the optimized condition of 300°C for 8 h and 450°C for 30 min in the N_2 atmosphere is used as the annealing condition for all the compositions including $\text{Au}_{0.8}\text{Ag}_{0.2}$. As explained earlier since EDX and XPS data showed homogeneous $\text{Au}_{0.8}\text{Ag}_{0.2}$ thin films for several microns with these parameters (Fig. 3.8d and 3.8f) I also use these parameters to alloy $\text{Au}_{0.8}\text{Ag}_{0.2}$ nanostructures which are several hundreds of nm large. However to maintain the continuity with the deposition, only for the nanostructures with $\text{Au}_{0.8}\text{Ag}_{0.2}$ composition I also use the three layer (Au-Ag-Au) configuration for deposition. For $\text{Au}_{0.2}\text{Ag}_{0.8}$ and $\text{Au}_{0.5}\text{Ag}_{0.5}$ compositions I continue to deposit bilayer of Au-Ag.

3.2.4 Long term stability studies

In order to understand the effects of the nitrogen chamber on the alloyed films, and to further explain that the success of low temperature alloying process I have taken SEM images of the films kept in the nitrogen chamber for 4-5 months after alloying and compared them to the freshly alloyed sample as shown in Fig. 3.11. It can be seen that for $\text{Au}_{0.2}\text{Ag}_{0.8}$ the film appears to be smoother and more crystalline, after 4-5 months in the N_2 chamber. For $\text{Au}_{0.5}\text{Ag}_{0.5}$, the

3.2. Fabrication of AuAg alloy thin films with low temperature annealing method

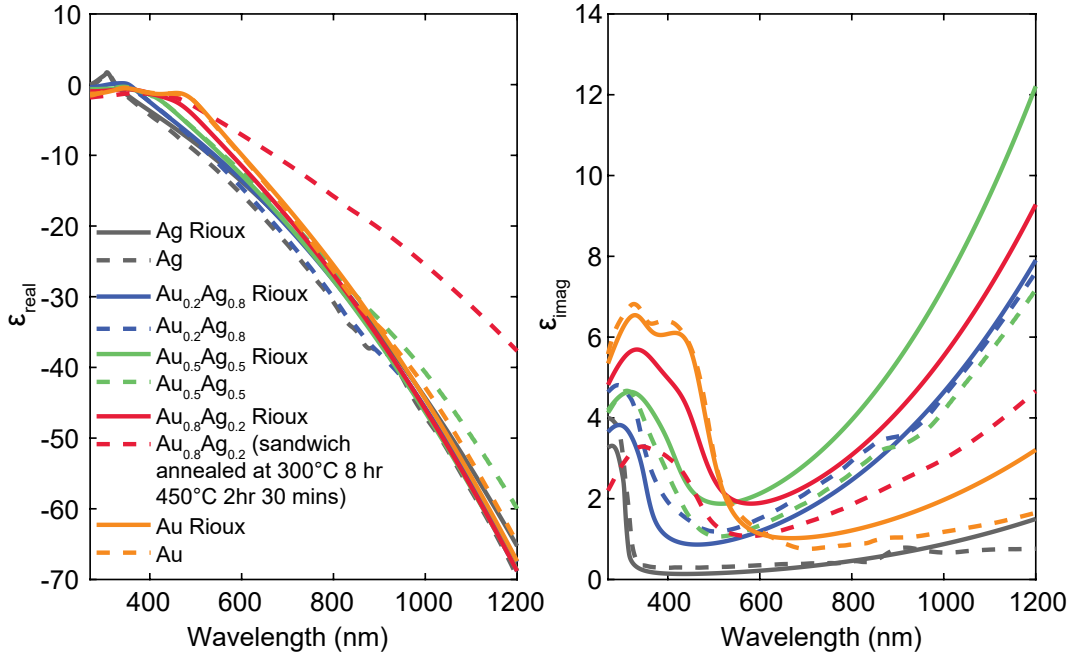


Figure 3.10 – Comparison of permittivity between values obtained from Rioux model and that measured using ellipsometry

film has been completely destroyed after long exposure in the N_2 chamber and it has formed islands. I see a similar transformation for the $Au_{0.8}Ag_{0.2}$ configuration; here also the film disarranges and forms islands. I believe that a prolonged exposure to the dry chamber has removed the humidity from the sample. This has led to a rearrangement of the atoms into a more stable and compact crystalline like configuration which takes up less space and leads to the formation of islands. The fact that a prolonged exposure to the nitrogen chamber makes the film more stable and compact can be further proved by Fig. 3.12. Here panel a shows SEM image of the wafer before annealing, taken within few days of deposition. Panel c shows a similar thin film, before annealing, but imaged after 4.5 months. During this period the wafer was kept in the N_2 chamber. The film shown in panel c, is annealed i.e. annealing after 4-5 months of deposition, at $300^\circ C$ for 8 hours and $450^\circ C$ for 60 min (30 min more than the optimized recipe), shown in Fig. 3.12d. This film can be compared to the film annealed within a few days of deposition in Fig. 3.12b. It can be seen that annealing a bilayer of Au-Ag after 4.5 months of deposition forms particles (Fig. 3.12d) instead of forming a smooth film when annealed within a few days of deposition avoiding prolonged exposure of the metal bilayer to N_2 in the N_2 chamber (Fig. 3.12b). It is because, with prolonged exposure in the N_2 chamber the deposited film is much more stable now and it would require much higher temperature to alloy successfully. Heating at low temperature is only sufficient to dewet a few particles and not to alloy the film uniformly. This indicates that with passing time the bilayer film becomes very stable and thus requires a higher temperature to form homogeneous alloy. So for low temperature alloying process it is necessary to take advantage of the unstable morphology

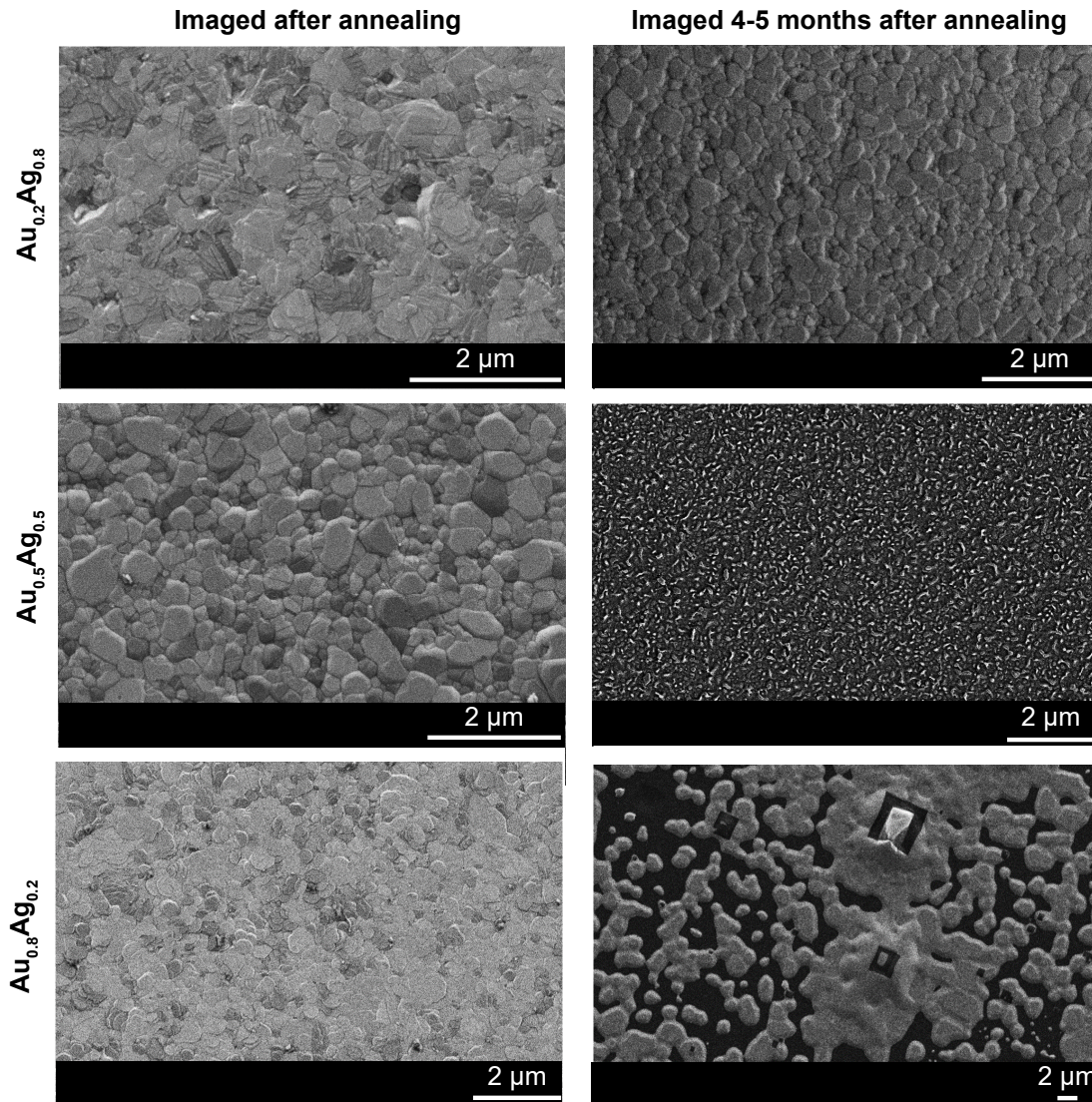


Figure 3.11 – SEM images of 150 nm AuAg thin film alloys taken right after annealing (on float glass substrate) and after 4-5 months after annealing (on Si substrate)

after deposition and anneal within a few days of deposition.

It should be mentioned here that the SEM images of the freshly alloyed sample, shown in left column of Fig. 3.11, have been fabricated on float glass substrates while those of the films imaged after 4-5 months, shown in the right column, have been prepared on Si substrates. Due to the native oxide layer, always present on Si substrates, the surfaces of float glass and Si substrates can be considered as to be very similar. Furthermore, the thickness of the alloyed film is 150 nm, which reduces the influence of the substrate even further. Thus, freshly annealed thin films on float glass substrates on the left column are appropriate representations of the annealed films regardless of the substrate and can, therefore, be used to compare with

3.2. Fabrication of AuAg alloy thin films with low temperature annealing method

the films on Si substrates imaged after 5 months. However, it should be kept in mind, for an ultimate conclusion on the stability of alloyed films deposited on the same substrate should be compared. Our experiments indicate that the long-term stability depends of the Au/Ag ratio and decreases with increasing percentage of gold. As shown by Wang *et al.* [376] silver thin films and nanostructures exhibit an excellent long-term stability after a nitrogen drying step.

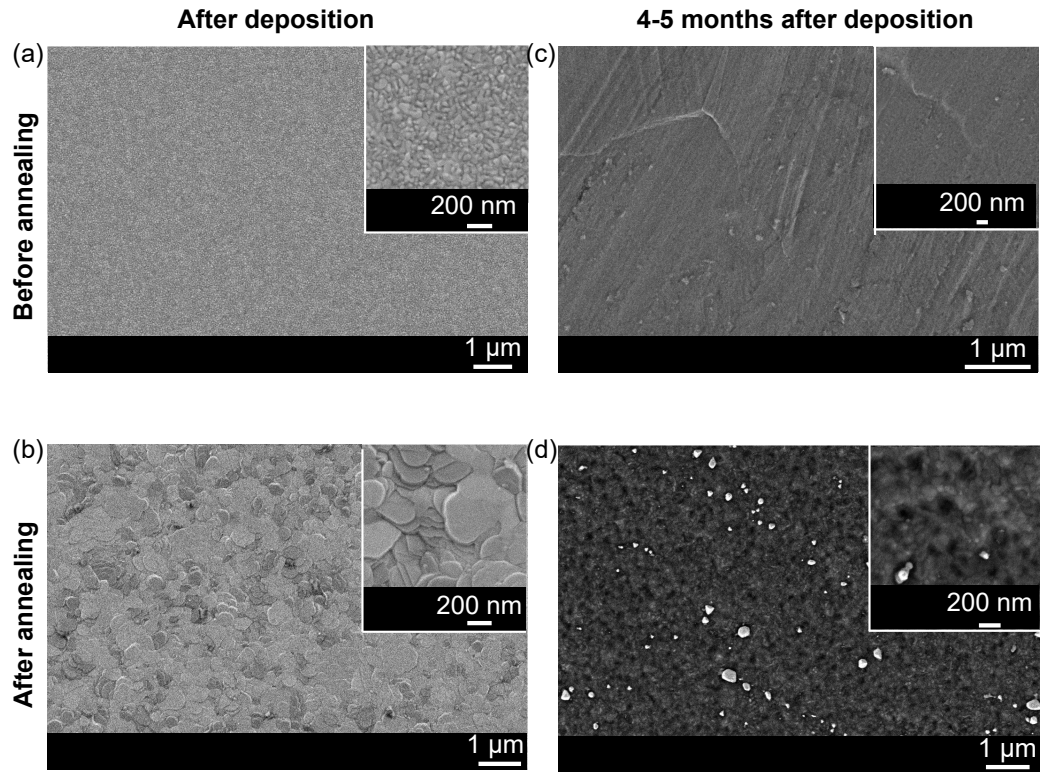


Figure 3.12 – SEM images of 150 nm $\text{Au}_{0.8}\text{Ag}_{0.2}$ thin film (a) not annealed after deposition (on float glass substrate) (b) annealed at 300°C for 8 h and 450°C for 30 min (on float glass substrate). SEM images of 150 nm $\text{Au}_{0.8}\text{Ag}_{0.2}$ thin film after 4.5 months (c) not annealed (on Si substrate) (d) annealed at 300°C for 8 h and 450°C for 60 min (on Si substrate).

3.3 Fabrication of alloyed nanostructures with the optimised recipe

3.3.1 Fabrication of alloyed nanorods and nanotriangles ($\text{Au}_{0.2}\text{Ag}_{0.8}$)

The advantages associated with the low temperature annealing presented in Sec. 3.2.2 are unleashed for the fabrication of nanostructures with different stoichiometries, as illustrated in Fig. 3.13a. Here I use the optimized parameter for annealing (300°C for 8 h and 450°C for 30 min in N_2 atmosphere) for all composition. Similar to the alloyed thin films the Au-Ag bilayers are deposited by e-beam evaporation. Figures 3.13b and 3.13c show SEM images of an array of 50 nm thick rods and triangles before and after annealing. The corresponding insets magnify a single $400\text{ nm} \times 50\text{ nm}$ nanorod and a nanotriangle with a 260 nm side length. It is remarkable that the nanostructure shapes are perfectly retained after annealing, even for very high aspect ratio structures. The yield of this approach is also very high, as indicated by the widefield images. EDX measurements shown in Fig. 3.14 reveal a homogeneous Au-Ag distribution over the entire nanostructure. The benefits of the low temperature annealing process can be better appreciated by looking at the SEM images for similar nanostructures obtained by high temperature annealing at 800°C for 3 hours in a nitrogen environment (bottom row of Fig. 3.13b and 3.13c). Those nanostructures do not retain their shape at all, as opposed to those of low temperature annealing. Consequently, nanostructures with a specific shape, annealed at high temperature will not exhibit the optical response they were designed for [163].

3.3.2 Fabrication and measurements of alloyed Fano resonance structures

More sophisticated arrangements like 4-rod Fano-resonant structures are fabricated [376, 206], Fig. 3.15a. The lengths of the longer and shorter rods are 130 nm and 68 nm, respectively. The gaps are 30 nm and the structures thickness is 40 nm. After annealing, the shape is perfectly retained. The Fano spectrum arises from the interference of a broad bright and narrow dark mode [148] and can be tuned by changing the alloy composition. Exactly the same geometry was fabricated in 5 different stoichiometries: Au, $\text{Au}_{0.8}\text{Ag}_{0.2}$, $\text{Au}_{0.5}\text{Ag}_{0.5}$, $\text{Au}_{0.2}\text{Ag}_{0.8}$ and Ag. The optical responses of these structures measured in dark field microscope (setup described in Fig. 3.16) are shown in Fig. 3.15c. The experiments confirm the variation of the spectra with the composition. Simulations were carried out using the non-periodic surface integral equation method [148, 91] and the dielectric functions obtained from the Rioux model [288]. The agreement between simulations and experiments is fair with some spectral features washed out by inhomogeneous broadening associated with the fabrication error and imperfections, Fig. 3.15c. Since the Fano spectra is dependent on the gap size and the length on the nanorods [206] it is also strongly affected by the fabrication errors and imperfections. So in Fig. 3.15c we represent the best optical measurements that match the simulation, among the numerous spectra measured [281], to represent the tuning of the spectra with alloy composition. The results presented in this section demonstrate the additional degree of freedom offered by the fabrication of alloyed AuAg nanostructures with varying stoichiometry.

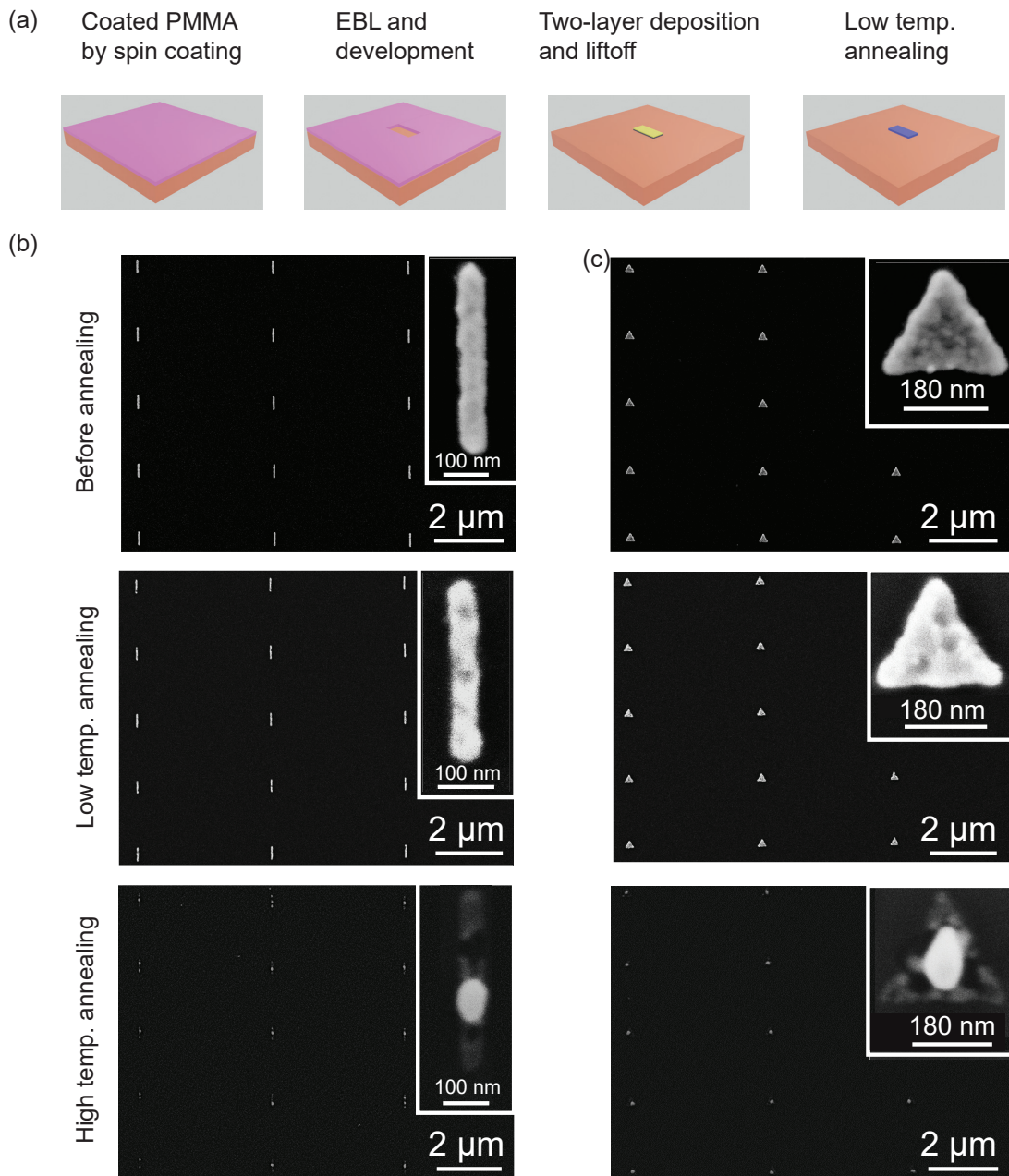


Figure 3.13 – Fabrication and optical characterization of alloyed nanostructures. (a) Process flow. SEM images of an array of $\text{Au}_{0.2}\text{Ag}_{0.8}$. The colour code is same as Fig. 3.7a. (b) $400 \text{ nm} \times 50 \text{ nm}$ rods and (c) 260 nm equilateral triangles before (top row), after (middle row) low temp annealing at 300°C for 8 hours followed by 450°C for 30 min, as well as (bottom row) high temp. annealing at 800°C for 3 hours. The insets show a single nanostructure from the corresponding array.

3.4 Conclusion

To conclude this chapter, I have introduced a facile and cost-effective nanofabrication technique to produce $\text{Au}_x\text{Ag}_{1-x}$ alloyed nanostructures with arbitrary stoichiometry solely det

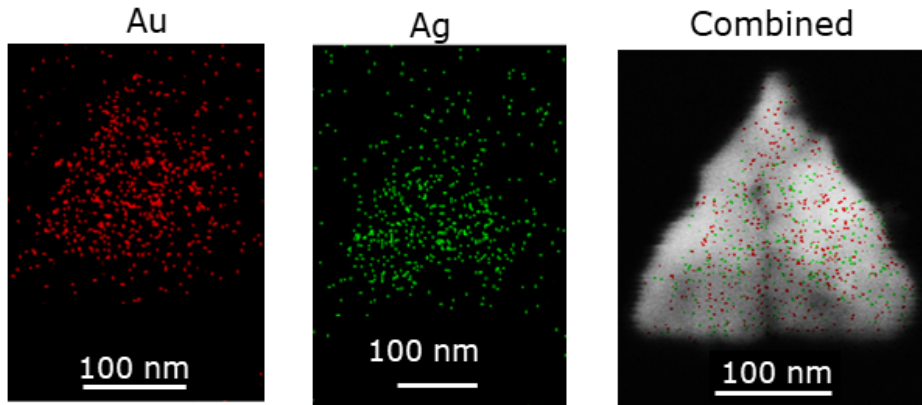


Figure 3.14 – EDX images of the nanotriangle showing distribution of Au, Ag and superimposed image of Au and Ag distribution.

mined by the thickness of the different deposited metals. Thanks to the low temperature annealing process, well-alloyed nanostructures with arbitrary shape can be fabricated, including those with a high aspect ratio. This is not the case for conventional high temperature annealing, in which nanostructures irreparably acquire an ill-defined blubbery geometry. Nanostructures fabricated with this technique retain their designed optical properties, as demonstrated with different systems, including Fano-resonant structures. The ellipsometric data of those alloys agree well with theoretical models. In the next chapter I show the successful fabrication of metaholograms and metalenses built from a collection of similar nanostructures with different stoichiometries demonstrated using this new fabrication technique. This technique unlocks additional degrees of freedom for the realization of advanced optical elements at the nanoscale.

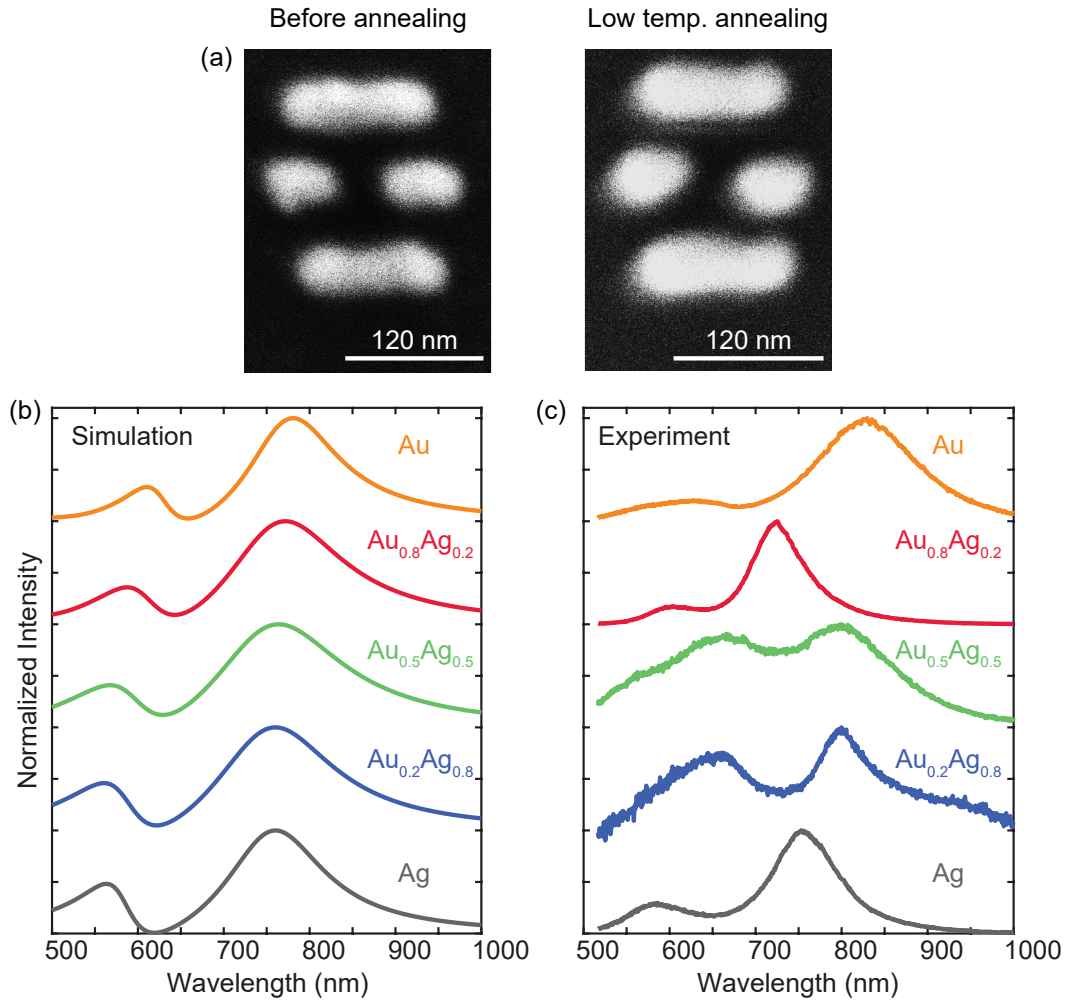


Figure 3.15 – Fabrication and optical characterization of Fano resonant structures. (a) SEM images of a $Au_{0.8}Ag_{0.2}$ 4-rod Fano-resonant structure before and after low. temp annealing. (b) Calculated and (c) measured optical spectra of the Fano-resonant structures with different stoichiometries. Measurements of the Fano resonant structures were performed by Jeonghyeon Kim.

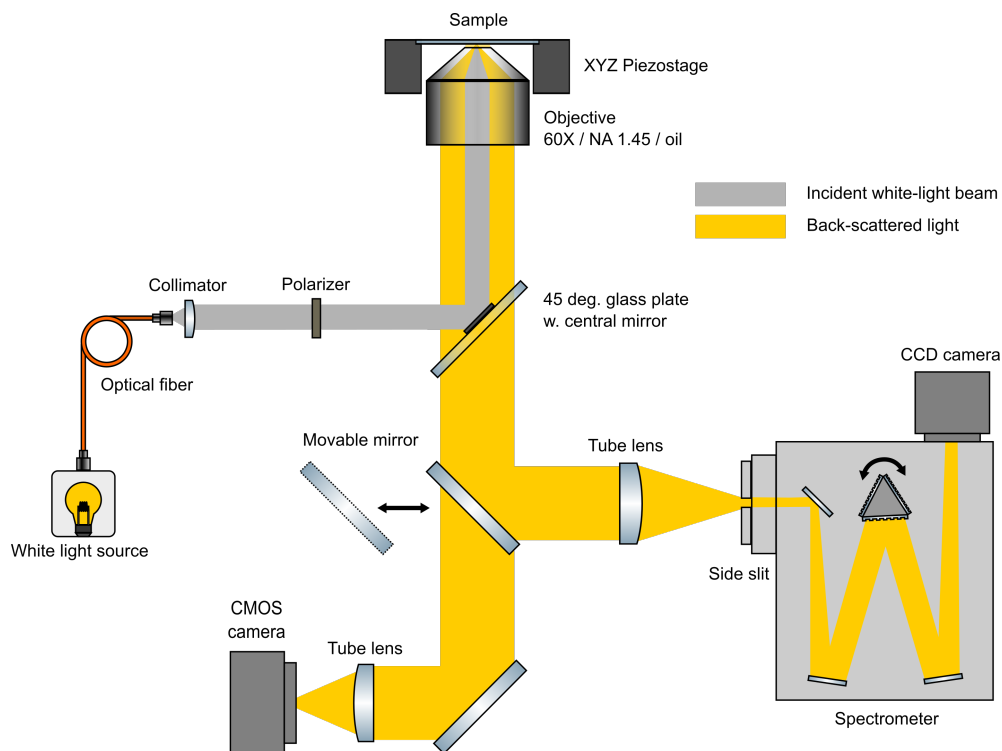


Figure 3.16 – The scatterings of the Fano resonant structures at different alloy compositions were imaged using an inverted optical microscope. The dark-field imaging was realized with a 45-degree glass plate with a circular mirror at the center, which reflected the incident light from a halogen lamp (grey columns) and transmitted the high-angle component of the back-scattered light from the sample (yellow columns). Once confirmed at the imaging CMOS camera, the same scattered signal was sent to a spectrometer, and the scattering spectrum for a single nanostructure was measured. Figure from Jeonghyeon Kim.

4 Optical applications of AuAg alloys

In the previous chapters I have discussed the importance of AuAg alloys in nanophotonics and developed a new technique for fabricating alloy nanostructures using low temperature annealing technique. In this chapter I am going to discuss several applications undertaken with AuAg alloys. This chapter is mainly divided into two main applications of alloys. In the first section I describe optical applications like hologram and Fresnel Zone lens with alloy nanostructures fabricated using the low temperature alloying technique. In the second section I describe the generation of hot electrons with alloys fabricated using a dewetting technique. I have concluded the chapter by briefly describing a broadband absorption system fabricated with Au nanoparticles that can be implemented for generation of photocurrent due to hot electrons. Even though this system does not include alloys, it is an extension of the work done on hot electron generation with AuAg alloy nanoparticles.

My contributions were fabrication, imaging and analysis of all the samples shown in this chapter and optimizing the 3-level e-beam alignment procedure. For Sec. 4.1 the simulations and the measurements of the alloyed metasurface were carried out by my colleague Hsiang-Chu Wang. For Sec. 4.2 the UV-Vis measurements and the photocurrent measurements were done by my colleague Dr. Madasamy Thangamuthu. The density functional theory calculations were carried out by Dr. Priyank Kumar from the School of Chemical Engineering, University of New South Wales (UNSW), Australia. Parts of this chapter has been submitted for publication [280] and will be published in scientific literature [341].

4.1 Applications in optics: Alloyed metasurface with $\text{Au}_{0.2}\text{Ag}_{0.8}$ and $\text{Au}_{0.8}\text{Ag}_{0.2}$ alloys

Let us now apply the low temperature annealing technique described in Chapter 3 to the fabrication of metasurfaces like holograms and Fresnel zone plates, which require combining alloyed nanostructures with different stoichiometries on the same substrate. Generally, tuning the response of a meta-atom is achieved by tailoring its geometry to produce the desired phase and amplitude response [368]. Here, instead of varying the shape, we change the material

whilst keeping the shape constant. Binary phase metasurfaces are fabricated with two different alloys, $\text{Au}_{0.8}\text{Ag}_{0.2}$ and $\text{Au}_{0.2}\text{Ag}_{0.8}$. It should be noted that in this work the meta-atoms shape is kept constant to emphasize the effect of changing the optical properties of the material; this nanotechnology can of course be applied to meta-atoms with different shapes as well as different stoichiometries, thus providing a very large number of degrees of freedom for the metasurface design.

4.1.1 3 level alignment for the binary metasurface

In order to fabricate a binary metasurface with two different alloy composition $\text{Au}_{0.2}\text{Ag}_{0.8}$ and $\text{Au}_{0.8}\text{Ag}_{0.2}$, I need to do two individual depositions leading to multiple e-beam exposures. In these exposures, the entire pattern is subdivided into two parts, better known as layers, each corresponding to a composition. The subpattern are consequently written one by one. To perform aligned multiple e-beam exposures on the same wafer, the consecutive pattern need to be aligned to the one previously written. The alignment is ensured by using the 3-level e-beam alignment markers (prealignment markers, global markers and local markers shown in Fig. 4.1) where the use of local markers are done to ensure enhanced accuracy in the alignment. These alignment markers need to be written first in order to define precise reference positions which are referred for the following exposure. In order to achieve precisions in the 10 nm range, the multiple e-beam procedure needs optimization which is described in details in this section.

As a test sample I first fabricated a binary grating with identical nanostructures but alternating compositions using an optimized double layer PMMA recipe [427]. It is composed of pairs of disks with each disk having a different composition and a radius of 105 nm. The disks are spaced by 200 nm and the pairs are periodically arranged with a period of 600 nm. In addition, I also fabricated nanorods of length 400 nm and width 50 nm and equilateral triangles with a side length of 300 nm. Nanorods and triangles of same composition are separated by 4 μm while rods and triangles of other compositions are separated by 2 μm . In the first try, these nanostructures were fabricated using two steps e-beam lithography, where the first layer of the nanostructures with disks, rods and triangles of same composition was written together with the alignment marks in the first step. In the subsequent e-beam exposure the next layer of the nanostructures of another composition was written. In order to execute the second exposure, I have used all the three levels of alignment markers, the prealignment markers, the global markers and the local markers marked in Fig. 4.1.

Unfortunately the result of two step e-beam lithography was not at all satisfactory. There were 6 chips on the wafer, shown in Fig. 4.1 written sequentially from Chip 1 to Chip 6. Progressively the chips were getting worst i.e Chip 1 and Chip 2 written initially had good alignment whereas subsequent chips gradually degraded. The reason is that the markers together with the first layer of the nanostructures were written together during the first exposure. The e-beam exposure took very long time (approximately 8 hours) to write the nanostructures since the

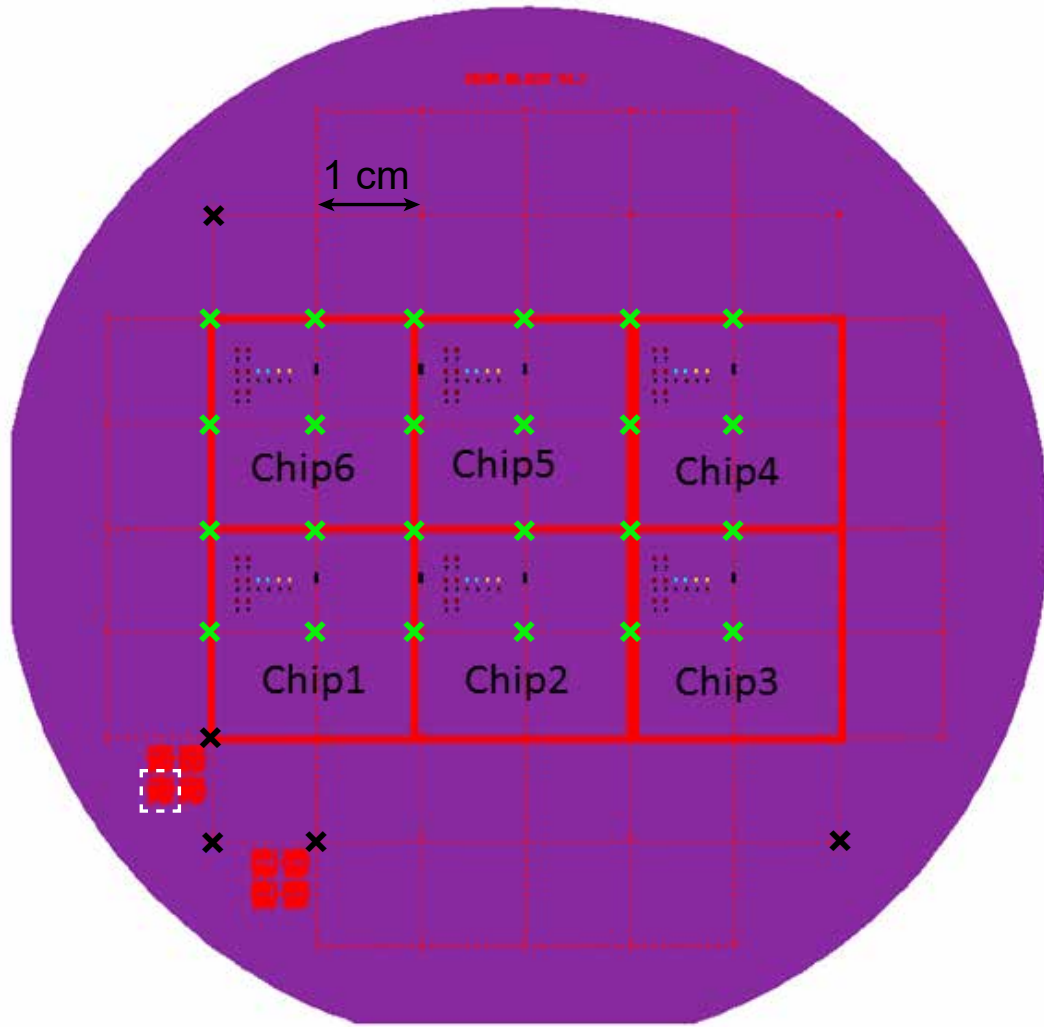


Figure 4.1 – Figure shows a representative wafer map with alignment markers used for fabricating binary metasurfaces. The white dashed square shows the prealignment marker. It consists of an array (29×29) of squares of side $10\mu\text{m}$. There are 8 such arrays. During each exposure one of these arrays are used for alignment. The 5 black cross shows the region of global marker while the green crosses shows the local alignment markers. Both the global markers and local markers consists of an array (3×3) of squares of side $10\mu\text{m}$ each. During each exposure, one of these squares are used as markers. The number of global markers is constant while local markers used are at the edges of each 1 cm chip. This array of 3×3 is present at the edges of each 1 cm square (marked in the figure). However, with each job the position of the chips vary, hence varying the number and the positions of the local markers.

patterns were very dense. The nanostructures were written with a beam current of 200 pA while the markers were written with a larger beam of 200 nA. Since the beam current of the nanostructures is small they are written first. During such long e-beam exposure drift becomes a severe issue. The overlay accuracy decreases since the alignment markers were not written at

the desired position and were "misaligned". Moreover, during writing of the nanostructures, if no additional measure was taken to compensate the beam drift, with time the nanostructures also suffered progressively from decrease of overlay accuracy. This affects the second e-beam exposure even worst, since the alignment marks were not at the desired locations. This lead to a misalignment of around 400-600 nm in the final sample, causing unsuccessful liftoff in Chip 5 and Chip 6 since nanostructures in second layer were written almost on top of the first layer. Figure 4.2 shows an example of lift-off from a badly aligned sample. This shift of the nanostructures can be seen better from the binary nanotriangles and the nanorods who had a large period of 2 μm as shown in Fig. 4.2. Thus these structures did not have a liftoff problem, but the misalignment is clearly visible (marked in Fig. 4.2b)

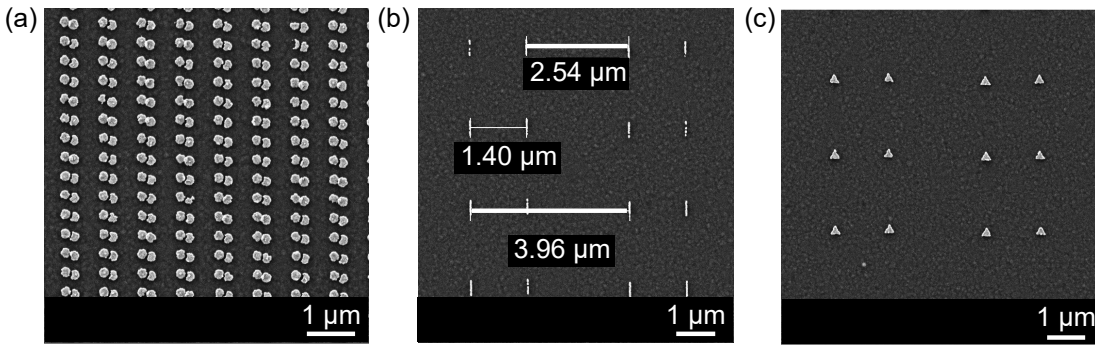


Figure 4.2 – SEM image of array of (a) nanodisks (b) nanorods (c) nanotriangles with bad alignment. The scale bar in (b) shows that the successive layer is misaligned by 500-600 nm.

To solve this problem, I performed three step e-beam exposures as shown in the schematic in Fig. 4.3. In the first exposure only the marker were written (which takes a few min). The 1st layer of the nanostructures was written in the second exposure. During the third and final exposure the 2nd layer of nanostructures was written. The 1st layer of nanostructures was accurately adjusted to the alignment marks in contrast to the previous trial. However, all the markers chosen for the second and the third exposure are different from each other because the markers are overexposed to the e-beam while aligning and thus over developed. This 3-step e-beam lithography decreased the misalignment problem drastically, made the lift-off better and all the chips were developed correctly. However SEM images showed, that for Chip 6 the misalignment was still approximately 60 nm for two successive layers. This misalignment was further decreased in the next trial by adding an additional step of alignment, where the local alignment markers were referenced after every pattern is written. Previously, the local alignment markers were referenced before writing patterns on each chip i.e. once per chip instead of multiple times per chip performed in the latest trial. The writing time for every chip was 1h 30 min to 2 h, allowing the beam to drift during this time, which resulted in a misalignment of around 60 nm for Chip 6. Aligning the beam with respect to the local alignment marks each time after writing the pattern of a single chip decreased the beam drift and the misalignment to 20-35 nm. I used the 3 step alignment technique to write the AuAg alloyed metasurfaces shown in Sec. 4.1.2 (Fig. 4.4c and Fig. 4.4f). The colouring of the

4.1. Applications in optics: Alloyed metasurface with $\text{Au}_{0.2}\text{Ag}_{0.8}$ and $\text{Au}_{0.8}\text{Ag}_{0.2}$ alloys

nanostructures in the inset, corresponding to the different compositions, illustrates the high degree of alignment achieved with the 3 step e-beam lithography.

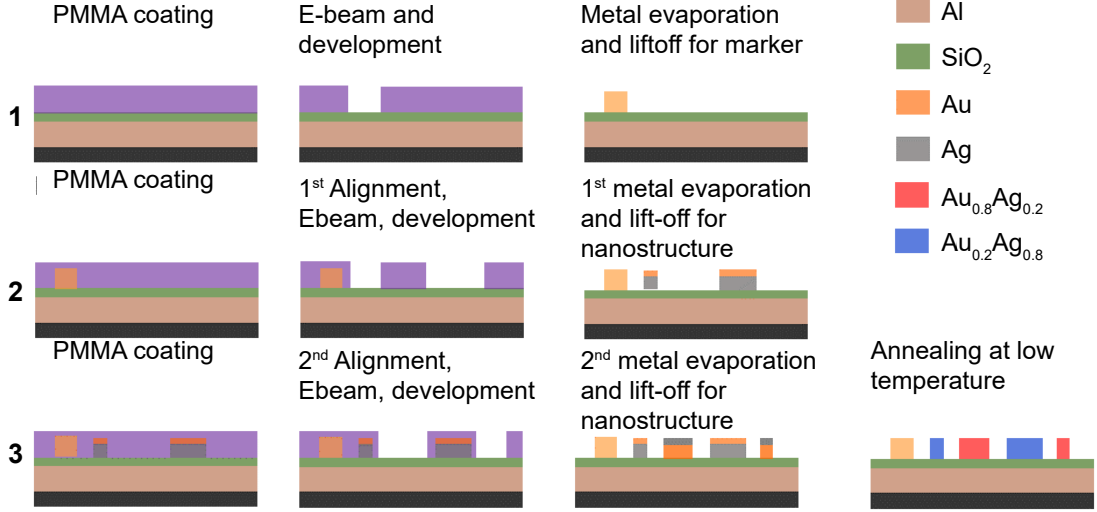


Figure 4.3 – The figure shows the schematic of the 3 step e-beam alignment process used for fabrication of alloyed binary metasurfaces. The numbers in bold in the left denotes the exposure number.

4.1.2 Fabrication of alloyed metasurfaces: Holograms and Fresnel Zone Plate

With AuAg alloys, it is straightforward to develop metasurfaces that operate in the visible; here we chose $\lambda = 532$ nm and fabricate a periodic array of meta-atoms with periodicity $p = 300$ nm to avoid any diffraction order. Alloyed discs $\text{Au}_x\text{Ag}_{1-x}$ with diameter $d = 110$ nm and thickness $h = 50$ nm, atop an Al mirror (thickness 150 nm) with a $t = 100$ nm thick SiO_2 spacer are used as meta-atoms, see the inset in Fig. 4.4a. Such a structure is polarization insensitive and supports a gap plasmon [113, 209], which enables the re-radiation of the incident wave with a phase shift that can be controlled over a 2π -range [66]. The reflectance and phase shift are computed as a function of the wavelength using the periodic surface integral equation method [148, 91], Fig. 4.4a. The permittivity for Al and SiO_2 originate from the literature [94], whereas that for $\text{Au}_x\text{Ag}_{1-x}$ are computed using Rioux's model [288]. Figure 4.4a indicates that at $\lambda = 532$ nm the reflectance is the same for $\text{Au}_{0.2}\text{Ag}_{0.8}$ and $\text{Au}_{0.8}\text{Ag}_{0.2}$ nanostructures, while the phase they produce is shifted by 165° ; this nanostructures pair can therefore serve as meta-atoms for a binary metasurface [127]. This is confirmed in Fig. 4.4b (setup described in Fig. 4.5a) by measurements on alloyed disc arrays with five different stoichiometries. The agreement between these measurements and simulations is good, especially the spectral locations of the reflection dip agree very well.

Having demonstrated the ability to manipulate the reflected light using arrays of alloyed nanostructures, let us now fabricate a meta-hologram and a Fresnel zone plate using the

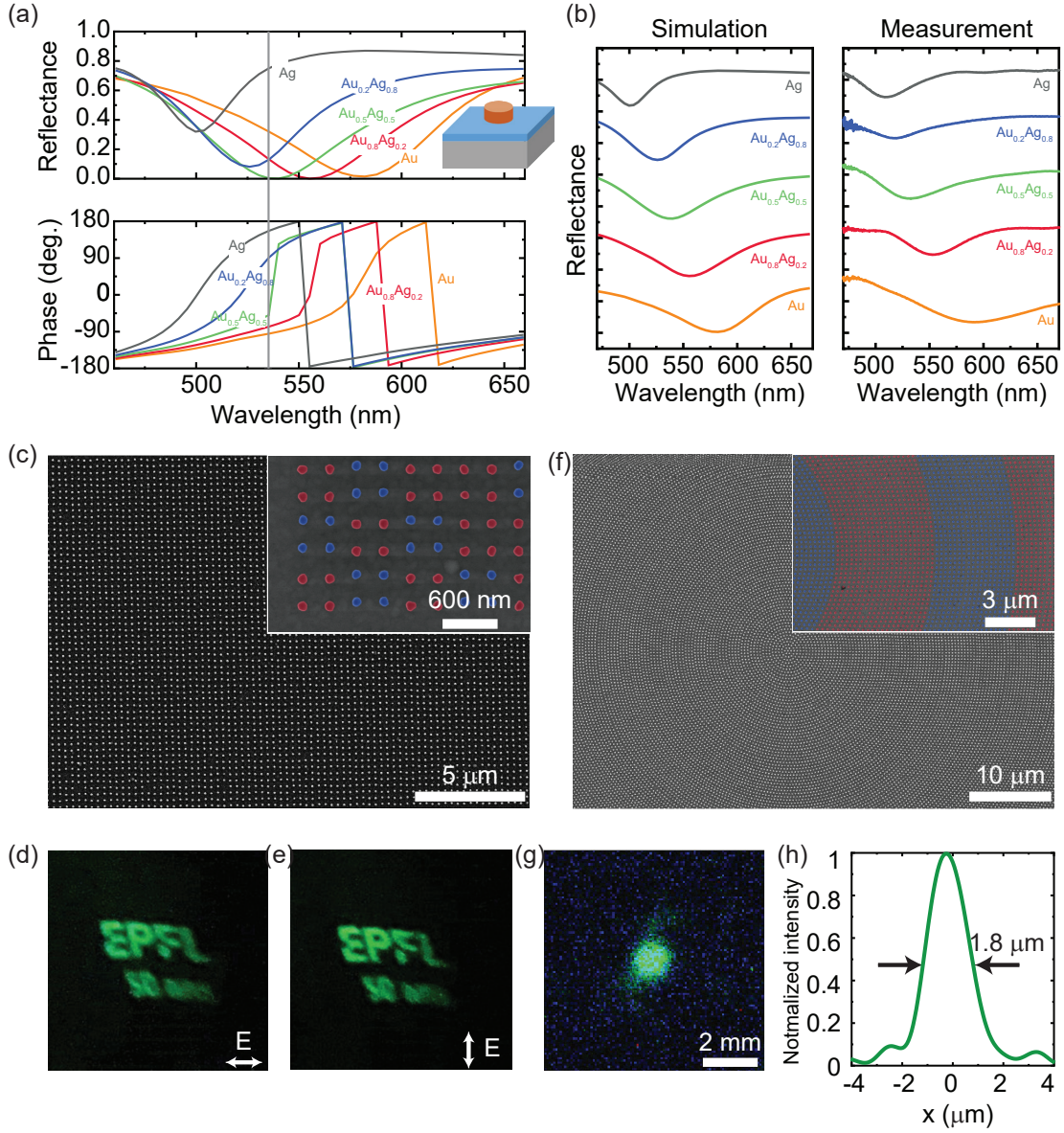


Figure 4.4 – Alloyed metasurfaces. (a) Simulated reflectance and phase for alloyed meta-atoms with different stoichiometries. The inset shows the meta-atom composed of an alloyed disc with diameter $d = 110$ nm, height $h = 50$ nm, positioned atop an Al mirror with a SiO₂ spacer of thickness $t = 100$ nm. The period is $p = 300$ nm. (b) Simulated and measured reflectance spectra for different disc stoichiometries. (a-b) Simulations and measurements done by Hsiang-Chu Wang. (c) SEM image of the hologram device and its optical projection under (d) horizontally and (e) vertically polarized light. (f) SEM image of the FZP with focal length $f = 400$ μ m and NA = 0.35. (g) Intensity distribution at the focal plane and (h) normalized intensity profile at the centre of the focal spot. The insets in panels (c) and (f) emphasize with colours the two different stoichiometries used for the meta-atoms. (d-e,g-h) Measurements done by Hsiang-Chu Wang.

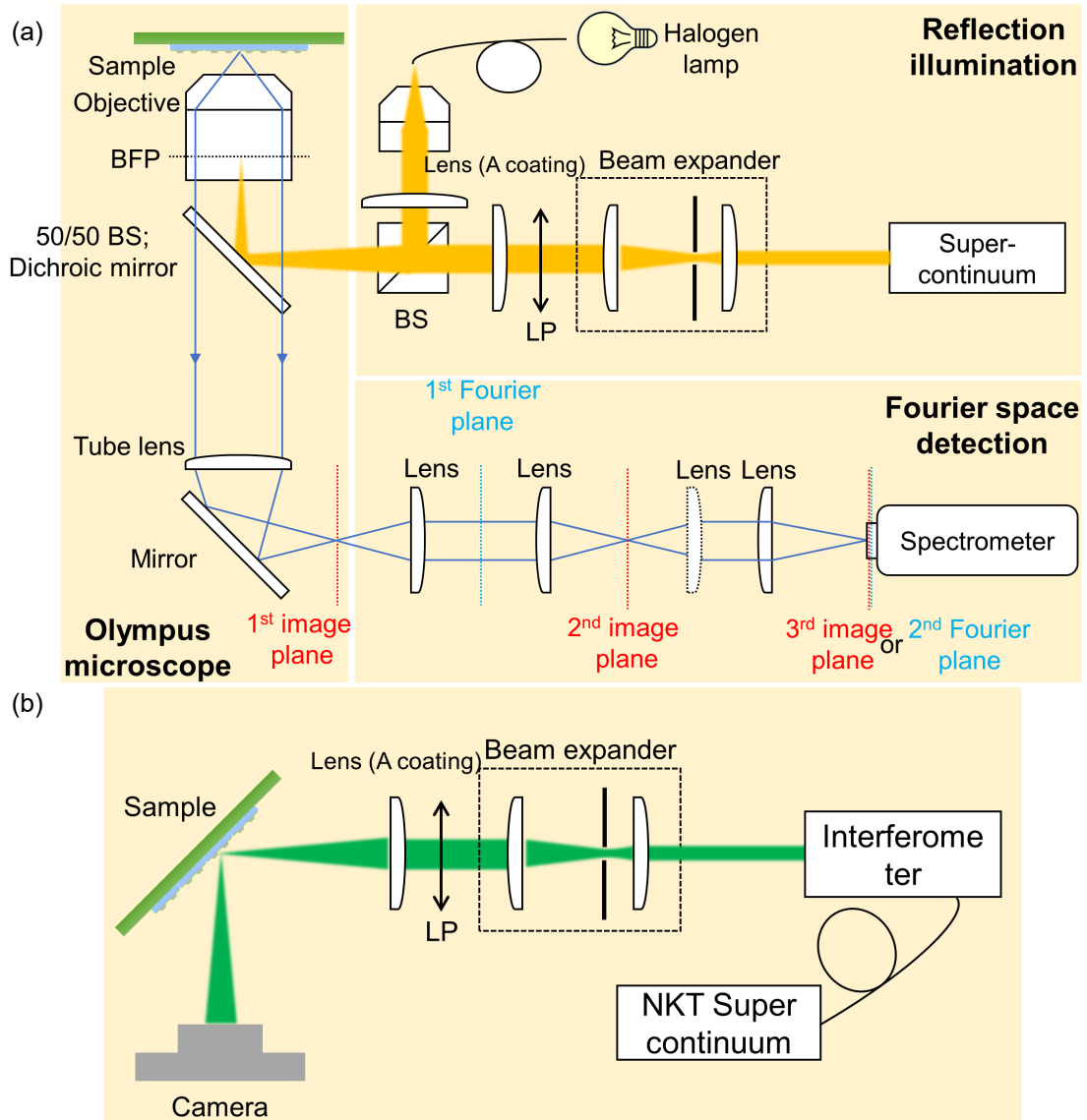


Figure 4.5 – (a)Optical setup for measuring reflectance. A silver (Ag) mirror is utilized as reference. The sample is illuminated with a Fianium supercontinuum white light source. A linear polarizer is also applied. Spectra are measured with the spectrometer at the 3rd image plane. (b)Optical setup for measuring metahologram. The focal spot is captured at the 2nd Fourier plane. The focal spot can be distinguished from the normal reflection with the sample tilt few degrees. The normal reflection is blocked in the 1st Fourier plane. Figures taken from Hsiang-Chu Wang.

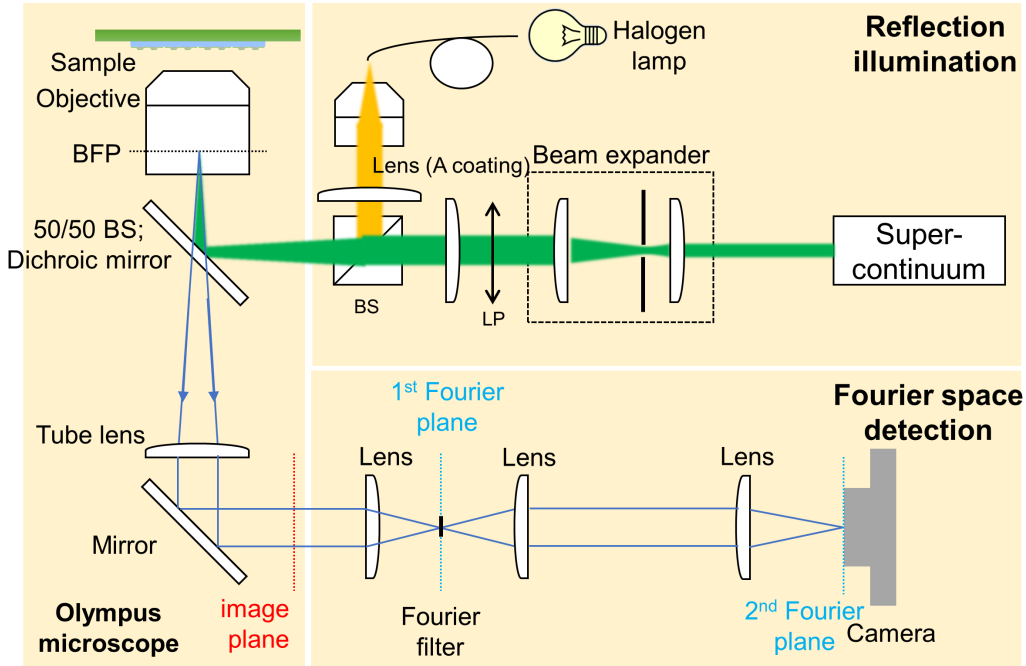


Figure 4.6 – Optical setup for measuring metalens. The focal spot is captured at the 2nd Fourier plane. The focal spot can be distinguished from the normal reflection with the sample tilt few degrees. The normal reflection is blocked in the 1st Fourier plane. Figure taken from Hsiang-Chu Wang.

stoichiometries $\text{Au}_{0.8}\text{Ag}_{0.2}$ and $\text{Au}_{0.2}\text{Ag}_{0.8}$ to realize the two different disc-shaped meta-atoms. For the meta-hologram, my colleague Hsiang-Chu Wang calculated the phase distribution using the computer generated hologram method [132]. Since the meta-hologram is built from two different alloys, the 3-step EBL process described in Sec. 4.1.1 was used for the fabrication. In the first step, alignment marks are written and in the consecutive 2nd, respectively 3rd steps, nanostructures with $\text{Au}_{0.8}\text{Ag}_{0.2}$, respectively $\text{Au}_{0.2}\text{Ag}_{0.8}$, are deposited. The annealing is performed after the final step, once all the meta-atoms with different stoichiometries have been deposited on the surface. The SEM images of the hologram device in Fig. 4.4c indicate that all the unit cells share the same physical dimensions and the different meta-atoms are well aligned over a very large area (the inset highlights with colours the two different stoichiometries used in the metasurface). This is quite remarkable since these nanostructures are written in two successive, independent steps, including photoresist coating, EBL, development, two-layer metal deposition and lift-off. Images of the hologram projection under polarized laser illumination are shown in Figs. 4.4d and 4.4e for two different incident polarizations (setup described in Fig. 4.5b). The holograms are polarization-independent thanks to the symmetrical arrangement of the meta-atoms.

4.2. Applications in Chemistry: Generation of hot electron with Au_{0.5}Ag_{0.5} alloys

For the Fresnel zone plate, the spatial phase profile follows the eqn. 4.1

$$\phi(r) = \frac{2\pi}{\lambda} \sqrt{r^2 + f^2} - f \quad (4.1)$$

where r is the distance from the centre of the lens and f represents the focal length [374]. For demonstration purposes, the lens is designed with a NA = 0.35 in air. The lens diameter is $D = 300 \mu\text{m}$ and the focal length is $f = 400 \mu\text{m}$. Figure 4.4f shows the SEM image of the fabricated lens. The inset in Fig. 4.4f provides a magnified view of the centre part of the lens, which is composed of meta-atoms with the same dimensions but different Au-Ag stoichiometries. The focal spot, displayed in Fig. 4.4g, is measured in the Fourier plane whereas the intensity profile, shown in Fig. 4.4h, is determined in the focal plane using the setup shown in Fig. 4.6. The full width at half maximum (FWHM) is $1.8 \mu\text{m}$, which agrees extremely well with the theoretical diffraction spot size $D_{\text{FWHM}} = 1.22\lambda/\text{NA} = 1.85 \mu\text{m}$.

Conclusion

The demonstration of plasmonic metahologram and metalens by only varying the alloy composition unlocks an additional degree of freedom in the metasurface design where now meta-atoms of varying size and composition can be fabricated to realize metasurfaces with more sophisticated optical applications.

4.2 Applications in Chemistry: Generation of hot electron with Au_{0.5}Ag_{0.5} alloys

This section describes the work done on measuring the photocurrent from an AuAg alloy nanoparticle (AuAgNPs)-TiO₂ interface due to the generation of hot electrons.

4.2.1 Motivation

So far we have been battling against the plasmonic losses of metals and focused our attention to find workarounds to design systems having less losses e.g. by alloying two metals. In this section and in the following one we show how we can use these losses to our advantage. Among several options one of the most recent configurations of using losses is generation and extraction of hot electrons at the metal-semiconductor interface. Au and Ag nanoparticles have excellent light trapping properties due to the excitation of the plasmons, which when decaying non-radiatively produce charge carriers with high energy, so-called hot electrons [112, 203, 33]. These charge carriers can be extracted from the metal to a semiconductor through a Schottky barrier. If the Schottky barrier between the semiconductor and the metal is lower than or equal to this energy, these electrons can move to the conduction band of the semiconductor. The concept of plasmonic hot electrons rose to prominence since photocatalysis and photocurrent generation can be enhanced using a suitable plasmonic configuration.

Hot electron generation and harvesting has been discussed thoroughly in several references [50, 212, 48, 411, 386], and can be detected chemically by two means i) measuring the reduction of adsorbate molecules due to direct/indirect injection of hot electrons [143, 29], or ii) measuring the photocurrent due to the transfer of hot electrons from metal into the conduction band of the adjacent n-type semiconductor [34]. The mechanism for direct hot-electron injection into the adsorbate is still under debate [69, 316], however, extracting them into the semiconductor through a Schottky junction, is a very well accepted approach [160] which can greatly extend the lifetime of hot electrons due to the reduced availability of the holes for recombination [70]. So far this approach has been successfully used for water splitting [380], decomposition of organic pollutants such as carbon dioxide [290, 85], dyes [43] and synthesis of selective chemical compounds [422]. Nevertheless, the external quantum efficiency remains very low and hence innovation to boost hot-electron extraction is essential for developing new commercial sustainable technologies.

Several reports have been shown for improving hot-electron extraction into TiO_2 by tuning the particle dimension based on the fact that smaller plasmonic nanoparticles have a higher absorption cross-section than the larger nanoparticles, leading to increasing hot-electron generation [412, 321, 152]. Govorov *et al.* studied hot-electron extraction using a quantum theory and showed that the hot electrons from smaller nanoparticles are likely to have higher energies above the Fermi level, and thus have higher probability to enter into the semiconductor [112]. Long *et al.* demonstrated the enhanced hot electron extraction using highly dense smaller particles on the semiconductor surface [205]. Beyond that, Negrin-Montecelo *et al.* used the advantage of thermoresponsive polymers to bring AuNPs closer to the TiO_2 nanorods for enhancing hot-electron injection [237]. The hot spot between two nanoparticles has been shown to generate a greater concentration of hot electrons when compared to a single nanoparticle due to the breaking of the linear momentum conservation of electrons in the hot-spot region [23]. In another study, the strong coupling between metal and semiconductor was shown to extract hot electrons efficiently through plasmon-induced interfacial charge-transfer transitions [169, 385].

Knight *et al.* identified that hot-electron extraction through a three-dimensional (3D) Schottky barrier interface is substantial by implanting the nanoparticles into the semiconductor [161]. Consequently, Ratchford *et al.* attained an increased hot-electron extraction by embedding the AuNPs into the semiconductor of dimensions less than the Au electron mean free path [275]. Similarly, Lee *et al.* developed a 3D Schottky barrier in a sandwich configuration by depositing lead sulfide (PbS) quantum dots on top of TiO_2 where hot electrons from AuNPs were first extracted into PbS followed by subsequent transfer to TiO_2 [176]. So far, we see that generation of hot electrons from Au- TiO_2 interfaces has been studied to some extent. Our aim in this project is to expand the scope of the metal nanoparticle- TiO_2 system to include AuAg alloys. Our strategy is based on the fact that in an alloy composition, the lower work function metal Ag can reduce the overall Schottky barrier height [79] at the AuAgNPs- TiO_2 interface compared to the height at the AuNPs- TiO_2 interface. This enables low-energy hot electrons, unlike conventional AuNPs- TiO_2 interface, to transfer into the conduction band of TiO_2 thus

increasing the overall harvest of the hot electrons. Thus tailoring the metal-semiconductor interface by changing the composition of the metal plays a crucial role in controlling the injection efficiency which in turn manipulates the photocurrent generated. Figure 4.7 shows the schematic explaining how the Schottky barrier height of an AuAgNPs-TiO₂ is reduced when compared to AuNPs-TiO₂ interface. Such an initial effort has been made by Valenti *et al.* where they have attempted to harvest hot-electrons from AuAgNPs-TiO₂ interface [356].

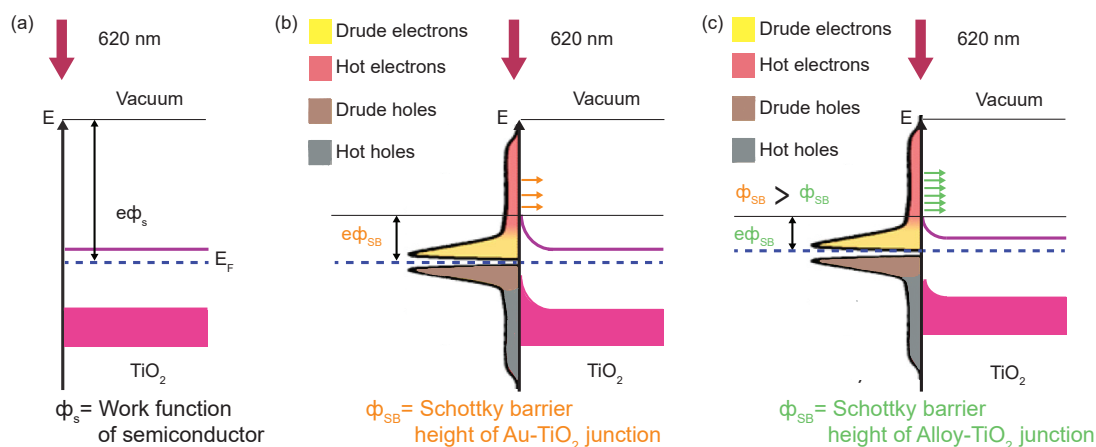


Figure 4.7 – The schematic shows how hot electrons are excited on a metal-TiO₂ interface. (a) shows the band diagram of a bare TiO₂ substrate. The blue line shows the Fermi energy level (b) shows a Au-TiO₂ interface. The distribution of the hot electrons and holes in the non-equilibrium condition is shown. The TiO₂ bends to have a continuous Fermi energy level across the interface. (c) shows the AuAg alloy-TiO₂ interface. (b-c) The x-axis on the right of the metal-TiO₂ indicates the distance x from the interface into TiO₂, while the x-axis on the left of the interface denotes the carrier excitation rate. Schematic adapted from [336] while the carrier excitation rate profile is adapted from [24].

However, additional experiments are needed to distinguish between the hot electrons and the charge carriers generated within TiO₂ through plasmonic near-field coupling. The search for a system with improved quantum efficiency propelled us to perform a thorough analysis of the novel AuAgNPs-TiO₂ geometry. We have further bolstered our arguments with comprehensive experiments. In this work we use alloy of composition Au_{0.5}Ag_{0.5} only.

4.2.2 Fabrication

In order to understand the advantages offered by the alloy we also fabricate AuNPs-TiO₂ and AgNPs-TiO₂ along with AuAgNPs-TiO₂. The nanoparticles were fabricated on fused silica substrates using a thermal dewetting method. Pre-treated fused silica wafers were diced into 2.5 × 2.5 cm² pieces. Pre-treatment of the fused silica wafers were performed with a mixture of 20 mL NH₄OH (25%):10 mL H₂O: 5 mL H₂O₂ (30%) at 75° C for 30 min. This process improved the adhesion of metal and indium tin oxide (ITO) thin films on the substrate. The ITO deposited substrates were used for the photoelectrochemical experiments explained later. To

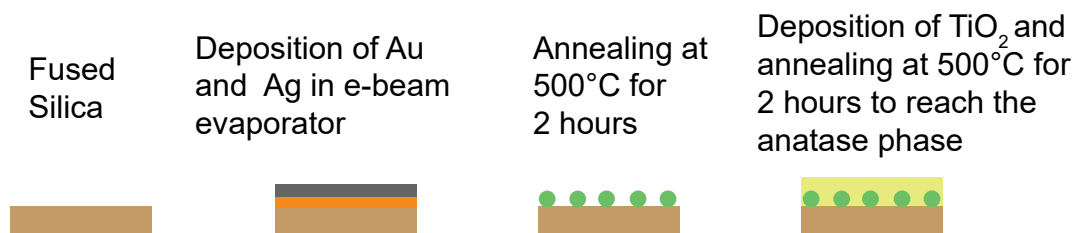


Figure 4.8 – Schematic of the steps of fabrication for AuAgNPs-TiO₂

obtain AuNPs or AgNPs decorated electrodes, first a 4 nm of Au or Ag thin films were deposited onto the respective substrates with a rate of 4 Å/s using long-distance electron beam (e-beam) evaporation with Leybold Optics LAB600H at a base pressure 1.5×10^{-6} mbar. Then, the films were dewetted at 500° C for 2 h under nitrogen atmosphere using a Neytech oven (Centurion QEX vacuum porcelain furnace). Gold-silver alloy nanoparticles (AuAgNPs) were obtained by depositing a 2 nm of each Ag and Au and annealing it at the same condition as mentioned above. Subsequently 100 nm TiO₂ was deposited onto the nanoparticles and then annealed in the same way to obtain the anatase phase [343]. Figure 4.8 shows the schematic drawing of the fabrication for the AuAgNPs-TiO₂ system. For the photoelectrochemical measurements explained later 170-200 nm ITO was deposited on fused silica substrates before NPs were fabricated. The ITO layer was deposited on fused silica substrates using Pfeiffer Spider 600, radio frequency magnetron sputtering (RF-MS) system with RF power of 500 W and an argon flow of 15 sccm at a pressure of around 5×10^{-3} mbar. Figure 4.9d shows the elemental mapping EDX images of the AuAgNPs. It can be clearly seen that Au (green) and Ag (red) are mixed very well in the AuAgNPs composition suggesting that the prepared AuAgNPs are homogeneously alloyed. Figure 4.9a-c show the SEM images of the AuNPs, AgNPs and AuAgNPs respectively. The homogeneous distribution of nanoparticles over the whole substrate is observed. The average sizes of the AuNPs and AgNPs is estimated to be 27 nm and 50 nm with area coverage of 31% and 22% respectively. For AuAgNPs, the average size is estimated to be 59 nm with 22% area coverage. Figure 4.10 shows the particle distribution analysis of the nanoparticles. The difference in the distribution of the particles can be attributed to the difference in the metal and their relative interaction with the surface. This effect can be seen more prominently on ITO substrates shown an the end of Sec. 4.2.4 in Fig. 4.15. The particle analysis was performed with ImageJ software.

4.2.3 Characterization

The optical properties of the samples are characterized with UV-Vis-NIR spectrometer (Schimadzu, UV-2600) with the integrating sphere accessory. The optical absorption spectra of the three different nanoparticle systems on fused silica substrates are shown in Fig. 4.11a. The plasmonic resonance bandwidths for AgNPs, AuNPs and AuAgNPs were broader and cover the region of 400-500 nm, 500-600 nm, and 450-550 nm, respectively. The spectral peak

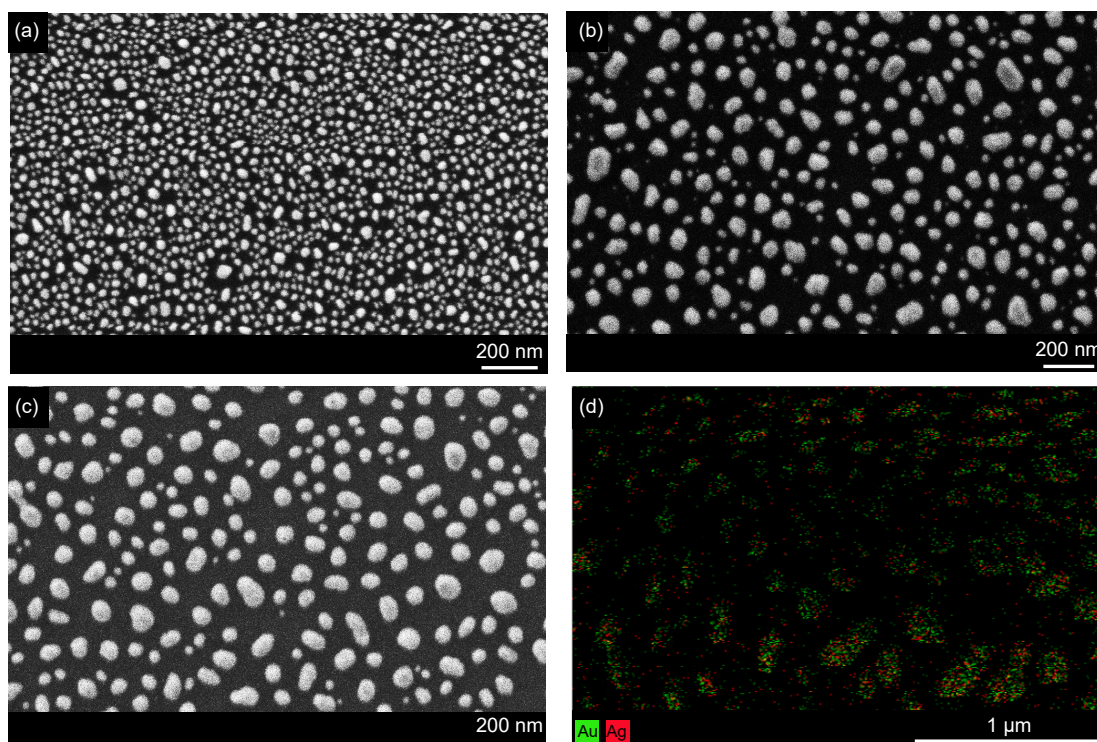


Figure 4.9 – SEM images on nanoparticles on fused silica substrates (a) AuNPs (b) AgNPs (c) AuAgNPs (d) EDX images showing presence of both Au and Ag homogeneously in the nanoparticle

position of the AuAgNPs situated in between those of AuNPs and AgNPs demonstrates the prepared alloy comprising equal distribution of Au and Ag. The wider spectral feature suggests that the NPs are distributed on the substrate with different sizes, which is beneficial as it can absorb in the visible-light solar spectrum. In the presence of TiO_2 , as shown in Fig. 4.11b, the resonance peak positions of the nanoparticles are red shifted as compared to Fig. 4.11a due to the high refractive index of TiO_2 . In addition, plasmonic resonance bandwidths become broader compared to the bare NPs and cover most of the visible region. It is also evident from Fig. 4.11 that the AuAgNPs-decorated electrode shows higher absorption in both cases (with or without TiO_2).

4.2.4 Detection of Hot electrons

Hot electron generation from plasmonic nanoparticles was estimated using electrochemical photocurrent measurements. For photocurrent measurements, 170 to 200 nm of ITO was deposited on the fused silica before the nanoparticles were fabricated. The photocurrent measurements were carried out using a 3 electrode system, shown in Fig. 4.12a. A 3 electrode system consists of a working electrode which is the sample whose response is to be measured, a reference electrode (Ag/AgCl) and a Pt counter electrode. A 3 electrode system was used

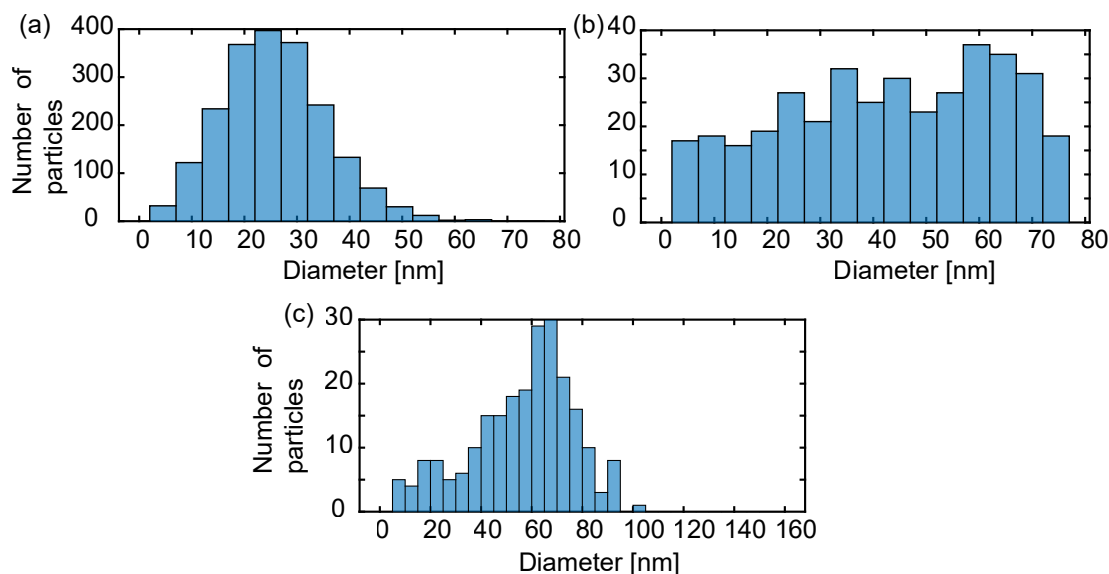


Figure 4.10 – Particle size distributions for (a) AuNPs, (b) AgNPs, and (c) AuAgNPs on fused silica substrates corresponding to Fig. 4.9

for accurate measurements of current. The voltage drop is measured across the working and the reference electrode whereas the photocurrent through the working and the counter electrode is measured. The electrolyte used was 0.1 M KNO_3 (pH 6) solution containing 10% ethanol acting as the electron donor. The incident light was provided by a white light tunable supercontinuum laser (Fianium, $\lambda=450\text{-}800$ nm) with a beam spot diameter of 1.5 mm enlarged to 1.5 cm with a power density of $1 \text{ mW}/\text{cm}^2$. The optical setup used for expanding the beam and measuring the photocurrent is shown in Fig. 4.12b.

Figures 4.13a and Fig. 4.13b show the photocurrent responses of the AuNPs, AgNPs, and AuAgNPs integrated photoelectrodes recorded under narrowband irradiation $\lambda=620\pm40$ nm during on and off conditions every 30 s. The observed photocurrents were stable and reproducible. In the absence of TiO_2 , no photocurrent changes were observed suggesting that the photogenerated hot electrons were recombined into holes through electron-electron and electron-phonon scattering within fs-ps time scale. However, in the presence of a 100 nm TiO_2 layer on top of the NPs, significant photocurrent changes were observed as shown in Fig. 4.13b. It clearly reveals that a Schottky junction at the metal- TiO_2 interface enabled the successful hot-electron transfer into the conduction band of TiO_2 . Figure 4.13c shows the photocurrent changes (ΔI) estimated for the three NP-coated electrodes including bare TiO_2 . ΔI is the difference of the photocurrent measured in the on (when the incident laser light is on) and off (when the incident laser light is off) state. It should also be mentioned here that the difference in photocurrent is not measured at the beginning of each interval where there are transient spikes, rather they are measured when the current stabilizes i.e. in the middle of each interval. The negligible ΔI observed for TiO_2 is from the defect states that are poorly excited under $\lambda=620$ nm irradiation. To verify whether the photocurrents observed for

4.2. Applications in Chemistry: Generation of hot electron with $\text{Au}_{0.5}\text{Ag}_{0.5}$ alloys

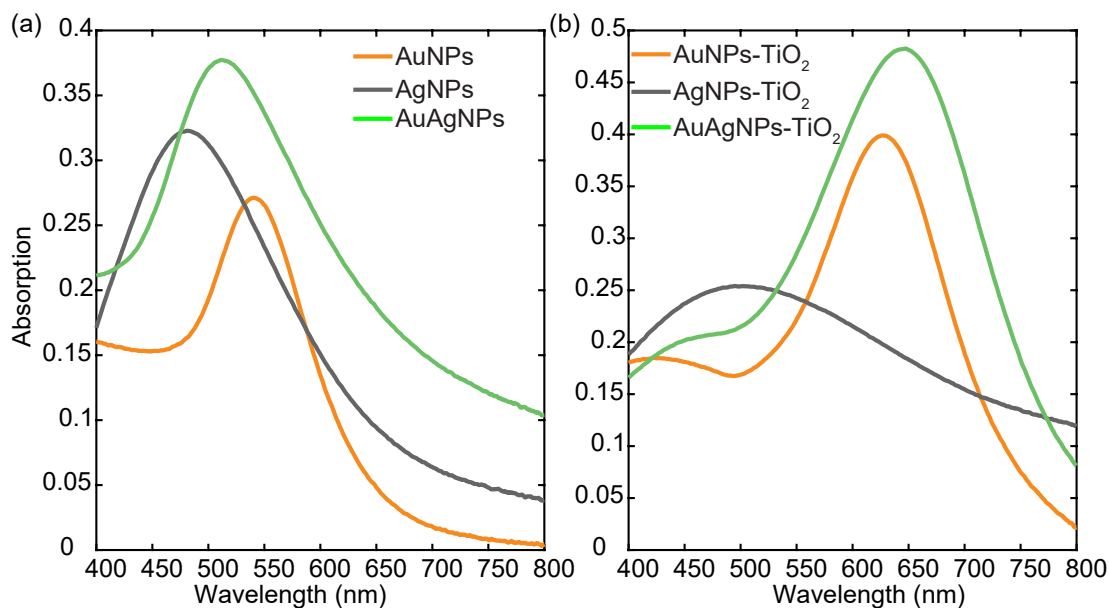


Figure 4.11 – Optical characterization. (a) Absorption spectra of the bare AuNPs, AgNPs, and AuAgNPs. (b) Absorption spectra of the AuNPs- TiO_2 , AgNPs- TiO_2 , and AuAgNPs- TiO_2 . Absorption spectra were plotted by 1-Reflection-Transmission. Measurements performed by Dr. Madasamy Thangamuthu.

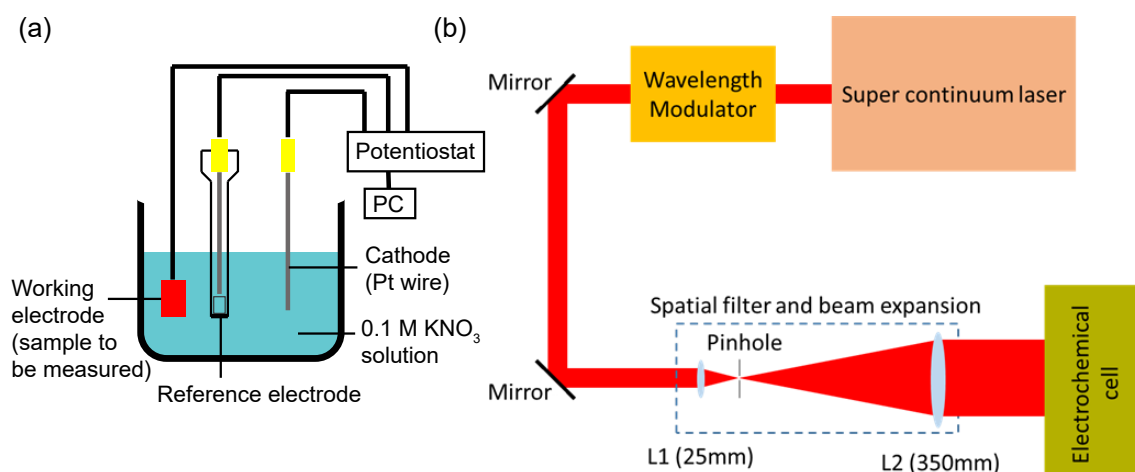


Figure 4.12 – Schematic drawing of the (a) 3 electrode system. Adapted from [390] (b) electrochemical photocurrent measurement setup. Figure from Dr. Madasamy Thangamuthu.

NP-integrated TiO₂ electrodes are solely due to hot-electron extraction, and are not due to the charge carriers generated within TiO₂ by plasmonic near-field coupling, we performed a comprehensive experiment with AuNPs-TiO₂ by irradiating it separately above the semiconductor bandgap (bandgap of TiO₂ is approximately around 3.2 eV, $\lambda=387.45$ nm) and below the plasmonic resonance energies. While irradiating at $\lambda=385$ nm, anodic photocurrent response was observed as shown in Fig. 4.13d suggesting that the generated charge carriers were solely within TiO₂. Irradiating the AuNPs-TiO₂ at $\lambda=620$ nm generates the cathodic photocurrent (Fig. 4.13e), strongly revealing the successful extraction of hot electrons from AuNPs into TiO₂. Hence the ΔI s shown in Fig. 4.13c for AgNPs-TiO₂, AuNPs-TiO₂, and AuAgNPs-TiO₂ are just the hot electrons extracted from the respective metals into the semiconductor. The ΔI for AgNPs-TiO₂ was estimated to be 6.5 nA corresponding to a hot-electron extraction rate of 0.04×10^{12} electrons/s with incident photon to photocurrent conversion efficiency (IPCE) of $8.6 \times 10^{-4}\%$ (Fig. 4.13f) whereas AuNPs-TiO₂ shows an enhanced $\Delta I = 12$ nA corresponding to the hot-electron extraction rate of 0.075×10^{12} electrons/s with an IPCE, of $16 \times 10^{-4}\%$. Fascinatingly, AuAgNPs-TiO₂ shows a $\Delta I = 50$ nA corresponding to the extraction rate of 0.31×10^{12} electrons/s with an IPCE of $66 \times 10^{-4}\%$ which is 4.2 and 8 times higher than AuNPs-TiO₂ and AgNPs-TiO₂ respectively. The number of hot electrons extracted from the AuNPs-TiO₂, AgNPs-TiO₂, and AuAgNPs-TiO₂ was calculated from the photocurrent changes (ΔI) value. Further, incident photon to photocurrent conversion efficiencies of these electrodes were estimated using the Eqn. 4.2 at a given irradiation wavelength:

$$\text{IPCE} = \frac{\text{No. of generated electrons}}{\text{No. of irradiating photons}} \quad (4.2)$$

In addition, we also shed light on the defect states of TiO₂ by irradiating bare TiO₂ under different wavelengths from 500 nm to 700 nm. Significant anodic photocurrent response was observed at 500 nm although it is far below the bandgap energy. This current can be attributed to the defect states. This indicates that hot electron extraction reported so far in the literature under similar conditions could include the response of plasmonic near-field coupling. Increasing the wavelengths to 700 nm drastically diminished the photocurrent response, suggesting that the TiO₂ defect states are not linear as shown in Fig. 4.14(a). Based on these results, we propose that the irradiation conditions observed here for extraction of hot electrons into the semiconductor should not excite the semiconductor or its defect states notably. Thus, the photocurrents generated in these cases are solely due to hot electrons. If the photocurrent from bare TiO₂ would not have decreased around $\lambda=650$ nm, then the resultant photocurrent from the metal-TiO₂ geometry obtained here would be a cumulative effect of hot-electron generation and near-field coupling.

We studied the influence of NPs stability for hot-electron extraction by measuring the photocurrent responses of the AgNPs-TiO₂, AuNPs-TiO₂, and AuAgNPs-TiO₂ from day1, twice a day, until day 30. Figure 4.14b shows the comparison of the ΔI observed at days 1 and 30. The ΔI for AgNPs-TiO₂ was significantly reduced, from 6.5 nA to 3 nA (retaining 46%) due to the

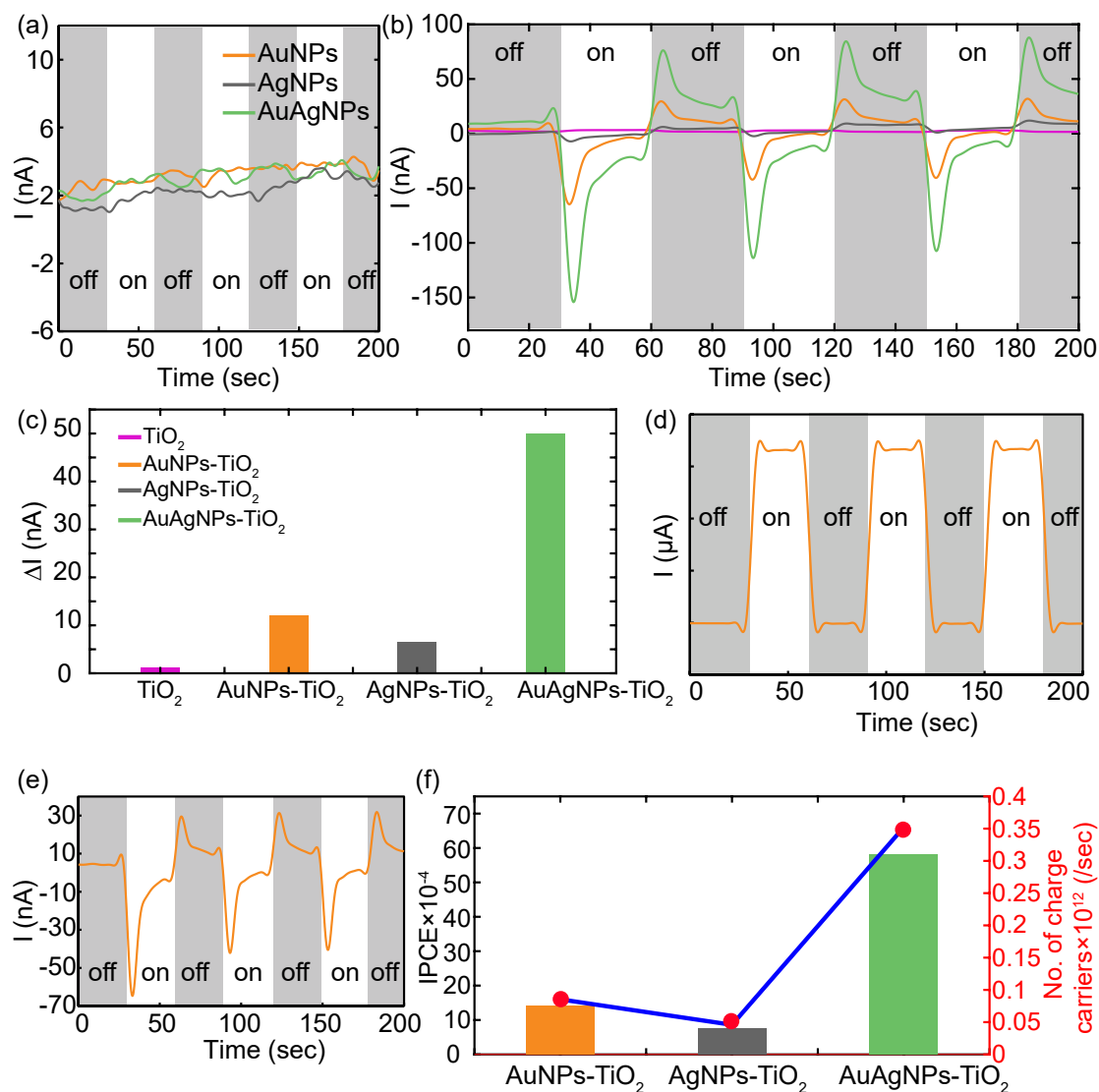


Figure 4.13 – Electrochemical photocurrent responses of the electrodes measured in the 0.1 M KNO_3 solution containing 10% ethanol under $\lambda=620\pm40$ nm (a, b and e) narrowband irradiation with a 1mW cm^{-2} power. (a) Photocurrent responses of the bare AuNPs, AgNPs, and AuAgNPs. (b) Photocurrent responses of the TiO_2 , AuNPs- TiO_2 , AgNPs- TiO_2 , and AuAgNPs- TiO_2 . (c) Photocurrent changes (ΔI) of the TiO_2 , AuNPs- TiO_2 , AgNPs- TiO_2 , and AuAgNPs- TiO_2 . (d) Photocurrent response of the AuNPs- TiO_2 measured under $\lambda=385\pm20$ nm irradiation. (e) Photocurrent response of the AuNPs- TiO_2 measured under $\lambda=620\pm40$ nm irradiation. (f) The hot electron extraction rate (right side) and the IPCE of the AuNPs- TiO_2 , AgNPs- TiO_2 , and AuAgNPs- TiO_2 (left side). Measurements performed by Dr. Madasamy Thangamuthu.

poor stability of the AgNPs as it can easily form an oxide coating. The AuNPs-TiO₂ shows 83% of its original response (from 12 nA to 10 nA) suggesting that the AuNPs are reasonably more stable. Interestingly, AuAgNPs-TiO₂ retains 84% of its original photocurrent (from 50 nA to 42 nA) suggesting that AuAgNPs are as stable as the AuNPs. Furthermore, the morphological changes of the NPs after a month of experiments were also obtained using SEM revealing the worsening of AgNPs compared to AuNPs and AuAgNPs that had not changed their dimensions significantly (data not shown). This morphological degradation is an important factor for the reduction of photocurrent from AgNPs-TiO₂ over time as compared to that of AuNPs-TiO₂ and AuAgNPs-TiO₂.

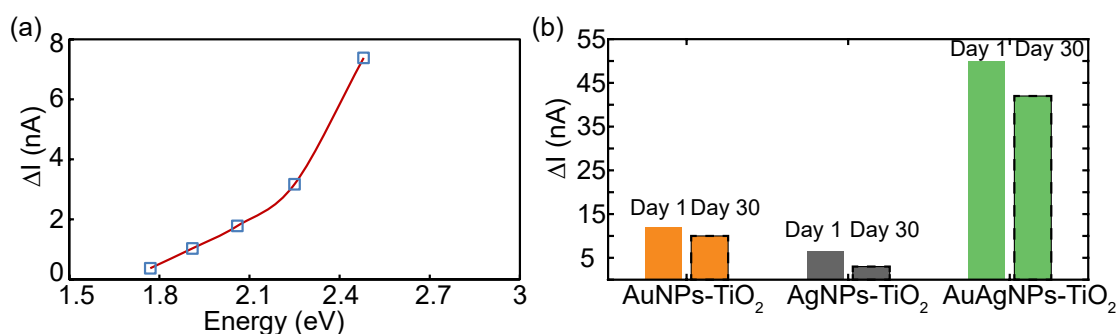


Figure 4.14 – (a) The photocurrent responses (ΔI) observed for TiO₂ under various excitation energies showing that the defect sites were not linear (b) The stability of nanoparticles integrated TiO₂ electrodes observed in terms of the photocurrent responses (ΔI) observed for Day 1 and Day 30. Measurements performed by Dr. Madasamy Thangamuthu.

DFT calculations carried out on these systems show that the Schottky barrier for the AuAgNPs-TiO₂ is 0.45 eV, which is lesser than 0.95 eV for the AuNPs-TiO₂ interface. Due to the lowering of this Schottky barrier the probability of transition of the hot electrons to the TiO₂ conduction band increases thus causing 4.2 times more photocurrent than the AuNPs-TiO₂ system. As for the AgNPs-TiO₂ system the Schottky barrier was calculated to be only 0.2 eV which we believe is small to limit the back transfer of hot electrons and their recombination with the holes in the metal. So this lowered the hot electron extraction efficiency across TiO₂.

Before we conclude this section I would like to mention some challenges that I had faced with fabrication of Ag nanoparticles on ITO substrates. The particle density of Ag nanoparticles on ITO substrates fabricated for photochemical measurements are much less than that of Ag nanoparticles on fused silica substrates as shown in Fig. 4.15b and Fig. 4.9b respectively. Moreover the particle sizes are also much larger than that on fused silica only. This effect is only more pronounced in case of Ag as can be seen by comparing AuNPs, AgNPs and AuAgNPs in Fig. 4.15 and Fig. 4.9 respectively. We believe this discrepancy arises due to increased hydrophobicity of Ag on ITO substrate [166] leading to larger sized nanoparticles with sparse distribution.

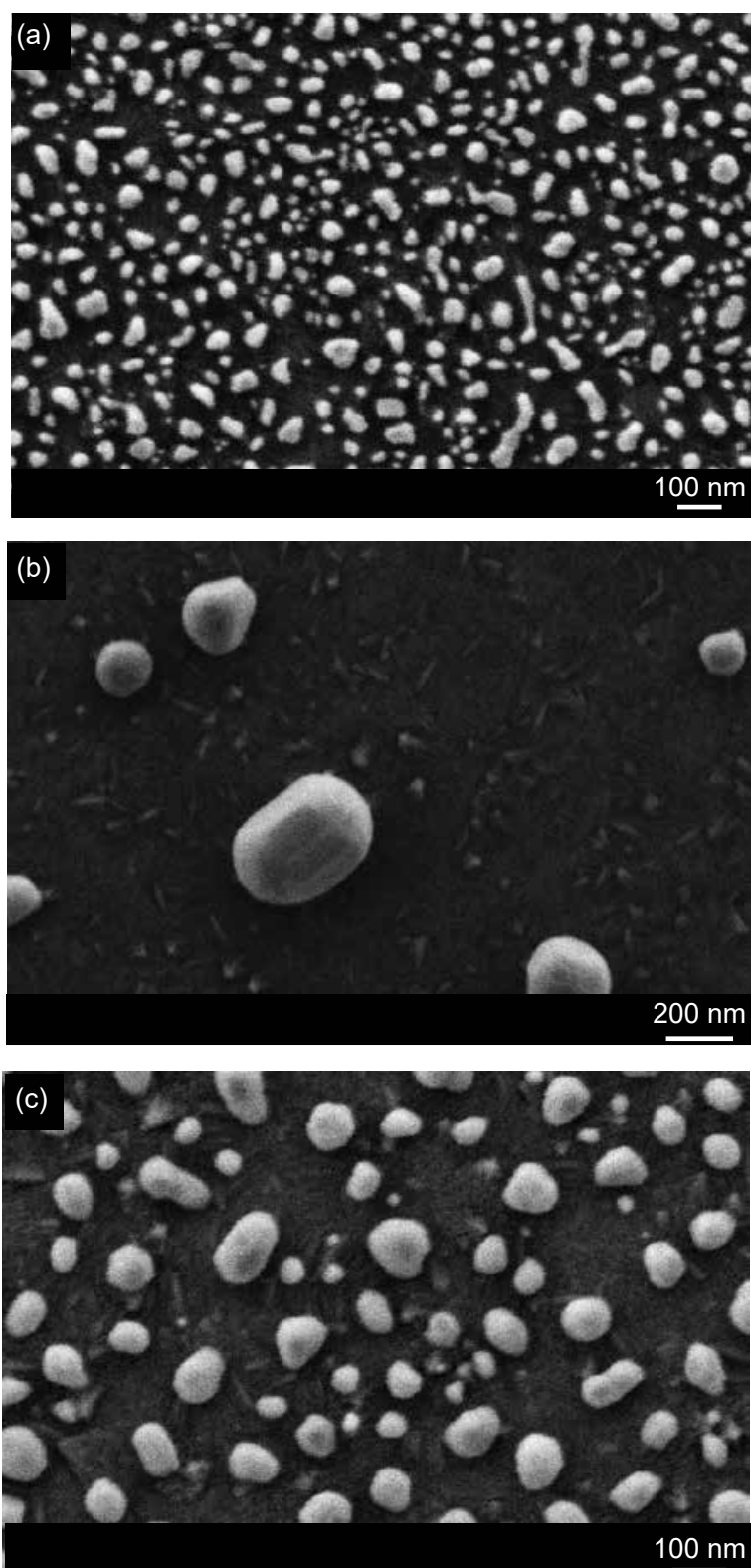


Figure 4.15 – SEM images of nanoparticles fabricated on ITO substrates for photochemical measurements (a) Au (b) Ag (c) AuAgNPs.

Conclusion

We have demonstrated a novel strategy for boosting hot-electron extraction from AuNPs by reducing the Schottky barrier height at the AuNPs-TiO₂ interface. The engineering of Schottky barrier height was achieved by mixing the Ag with Au at 50:50 ratio, forming an alloy with a reduced barrier height of 0.45 eV that increases the transfer of hot electrons into the conduction band of the TiO₂ by enabling additional low energy hot electrons to take part. We proved that the observed photocurrent response is solely due to successful hot-electron extraction and recommend a comprehensive experiment for distinguishing plasmonic hot-electron and near-field coupling if the metal and the semiconductor are in direct contact under high energy irradiation conditions.

4.3 Outlook

4.3.1 Broadband absorption

One of the major drawbacks of hot electron generation from metal nanoparticles demonstrated in the previous section is that it is very small in number and thus the generated photocurrent is very low. One of the way suggested in literature for increasing the generation of hot electrons is to increase the absorption in the system [238, 82, 289], which in turn increases the amount of light absorbed by the metal nanoparticles. One way to increase the absorption is to introduce a mirror at the bottom of that sample, resulting in a Fabry-Perot cavity [238, 82, 289]. However very few literature exists where they have experimentally demonstrated hot electron generation using such configurations. So we intended on fabricating such a broadband absorber that can be implemented for studying hot electron.

We decided to use Aluminium and Tungsten as the metal for mirrors instead of Au which is commonly reported in the literature [238, 82]. This study is an extension of the work on hot electrons reported in the previous section, where measuring hot electrons from alloy nanoparticles is what made the project unique. Here instead of using alloys we use Au nanoparticles. The use of broadband absorption system for generation of hot electrons was inspired by the work on perfect absorber system carried out by my colleague Sebastien Mader. Along with him I have also received valuable comments and feedback from my colleague Dr. Madasamy Thangamuthu throughout the duration of this work. Before we go into further details it should also be noted at this point that this work is a preliminary investigation of using perfect absorption systems with Al or W as back mirror for generation of hot electrons. Here I only describe the samples fabricated using the broadband absorber configuration. We believe that this system can be used for generation of hot electrons albeit with further optimizations and thorough investigations.

The samples are also prepared on fused silica substrates by dewetting of 4 nm Au thin films as explained previously in Sec. 4.2.2. The machines used for fabrication of samples are same as those used in the previous Sec. 4.2. A general schematic of the steps of sample preparation is

shown in Fig. 4.16a. The mirror forms the bottom-most layer, with 50 nm of TiO_2 deposited on top. Subsequently 4 nm of Au is deposited by sputtering and then annealed with the Neytech-Qex oven. As has been mentioned in the previous Sec. 4.2, that we need to anneal the TiO_2 at 500°C in order to convert it from amorphous to anatase phase. Annealing the samples at this high temperature with a Au mirror might diffuse Au in the TiO_2 creating undesired effects [286]. Due to this, we decided to use Al as the mirror since Al is cheap and is known not to diffuse easily thanks to the 2-3 nm of Al_2O_3 on the Al which is very difficult to dissociate.

Figure 4.16b shows the sample fabricated with 200 nm Al as mirror ($\text{Al}_{200}\text{-TiO}_2\text{-AuNPs}$). To fabricate this sample after deposition of TiO_2 , I annealed the sample at 500°C whereupon the temperature has been risen very slowly by $0.5^\circ\text{C}/\text{min}$. After desired temperature was reached the sample was annealed for 2 hours. Upon completion of annealing the N_2 gas was switched off and the vacuum pump was turned on. Due to this, the temperature decreased slowly which helped to retain the mirror reflectivity. The quality of the Al film with these annealing conditions is much better as it oxidises less, resulting in less porous film. 4 nm of Au was deposited on them and then annealed applying similar conditions. Unfortunately, the photocurrent measurements obtained with this sample was almost negligible. In addition to that the absorption from the sample had a moderate value of around 60%.

In order to circumvent the problem with the Al mirror, I decided to use a Tungsten mirror. Tungsten is a metal and has the highest melting temperature of 3422°C as compared to 660.3°C for Aluminium. I decided to use tungsten because of three reasons. The first one being that since Tungsten has very high melting point, the annealing of TiO_2 deposited on W at 500°C will have little effect on it. Second, we expected the reflectivity of tungsten to remain unaltered after annealing, an effect we did not see with Aluminium. Finally, the work function of Tungsten is in the range of 4.32-5.22 eV and can thus form a Schottky barrier with the TiO_2 junction. To start with we deposited 50 nm W as the backplane. W was deposited by sputtering in Alliance DP 650. However, much to our dismay, when 50 nm of tungsten was annealed with 50 nm of TiO_2 on top the former turned transparent. The annealing conditions were 500°C @ $10^\circ\text{C}/\text{min}$ in N_2 atmosphere. The rate of rise of temperature is faster than the condition used for $\text{Al}_{200}\text{-TiO}_2\text{-AuNPs}$. 4 nm Au deposited after TiO_2 was also annealed similarly. The SEM image of the sample ($\text{W}_{50}\text{-TiO}_2\text{-AuNPs}$) is shown in Fig. 4.16c.

Finally, to obtain more reflective samples than $\text{W}_{50}\text{-TiO}_2\text{-AuNPs}$, I proceeded to increase the thickness of the Tungsten mirror to 200 nm. Unlike for $\text{W}_{50}\text{-TiO}_2\text{-AuNPs}$, this time we tried to anneal it slowly, similar to the $\text{Al}_{200}\text{-TiO}_2\text{-AuNPs}$. The SEM image of the final sample ($\text{W}_{200}\text{-TiO}_2\text{-AuNPs}$) is shown in Fig. 4.16d. Much to our relief this time tungsten had retained its opacity better than than $\text{W}_{50}\text{-TiO}_2\text{-AuNPs}$.

Unfortunately, preliminary photocurrent measurements with both $\text{W}_{50}\text{-TiO}_2\text{-AuNPs}$ and $\text{W}_{200}\text{-TiO}_2\text{-AuNPs}$ were not encouraging. We believe that in order to have successful investigations in future it would be better to thoroughly understand the Au- TiO_2 and the $\text{TiO}_2\text{-W}$ interface. One possible solution might be to use TiO_2 anatase powder directly, thus precluding the step of

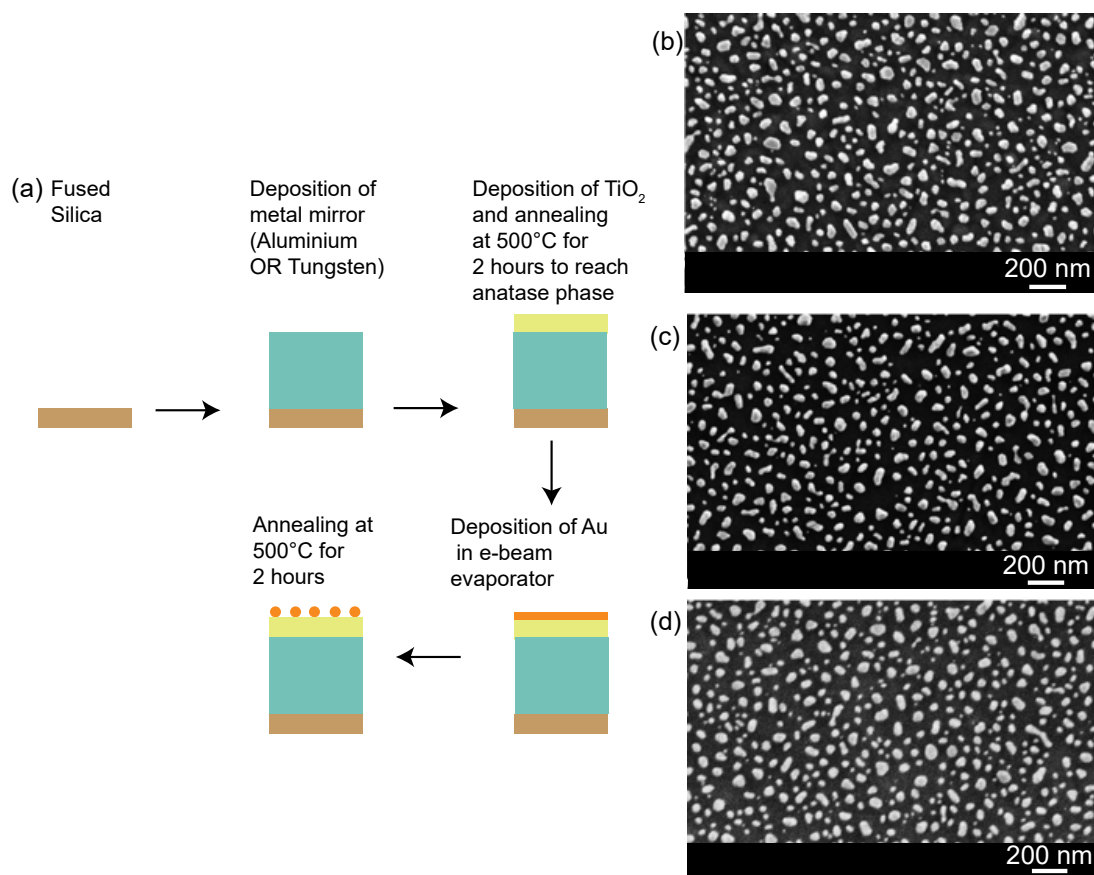


Figure 4.16 – (a) General schematic of the process for fabrication of broadband absorber system with metal mirror. SEM image of the (b) Al₂₀₀-TiO₂-AuNPs (c) W₅₀-TiO₂-AuNPs (d) W₂₀₀-TiO₂-AuNPs on fused silica substrates.

annealing at 500°, which can better retain the TiO₂-W interface. We can also use commercially available AuNPs to avoid the final annealing step as well. However, even though this work did not give us successful results and leaves many scopes for further investigation, we believe that it was worth mentioning due to its use of unconventional metals like Al and W. We believe that this work laid the foundation for use of Al and W in many more plasmonic systems to come in future.

Hybrid nanoantenna : Theory, Part II

Fabrication and application

5 Hybrid Nanoantenna

In the previous part I have shown, the use of AuAg alloys in plasmonic metasurfaces. In this part I will talk about another type of meta-atom, hybrid-metal dielectric nanoantenna, used in metasurfaces and investigate the effect of various geometrical parameters of this hybrid geometry that contribute to the spectra. These hybrid nanostructures rose to prominence since they combine best of both worlds: low loss from dielectric and high enhancement from metal. In this chapter, we describe bulk refractive index sensing with hybrid metal-dielectric nanoantenna made of Si-cylinder and Al disk. My contributions were performing all the numerical simulations and multipolar analysis shown in this chapter. I also fabricated, imaged and measured all the samples presented in this chapter. Parts of this chapter has been published in scientific literature [279].

5.1 Introduction

Plasmonic nanostructures exhibit strong electric field enhancement caused by the resonant oscillation of free electrons [369, 229]. Unfortunately, the intrinsic absorption associated with plasmonic metals results in high losses, which represent a serious drawback for practical applications[164]. To overcome this problem, dielectric nanostructures, which exhibit modest losses but also lower field enhancement have been recently proposed [401, 188, 369, 284, 30, 347]. Furthermore, to take advantage of both low losses and high field enhancement, hybrid metal-dielectric nanostructures, which combine the advantages of both the plasmonic and dielectric properties, are emerging as promising approach. It has been theoretically predicted that hybrid nanostructures acting as nanoantennas provide high directivity and radiation enhancement [64, 409, 330], and are potential candidates for fluorescence enhancement [64, 327, 328, 330].

However, there is a dearth of experimental demonstrations with these hybrid nanoantennas, probably because their fabrication is extremely difficult. The unidirectional radiation of light from hybrid metasurfaces [293, 116] and hybrid Yagi-Uda nanoantennas [126] has been experimentally demonstrated. Experiments have been conducted with quantum dots (QDs) to

show the directionality of the hybrid nanoantennas [348] and the increment of the decay rate of the QDs [397]. Hybrid metal-dielectric nanoantennas have also been used for subtractive colour filtering [408] and efficient generation of second [100], and third harmonics [309]. Hentschel *et al.* have studied the linear and nonlinear optical properties of a hybrid metal dielectric nanoantenna made of Au bow tie nanoantenna with LiNbO₃ nanoparticles in the gap [125]. Additional nanostructures that combine more than one material include heterodimers [35, 307, 89], and core-shell particles [251, 99].

In this letter, we are concerned with hybrid nanostructures that combine in themselves a dielectric and a metallic part with a fabrication friendly sandwich design and demonstrate experimentally these nanoantennas as candidates for biosensing. The world of biosensing is mainly dominated by plasmonic biosensors, especially surface plasmon-polaritons (SPPs) or propagating plasmon resonances, yielding an experimental bulk sensitivity of 5.9×10^4 nm/RIU [355, 363], and around 2×10^5 nm/RIU predicted theoretically [129, 266, 363]. Localised surface plasmon resonance (LSPR) sensors, based on plasmonic nanoantennas, can potentially be used for point of care testing thanks to their miniature size [363, 345, 378]. Although their sensitivity is lower than SPP sensors, values taken from Ref. [363] for bulk refractive index sensing are in the order of 400-600 nm/RIU for LSPR sensors. On the other hand, dielectric sensors reach a typical bulk sensitivity up to 300 nm/RIU [49, 404, 324].

We investigate the sensing performances of metasurfaces consisting of hybrid nanoantennas built by a sandwich structure of an Al disk and a Si cylinder separated by a SiO₂ spacer. This hybrid nanoantenna is fabricated by e-beam lithography and dry etching of the SiO₂ and Si. I compute the scattering properties of the nanostructure, conduct a multipolar analysis by decomposing the optical field into vector spherical harmonics, and interpret the response of the hybrid system in terms of the scattering of its separate components, thus providing an understanding of the working principles of the hybrid nanoantenna. A refined nanofabrication technology is developed to produce hybrid structures on a large area and experimental results demonstrate the applications of this hybrid nanoantenna for bulk refractive index sensing. Combining different etching approaches, I further extend the nanofabrication to nanoantennas with an undercut to favour near-field interactions between the structure and the analyte. This work paves the path for hybrid geometries being incorporated as refractive index sensors.

5.2 Nanofabrication

Figure 5.1a shows the geometry of the hybrid metal-dielectric nanoantenna, which represents the building block or meta-atom for the hybrid metasurface. The nanoantenna of diameter 470 nm, consists of a 220 nm thick Si cylindrical base covered with a 60 nm thick Al cylindrical cap; a 75 nm thick SiO₂ spacer is introduced between the Si and the Al to control their near-field interaction. There is a recent effort to use Al in plasmonics because of its low cost, high abundance in nature, compatibility with CMOS processes [234, 159, 189, 404] and chemical

stability due to self-limiting oxide layer. Since Al and Si are CMOS compatible materials, such hybrid nanoantennas can potentially be integrated into optoelectronic CMOS chips [55]. Note that Al is key for the fabrication process used in this study, since it serves as a hard mask for the dry etching of pure Si and SiO₂, and as a plasmonic component.

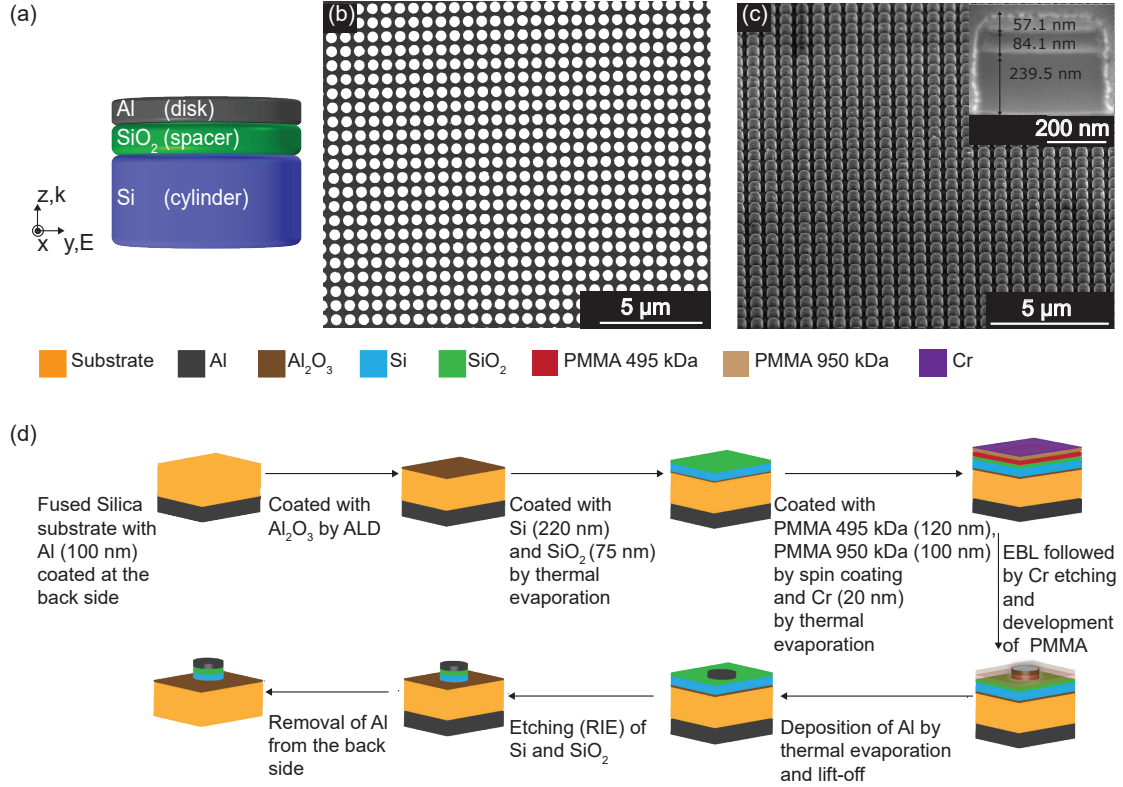


Figure 5.1 – (a) Geometry of the hybrid metal-dielectric nanoantenna. k denotes the propagation direction of the incident wave, whereas E denotes the direction of the electric field. SEM images of the nanoantenna array with a period of 670 nm: (b) top view and (c) 52° tilt; the inset shows the cross-section, made by Focussed Ion Beam (FIB) etching, of a single nanoantenna. (d) Process flow for the fabrication of the hybrid nanoantenna

The process developed in this study is intended for the fabrication of large area samples, typically $200 \times 200 \mu\text{m}^2$, that are suitable for realistic sensing applications [347, 138, 76]. Figure 5.1 shows a sample under normal view (panel b) and 52° tilt (panel c). The SEM image of an area containing over 700 nanoantennas shows a very high level of fabrication uniformity. The different process steps are detailed in Figure 5.1d. The hybrid nanoantennas are fabricated on a fused silica substrate which is coated with 100 nm Al at the back to ensure electrostatic clamping of the wafer for etching of the Si and SiO₂ at later stages. 10 nm thick Al₂O₃ is deposited by atomic layer deposition (ALD BENEQ TFS200) on the substrate to serve as stopping layer for the HF vapour dry etch, which is used later to modify the antennas by undercutting the SiO₂ spacer layer. This is followed by the evaporation (Leybold Optics LAB 600H) of pure Si and SiO₂ with 220 nm and 75 nm thicknesses, respectively. Two layers of

electron beam resist PMMA (Microresist Technology GmbH) with different molecular weights: first 120 nm with 495 kDa, second 100 nm with 950 kDa are subsequently spin-coated on the SiO₂. Since the substrate is fused silica, 20 nm of Cr is deposited on top of the PMMA to dissipate the charges during electron beam lithography. After electron beam lithography (EBL), Cr is removed using wet-etching (18 s in TechniEtch Cr01 at room temperature) prior to the development of the PMMA. The Al nanodisks are realised by lift-off technique consisting of Al deposition using an AgO_x seed layer to improve the quality of the Al structures, as described in Ref. [345]. Since the Al disks are used as hard mask for deep reactive ion etching (RIE) to define the underlying SiO₂ and Si structures but also as plasmonic component, a relatively thick Al layer of 60 nm is deposited. The reactive ion etching is performed using Alcatel AMS 200 SE dry etcher with fluorine chemistry. To remove Al from the backside using wet-etching (ANP VLSI at 35°C) the entire wafer top surface is protected by coating with 1 µm thick photoresist AZ 1512 (MicroChemicals @6000 rpm, postbake at 100°C for 1 min). Finally, the protective photoresist is removed (two runs in Remover 1165 for 5 mins each at 70°C) giving rise to the final hybrid metal-dielectric nanoantennas shown in Figure 5.1b-c.

5.3 Multipole analysis

In order to study the working principle of the proposed design I first simulated the nanostructures by multipole analysis. In particular, the interplay of the different modes supported by the structure is investigated by considering a single hybrid nanoantenna under normal incidence since multipole analysis cannot be performed on a periodic system. The illumination condition is shown in Figure 5.1a. The refractive index of Al has been taken from Ref. [345] and that of Si from Ref. [265]. First, the scattering cross-section for the different structures is computed using the full wave surface integral equation method and shown as red curves in Figure 5.2 [149, 282]. The radiated electromagnetic field computed for the different structures is then used to perform a multipole decomposition into vector spherical harmonics [231, 396, 9]. The electric dipole (ED), electric quadrupole (EQ), magnetic dipole (MD) and magnetic quadrupole (MQ) are sufficient to build the entire response of the system (i.e. the scattering cross-section can be decomposed into those four modes as shown in Figure 5.2). The scattering cross section of the nanoantenna along with the contribution from the individual multipoles are indicated by the y axis. The calculation reveals that the Al disk has a broad electric dipole, whereas the Si cylinder has additional higher order multipoles such as a magnetic dipole and electric quadrupole, which agrees with previous studies on Si cylinders [322]. Upon combining them, the interaction of the Al disk with the Si cylinder gives rise to a large number of higher order multipoles like electric and magnetic quadrupoles and magnetic dipole in addition to the lower order electric dipole. This results in a spectrum with multiple features as seen in Fig 5.2c.

In order to understand how the Al disk and Si cylinder contribute to the total response in greater detail, I have computed in Figure 5.2d the multipole decomposition by considering separately the Al disk and the Si cylinder. This is done by taking the surface currents obtained

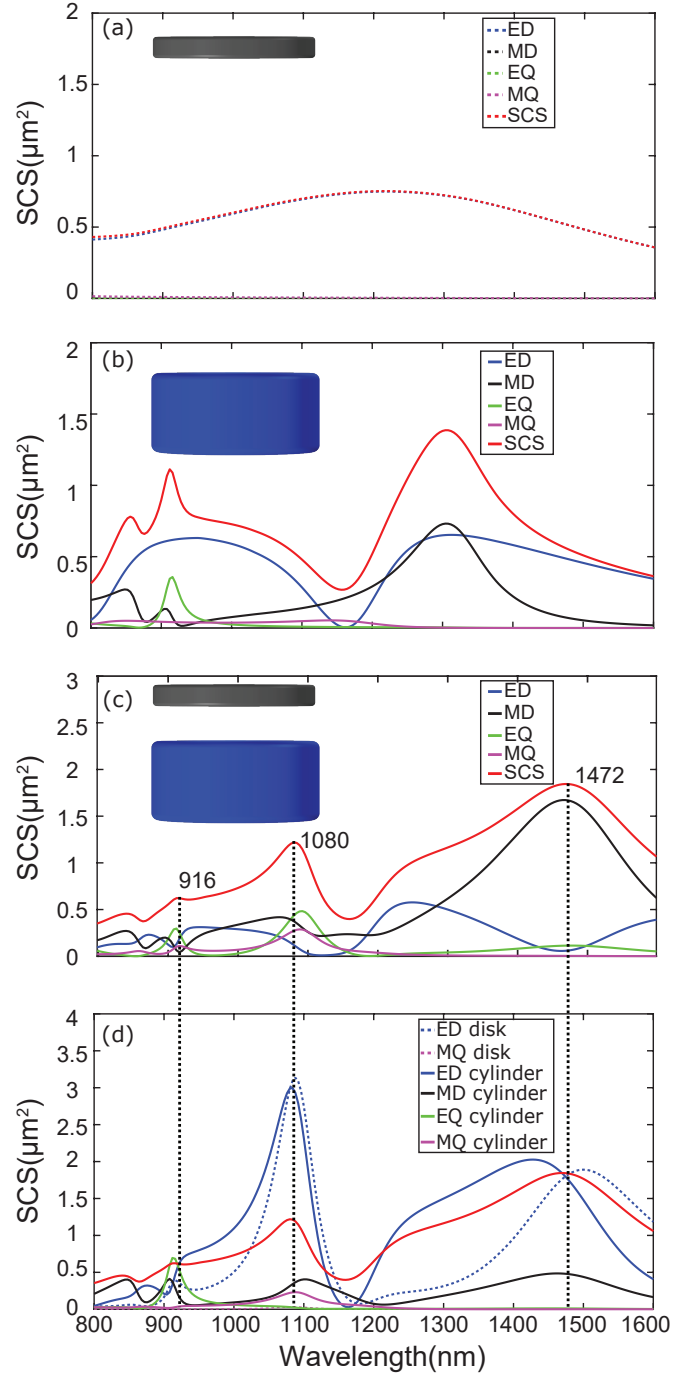


Figure 5.2 – Multipole decomposition using vector spherical harmonics for a single (a) 60 nm thick Al disk (b) 220 nm thick Si cylinder (c) hybrid nanoantenna comprising these two elements with a 75 nm thick air spacer. ED, MD, EQ and MQ denote the electric dipole, the magnetic dipole, the electric quadrupole and the magnetic quadrupole, respectively. (d) Contribution of the different multipoles from the Al disk and the Si cylinder to that of the hybrid nanostructure. The red curves in (a)-(d) represent the scattering cross-section of the nanostructure, which is equal to the sum of all the multipoles considered. The individual multipoles in (c) are decomposed in (d) where the contributions from the Al disk and the Si cylinder are plotted separately.

when the entire hybrid structure is illuminated but computing the scattered fields from each separate subpart, ignoring the other one and performing a multipole decomposition of that scattered field. Let us consider three scattering peak wavelengths of the hybrid structure $\lambda=916$ nm, $\lambda=1080$ nm and $\lambda=1472$ nm, (Figure 5.2c) to illustrate the interplay of the different modes. At $\lambda=916$ nm we observe in Figure 5.2d strong EQ and MD coming from the Si cylinder; yet, these two modes are weaker for the hybrid structure (Figure 5.2c). This is because the EDs from the Al disk and the Si cylinder are out of phase and thus give rise to an EQ and a MD that interfere with those contributed by the Si cylinder [158], leading to reduced moments for the hybrid system. At $\lambda=1080$ nm we observe in Figure 5.2d that both the Si cylinder and the Al disk produce very strong ED, whereas ED is reduced in the hybrid system in Figure 5.2c, where a sizeable MQ is also visible. This can be explained by partial cancellation of the EDs from the Al disk and the Si cylinder since they are out of phase, leading to enhanced EQ and MD in the hybrid system. This resulting MD interacts with the MD of the Si disk, increasing the net MD as well as the MQ in the hybrid structure; while the enhanced EQ increases the resulting EQ. At $\lambda=1472$ nm, we see from Figure 5.2d that the EDs from both the Si cylinder and the Al disk are the respective dominant multipoles, whereas in the case of the hybrid structure in Figure 5.2c the MD is dominant. This dominant MD along with the weaker EQ results from the interaction between the individual ED moments from the Al and Si subparts, leaving the resulting ED in the coupled system to be small. This illustrates how the interaction of a dielectric with a metal results in a abundance of spectral features, a quality unseen in metal alone.

To assess the suitability of this hybrid nanoantenna as a localized refractive index sensor, we first compute in Figure 5.3 the spectra of a single nanoantenna and its two subparts, for four different surrounding media: air ($n=1$), water ($n=1.33$), water with 42% mass glucose ($n=1.40$) and water with 60% mass glucose ($n=1.44$). The Sensitivity (S)= $\Delta\lambda/\Delta n$ calculated from these plots for the different spectral features are shown in Table 5.1 [353]. It can be seen from Figure 5.3a that for the Al disk, the peak varies strongly with the surrounding medium, giving rise to very high theoretical sensitivity (1134 nm/RIU). Figure 5.3b shows that due to the absence of the field enhancement, the multiple features of the Si cylinder vary much less with the changing surrounding medium. This is also reflected in the low S values, which are an order of magnitude lower than that of the Al disk, Table 5.1. Finally, Figure 5.3c shows the response of the hybrid nanoantenna, which inherits multiple features from the Si cylinder but has much better sensitivity since it also benefits from the field enhancement of the metal disk. Such a system that exhibits multiple spectral features that vary differently upon interaction with the surrounding environment can bring advantages for sensing. However, it should also be noted that the S value of the hybrid nanoantenna is lower than that of the Al disk alone, due to the interaction of the two subparts as explained in the previous multipole analysis.

5.4 Experiments

Next, we investigate the hybrid nanoantenna for bulk refractive index sensing with four different background media using a FTIR microscope (Bruker 80v FTIR spectrometer coupled with

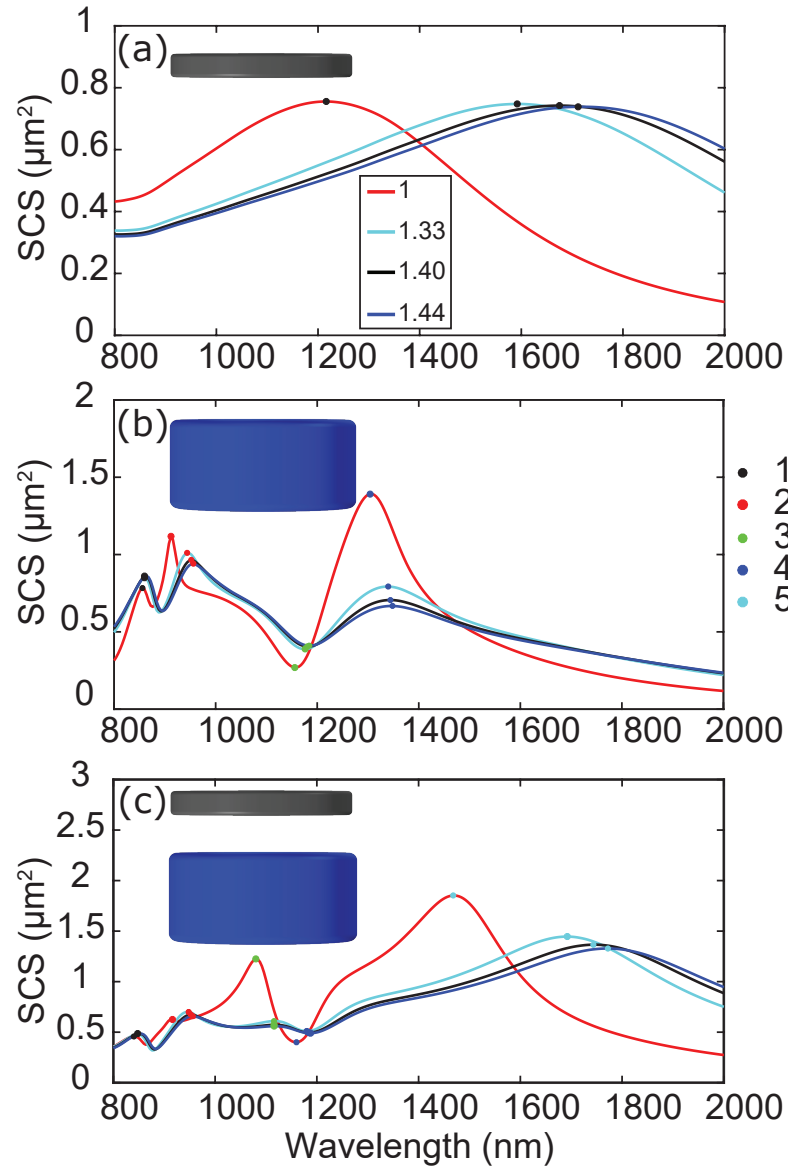


Figure 5.3 – Simulations for (a) a 60 nm thick Al disk (b) a 220 nm thick Si cylinder, and (c) the hybrid nanoantenna comprising these two elements with a 75 nm thick air spacer, for four different background refractive indices corresponding to different mass percentages of glucose in the solution. The evolution of 1 (panel a), 4 (panel b) or 5 (panel c) spectral features as a function of the background is indicated with color dots and corresponds to the values reported in Table 5.1.

Table 5.1 – Sensitivity values for a single nanoantenna computed from Fig. 5.3a-c

Structure	Feature no.	$S=\Delta\lambda/\Delta n$ nm/RIU
Al disk	1	1134
Si cylinder	1	9.9
	2	99.2
	3	61.8
	4	101.3
Coupled nanoantenna	1	19.8
	2	91.4
	3	88.9
	4	61.8
	5	779.4

Hyperion 3000). The measurements are all done in transmission mode, with the incident light oblique at a 16.7° angle of incidence with a 6.9° spread. I estimate that about 295×295 nanoantennas are probed simultaneously in the experiment. The experimental results are shown in Figure 5.4, where we clearly observe that the spectral features (either scattering minima or maxima) shift with the change of background refractive index. For all the plots in Figure 5.4 an area without nanoantennas but with a similar background medium as the nanoantennas has been considered as reference. Table 5.2 shows the sensitivity values obtained from the experiment for different spectral features. Feature 2 gives the highest sensitivity value $S = 208$ nm/RIU. Figure 5.4 also includes the numerically calculated spectrum in air, which agrees quite well with the experimental data. Note that – contrary to the previous calculations used for the modes analysis – this calculation takes into account the periodic nature of the sample, the substrate, the tilted illumination and mimics the numerical aperture used in the experiment by integrating all the light that is collected by the objective [91]. The wider resonances obtained experimentally compared to the simulations originate from inhomogeneous broadening caused by fabrication variations over the sample area.

Table 5.2 – Sensitivity values obtained from the experiment and corresponding spectral range.

Feature no.	$S=\Delta\lambda/\Delta n$ (nm/RIU)	Range (nm)
1	144	1079–1095
2	208	1106–1129
3	120	1229–1283
4	111	1259–1309

5.5 Nanoantenna with an undercut

The spatial overlap between the near-field of the structure and the analyte is important for refractive index sensing [362, 299, 418]. If we calculate the intensity distribution around the

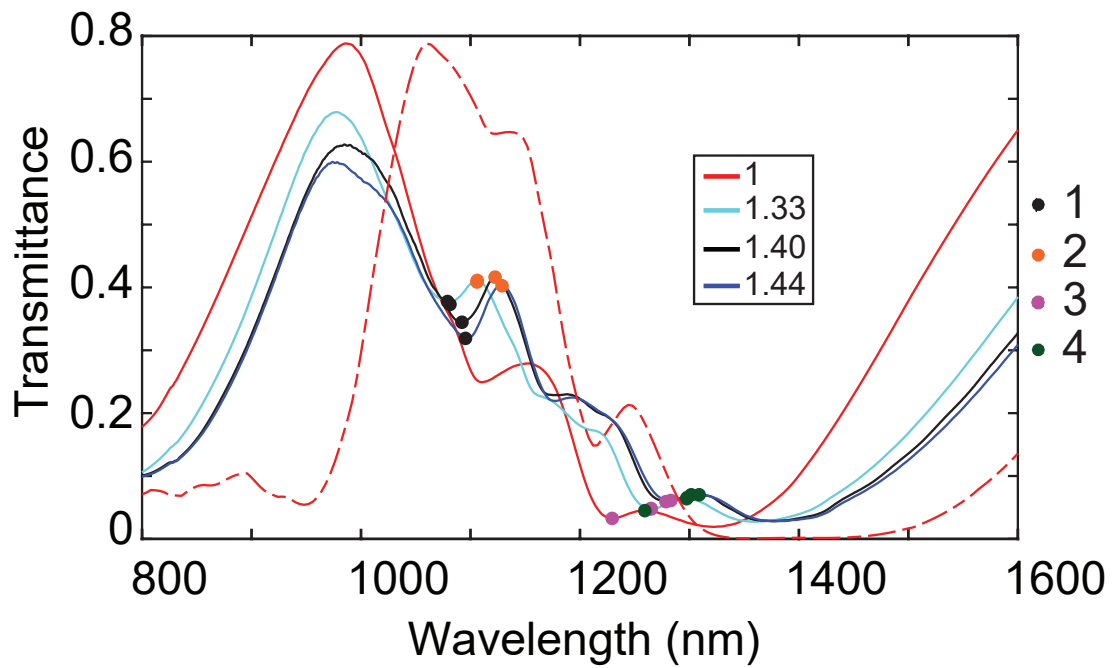


Figure 5.4 – Experimental results for bulk refractive index sensing performed with the hybrid nanoantenna with four different glucose solution as background. The red dashed curve show the calculation for an air background ($n=1$), scaled to the same magnitude as the experimental data.

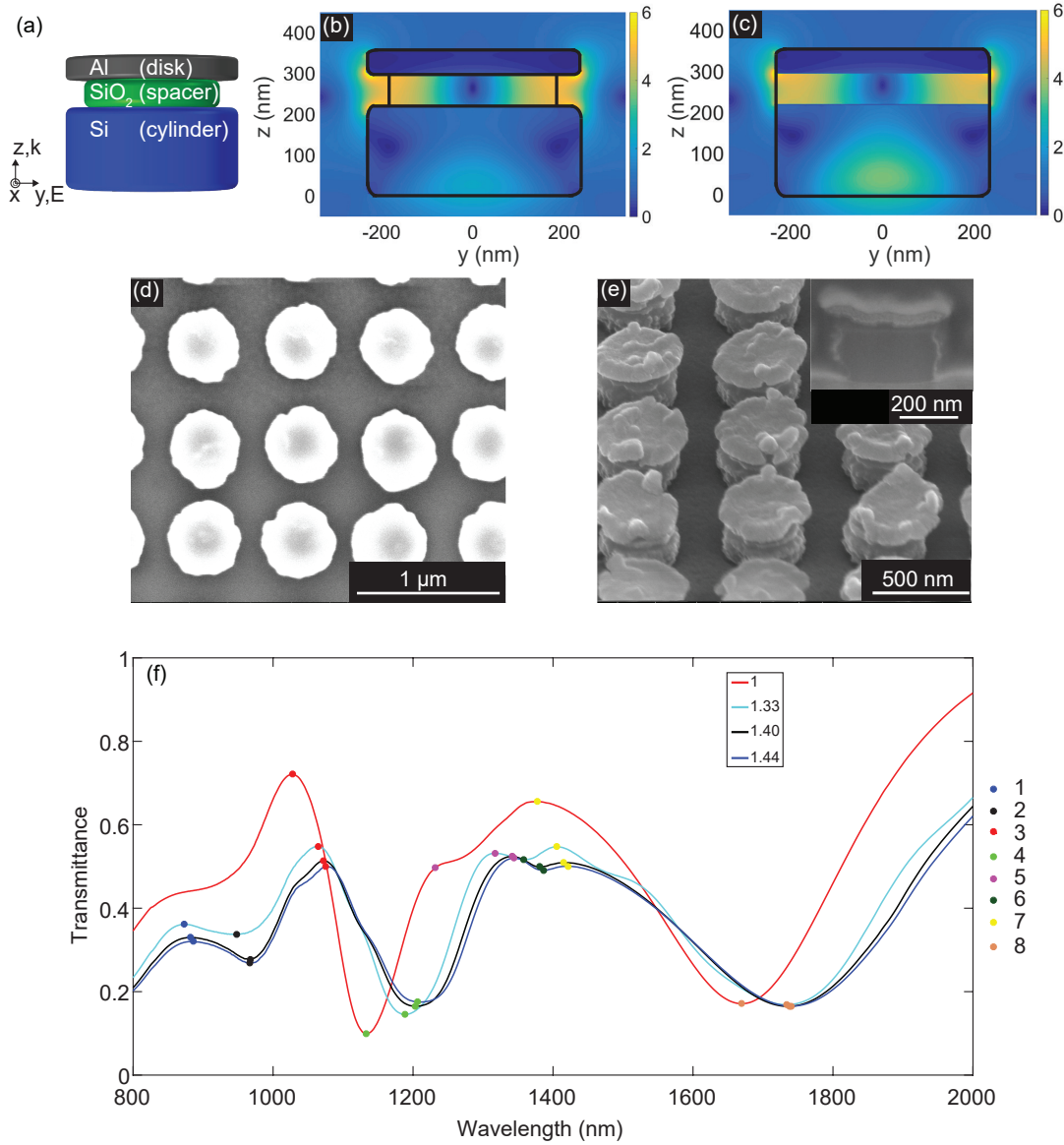


Figure 5.5 – (a) Geometry of the hybrid nanoantenna with 50 nm undercut in SiO₂. Surface plots of electric field amplitude enhancement (the amplitude of the incident field is 1) in the yz plane for a periodic array of hybrid nanoantennas (b) with and (c) without a 50 nm undercut in the SiO₂. The outline of the nanoantenna is indicated in black. (d) Top view SEM image of the hybrid nanoantenna array with a period of 670 nm. (e) SEM image of the hybrid nanoantenna array imaged at a tilt of 52° to evidence the undercut in the SiO₂ spacer. The inset shows the cross-section made by FIB for a single nanoantenna. (f) Experimental transmittance for bulk refractive index sensing performed with hybrid nanoantenna with a 50 nm undercut in the SiO₂ for four different background conditions.

hybrid nanoantenna, we observe that, due to the boundary conditions imposed by Maxwell's equations, the area with strongest field intensity is buried inside the dielectric spacer and thus inaccessible to the analyte, Figure 5.5c. To allow the analyte access the region of high electromagnetic field, an undercut in the spacer region is proposed, Figure 5.5a [31, 252, 133].

The undercut decreases the effective refractive index of the spacer region, which modifies the field distribution, and pushes out more field into the analyte, thus increasing their interaction, Figure 5.5b; compare Figs. 5.5b and c. These calculations were performed for a periodic array of antennas in air at the wavelength corresponding to the main absorption peak, $\lambda=1142$ nm for the antenna without undercut and $\lambda=1122$ nm for the antenna with an undercut. Both structures provide a similar field amplitude enhancement of the order of 6 times, but this enhanced field is clearly outside the structure in the case of an undercut, while it remains buried within the dielectric spacer without an undercut. Readers versed in the boundary conditions of Maxwell's equations might be surprised that the electric field appears continuous as it crosses the spacer interface in Figure 5.5b, although the incident field is along the y -direction, i.e. normal to that interface. The reason for this is that the total field between the Si cylinder and the Al disk is dominantly polarized in the z -direction, as indicated in Figure 5.6.

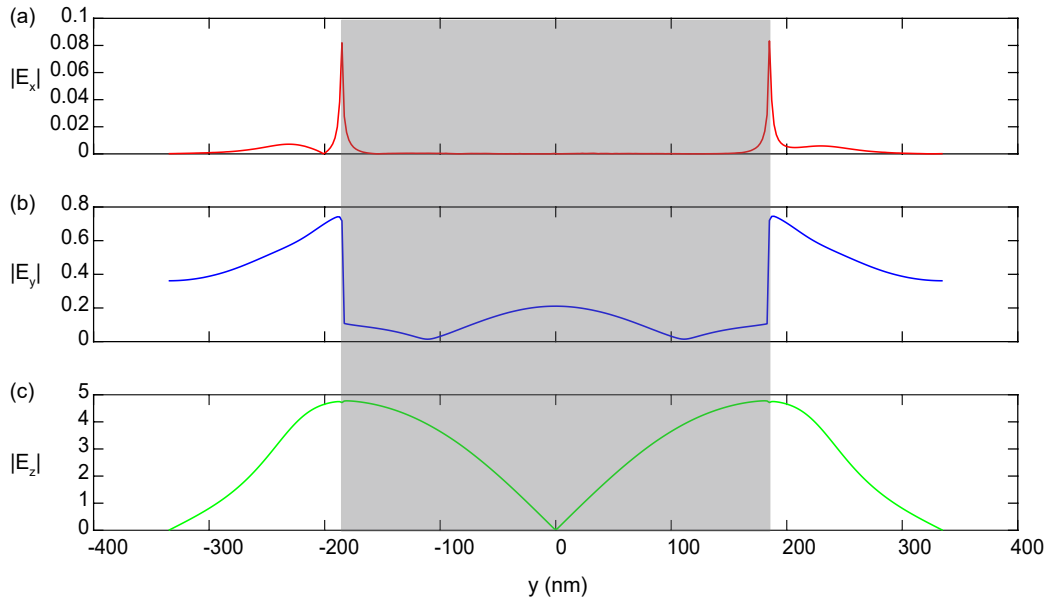


Figure 5.6 – Distribution of $|E|$ field: (a) $|E_x|$ (b) $|E_y|$ and (c) $|E_z|$ for the nanoantenna with undercut shown in Figure 5.5b, at $z=256$ nm and across y . The shaded region shows the region inside the dielectric spacer.

The proposed nanoantenna with an undercut can be fabricated with an additional step of hydrofluoric acid (HF) vapour phase etching after the completion of the hybrid nanoantennas. The nanoantennas were etched for around 33 mins at an average pressure of 67 Torr ,

Figure 5.5d. The 10 nm Al_2O_3 deposited on the fused silica substrate at the beginning of the fabrication protects the fused silica substrate from being etched during this step. The inset in Figure 5.5e shows a cross-section made by FIB on a single nanoantenna. The three layers, with an undercut in the SiO_2 can be seen from the cross-section as well as from Figure 5.5e. The latter demonstrates that hybrid nanoantennas with an undercut in the SiO_2 spacer have been successfully fabricated on a large area. We note that the top Al layer is quite grainy; this is very hard to avoid using a lift-off process [345]. Fortunately, this vertical roughness has limited influence on the response of the structure.

We investigate undercut structures for bulk refractive index sensing, under similar conditions as those used in Figure 5.4. The results in Figure 5.5f show that due to the removal of the spacer region their spectral features are very different compared to the nanostructures without an undercut. We identify 8 different spectral features and feature 5 gives the highest sensitivity, with a value of 245 nm/RIU. Table 5.3 shows the sensitivity values calculated from the experiment. It can be seen from Figures 5.4 and 5.5f that the undercut produces a modest improvement in the sensitivity, in the order of 40 nm/RIU due to enhanced interaction of the analyte with the electric field. Although the enhancement is smaller than that associated with substrate effects [68], such an undercut would certainly be favourable for surface sensing as it will allow a few monolayers of the molecules to fully access the hotspot [252]. Surface functionalization of Al can be performed by silanization [189, 346].

Table 5.3 – Sensitivity values obtained from the experiment and corresponding spectral range for nanoantennas with 50 nm undercut.

Feature no.	$S=\Delta\lambda/\Delta n$ nm/RIU	Range (nm)
1	110	873–886
2	153	948–968
3	110	1027–1075
4	169	1133–1206
5	245	1232–1344
6	169	1358–1387
7	98	1378–1422
8	167	1669–1740

5.6 Conclusions

In conclusion, to benefit from the strengths of plasmonics and dielectrics we have introduced a new fabrication friendly hybrid nanoantenna made out of Al and Si materials in a layered stack (sandwich) geometry. We have explained the working principle of the hybrid metal-dielectric nanostructure by multipolar decomposition. Such nanoantennas are fabricated uniformly over large areas and used for bulk refractive index sensing, with a sensitivity of 208 nm/RIU. To increase the overlap between the electric field and the background medium a 50

nm undercut was introduced in the SiO₂ spacer, which increased the sensitivity to 245 nm/RIU and provided additional spectral features, compared to the antennas without undercut. The hybrid nanostructure developed in this work could also be used for surface sensing or for fluorescence enhancement.

6 Theory of hybrid nanoantenna

In the previous chapter we have demonstrated bulk refractive index sensing with hybrid metal-dielectric nanostructure. However, we felt in order to harness the full potential of the hybrid nanoantenna it is important to do a systematic study, investigating how the variation of the geometrical parameters influence the final spectra. We believe that such a study will help providing a detailed understanding of the interplay between metal and dielectric and help the community make an educated choice of geometry of the hybrid metal-dielectric nanoantenna based on their desired application. My contributions were performing all the numerical simulations presented in this chapter. Parts of this chapter has been submitted for publication [276].

6.1 Introduction

Metallic nanostructures can produce a strong field enhancement by the resonant oscillation of free electrons and have thus been a popular research topic for several decades [213]. There are however two main limitations to those resonances: the intrinsic losses associated with metals, which limit the quality factor that can be achieved [164]; and their essentially electric dipolar character, which restricts the degrees of freedom for engineering arbitrary electromagnetic responses [72]. These issues can be solved by replacing metals with low loss dielectrics, which have recently emerged as a vivid research topic [401, 172, 404, 352, 86]. Dielectric nanostructures exhibit both electric and magnetic resonances, which enable several interesting phenomena like unidirectional scattering [156, 2] Fano resonances [191], or even anapole states that do not radiate in the far field and are formed by the destructive interference between electric and toroidal dipoles [224]. Unfortunately, despite all their advantages, the use of dielectrics reduces the field enhancement in the vicinity of the structure, which is detrimental for applications like fluorescence [56] and sensing [120]. In order to circumvent the drawbacks of both metals and dielectrics, hybrid metal-dielectric nanostructures have recently come up as a promising option. These nanostructures are expected to provide the best of both worlds by combining low losses from dielectric and high field enhancement from metal.

The significant progress made in various facets of hybrid nanophotonics has been efficiently collated in a review by Lepeshov et al. [182], which illustrates experimentally achievable hybrid geometries based on different working principles like the whispering gallery modes in Si-Al₂O₃-Ag dimers leading to directional radiation [372] and the coupling of a hybrid mode at the Si-Ag interface of a Si nanoparticle on an Ag film to the propagating surface plasmon-polariton [402]. Unconventional and newer hybrid core-shell geometries like an Ag rod covered by a semiconductor layer for broadband absorption enhancement [218] and a gold rod covered by a Cu₂O shell for generation of third harmonic [20], to name a few, has also been mentioned. The hybrid nanoantenna, due to the presence of dielectrics, boasts of some unique features like the pure magnetic dipole resonance or the anapole states, which will also be seen in the later sections of this work. Predominantly Magnetic Fano resonances have also been observed in hybrid oligomers formed from a combination of Si cones and Au particles, which can be tuned by laser melting of the Au particles [183, 181]. Additionally there are several other recent works on hybrid nanoantenna that also need to be acknowledged such as the ones that discuss the efficient generation of the second [100, 130], and third harmonics [309]; nonlinear optical properties [125], subtractive color filtering [408, 233], sensing [279], unidirectional radiation [126] and asymmetric absorption [398].

Upon careful considerations of these articles it can be noted that core-shell or stacked cylindrical geometries are the most popular. While the core-shell geometry has analytical solutions, the stacked cylindrical geometry still lacks a consistent theoretical tool for the analysis. One possible way to fulfill this gap is to perform a comprehensive systematic parametric study on how the geometrical parameters of the system influence the scattering characteristics of these structures, which represents the focus of this chapter.

To the author's knowledge, only a few publications have unveiled some of these dependencies. For example, the scattering characteristics of dielectric core coated with metal shell have been implemented experimentally and studied analytically for spherical and numerically for co-axial cylindrical configurations [86, 187, 391, 201]. A hybrid geometry with metal nanorods on top of Si cylinders was studied, noting the influence of a spacer between a metal rod and a dielectric cylinder to enhance directional radiation [293, 116]. The effects of thickness and permittivity of the dielectric spacer and the metal nanodisk in a metal-dielectric-metal sandwiched geometry on the directional radiation and manipulation of multipoles were also investigated [421, 271].

In principle, the coupled electric and magnetic dipole theory that works for spherical objects [329] could be applied to predict scattering from cylindrical geometries. Unfortunately, from our experience, this approach does not give sufficiently accurate results and we have to resort to numerical methods to explain how various features of these hybrid geometries appear and disappear as we perform a systematic study of one specified hybrid geometry by varying its dimensions. For our work we chose a metal-dielectric nanostructure made of Si cylinder and Ag disk placed on top of one another. I start by varying the geometrical parameters like height and radius of a Si cylinder, followed by Ag disk and finally that of a hybrid structure. Since the

parameters considered here are experimentally meaningful, this systematic analysis showing how each geometrical parameter affects the spectral response is also very beneficial from an engineering perspective for designing hybrid geometry. This analysis and the underlying physics can also be extended to several other similar hybrid geometries like core-shell particle [301, 202, 367] and cylinder-disk [408, 233] and cylinder-nanorod geometries [293, 116].

We perform the numerical simulations with the surface integral method, which has been proven a very accurate frequency domain technique [90, 149]. To avoid the singularities of the Green's tensor close to the scatterer's surface, we use the singularity subtraction technique [282, 150]. Refs. [149] and [282] discuss in detail the performance of this technique and the accuracy of the algorithm in computing the response from various nanostructures. Numerical simulations are challenging and choosing a method that is best suited to the needs of the analysis with minimal trade offs is always an art. In this work I have presented all the results of the parametric study using a well-established SIE method. The use of a single method throughout the chapter helps in building a coherent understanding as the geometry progresses from a single Si cylinder to a more complicated Ag disk-Si cylinder hybrid nanoantenna. The Cartesian multipoles decomposition is performed with the vector spherical harmonic basis [232], which is available online [157, 158, 396]. The resultant multipole for any structure strongly depends on the choice of origin of the coordinate system [37]. We make the choice of origin at the geometrical center of the mesh to provide a coherent analysis. Aiming at clarifying how different geometrical parameters affect the overall spectrum, I vary the size of each component and monitor the evolution of the multipolar response traces. The system is illuminated with a planewave propagating along the symmetry axis z , leading to a polarization insensitive scattering response. Such a geometry can be fabricated with a high level of control [398, 279]. I have chosen Si as the dielectric material since it has high permittivity and modest losses in the visible and has been widely used experimentally [172, 62, 323] and Ag as the metal for its low losses [384, 58, 151]. For our simulations I use available data for Si from Ref.[265]. To put an effort to be consistent with our recent experimental research on hybrid antenna for sensing, I use our experimentally measured data for Ag [277] that, in comparison to the data from Johnson and Christy [139], show almost the same real part and slightly lower imaginary part of the dielectric permittivity of silver in the region 1100-1700 nm.

6.2 Results and discussion

The results are divided into several sections to explore in details the influence of the different geometrical parameters on the spectral features supported by the system. I first explore the scattering cross-section (SCS) for a bare Si cylinder, then add a metal disk of varying thickness and diameter. Finally, I investigate the coupling between the dielectric and metallic parts as a function of their separation.

6.2.1 Response of the dielectric cylinder

To understand the advantages of a hybrid nanoantenna and the additional control it offers, I begin by analyzing the SCS of an isolated Si cylinder illuminated with a planewave. Although this has been reported by others [322, 78, 224, 357, 358], it will help us form a coherent understanding as we proceed to the subsequent sections, where I modify the geometry gradually by adding Ag to the Si cylinder.

I first vary the radius R of the Si cylinder from 235 nm until 47 nm in steps of 47 nm, as shown in Fig. 6.1(a); for the time being, I retain the height H of the Si cylinder as 220 nm. Already in this simple system, we observe a rather rich spectrum with many different features, especially for the larger cylinders. The entire SCS can be decomposed into an electric dipole (ED), a magnetic dipole (MD) and an electric quadrupole (EQ) Cartesian multipoles. It can be observed that with the decrease in radius, both the ED and MD blueshift. Interestingly, the ED is shifting more than the MD, such that the ED leaves the MD far away behind, on the left side of the spectrum, as the radius decreases, as seen for $R = 94$ nm in Fig. 6.1(a). This faster shift of the ED is actually not surprising and has been observed previously for the case of a dielectric sphere (see e.g. Fig. 1(c) in Ref. [182]), and is explained by analyzing the electric and magnetic Mie coefficients a_1 and b_1 in the framework of the Padé expansion[352]. The magnitudes of both ED peaks decrease as the cylinder shrinks, while the MD resonance retains its magnitude.

Let us now vary the height H of the Si cylinder from 220 nm to 44 nm in steps of 44 nm, Fig. 6.1(b). Again, the ED and MD resonance positions blueshift with decreasing sizes. Opposite to what was observed for a change of radius, now the ED magnitudes remain rather constant, while the MD magnitude drastically decreases as I diminish the height. Also, we notice that the position of the MD peak blueshifts much faster than the ED ones, leading to significant "overtaking" of the MD resonance over the ED, as seen for $H = 132$ nm in Fig. 6.1(b). Actually, this observation is important for engineering directional scattering [8, 200, 156, 2], or producing a far-field response constituting of only one particular mode, e.g. the MD for "magnetic light" [171, 187]. The ED and MD resonances of dielectric structures can have strong spectral overlap between them; a difference in their shift rate enables their efficient spectral separation. For example, by varying the Si height, we can control the ED and MD responses and achieve a good spectral separation for $H = 176$ nm, Fig. 6.1(b).

The different spectral behaviour for ED and MD stems from the physical nature of these multipoles. The MD response is known to be produced by a current loop induced in this particular case in the xz -plane. With the decrease in height, the effective space volume pertaining to the current loop decreases, reducing the resonance energy of the MD mode. On the contrary, the ED energy is related to the bulk polarization distributed mostly in the yx -plane inside the structure. Consequently, because of the asymmetry of the structure with respect to the z -axis, these two multipoles are affected differently as I vary radius and height [357].

In order to get a complete picture, I also present the spectra attributed to the simultaneous

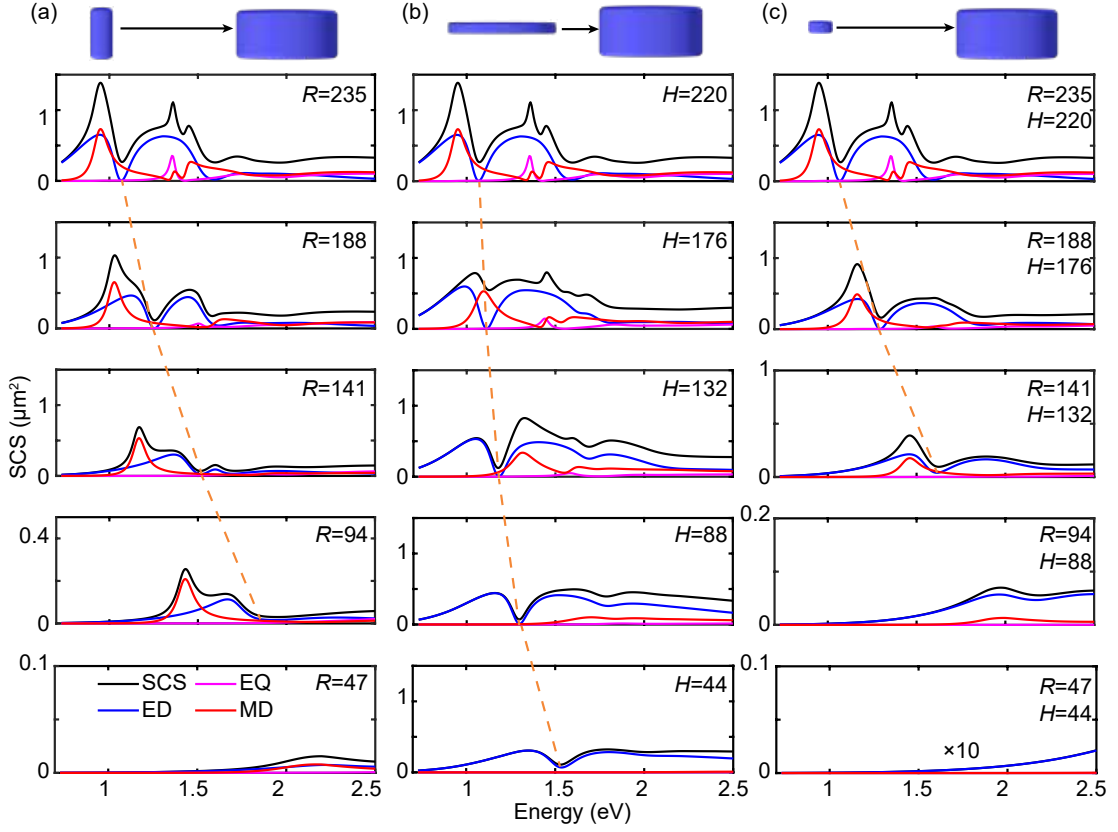


Figure 6.1 – Scattering cross section (SCS) and its decomposition into Cartesian multipoles: electric dipole (ED), magnetic dipole (MD) and electric quadrupole (EQ). (a) Constant height $H = 220$ nm and varying radius R , (b) constant radius $R = 235$ nm and varying height H , (c) varying height H and radius R . All dimensions are in nm and the orange dashed line traces the position of the anapole state.

variation of height and radius in Fig. 6.1(c). In this case, the blueshift rate is almost the same for the ED and MD. Also, I observe a simultaneous magnitude reduction for both resonances as I decrease the cylinder volume.

Figure 6.2 shows the position of the peaks obtained from Fig. 6.1 for the ED and MD resonances as a function of the geometrical parameters. Here, the circles stand for the resonance peaks at lower energies while the diamonds stand for the resonance peaks at higher energies. It should also be noted that in this plot I have no data pertaining to $R = 47$ nm and $H = 44$ nm since there is no resonance peak for the ED or the MD in the considered energy range, Fig. 6.1(c). At 1.07 eV I observe a dip in the dipolar trace for $R = 235$ nm $H = 220$ nm, which is associated with the excitation of the anapole state [230]. This rather unusual mode stems from the destructive interference between the ED and the toroidal dipole (TD)[224, 302, 165]. This is confirmed by plotting the SCS of the ED and TD, which indeed intersect at this wavelength with a phase difference of $\pi/2$ (data not shown). Interestingly, the anapole state also blueshifts more with decreasing radii, as compared to the decrease in height, since the anapole state appears due

to the destructive interference of ED and TD; since the ED shifts more with change in radius, so does the anapole state.

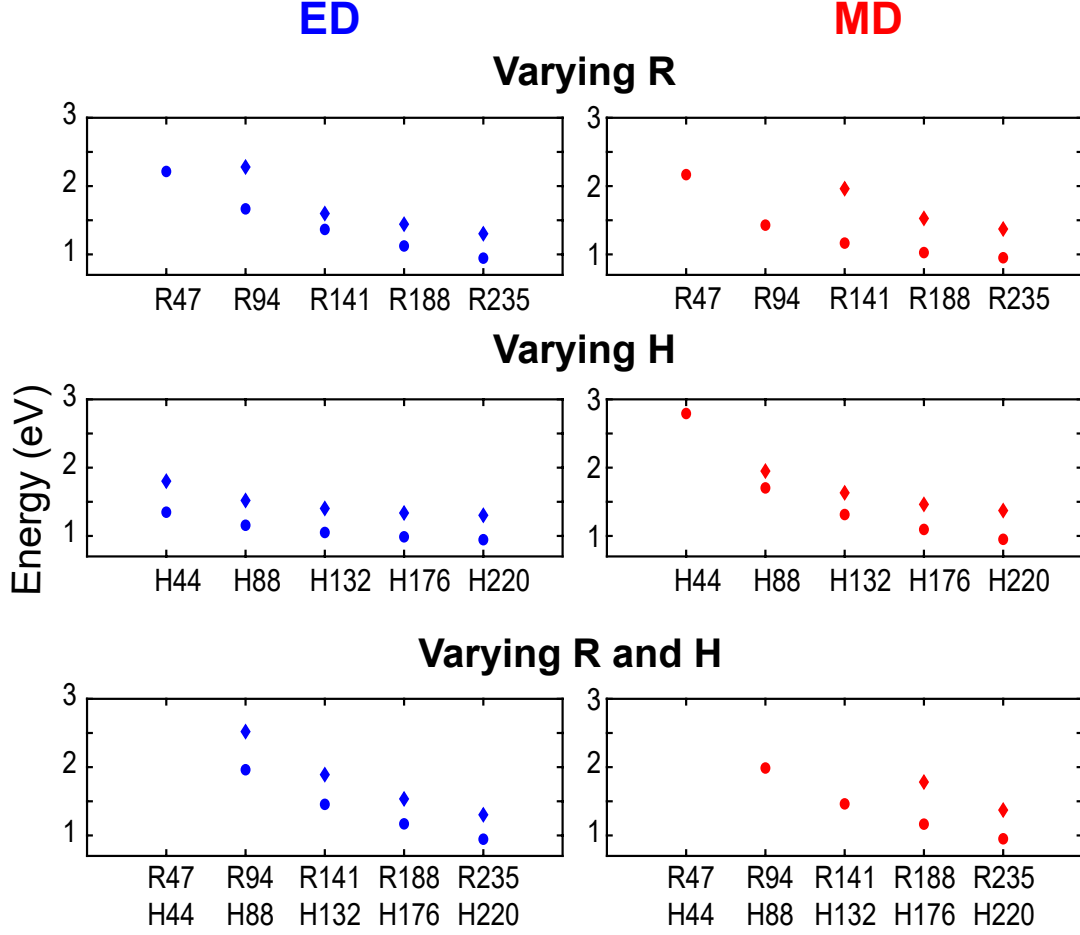


Figure 6.2 – Resonance peak positions of the ED and MD varying with the change in dimensions. The circles refer to peaks at lower energy while the diamonds refer to peaks at higher energy.

6.2.2 Influence of the metal disk

Having studied the effects caused by increasing the dimensions of the Si cylinder, I now study the effects caused by adding a metallic component in the system, i.e. by appending a few nm thick metallic disk on top of the Si cylinder. Indeed, quite significant level of control over the position of the resonances can be achieved by introducing a metal in the system [187, 77]. I choose a Si cylinder with $H = 220$ nm and $R = 235$ nm since it has prominent additional multipoles, like MD and EQ. The advantage of involving these multipoles in the analysis can be appreciated in the following where "magnetic light" is achieved. I start with the Ag thickness $t = 10$ nm, as this is experimentally achievable [344, 364, 226], and increase the thickness of

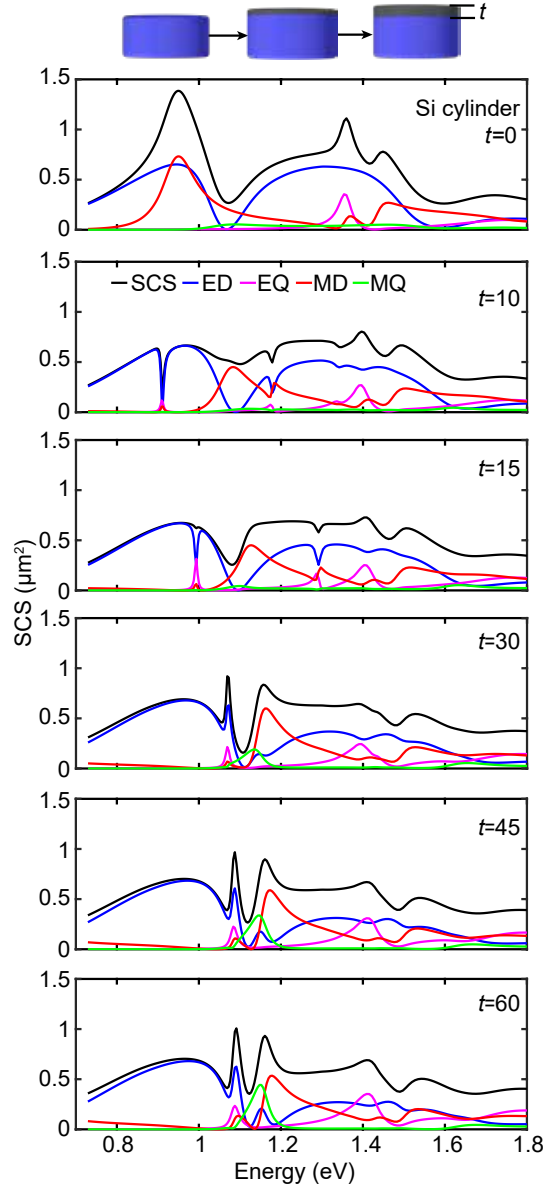


Figure 6.3 – SCS and its Cartesian multipoles decomposition for a Si cylinder ($R = 235$ nm, $H = 220$ nm) covered with an Ag disk of varying thicknesses t . Note that for $t = 15$ nm, the SCS at 1.11 eV is solely defined by the MD. All dimensions are in nm.

Ag up to 60 nm [279], as shown in Fig. 6.3.

An addition of metal, albeit extremely thin, drastically modifies the spectrum. In contrast to the dielectric cylinder, where we were able to only manipulate the position and the magnitude of the resonances, we are now able to modify the profile of the resonance itself. Indeed, by inspecting the dipolar trace of the spectrum achieved by adding only 10 nm of Ag we notice sudden dips at 0.91, 1.18 and 1.34 eV, compare $t = 0$ and $t = 10$ in Fig. 6.3. The dip at 0.91 eV is fairly sharp with a full width at half-maximum of 0.01 eV. The emergence of these dips can be

explained by the interference between two π -shifted Cartesian electric dipoles excited in the metal and dielectric parts, giving rise to the effective excitation of the EQ and MD resonances in the far-field [279]. Quite interestingly, this effect of efficient translation of two ED Cartesian multipoles into EQ and MD is seen only at particular frequencies. Moreover, it becomes less noticeable as the metal thickness increases; possibly because the intrinsic losses in the metal take over.

From the findings for a dielectric cylinder, it is expected to observe a redshift of the MD resonance as the height of the structure is increased. Surprisingly, here the overall profile of the MD spectrum retains its position and magnitude, once the Ag thickness is increased above 15 nm. In the meanwhile the position and the profile of the ED resonance is subject to more noticeable changes. Thanks to these features, almost pure MD resonance can be achieved in this geometry at 1.11 eV, Fig. 6.3 for $t = 15$ nm. Similar results have been reported for the geometries of two co-axial metal-dielectric cylinders [86] and two metallic cylinders placed one on top of another and separated by a dielectric [421]. The decoupling of the ED and MD in the range of 1-1.2 eV is also very beneficial for the generation of an excellent anapole state. For example, for Ag thicknesses between $t = 30$ nm and 60 nm in Fig. 6.3 we observe around 1.1 eV negligible ED and MD components, but still a sufficiently strong MQ contribution. It has been shown that, by using radially polarized excitation instead of linearly polarized one, the magnetic contributions can be suppressed [187, 57]. This will result in an excellent anapole state making the structure non-radiating at this wavelength. The broad dip in the ED at 1.1 eV for Ag disk of height $t = 30$ nm (Fig. 6.3) is attributed to the anapole state, which leads to the minimum in the ED response and so only a contribution from the MQ is seen [224]. This anapole state suffers negligible blueshifting with an increase in the thickness of Ag. Also, we noticed that increasing the height of silver above 60 nm barely affects the spectral features of the system. Thus, I take the Si cylinder with 60 nm thick Ag disk as a final structure on which I carry out further modifications to understand the interaction between the Si cylinder and the Ag disk.

The spectra reported in Fig. 6.3 have multiple prominent resonant features, which distinguish these hybrid nanostructures from their pure metal or dielectric counterparts. However, sometimes there is a need for a spectrum with only one or two sharp features in the SCS, e.g. for sensing when the change in the refractive index of the background analyte is measured by tracking one or two spectral features [354]. In this case, the sharper the resonance, the higher is their figure of merit. This can be achieved in the nanostructure at hand by varying the radius of the Ag disk as shown in Fig. 6.4 for Ag disks with radii between $r = 120$ nm and 235 nm (for clarity, the baseline for the Ag disk SCS is shifted by $1\mu\text{m}^2$). We notice that the MD position can be adjusted within the range of 1.08-1.35 eV by changing the Ag disk radius. Specifically, the magnitude of both MD resonances within this region is much stronger than in the remaining part of the spectrum. For $r = 160$ nm, we find the MDs at 1.15 and 1.24 eV, Fig. 6.4. For larger Ag radii, the lower energy MD remains around 1.15 eV, while the higher energy MD slightly redshifts for $r = 175$ nm, and then begins to fuse with the low energy MD, producing a very strong spectral feature for $r = 185$ nm. This feature becomes even more

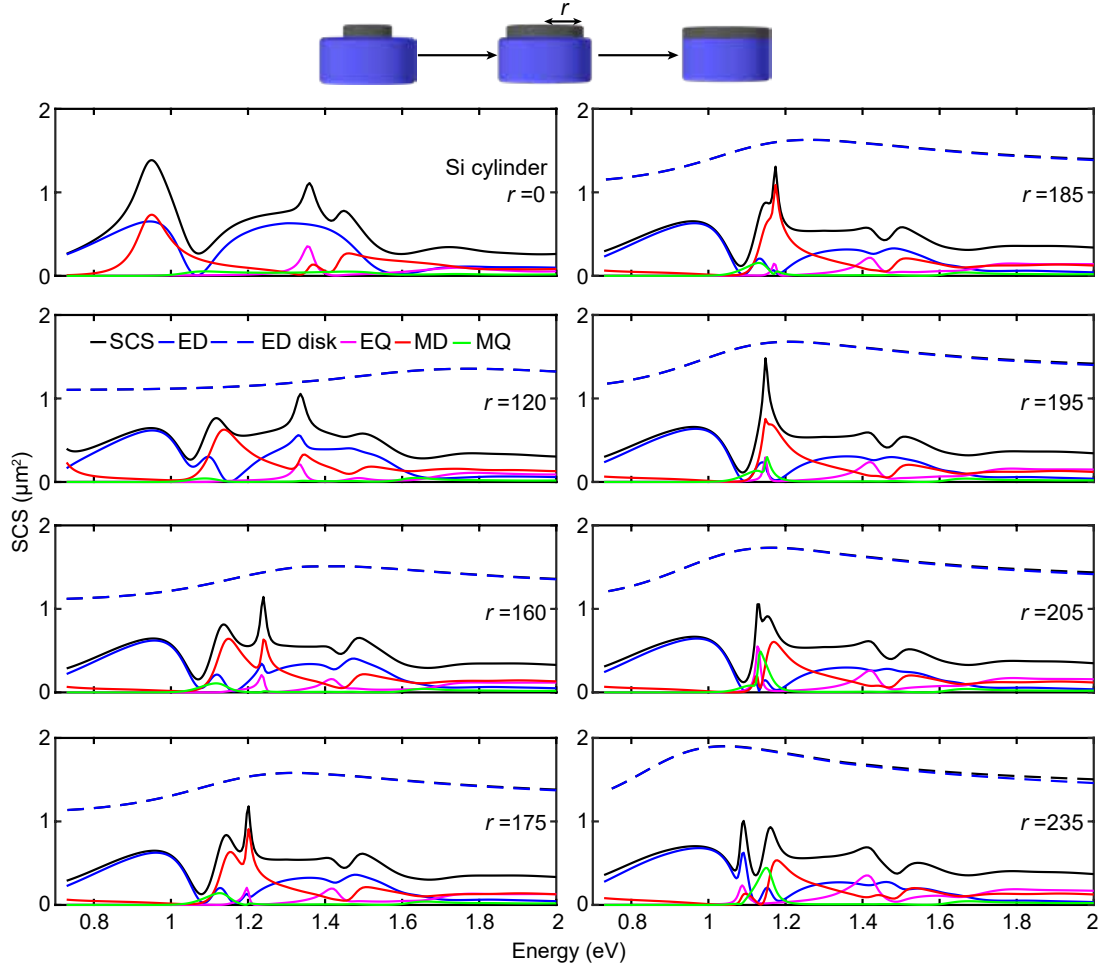


Figure 6.4 – SCS and its Cartesian multipoles decomposition for a Si cylinder ($R = 235$ nm, $H = 220$ nm) covered with a $t = 60$ nm thick Ag disk of varying radii r . All dimensions are in nm.

prominent for $r = 195$ nm, where it dominates the entire SCS, Fig. 6.4. This peak can also be explained by the interference between two π -shifted Cartesian electric dipoles excited in the metal and dielectric parts giving rise to effective excitation of EQ and MD resonances in the far field. The MD resonance arising from this phenomenon interferes with the MD from the Si cylinder and reduces the net MD of the system [279]. Such a very sharp feature could be very useful for sensing applications as it will give high figure of merit [354, 363]. Beyond $r = 195$ nm, this sharp feature at 1.15 eV starts again to split into two peaks as shown in Fig. 6.4 for $r = 205$ and 235 nm.

6.2.3 Coupling between the dielectric cylinder and the metal disk

Finally, I investigate an additional control over the spectrum offered by this hybrid nanostructure by introducing a spacing of varying thickness δ between the Si cylinder and the Ag

disk. For the ease of understanding, I consider an air spacer; a dielectric spacer will merely increase the coupling as is the case for a dielectric loaded plasmonic structure [1]. This study complements the one done previously for Si cylinder sandwiched between two Ag disks [421]. In Fig. 6.5 I slowly increase the spacing from $\delta = 5$ nm, which is achievable with current standards of nanofabrication [210], to $\delta = 75$ nm.

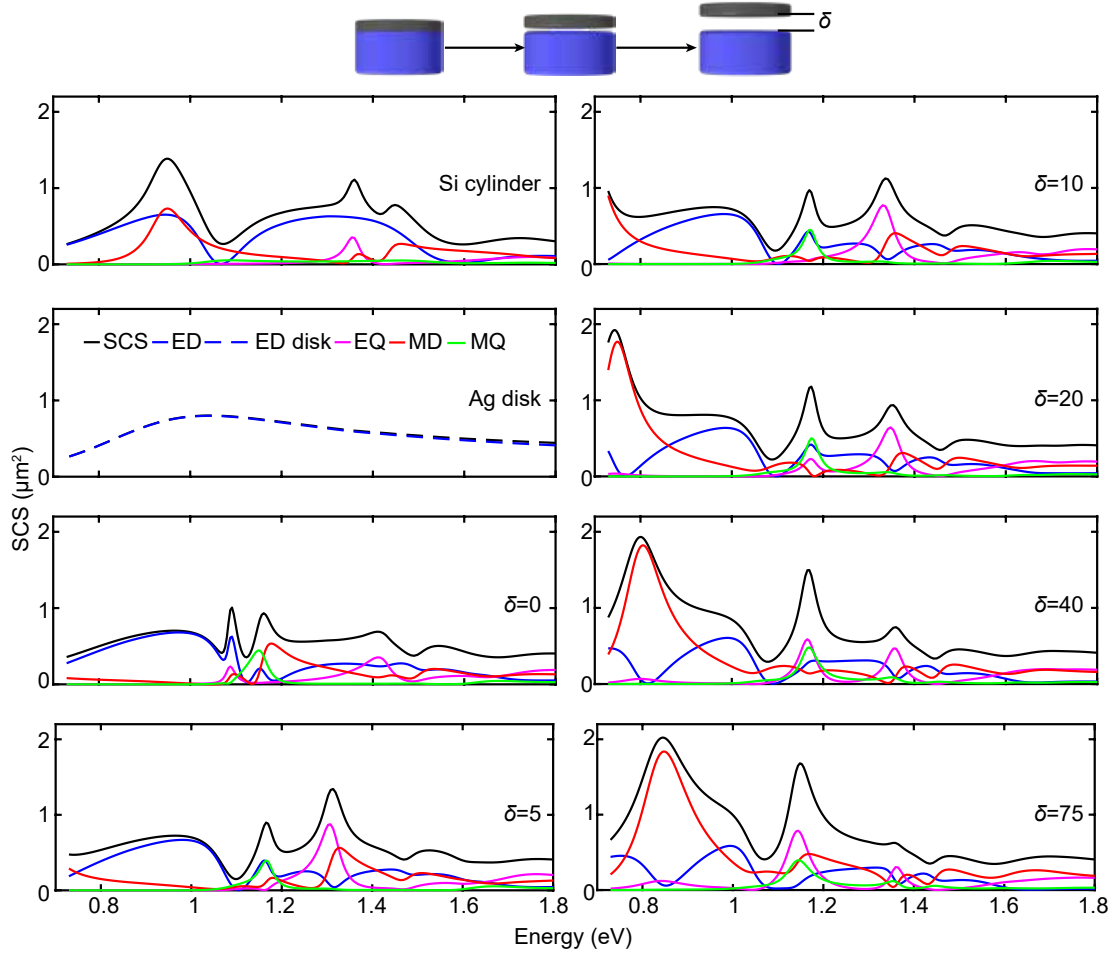


Figure 6.5 – SCS and its Cartesian multipoles decomposition for a Si cylinder ($R = 235$ nm, $H = 220$ nm) covered with an Ag disk ($t = 60$ nm, $r = 235$ nm) placed at a spacing distance δ . The first two panels show the response for the individual cylinder and disk.

The most prominent feature that can be noticed as the spacing is increased is the appearance of a broader resonance in the SCS at 0.74 eV due to the emergence in the spectral window of a very strong MD resonance for a separation larger than $\delta = 10$ nm. Such a feature in the near infrared can be useful for applications in surface enhanced infrared absorption [3]. It can also be used in applications requiring only the magnetic response from the structure. However, overall, the spectral features observed for large spacings are relatively broad and will not be well suited for practical applications. Another feature in the spectrum attracted our attention

Table 6.1 – The spectral changes due to changes in the Si cylinder radius R and height H , the metal disk thickness t and radius r , or the spacing distance δ . The symbols indicate: \leftarrow = redshift, \rightarrow = blueshift, \uparrow = increase, \downarrow = decrease, \times = no significant change.

Nanostructure	Parameter	ED		MD	
		Energy	Amplitude	Energy	Amplitude
Si cylinder	$R \uparrow$	\leftarrow	\uparrow	\leftarrow	\times
	$H \uparrow$	\times	\uparrow	\leftarrow	\uparrow
	$R \& H \uparrow$	\leftarrow	\uparrow	\leftarrow	\uparrow
Hybrid structure	$t \uparrow$	\rightarrow	\times^1	\times	\times
	$r \uparrow$	\times	\times	\times	\times^2
	$\delta \uparrow$	\times	\times^3	\rightarrow	\times

¹ Sharp optical features.

² Both MD fuse to give rise to a sharp peak at $r = 195$ nm and then split again.

³ Strong interaction between ED and MD.

and is worth mentioning. The two peaks at 1.09 eV and 1.16 eV in the SCS shown in Fig. 6.5 for $\delta = 0$, are relatively sharp. By increasing the spacing between dielectric and metal, the peak at higher energy becomes less pronounced while the magnitude of that at lower energy significantly increases. This is in contrast to the effect shown in Fig. 6.3, where adding Ag on top of the Si cylinder introduced sharp small dips in the ED spectra in the range of 1-1.5 eV which affected the SCS in this range likewise.

6.3 Conclusion

To conclude, a hybrid dielectric–metal nanostructure provides many degrees of freedom to control different spectral features, including pure magnetic modes and anapoles, as well as extremely narrow resonances. The results of the geometrical variations are summarised in Table. 6.1. It can be seen that, depending on the geometry, the ED and MD resonances can be spectrally overlapped or separated and the knowledge gathered in this study could be combined with advanced design approaches to develop systems that support a given set of multipolar characteristics [27, 271]. Overall, hybrid metal-dielectric nanostructures provide both a very high degree of freedom and a good control for engineering resonant systems with tailored spectral characteristics.

7 Conclusion and Outlook

This thesis has aimed at expanding the horizons of fabrication of plasmonic nanostructures by using new materials like AuAg alloys and hybrid metal (Al)-dielectric (Si) meta-atoms. Incorporation of any new materials to demonstrate successful experimental results either requires the development of a new technology or the rigorous modifications and optimization of the existing ones. Moreover, such new processes become widely accepted only if they can be achieved only by a few additional steps to the existing conventional ones rather than in-depth modifications requiring new tools. In this thesis, I have tried to achieve these above mentioned goals by providing recipes for incorporating new materials with only a few additional steps to the existing processes. Incorporation of new materials can unleash new physical phenomena, which - in the case of nanophotonics - emerge as additional spectral features, which have also been investigated and addressed in this thesis. The thesis has been divided into two subparts, the first detailing the work undertaken with AuAg alloys and the second with hybrid metal-dielectric nanoantennas.

In the first part of the thesis we have developed a low-temperature alloying technology (Chapter 3) for fabricating AuAg alloyed nanostructures and metasurfaces by annealing a bilayer of metal at low temperature of 300°C, much below the melting points of the individual metals, without covering the nanostructures with any insulating materials like SiO₂. We were able to maintain after annealing the nanostructures shape (nanorods, nanotriangles, as well as complex nanostructures like 4-rod Fano resonant antennas with a gap of 30 nm in-between the rods). Such well-controlled plasmonic geometries are required to maintain the designed optical response. The recipe enabled fabricating AuAg alloyed nanostructures of varying stoichiometries by merely varying the relative thickness of the Au and Ag in the initial bilayer film. Experimental spectra obtained with 4-rod Fano resonant structures and metal disks demonstrated the successful tuning of the spectra with the varying composition. Furthermore, with this recipe it is possible to fabricate on the same substrate alloyed nanostructures of different stoichiometries with only a single additional annealing step after all the conventional nanofabrication processes are completed. In addition to this, the recipe is versatile and cost effective, as it avoids the need for expensive alloyed targets with the different required compo-

sitions or the need of co-deposition machines. In Chapter 4, we have also used this optimized parameters to fabricate and successfully demonstrate alloyed metasurfaces, metaholograms and Fresnel Zone plates, with meta-atoms of similar nanostructures (nanodisks) but of varying composition ($\text{Au}_{0.2}\text{Ag}_{0.8}$ and $\text{Au}_{0.8}\text{Ag}_{0.2}$). In this case the phase response comes from variation in the material parameters as compared to the variation of geometrical parameters used conventionally in the literature. This demonstrates additional degrees of freedom for the fabrication of sophisticated metasurfaces. Since AuAg alloyed nanostructures are much more stable than Ag nanostructures and have lower losses than pure Au, this work paves the path for successful incorporation of Ag in plasmonic metasurfaces, leading to superior performance in applications like biosensing and SERS. In Chapter 2, I have carried out a detailed literature review showing the advantages and applications of AuAg alloys in nanophotonics.

Interestingly, from that review it became clear that almost all the alloy nanostructures existing in the literature have been fabricated using bottom-up approaches where the control over the nanostructures is lower than that of top-down approaches like e-beam lithography. As an outlook, I believe that the technology proposed in this thesis will contribute positively in overcoming this dearth of top-down processes and pave the way to fabrication of original alloyed plasmonic metasurfaces for optical applications. There are countless nanostructure geometries that have been fabricated in Au and would be interesting to fabricate in AuAg alloy to tune their spectral responses. In Chapter 3, I have briefly touched upon Fano resonances and shown that the response of such a system, which originates from the interplay of different modes in the structure, can be tuned by changing the stoichiometry. It would certainly be interesting to investigate this further, possibly along the lines of electromagnetic induced transparency, since an alloy has less losses than pure Au. Phase gradient metasurfaces have enormous application potential and the utilization of alloys to build them is certainly appealing. For example, by keeping the size of the meta-atom the same and changing the material by using different stoichiometries, one could probably reduce the metasurface unit cell, thus avoiding disturbing effects associated with diffraction orders. Furthermore, this technology can be applied to any type of meta-atom, irrespective of its shape (dots, nanorods or V-shape, for example). Metasurfaces have enormous applications in biosensing and the technology developed in Chapter 3 will allow fabricating plasmonic biosensors of various shapes and sizes for biosensing, not limited to affinity sensing, but also to sense chirality or to enhance Raman signal or infrared absorption. Since AuAg alloys are more stable than Ag and have lower losses than Au, these metasurfaces hold promise of superior performances than the existing ones. Finally, AuAg alloys could also be incorporated in plasmonic heterostructures, e.g. heterodimers, to tailor their response. We have seen in Chapter 2 that core-shell particles that incorporated an alloy had interesting properties, with the technology of Chapter 3, one could translate these properties to nanostructures fabricated with a top-down approach.

In the next part of the thesis, I have demonstrated metasurfaces with hybrid metal-dielectric nanostructures (Chapter 5). The intention of using such hybrid nanostructures was to provide a meta-atom with qualities from best of both worlds: the low losses of the dielectric and the high field enhancement of the metal. For the ease of nanofabrication, I chose a stacked

geometry, where an Al disk was placed on top of Si cylinder separated by a SiO₂ spacer. The choice of Al and Si made this nanoantenna also CMOS compatible. This hybrid nanoantenna had a spectrum with several features arising from higher order multipoles, like quadrupoles, in addition to electric and magnetic dipoles. These quadrupoles and magnetic dipoles arose from the Si cylinder, while the metal disk only contributed electric dipoles. Since the hybrid geometry consisted of two different materials, I did a multipolar analysis using vector spherical harmonics to study how the multipoles from the Si cylinder interact and hybridize with that of the Al metal disk to produce the resultant multipoles of the hybrid nanoantenna. We continued to the next step where I fabricated this nanoantenna using e-beam lithography, liftoff and dry etching of the Si and SiO₂ using deep reactive ion etching. During fabrication, Al acted as a hard mask to etch Si and SiO₂ thus avoided the need to use another etching masks, thus simplifying the fabrication process significantly. These nanoantennas were then used for bulk refractive index sensing of glucose with a moderate sensitivity of 208 nm/RIU in the wavelength range of 1106 to 1129 nm. In order to increase the sensitivity, I underetched the SiO₂ spacer of the stacked nanoantenna using HF vapour phase, to increase the interaction of the analyte with the electric field. This resulted in a moderate sensitivity increase to 245 nm/RIU in the wavelength range between 1232 and 1344 nm. During this work the emergence of several spectral features, a phenomena unseen in plasmonic nanostructures, caught my attention. To understand in greater detail how these features vary with the geometrical dimensions, especially how the dielectric and metallic parts couple together, we decided to undertake a systematic analysis of the stacked hybrid nanoantenna geometry. Chapter 6 is devoted to this study, where I started by varying the height and radius of the Si disk followed by addition of metal on top of it. In this study we used Ag as a metal, since it has low losses. The addition of a few nm of Ag led to the appearance of several small and sharp dips within the electric dipole response and, consequently, in the scattering spectra. These features provide the opportunity to manipulate the resonance profile, as compared to only red-shifting of resonances when the radius and the height of the cylinder are varied. Moreover, as I increased the height of the metal disk, very sharp peaks emerged in the spectrum for disk height of 45 and 60 nm. I continued the analysis, by varying the radius of the metal disk on the Si cylinder and a very sharp spectral feature emerged for the metal disk of radius 195 nm. Such features are ideal for sensing since they provide higher figure of merit. It was also noticed that variation of the metal disk radius modified the magnetic dipole response in the range of 1.08-1.35 eV, whereas addition of the metal affected the electric dipole response more in the range of 0.1-1.34 eV. Finally the spacing in between the Si cylinder and Ag disk was varied in order to understand the interaction between them. Variation of the spacer modified the magnetic response, but this time at lower energies below 1 eV. In order to facilitate the understanding of our findings we have also provided a table summarising the influence of the different geometrical parameters. This analysis showed that it is possible to obtain a "magnetic light" phenomenon at energies above 1 eV by varying the height of the Ag disk on the Si cylinder, and below 1 eV by varying the spacing between them. Anapole states, a spectral feature seen in dielectrics, was also observed in the hybrid nanoantenna geometry. I believe that this study clearly demonstrates the uniqueness of a hybrid geometry with its multiple spectral features.

Chapter 7. Conclusion and Outlook

As an outlook, I would find extremely interesting to study more complicated hybrid systems that would incorporate in a single structure several periods of dielectric and metal layers. The technology provided in Chapter 5 is perfectly suitable for the fabrication of such structures. The coupling within the different modes in that system could be quite complicated, but one could also investigate them with an effective medium approach as is done in epsilon near zero stratified media. In terms of applications, hybrid nanoantennas are potential candidates for fluorescence enhancement: the strong field provided by the metal can enhance the excitation of fluorescence, while the dielectric part can help that fluorescence radiate well. The undercut geometry shown in Chapter 5, has promising potential for surface sensing, thanks to higher interaction of the adsorbed molecule with the analyte. Moreover, in Chapter 6, it has been shown that it is possible to obtain very sharp resonances above 1 eV. This knowledge along with the technology developed in Chapter 5 can also be used for demonstration of sensors with extremely high figure of merit. Finally, the know-how of the existing higher order multipoles in a hybrid geometry, shown in Chapter 6, can be used to engineer an optical beam, or - conversely - azimuthally or radially polarized light can be applied to control which multipoles are excited in the structure and spectrally tune specific features.

I believe that the technologies developed in this thesis for fabricating AuAg alloyed nanostructures and hybrid metal-dielectric nanoantennas will provide the basis of many more future developments for nanostructures and metasurfaces with new optical properties.

Bibliography

- [1] B. Abasahl, C. Santschi, and O. J. F. Martin. Quantitative extraction of equivalent lumped circuit elements for complex plasmonic nanostructures. *ACS Photonics*, 1(5):403–407, 2014.
- [2] K. Achouri, A. Kiselev, and O. J. F. Martin. Multipolar origin of electromagnetic transverse force resulting from two-wave interference. *Phys. Rev. B*, 102:085107, Aug 2020.
- [3] R. Adato and H. Altug. In-situ ultra-sensitive infrared absorption spectroscopy of biomolecule interactions in real time with plasmonic nanoantennas. *Nature communications*, 4:2154, 07 2013.
- [4] O. Adegoke, M. Morita, T. Kato, M. Ito, T. Suzuki, and E. Y. Park. Localized surface plasmon resonance-mediated fluorescence signals in plasmonic nanoparticle-quantum dot hybrids for ultrasensitive zika virus rna detection via hairpin hybridization assays. *Biosensors and Bioelectronics*, 94:513–522, 2017.
- [5] H. B. Ahmed, M. A. Attia, F. M. S. E. El-Dars, and H. E. Emam. Hydroxyethyl cellulose for spontaneous synthesis of antipathogenic nanostructures: (ag & au) nanoparticles versus ag-au nano-alloy. *International journal of biological macromolecules*, 128:214–229, 2019.
- [6] A. Ajayan, V. Madhavan, S. Chandran, and P. Raveendran. A simple anti-solvent method for the controlled deposition of metal and alloy nanoparticles. *New Journal of Chemistry*, 42(14):11979–11983, 2018.
- [7] M. A. Al-Azawi, N. Bidin, M. Bououdina, and S. M. Mohammad. Preparation of gold and gold–silver alloy nanoparticles for enhancement of plasmonic dye-sensitized solar cells performance. *Solar Energy*, 126:93–104, 2016.
- [8] R. Alaei, R. Filter, D. Lehr, F. Lederer, and C. Rockstuhl. A generalized kerker condition for highly directive nanoantennas. *Opt. Lett.*, 40(11):2645–2648, Jun 2015.
- [9] R. Alaei, C. Rockstuhl, and I. Fernandez-Corbaton. Exact multipolar decompositions with applications in nanophotonics. *Advanced Optical Materials*, 7(1):1800783, 2019.
- [10] M. J. Alam and M. Tsuji. Effects of gas bubbling for shape, size, and composition changes in au–ag bimetallic nanoparticles including polygonal au seeds under oil-bath heating at 150 °c. *CrystEngComm*, 13(21):6499–6506, 2011.

Bibliography

- [11] W. Albrecht, J. E. S. van der Hoeven, T.-S. Deng, P. E. de Jongh, and A. van Blaaderen. Fully alloyed metal nanorods with highly tunable properties. *Nanoscale*, 9(8):2845–2851, 2017.
- [12] M. Amoli-Diva, A. Anvari, and R. Sadighi-Bonabi. Synthesis of magneto-plasmonic Au-Ag nps-decorated tio₂-modified fe₃o₄ nanocomposite with enhanced laser/solar-driven photocatalytic activity for degradation of dye pollutant in textile wastewater. *Ceramics International*, 45(14):17837–17846, 2019.
- [13] H. An, M. Li, R. Liu, Z. Gao, and Z. Yin. Design of Ag_xAu_{1-x} alloy/ZnIn₂S₄ system with tunable spectral response and schottky barrier height for visible-light-driven hydrogen evolution. *Chemical Engineering Journal*, 382:122953, 2020.
- [14] J. Ando, A. Nakamura, M. Yamamoto, C. Song, K. Murata, and R. Iino. Multicolor high-speed tracking of single biomolecules with silver, gold, and silver–gold alloy nanoparticles. *ACS Photonics*, 6(11):2870–2883, 2019.
- [15] B. Ankudze and T. T. Pakkanen. Gold nanoparticle decorated Au-Ag alloy tubes: A bifunctional substrate for label-free and in situ surface-enhanced raman scattering based reaction monitoring. *Applied Surface Science*, 453:341–349, 2018.
- [16] M. D. Argyle and C. H. Bartholomew. Heterogeneous catalyst deactivation and regeneration: A review. *Catalysts*, 5(1):145–269, 2015.
- [17] M. M. P. Arnob, F. Zhao, J. Li, and W.-C. Shih. Ebl-based fabrication and different modeling approaches for nanoporous gold nanodisks. *ACS Photonics*, 4(8):1870–1878, 2017.
- [18] Y. Bai, C. Gao, and Y. Yin. Fully alloyed ag/au nanorods with tunable surface plasmon resonance and high chemical stability. *Nanoscale*, 9(39):14875–14880, 2017.
- [19] A. Bansal and S. S. Verma. Optical response of noble metal alloy nanostructures. *Physics Letters A*, 379(3):163–169, 2015.
- [20] O. Bar-Elli, E. Grinvald, N. Meir, L. Neeman, and D. Oron. Enhanced third-harmonic generation from a metal/semiconductor core/shell hybrid nanostructure. *ACS Nano*, 9(8):8064–8069, 2015. PMID: 26197215.
- [21] W. L. Barnes, A. Dereux, and T. W. Ebbesen. Surface plasmon subwavelength optics. *Nature*, 424:824, 2003.
- [22] W. Bente, N. Nilius, N. Ernst, and H. J. Freund. Photon emission spectroscopy of single oxide-supported ag-au alloy clusters. *Physical Review B*, 72(4):045403, 2005.
- [23] L. V. Besteiro and A. O. Govorov. Amplified generation of hot electrons and quantum surface effects in nanoparticle dimers with plasmonic hot spots. *The Journal of Physical Chemistry C*, 120(34):19329–19339, 2016.

- [24] L. V. Besteiro, X.-T. Kong, Z. Wang, G. Hartland, and A. O. Govorov. Understanding hot-electron generation and plasmon relaxation in metal nanocrystals: Quantum and classical mechanisms. *ACS Photonics*, 4(11):2759–2781, 2017.
- [25] H. T. Beyene, V. S. K. Chakravadhanula, C. Hanisch, M. Elbahri, T. Strunskus, V. Zaporojtchenko, L. Kienle, and F. Faupel. Preparation and plasmonic properties of polymer-based composites containing ag–au alloy nanoparticles produced by vapor phase co-deposition. *Journal of Materials Science*, 45(21):5865–5871, 2010.
- [26] M. G. Blaber, M. D. Arnold, and M. J. Ford. A review of the optical properties of alloys and intermetallics for plasmonics. *Journal of Physics: Condensed Matter*, 22(14):143201, 2010.
- [27] A.-P. Blanchard-Dionne and O. J. F. Martin. Teaching optics to a machine learning network. *Opt. Lett.*, 45(10):2922–2925, May 2020.
- [28] N. Blommaerts, H. Vanrompay, S. Nuti, S. Lenaerts, S. Bals, and S. W. Verbruggen. Unraveling structural information of turkevich synthesized plasmonic gold–silver bimetallic nanoparticles. *Small*, 15(42):1902791, 2019.
- [29] C. Boerigter, R. Campana, M. Morabito, and S. Linic. Evidence and implications of direct charge excitation as the dominant mechanism in plasmon-mediated photocatalysis. *Nature communications*, 7, 2016.
- [30] N. Bontempi, K. E. Chong, H. W. Orton, I. Staude, D.-Y. Choi, I. Alessandri, Y. S. Kivshar, and D. N. Neshev. Highly sensitive biosensors based on all-dielectric nanoresonators. *Nanoscale*, 9(15):4972–4980, 2017.
- [31] B. Brian, B. Sepúlveda, Y. Alaverdyan, L. M. Lechuga, and M. Käll. Sensitivity enhancement of nanoplasmonic sensors in low refractive index substrates. *Optics Express*, 17(3):2015–2023, Feb 2009.
- [32] R. Britto Hurtado, M. Cortez-Valadez, H. Arizpe-Chávez, N. S. Flores-Lopez, G. Calderón-Ayala, and M. Flores-Acosta. Random alloy of Au-Ag bimetallic nanoparticles at room temperature—facile synthesis and vibrational properties. *Gold Bulletin*, 50(2):85–92, 2017.
- [33] M. L. Brongersma, N. J. Halas, and P. Nordlander. Plasmon-induced hot carrier science and technology. *Nature nanotechnology*, 10(1):25–34, 2015.
- [34] M. L. Brongersma, N. J. Halas, and P. Nordlander. Plasmon-induced hot carrier science and technology. *Nature Nanotechnology*, 10(1):25–34, 2015.
- [35] L. V. Brown, H. Sobhani, J. B. Lassiter, P. Nordlander, and N. J. Halas. Heterodimers: Plasmonic properties of mismatched nanoparticle pairs. *ACS Nano*, 4(2):819–832, 2010.
- [36] S. Burgener, S. Luo, R. McLean, T. E. Miller, and T. J. Erb. A roadmap towards integrated catalytic systems of the future. *Nature Catalysis*, 3(3):186–192, 2020.

- [37] L. M. Burko. Multipole structure and coordinate systems. *European Journal of Physics*, 28(3):593–602, may 2007.
- [38] M. Cao, Q. Liu, M. Chen, L. Chen, D. Yang, H. Hu, L. He, G. Zhang, and Q. Zhang. Fully alloying AuAg nanorods in a photothermal nano-oven: Superior plasmonic property and enhanced chemical stability. *ACS Omega*, 3(12):18623–18629, 2018.
- [39] P. Cao Van, S. Surabhi, V. D. Quoc, J. W. Lee, C. C. Tae, R. Kuchi, and J.-R. Jeong. Broad-band tunable plasmonic substrate using self-assembled gold–silver alloy nanoparticles. *Current Applied Physics*, 19(11):1245–1251, 2019.
- [40] E. Chaffin, R. T. O’Connor, J. Barr, X. Huang, and Y. Wang. Dependence of SERS enhancement on the chemical composition and structure of ag/au hybrid nanoparticles. *The Journal of Chemical Physics*, 145(5):054706, 2016.
- [41] S. Chattopadhyay, S. Bysakh, P. M. Mishra, and G. De. In situ synthesis of mesoporous tio₂ nanofibers surface-decorated with AuAg alloy nanoparticles anchored by heterojunction exhibiting enhanced solar active photocatalysis. *Langmuir*, 35(44):14364–14375, 2019.
- [42] D. Chen, Z. Song, F. Chen, J. Huang, J. Wei, and Y. Zhao. Simply controllable growth of single crystal plasmonic au–ag nano-spines with anisotropic multiple sites for highly sensitive and uniform surface-enhanced raman scattering sensing. *RSC Advances*, 6(70):66056–66065, 2016.
- [43] F. Chen, Q. Yang, C. Niu, X. Li, C. Zhang, and G. Zeng. Plasmonic photocatalyst ag@agcl/znsn(oh)₆: synthesis, characterization and enhanced visible-light photocatalytic activity in the decomposition of dyes and phenol. *RSC Advances*, 5(78):63152–63164, 2015.
- [44] H.-C. Chen, S.-W. Chou, W.-H. Tseng, I. W. P. Chen, C.-C. Liu, C. Liu, C.-L. Liu, C.-h. Chen, C.-I. Wu, and P.-T. Chou. Large AuAg alloy nanoparticles synthesized in organic media using a one-pot reaction: Their applications for high-performance bulk heterojunction solar cells. *Advanced Functional Materials*, 22(19):3975–3984, 2012.
- [45] J. Chen, F. Jiang, and Y. Yin. Manipulation of interfacial diffusion for controlling nanoscale transformation. *Accounts of Chemical Research*, 54(5):1168–1177, 2021. PMID: 33440942.
- [46] P. Chen, Z. Yin, X. Huang, S. Wu, B. Liedberg, and H. Zhang. Assembly of graphene oxide and au_{0.7}ag_{0.3} alloy nanoparticles on sio₂: A new raman substrate with ultrahigh signal-to-background ratio. *The Journal of Physical Chemistry C*, 115(49):24080–24084, 2011.
- [47] Y. Chen. Nanofabrication by electron beam lithography and its applications: A review. *Microelectronic Engineering*, 135:57–72, 2015.

-
- [48] P. Christopher and M. Moskovits. Hot charge carrier transmission from plasmonic nanostructures. *Annual Review of Physical Chemistry*, 68(1):379–398, 2017. PMID: 28301756.
- [49] T. Claes, J. G. Molera, K. D. Vos, E. Schacht, R. Baets, and P. Bienstman. Label-free biosensing with a slot-waveguide-based ring resonator in silicon on insulator. *IEEE Photonics Journal*, 1(3):197–204, 2009.
- [50] C. Clavero. Plasmon-induced hot-electron generation at nanoparticle/metal-oxide interfaces for photovoltaic and photocatalytic devices. *Nature Photonics*, 8(2):95–103, 2014.
- [51] C. M. Cobley and Y. Xia. Engineering the properties of metal nanostructures via galvanic replacement reactions. *Materials science & engineering. R, Reports : a review journal*, 70(3-6):44–62, 2010.
- [52] M. B. Cortie and A. M. McDonagh. Synthesis and optical properties of hybrid and alloy plasmonic nanoparticles. *Chemical Reviews*, 111(6):3713–3735, 2011.
- [53] J. Crespo, A. Falqui, J. García-Barrasa, J. M. López-de Luzuriaga, M. Monge, M. E. Olmos, M. Rodríguez-Castillo, M. Sestu, and K. Soulantica. Synthesis and plasmonic properties of monodisperse au–ag alloy nanoparticles of different compositions from a single-source organometallic precursor. *Journal of Materials Chemistry C*, 2(16):2975–2984, 2014.
- [54] C. Cretu and E. Van der Lingen. Coloured gold alloys. *Gold Bulletin*, 32:115–126, 1999.
- [55] G. Dabos, A. Manolis, D. Tsiokos, D. Ketzaki, E. Chatzianagnostou, L. Markey, D. Rusakov, J.-C. Weeber, A. Dereux, A.-L. Giesecke, C. Porschatis, T. Wahlbrink, B. Chmielak, and N. Pleros. Aluminum plasmonic waveguides co-integrated with si₃n₄ photonics using cmos processes. *Scientific Reports*, 8(1):13380, 2018.
- [56] D. Darvill, A. Centeno, and F. Xie. Plasmonic fluorescence enhancement by metal nanostructures: shaping the future of bionanotechnology. *Phys. Chem. Chem. Phys.*, 15:15709–15726, 2013.
- [57] T. Das, P. P. Iyer, R. A. DeCrescent, and J. A. Schuller. Beam engineering for selective and enhanced coupling to multipolar resonances. *Phys. Rev. B*, 92:241110, Dec 2015.
- [58] B. Dastmalchi, P. Tassin, T. Koschny, and C. M. Soukoulis. A new perspective on plasmonics: Confinement and propagation length of surface plasmons for different materials and geometries. *Advanced Optical Materials*, 4(1):177–184, 2016.
- [59] W. P. Davey. Precision measurements of the lattice constants of twelve common metals. *Physical Review*, 25(6):753–761, 1925.

Bibliography

- [60] G. De, S. Medda, S. De, and S. Pal. Metal nanoparticle doped coloured coatings on glasses and plastics through tuning of surface plasmon band position. *Bulletin of Materials Science*, 31:479–485, 2008.
- [61] S. Debela, B. Mesfin, and T. Senbeta. Surface plasmon resonances in ellipsoidal bimetallic nanoparticles. *Photonics and Nanostructures - Fundamentals and Applications*, 33:48–54, 2019.
- [62] M. Decker, I. Staude, M. Falkner, J. Dominguez, D. N. Neshev, I. Brener, T. Pertsch, and Y. S. Kivshar. High-efficiency dielectric huygens’ surfaces. *Advanced Optical Materials*, 3(6):813–820, 2015.
- [63] Z.-L. Deng and G. Li. Metasurface optical holography. *Materials Today Physics*, 3:16–32, 2017.
- [64] A. Devilez, B. Stout, and N. Bonod. Compact metallo-dielectric optical antenna for ultra directional and enhanced radiative emission. *ACS Nano*, 4(6):3390–3396, 2010.
- [65] D. Ding, Q. Fan, K. Liu, and S. Ding. Au/ag alloy nanostructure with built-in hotspots fabricated by galvanic-replacement-assisted growth on agi for surface-enhanced raman spectroscopy. *Journal of Alloys and Compounds*, 809:151677, 2019.
- [66] F. Ding, A. Pors, and S. I. Bozhevolnyi. Gradient metasurfaces: a review of fundamentals and applications. *Reports on Progress in Physics*, 81(2):026401, 2017.
- [67] Y. Ding and M. Chen. Nanoporous metals for catalytic and optical applications. *MRS Bulletin*, 34(8):569–576, 2009.
- [68] A. Dmitriev, C. Hagglund, S. Chen, H. Fredriksson, T. Pakizeh, M. Kall, and D. S. Sutherland. Enhanced nanoplasmonic optical sensors with reduced substrate effect. *Nano Letters*, 8(11):3893–3898, 2008.
- [69] Y. Dubi and Y. Sivan. “hot” electrons in metallic nanostructures—non-thermal carriers or heating? *Light: Science & Applications*, 8(1):89, 2019.
- [70] J. S. DuChene, B. C. Sweeny, A. C. Johnston-Peck, D. Su, E. A. Stach, and W. D. Wei. Prolonged hot electron dynamics in plasmonic-metal/semiconductor heterostructures with implications for solar photocatalysis. *Angewandte Chemie International Edition*, 53(30):7887–7891, 2014.
- [71] N. E.A.K, D. S, V. Narayanan, and S. A. Chitosan stabilized ag-au nanoalloy for colorimetric sensing and 5-fluorouracil delivery. *International Journal of Biological Macromolecules*, 95:862–872, 2017.
- [72] Y. Ekinici, A. Christ, M. Agio, O. J. F. Martin, H. H. Solak, and J. F. Löffler. Electric and magnetic resonances in arrays of coupled gold nanoparticle in-tandem pairs. *Opt. Express*, 16(17):13287–13295, Aug 2008.

-
- [73] J. A. Elegbede, A. Lateef, M. A. Azeez, T. B. Asafa, T. A. Yekeen, I. C. Oladipo, A. S. Hakeem, L. S. Beukes, and E. B. Gueguim-Kana. Silver-gold alloy nanoparticles biofabricated by fungal xylanases exhibited potent biomedical and catalytic activities. *Biotechnology Progress*, 35(5):e2829, 2019.
- [74] H. E. Emam. Arabic gum as bio-synthesizer for ag–au bimetallic nanocomposite using seed-mediated growth technique and its biological efficacy. *Journal of Polymers and the Environment*, 27(1):210–223, 2019.
- [75] E. Engel, A. Michiardi, M. Navarro, D. Lacroix, and J. A. Planell. Nanotechnology in regenerative medicine: the materials side. *Trends in Biotechnology*, 26(1):39–47, 2008.
- [76] D. Etezadi, J. B. Warner, H. A. Lashuel, and H. Altug. Real-time in situ secondary structure analysis of protein monolayer with mid-infrared plasmonic nanoantennas. *ACS Sensors*, 3(6):1109–1117, 2018.
- [77] A. B. Evlyukhin and S. I. Bozhevolnyi. Resonant unidirectional and elastic scattering of surface plasmon polaritons by high refractive index dielectric nanoparticles. *Phys. Rev. B*, 92:245419, Dec 2015.
- [78] A. B. Evlyukhin, C. Reinhardt, and B. N. Chichkov. Multipole light scattering by non-spherical nanoparticles in the discrete dipole approximation. *Phys. Rev. B*, 84:235429, Dec 2011.
- [79] S. C. Fain and J. M. McDavid. Work-function variation with alloy composition: Ag–au. *Physical Review B*, 9(12):5099–5107, 1974.
- [80] M. Fan, F.-J. Lai, H.-L. Chou, W.-T. Lu, B.-J. Hwang, and A. G. Brolo. Surface-enhanced raman scattering (sers) from au:ag bimetallic nanoparticles: the effect of the molecular probe. *Chemical Science*, 4(1):509–515, 2013.
- [81] Q. Fan, K. Liu, J. Feng, F. Wang, Z. Liu, M. Liu, Y. Yin, and C. Gao. Building high-density au–ag islands on au nanocrystals by partial surface passivation. *Advanced Functional Materials*, 28(41):1803199, 2018.
- [82] Y. Fang, Y. Jiao, K. Xiong, R. Ogier, Z.-J. Yang, S. Gao, A. B. Dahlin, and M. Käll. Plasmon enhanced internal photoemission in antenna-spacer-mirror based au/tio₂ nanostructures. *Nano Letters*, 15(6):4059–4065, 2015.
- [83] M. Farokhnezhad and M. Esmaeilzadeh. Optical and photothermal properties of graphene coated au–ag hollow nanoshells: A modeling for efficient photothermal therapy. *The Journal of Physical Chemistry C*, 123(47):28907–28918, 2019.
- [84] J. Feng, C. Gao, and Y. Yin. Stabilization of noble metal nanostructures for catalysis and sensing. *Nanoscale*, 10(44):20492–20504, 2018.

Bibliography

- [85] S. Feng, M. Wang, Y. Zhou, P. Li, W. Tu, and Z. Zou. Double-shelled plasmonic ag-tio₂ hollow spheres toward visible light-active photocatalytic conversion of co₂ into solar fuel. *APL Materials*, 3(10):104416, 2015.
- [86] T. Feng, Y. Xu, W. Zhang, and A. E. Miroshnichenko. Ideal magnetic dipole scattering. *Phys. Rev. Lett.*, 118:173901, Apr 2017.
- [87] R. Ferrando, J. Jellinek, and R. L. Johnston. Nanoalloys: From theory to applications of alloy clusters and nanoparticles. *Chemical Reviews*, 108(3):845–910, 2008.
- [88] M. Fichtner. Nanotechnological aspects in materials for hydrogen storage. *Advanced Engineering Materials*, 7(6):443–455, 2005.
- [89] V. Flauraud, G. D. Bernasconi, J. Butet, D. T. L. Alexander, O. J. F. Martin, and J. Brugger. Mode coupling in plasmonic heterodimers probed with electron energy loss spectroscopy. *ACS Nano*, 11(4):3485–3495, 2017.
- [90] B. Gallinet, J. Butet, and O. J. F. Martin. Numerical methods for nanophotonics: standard problems and future challenges. *Laser & Photonics Reviews*, 9(6):577–603, 2015.
- [91] B. Gallinet, A. M. Kern, and O. J. F. Martin. Accurate and versatile modeling of electromagnetic scattering on periodic nanostructures with a surface integral approach. *Journal of the Optical Society of America A*, 27(10):2261–2271, 2010.
- [92] Y. X. Gan, Y. Zhang, and J. B. Gan. Nanoporous metals processed by dealloying and their applications. *AIMS Materials Science*, 5(6):1141–1183, 2018.
- [93] C. Gao, Y. Hu, M. Wang, M. Chi, and Y. Yin. Fully alloyed ag/au nanospheres: Combining the plasmonic property of ag with the stability of au. *Journal of the American Chemical Society*, 136(20):7474–7479, 2014.
- [94] L. Gao, F. Lemarchand, and M. Lequime. Refractive index determination of sio₂ layer in the uv/vis/nir range: spectrophotometric reverse engineering on single and bi-layer designs. *Journal of the European Optical Society - Rapid publications; Vol 8 (2013)*, 2013.
- [95] Y. Gao, Y. Feng, L. Zhou, L. Petti, Z. Wang, J. Zhou, S. Xie, J. Chen, and Y. Qing. Ultrasensitive sers-based immunoassay of tumor marker in serum using au–ag alloy nanoparticles and ag/agbr hybrid nanostructure. *Nano*, 13(01):1850001, 2017.
- [96] A. Garcia-Leis, A. Torreggiani, J. V. Garcia-Ramos, and S. Sanchez-Cortes. Hollow au/ag nanostars displaying broad plasmonic resonance and high surface-enhanced raman sensitivity. *Nanoscale*, 7(32):13629–13637, 2015.
- [97] A. Genç, J. Patarroyo, J. Sancho-Parramon, R. Arenal, M. Duchamp, E. E. Gonzalez, L. Henrard, N. G. Bastús, R. E. Dunin-Borkowski, V. F. Puentes, and J. Arbiol. Tuning the plasmonic response up: Hollow cuboid metal nanostructures. *ACS Photonics*, 3(5):770–779, 2016.

- [98] H. Gholamali, A. Shafiekhani, E. Darabi, and S. M. Elahi. Ag/au alloy lspr engineering by co-deposition of rf-sputtering and rf-pecvd. *Applied Organometallic Chemistry*, 32(5):e4316, 2018.
- [99] R. Ghosh Chaudhuri and S. Paria. Core/shell nanoparticles: Classes, properties, synthesis mechanisms, characterization, and applications. *Chemical Reviews*, 112(4):2373–2433, 2012.
- [100] V. F. Gili, L. Ghirardini, D. Rocco, G. Marino, I. Favero, I. Roland, G. Pellegrini, L. Duò, M. Finazzi, L. Carletti, A. Locatelli, A. Lemaître, D. Neshev, C. De Angelis, G. Leo, and M. Celebrano. Metal–dielectric hybrid nanoantennas for efficient frequency conversion at the anapole mode. *Beilstein Journal of Nanotechnology*, 9:2306–2314, 2018.
- [101] K. D. Gilroy, A. Ruditskiy, H.-C. Peng, D. Qin, and Y. Xia. Bimetallic nanocrystals: Syntheses, properties, and applications. *Chemical Reviews*, 116(18):10414–10472, 2016.
- [102] A. V. Girão, P. C. Pinheiro, M. Ferro, and T. Trindade. Tailoring gold and silver colloidal bimetallic nanoalloys towards sers detection of rhodamine 6g. *RSC Advances*, 7(26):15944–15951, 2017.
- [103] M. A. Gondal, A. A. Adeseda, S. G. Rashid, A. Hameed, M. Aslam, I. M. I. Ismail, U. Baig, M. A. Dastageer, A. R. Al-Arfaj, and A. U. Rehman. Facile synthesis, characterization and photocatalytic performance of Au-Ag alloy nanoparticles dispersed on graphitic carbon nitride under visible light irradiations. *Journal of Molecular Catalysis A: Chemical*, 423:114–125, 2016.
- [104] C. Gong, M. R. S. Dias, G. C. Wessler, J. A. Taillon, L. G. Salamanca-Riba, and M. S. Leite. Near-field optical properties of fully alloyed noble metal nanoparticles. *Advanced Optical Materials*, 5(1):1600568, 2017.
- [105] C. Gong, A. Kaplan, Z. A. Benson, D. R. Baker, J. P. McClure, A. R. Rocha, and M. S. Leite. Band structure engineering by alloying for photonics. *Advanced Optical Materials*, 6(17):1800218, 2018.
- [106] C. Gong and M. S. Leite. Noble metal alloys for plasmonics. *ACS Photonics*, 3(4):507–513, 2016.
- [107] C. M. Gonzalez, Y. Liu, and J. C. Scaiano. Photochemical strategies for the facile synthesis of Gold-Silver Alloy and Core-Shell bimetallic nanoparticles. *The Journal of Physical Chemistry C*, 113(27):11861–11867, 2009.
- [108] J. R. González-Castillo, E. Rodríguez-González, E. Jiménez-Villar, C. L. Cesar, and J. A. Andrade-Arvizu. Assisted laser ablation: silver/gold nanostructures coated with silica. *Applied Nanoscience*, 7(8):597–605, 2017.
- [109] S. Goodnick, A. Korkin, P. Krstic, P. Mascher, J. Preston, and A. Zaslavsky. Semiconductor nanotechnology: novel materials and devices for electronics, photonics and renewable energy applications. *Nanotechnology*, 21(13):130201, 2010.

Bibliography

- [110] R. Gopalakrishnan, B. Loganathan, and K. Raghu. Green synthesis of au–ag bimetallic nanocomposites using silybum marianum seed extract and their application as a catalyst. *RSC Advances*, 5(40):31691–31699, 2015.
- [111] E. Gottlieb, H. Qian, and R. Jin. Atomic-level alloying and de-alloying in doped gold nanoparticles. *Chemistry (Weinheim an der Bergstrasse, Germany)*, 19(13):4238–4243, 2013.
- [112] A. O. Govorov, H. Zhang, and Y. K. Gun’ko. Theory of photoinjection of hot plasmonic carriers from metal nanostructures into semiconductors and surface molecules. *The Journal of Physical Chemistry C*, 117(32):16616–16631, 2013.
- [113] D. K. Gramotnev and S. I. Bozhevolnyi. Plasmonics beyond the diffraction limit. *Nature Photonics*, 4(2):83–91, 2010.
- [114] G. Guisbiers, R. Mendoza-Cruz, L. Bazán-Díaz, J. J. Velázquez-Salazar, R. Mendoza-Perez, J. A. Robledo-Torres, J.-L. Rodriguez-Lopez, J. M. Montejano-Carrizales, R. L. Whetten, and M. José-Yacamán. Electrum, the gold–silver alloy, from the bulk scale to the nanoscale: Synthesis, properties, and segregation rules. *ACS Nano*, 10(1):188–198, 2016.
- [115] J. Guo, F. Lu, Y. Zhang, Q. Ma, S. Yang, G. Liu, and W. Cai. Controllable corrosion-assisted fabrication of au–ag alloyed hollow nanocrystals for highly efficient and environmentally-stable - surface enhanced raman scattering (sers) substrates. *Nanotechnology*, 29(45):455604, 2018.
- [116] R. Guo, E. Rusak, I. Staude, J. Dominguez, M. Decker, C. Rockstuhl, I. Brener, D. N. Neshev, and Y. S. Kivshar. Multipolar Coupling in Hybrid Metal Dielectric Metasurfaces. *ACS Photonics*, 3(3):349–353, 2016.
- [117] T. Guo and Y. Tan. Formation of one-dimensional ag–au solid solution colloids with au nanorods as seeds, their alloying mechanisms, and surface plasmon resonances. *Nanoscale*, 5(2):561–569, 2013.
- [118] C. Han, X. Yang, G. Gao, J. Wang, H. Lu, J. Liu, M. Tong, and X. Liang. Selective oxidation of methanol to methyl formate on catalysts of au–ag alloy nanoparticles supported on titania under uv irradiation. *Green Chemistry*, 16(7):3603–3615, 2014.
- [119] Q. Han, C. Zhang, W. Gao, Z. Han, T. Liu, C. Li, Z. Wang, E. He, and H. Zheng. Ag-au alloy nanoparticles: Synthesis and in situ monitoring sers of plasmonic catalysis. *Sensors and Actuators B: Chemical*, 231:609–614, 2016.
- [120] X. Han, K. Liu, and C. Sun. Plasmonics for biosensing. *Materials*, 12:1411, 04 2019.
- [121] K. Hareesh, D. V. Sunitha, S. D. Dhole, V. N. Bhoraskar, D. M. Phase, and J. Williams. One-step gamma radiation aided diffusion of ag-au alloy nanoparticles into polycarbonate and its application towards the reduction of 4-nitrophenol. *Radiation Physics and Chemistry*, 162:126–130, 2019.

- [122] M. R. Hartings and Z. Ahmed. Chemistry from 3d printed objects. *Nature Reviews Chemistry*, 3(5):305–314, 2019.
- [123] A. Hatef, B. Darvish, A. Dagallier, Y. R. Davletshin, W. Johnston, J. C. Kumaradas, D. Rioux, and M. Meunier. Analysis of photoacoustic response from gold-silver alloy nanoparticles irradiated by short pulsed laser in water. *Journal of Physical Chemistry C*, 119(42):24075–24080, 2015.
- [124] G. Hegde, M. Povolotskyi, T. Kubis, T. Boykin, and G. Klimeck. An environment-dependent semi-empirical tight binding model suitable for electron transport in bulk metals, metal alloys, metallic interfaces, and metallic nanostructures. i. model and validation. *Journal of Applied Physics*, 115(12):123703, 2014.
- [125] M. Hentschel, B. Metzger, B. Knabe, K. Buse, and H. Giessen. Linear and nonlinear optical properties of hybrid metallic–dielectric plasmonic nanoantennas. *Beilstein Journal of Nanotechnology*, 7:111–120, 2016.
- [126] J. Ho, Y. H. Fu, Z. Dong, R. Paniagua-Dominguez, E. H. H. Koay, Y. F. Yu, V. Valuckas, A. I. Kuznetsov, and J. K. W. Yang. Highly directive hybrid metal–dielectric yagi-uda nanoantennas. *ACS Nano*, 12(8):8616–8624, 2018.
- [127] Y. Z. Ho, B. H. Cheng, W.-L. Hsu, C.-M. Wang, and D. P. Tsai. Anomalous reflection from metasurfaces with gradient phase distribution below 2π . *Applied Physics Express*, 9(7):072502, 2016.
- [128] J. H. Hodak, A. Henglein, M. Giersig, and G. V. Hartland. Laser-induced inter-diffusion in AuAg core-shell nanoparticles. *The Journal of Physical Chemistry B*, 104(49):11708–11718, 2000.
- [129] J. Homola, S. S. Yee, and G. Gauglitz. Surface plasmon resonance sensors: review. *Sensors and Actuators B: Chemical*, 54(1):3–15, 1999.
- [130] H.-G. Hu, M. Yang, P. Yue, Y.-T. Bai, W.-J. Wang, and S.-D. Liu. Second-harmonic generation with metal/dielectric/metal hybridized nanoantennas: enhanced efficiency, reduced mode volume and ideal magnetic/electric dipole scattering. *Journal of Physics D: Applied Physics*, 53(21):215101, mar 2020.
- [131] J.-S. Huang, V. Callegari, P. Geisler, C. Brünig, J. Kern, J. C. Prangsma, X. Wu, T. Feichtner, J. Ziegler, P. Weinmann, M. Kamp, A. Forchel, P. Biagioni, U. Sennhauser, and B. Hecht. Atomically flat single-crystalline gold nanostructures for plasmonic nanocircuitry. *Nature Communications*, 1:150, 2010.
- [132] Y.-W. Huang, W. T. Chen, W.-Y. Tsai, P. C. Wu, C.-M. Wang, G. Sun, and D. P. Tsai. Aluminum plasmonic multicolor meta-hologram. *Nano Letters*, 15(5):3122–3127, 2015.
- [133] C. Huck, A. Toma, F. Neubrech, M. Chirumamilla, J. Vogt, F. De Angelis, and A. Pucci. Gold nanoantennas on a pedestal for plasmonic enhancement in the infrared. *ACS Photonics*, 2(4):497–505, 2015.

Bibliography

- [134] C. S. H. Hwang, M.-S. Ahn, Y. Lee, T. Chung, and K.-H. Jeong. Ag/au alloyed nanoislands for wafer-level plasmonic color filter arrays. *Scientific Reports*, 9(1):9082, 2019.
- [135] M. Iranifam. Chemiluminescence reactions enhanced by silver nanoparticles and silver alloy nanoparticles: Applications in analytical chemistry. *TrAC Trends in Analytical Chemistry*, 82:126–142, 2016.
- [136] H. Jang and D.-H. Min. Spherically-clustered porous au–ag alloy nanoparticle prepared by partial inhibition of galvanic replacement and its application for efficient multimodal therapy. *ACS Nano*, 9(3):2696–2703, 2015.
- [137] T. Ji, H. Zhang, N. Han, W. Wang, B. Wu, G. Li, M. Fan, Z. Li, Y. Hao, F. Zhu, Y. Wu, and Y. Cui. Plasmonic nanoprism enhanced quasi-2d ruddlesden–popper layered perovskite photodetectors. *Journal of Materials Chemistry C*, 8(3):1110–1117, 2020.
- [138] A. John-Herpin, A. Tittl, and H. Altug. Quantifying the limits of detection of surface-enhanced infrared spectroscopy with grating order-coupled nanogap antennas. *ACS Photonics*, 5(10):4117–4124, 2018.
- [139] P. B. Johnson and R. W. Christy. Optical constants of the noble metals. *Phys. Rev. B*, 6:4370–4379, Dec 1972.
- [140] D. Joseph, C. H. Kwak, Y. S. Huh, and Y.-K. Han. Synthesis of AuAg@Ag core@shell hollow cubic nanostructures as SERS substrates for attomolar chemical sensing. *Sensors and Actuators B: Chemical*, 281:471–477, 2019.
- [141] S. Kadkhodazadeh, F. A. A. Nugroho, C. Langhammer, M. Beleggia, and J. B. Wagner. Optical property–composition correlation in noble metal alloy nanoparticles studied with eels. *ACS Photonics*, 6(3):779–786, 2019.
- [142] M. Kahraman, E. R. Mullen, A. Korkmaz, and S. Wachsmann-Hogiu. Fundamentals and applications of SERS-based bioanalytical sensing. *Nanophotonics*, 6(5):831–852, 2017.
- [143] M. J. Kale and P. Christopher. Plasmons at the interface. *Science*, 349(6248):587–588, 2015.
- [144] M. Kamiko, W.-S. Kim, J.-H. Ha, and J.-G. Ha. Fabrication of self-organized fcc-AuAg(001) alloy nanodots on MgO(001) substrates. *Japanese Journal of Applied Physics*, 58(SD):SDDF01, 2019.
- [145] M. Kang, M.-S. Ahn, Y. Lee, and K.-H. Jeong. Bioplasmonic alloyed nanoislands using dewetting of bilayer thin films. *ACS Applied Materials & Interfaces*, 9(42):37154–37159, 2017.
- [146] P. Kapoor, A. Kumar, M. Sharma, J. Kumar, A. Kumar, and P. K. Ahluwalia. Alloyed monolayers of cu, ag, au and pt in hexagonal phase: A comprehensive first principles study. *Materials Science and Engineering: B*, 228:84–90, 2018.

- [147] R. Kavitha and S. G. Kumar. Review on bimetallic-deposited tio₂: preparation methods, charge carrier transfer pathways and photocatalytic applications. *Chemical Papers*, 74(3):717–756, 2020.
- [148] A. M. Kern and O. J. F. Martin. Surface integral formulation for 3d simulations of plasmonic and high permittivity nanostructures. *J. Opt. Soc. Am. A*, 26(4):732–740, 2009.
- [149] A. M. Kern and O. J. F. Martin. Surface integral formulation for 3d simulations of plasmonic and high permittivity nanostructures. *J. Opt. Soc. Am. A*, 26(4):732–740, Apr 2009.
- [150] A. M. Kern and O. J. F. Martin. Pitfalls in the determination of optical cross sections from surface integral equation simulations. *IEEE Transactions on Antennas and Propagation*, 58(6):2158–2161, June 2010.
- [151] J. Khurgin. Replacing noble metals with alternative materials in plasmonics and meta-materials: how good an idea? *Philosophical Transactions of The Royal Society A Mathematical Physical and Engineering Sciences*, 375, 08 2016.
- [152] H. J. Kim, S. H. Lee, A. A. Upadhye, I. Ro, M. I. Tejedor-Tejedor, M. A. Anderson, W. B. Kim, and G. W. Huber. Plasmon-enhanced photoelectrochemical water splitting with size-controllable gold nanodot arrays. *ACS nano*, 8(10):10756–10765, 2014.
- [153] M. Kim, K. Y. Lee, G. H. Jeong, J. Jang, and S. W. Han. Fabrication of au–ag alloy nanoprisms with enhanced catalytic activity. *Chemistry Letters*, 36(11):1350–1351, 2007.
- [154] M. Kim, M. Lin, J. Son, H. Xu, and J.-M. Nam. Hot-electron-mediated photochemical reactions: Principles, recent advances, and challenges. *Advanced Optical Materials*, 5(15):1700004, 2017.
- [155] W. Kim, K. Park, S. J. Yoo, P. Matteini, B. Hwang, B. Kim, and S. M. Han. Deformation twinning in au₃₀ag₇₀ alloy nanowires under tensile strain. *Journal of Alloys and Compounds*, 816:152586, 2020.
- [156] A. Kiselev, K. Achouri, and O. J. F. Martin. Multipole interplay controls optical forces and ultra-directional scattering. *Opt. Express*, 28(19):27547–27560, Sep 2020.
- [157] A. Kiselev, G. Bernasconi, and O. J. F. Martin. Vector spherical decomposition code and nonlinear scattering data, Dec. 2019.
- [158] A. Kiselev, G. D. Bernasconi, and O. J. F. Martin. Modes interplay and dynamics in the second harmonic generation of plasmonic nanostructures. *Optics Express*, 27(26):38708–38720, 2019.
- [159] M. W. Knight, N. S. King, L. Liu, H. O. Everitt, P. Nordlander, and N. J. Halas. Aluminum for plasmonics. *ACS Nano*, 8(1):834–840, 2013.

Bibliography

- [160] M. W. Knight, H. Sobhani, P. Nordlander, and N. J. Halas. Photodetection with active optical antennas. *Science*, 332(6030):702–704, 2011.
- [161] M. W. Knight, Y. Wang, A. S. Urban, A. Sobhani, B. Y. Zheng, P. Nordlander, and N. J. Halas. Embedding plasmonic nanostructure diodes enhances hot electron emission. *Nano Letters*, 13(4):1687–1692, 2013.
- [162] J. P. Kottmann and O. J. F. Martin. Influence of the cross section and the permittivity on the plasmon-resonance spectrum of silver nanowires. *Applied Physics B*, B73(4):299–304, 2001.
- [163] J. P. Kottmann, O. J. F. Martin, D. R. Smith, and S. Schultz. Dramatic localized electromagnetic enhancement in plasmon resonant nanowires. *Chemical Physics Letters*, 341(1-2):1–6, 2001.
- [164] J. P. Kottmann, O. J. F. Martin, D. R. Smith, and S. Shultz. Field polarization and polarization charge distributions in plasmon resonant nanoparticles. *New Journal of Physics*, 2, 2000.
- [165] A. Krasnok, D. Baranov, H. Li, M.-A. Miri, F. Monticone, and A. Alú. Anomalies in light scattering. *Adv. Opt. Photon.*, 11(4):892–951, Dec 2019.
- [166] Z. O. Králová, A. Oriňák, R. Oriňáková, O. Petruš, J. Macko, J. Radoňák, L. S. Lakyová, Z. Jurašková, R. M. Smith, M. Strečková, and K. Koval. Electrochemically deposited silver detection substrate for surface-enhanced Raman spectroscopy cancer diagnostics. *Journal of Biomedical Optics*, 23(7):1–11, 2018.
- [167] R. Kuladeep, L. Jyothi, K. S. Alee, K. L. N. Deepak, and D. N. Rao. Laser-assisted synthesis of Au-Ag alloy nanoparticles with tunable surface plasmon resonance frequency. *Optical Materials Express*, 2(2):161–172, 2012.
- [168] D. Kumar, S. Bala, H. Wadhwa, G. Kandhol, S. Mahendia, F. Chand, and S. Kumar. Tuning of lspr of gold-silver alloy nanoparticles with their composition. *AIP Conference Proceedings*, 2093(1):020048, 2019.
- [169] P. V. Kumar, T. P. Rossi, D. Marti-Dafcik, D. Reichmuth, M. Kuisma, P. Erhart, M. J. Puska, and D. J. Norris. Plasmon-induced direct hot-carrier transfer at metal–acceptor interfaces. *ACS Nano*, 13(3):3188–3195, 2019.
- [170] S. Kumar, G. C. Yadav, G. Sharma, and V. Singh. Study of surface plasmon resonance sensors based on silver–gold nanostructure alloy film coated tapered optical fibers. *Applied Physics A*, 124(10):695, 2018.
- [171] A. Kuznetsov, A. Miroshnichenko, Y. H. Fu, J. Zhang, and B. Luk’yanchuk. Magnetic light. *Scientific reports*, 2:492, 07 2012.
- [172] A. I. Kuznetsov, A. E. Miroshnichenko, M. L. Brongersma, Y. S. Kivshar, and B. Luk’yanchuk. Optically resonant dielectric nanostructures. *Science*, 354(6314), 2016.

- [173] J. Lapujoulade. The roughening of metal surfaces. *Surface Science Reports*, 20(4):195–249, 1994.
- [174] M. Lasserus, M. Schnedlitz, D. Knez, R. Messner, A. Schiffmann, F. Lackner, A. W. Hauser, F. Hofer, and W. E. Ernst. Thermally induced alloying processes in a bimetallic system at the nanoscale: AgAu sub-5 nm core-shell particles studied at atomic resolution. *Nanoscale*, 10(4):2017–2024, 2018.
- [175] M. Lau, F. Waag, and S. Barcikowski. Direct integration of laser-generated nanoparticles into transparent nail polish: The plasmonic “goldfinger”. *Industrial & Engineering Chemistry Research*, 56(12):3291–3296, 2017.
- [176] C. Lee, H. Choi, I. I. Nedrygailov, Y. K. Lee, S. Jeong, and J. Y. Park. Enhancement of hot electron flow in plasmonic nanodiodes by incorporating pbs quantum dots. *ACS Applied Materials & Interfaces*, 10(5):5081–5089, 2018.
- [177] H. M. Lee, M. Ge, B. R. Sahu, P. Tarakeshwar, and K. S. Kim. Geometrical and electronic structures of gold, silver, and gold-silver binary clusters: Origins of ductility of gold and gold-silver alloy formation. *The Journal of Physical Chemistry B*, 107(37):9994–10005, 2003.
- [178] I. Lee, S. W. Han, and K. Kim. Production of Au–Ag alloy nanoparticles by laser ablation of bulk alloys. *Chemical Communications*, (18):1782–1783, 2001.
- [179] K.-S. Lee and M. A. El-Sayed. Gold and silver nanoparticles in sensing and imaging: sensitivity of plasmon response to size, shape, and metal composition. *The Journal of Physical Chemistry B*, 110(39):19220–19225, 2006.
- [180] S. Lee and R. Hoffmann. Bcc and fcc transition metals and alloys: a central role for the Jahn-Teller effect in explaining their ideal and distorted structures. *Journal of the American Chemical Society*, 124(17):4811–4823, 2002.
- [181] S. Lepeshov, A. Krasnok, I. Mukhin, D. Zuev, A. Gudovskikh, V. Milichko, P. Belov, and A. Miroshnichenko. Fine-tuning of the magnetic fano resonance in hybrid oligomers via fs-laser-induced reshaping. *ACS Photonics*, 4(3):536–543, 2017.
- [182] S. I. Lepeshov, A. E. Krasnok, P. A. Belov, and A. E. Miroshnichenko. Hybrid nanophotonics. *Physics-Uspekhi*, 61(11):1035–1050, nov 2018.
- [183] S. I. Lepeshov, D. A. Zuev, S. V. Makarov, V. A. Milichko, I. S. Mukhin, A. E. Krasnok, and P. A. Belov. Manipulating fano resonance via fs-laser melting of hybrid oligomers at nanoscale. *Journal of Physics: Conference Series*, 741:012140, aug 2016.
- [184] D. Li, L. Meng, S. Dang, D. Jiang, and W. Shi. Hydrogen peroxide sensing using Cu₂O nanocubes decorated by Ag-Au alloy nanoparticles. *Journal of Alloys and Compounds*, 690:1–7, 2017.

Bibliography

- [185] G. G. Li and H. Wang. Dealloyed nanoporous gold catalysts: From macroscopic foams to nanoparticulate architectures. *ChemNanoMat*, 4(9):897–908, 2018.
- [186] J. Li, J. Wang, Y. S. Grewal, C. B. Howard, L. J. Raftery, S. Mahler, Y. Wang, and M. Trau. Multiplexed SERS detection of soluble cancer protein biomarkers with gold–silver alloy nanoboxes and nanoyeast single-chain variable fragments. *Analytical Chemistry*, 90(17):10377–10384, 2018.
- [187] P. Li, K. Du, F. Lu, K. Gao, F. Xiao, W. Zhang, and T. Mei. Excellent anapole by decoupling electric multipoles of ag/si core–shell nanoparticles. *The Journal of Physical Chemistry C*, 124(35):19252–19258, 2020.
- [188] S. V. Li, D. G. Baranov, A. E. Krasnok, and P. A. Belov. All-dielectric nanoantennas for unidirectional excitation of electromagnetic guided modes. *Applied Physics Letters*, 107(17):171101, 2015.
- [189] W. Li, K. Ren, and J. Zhou. Aluminum-based localized surface plasmon resonance for biosensing. *TrAC Trends in Analytical Chemistry*, 80:486–494, 2016.
- [190] S. Liang, C. Cai, R. Gao, M. Zhang, N. Xue, and Z.-m. Qi. Auag alloy film-based colorful spr imaging sensor for highly sensitive immunodetection of benzo[a]pyrene in water. *Applied Optics*, 58(25):6942–6948, 2019.
- [191] M. Limonov, M. Rybin, A. Poddubny, and Y. Kivshar. Fano resonances in photonics. *Nature Photonics*, 11:543–554, 09 2017.
- [192] Y.-C. Lin, L.-C. Hsu, C.-Y. Lin, C.-L. Chiang, C.-M. Chou, W.-W. Wu, S.-Y. Chen, and Y.-G. Lin. Sandwich-nanostructured n-Cu₂O/AuAg/p-Cu₂O photocathode with highly positive onset potential for improved water reduction. *ACS Applied Materials & Interfaces*, 11(42):38625–38632, 2019.
- [193] S. Link, Z. L. Wang, and M. A. El-Sayed. Alloy formation of Gold-Silver nanoparticles and the dependence of the plasmon absorption on their composition. *The Journal of Physical Chemistry B*, 103(18):3529–3533, 1999.
- [194] C. Liu, H. Chen, S. Wang, Q. Liu, Y.-G. Jiang, D. W. Zhang, M. Liu, and P. Zhou. Two-dimensional materials for next-generation computing technologies. *Nature Nanotechnology*, 15(7):545–557, 2020.
- [195] H. Liu, Z. Li, Y. Yan, J. Zhao, and Y. Wang. Chiroptical study of the bimetal–cysteine hybrid composite: interaction between cysteine and au/ag alloyed nanotubes. *Nanoscale*, 11(45):21990–21998, 2019.
- [196] H. Liu, M. Shen, J. Zhao, J. Zhu, T. Xiao, X. Cao, G. Zhang, and X. Shi. Facile formation of folic acid-modified dendrimer-stabilized gold–silver alloy nanoparticles for potential cellular computed tomography imaging applications. *Analyst*, 138(7):1979–1987, 2013.

- [197] H. Liu, K. Sun, J. Zhao, R. Guo, M. Shen, X. Cao, G. Zhang, and X. Shi. Dendrimer-mediated synthesis and shape evolution of gold–silver alloy nanoparticles. *Colloids and Surfaces A: Physicochemical and Engineering Aspects*, 405:22–29, 2012.
- [198] J.-H. Liu, A.-Q. Wang, Y.-S. Chi, H.-P. Lin, and C.-Y. Mou. Synergistic effect in an Au-Ag alloy nanocatalyst: co oxidation. *The Journal of Physical Chemistry B*, 109(1):40–43, 2005.
- [199] K. Liu, Y. Bai, L. Zhang, Z. Yang, Q. Fan, H. Zheng, Y. Yin, and C. Gao. Porous au–ag nanospheres with high-density and highly accessible hotspots for SERS analysis. *Nano Letters*, 16(6):3675–3681, 2016.
- [200] W. Liu and Y. S. Kivshar. Generalized kerker effects in nanophotonics and meta-optics [invited]. *Opt. Express*, 26(10):13085–13105, May 2018.
- [201] W. Liu, A. E. Miroshnichenko, D. N. Neshev, and Y. S. Kivshar. Broadband unidirectional scattering by magneto-electric core–shell nanoparticles. *ACS Nano*, 6(6):5489–5497, 2012.
- [202] W. Liu, A. E. Miroshnichenko, D. N. Neshev, and Y. S. Kivshar. Broadband unidirectional scattering by magneto-electric core–shell nanoparticles. *ACS Nano*, 6(6):5489–5497, 2012. PMID: 22545872.
- [203] Z. Liu, W. Hou, P. Pavaskar, M. Aykol, and S. B. Cronin. Plasmon resonant enhancement of photocatalytic water splitting under visible illumination. *Nano Letters*, 11(3):1111–1116, 2011. PMID: 21319840.
- [204] Z. Liu, D. Ji, X. Zeng, H. Song, J. Liu, S. Jiang, and Q. Gan. Surface dispersion engineering of ag–au alloy films. *Applied Physics Express*, 8(4):042601, 2015.
- [205] P. D. Long, D. T. Chien, N. T. Trung, N. S. Hieu, L. H. Chi, V. Van Cat, and V. D. Lam. Plasmonic effect enhanced photocurrent in nanostructured tio₂ films decorated with gold nanoparticles. *Journal of Electronic Materials*, 46(7):4448–4454, 2017.
- [206] A. Lovera, B. Gallinet, P. Nordlander, and O. J. Martin. Mechanisms of fano resonances in coupled plasmonic systems. *ACS Nano*, 7(5):4527–4536, 2013.
- [207] F. Lu, H. Xin, W. Xia, M. Liu, Y. Zhang, W. Cai, and O. Gang. Tailoring surface opening of hollow nanocubes and their application as nanocargo carriers. *ACS Central Science*, 4(12):1742–1750, 2018.
- [208] J. Lu, Z. Chen, Z. Ma, F. Pan, L. A. Curtiss, and K. Amine. The role of nanotechnology in the development of battery materials for electric vehicles. *Nature Nanotechnology*, 11(12):1031–1038, 2016.
- [209] G. L  v  que and O. J. F. Martin. Optical interactions in a plasmonic particle coupled to a metallic film. *Optics Express*, 14(21):9971–9981, 2006.

Bibliography

- [210] H.-P. Ma, J.-H. Yang, J.-G. Yang, L.-Y. Zhu, W. Huang, G.-J. Yuan, J.-J. Feng, T.-C. Jen, and L. Hong. Systematic study of the siox film with different stoichiometry by plasma-enhanced atomic layer deposition and its application in siox/sio₂ super-lattice. *Nano-materials*, 9:55, 01 2019.
- [211] J. Ma, X. Wang, J. Feng, C. Huang, and Z. Fan. Individual plasmonic nanoprobe for biosensing and bioimaging: Recent advances and perspectives. *Small*, 17(8):2004287, 2021.
- [212] X.-C. Ma, Y. Dai, L. Yu, and B.-B. Huang. Energy transfer in plasmonic photocatalytic composites. *Light: Science & Applications*, 5(2):e16017, 2016.
- [213] S. Maier. *Plasmonics: Fundamentals and Applications*. Springer US, 2007.
- [214] K. J. Major, C. De, and S. O. Obare. Recent advances in the synthesis of plasmonic bimetallic nanoparticles. *Plasmonics*, 4(1):61–78, 2009.
- [215] M. P. Mallin and C. J. Murphy. Solution-phase synthesis of sub-10 nm Au-Ag alloy nanoparticles. *Nano Letters*, 2(11):1235–1237, 2002.
- [216] S. Manchala, L. R. Nagappagari, S. M. Venkatakrishnan, and V. Shanker. Solar-light harvesting bimetallic ag/au decorated graphene plasmonic system with efficient photo-electrochemical performance for the enhanced water reduction process. *ACS Applied Nano Materials*, 2(8):4782–4792, 2019.
- [217] S. Manivannan, J. Jeong, D.-K. Kang, and K. Kim. One-step synthesis of AuAg alloy nanodots and its electrochemical studies towards nitrobenzene reduction and sensing. *Electroanalysis*, 30(1):57–66, 2018.
- [218] S. A. Mann and E. C. Garnett. Extreme light absorption in thin semiconductor films wrapped around metal nanowires. *Nano Letters*, 13(7):3173–3178, 2013. PMID: 23758555.
- [219] T. B. Massalski and H. W. King. Alloy phases of the noble metals. *Progress in Materials Science*, 10:3–78, 1963.
- [220] E. Mauriz. Recent progress in plasmonic biosensing schemes for virus detection. *Sensors*, 20(17), 2020.
- [221] M. Q. Mehmood, S. Mei, S. Hussain, K. Huang, S. Y. Siew, L. Zhang, T. Zhang, X. Ling, H. Liu, J. Teng, A. Danner, S. Zhang, and C.-W. Qiu. Visible-frequency metasurface for structuring and spatially multiplexing optical vortices. *Advanced Materials*, 28(13):2533–2539, 2016.
- [222] H. Mei, H. Bai, S. Bai, X. Li, X. Zhao, and L. Cheng. Tuning ag content in AuAg nanosponges for superior SERS detection. *Materials Letters*, 230:24–27, 2018.

- [223] C. Min, J. Liu, T. Lei, G. Si, Z. Xie, J. Lin, L. Du, and X. Yuan. Plasmonic nano-slits assisted polarization selective detour phase meta-hologram. *Laser & Photonics Reviews*, 10(6):978–985, 2016.
- [224] A. E. Miroshnichenko, A. B. Evlyukhin, Y. F. Yu, R. M. Bakker, A. Chipouline, A. I. Kuznetsov, B. Luk'yanchuk, B. N. Chichkov, and Y. S. Kivshar. Nonradiating anapole modes in dielectric nanoparticles. *Nature Communications*, 6, 2015.
- [225] I. Misbah, F. Zhao, and W.-C. Shih. Symmetry breaking-induced plasmonic mode splitting in coupled gold–silver alloy nanodisk array for ultrasensitive rgb colorimetric biosensing. *ACS Applied Materials & Interfaces*, 11(2):2273–2281, 2019.
- [226] M. Mäkelä, T. Hatanpää, K. Mizohata, K. Meinander, J. Niinistö, J. Räisänen, M. Ritala, and M. Leskelä. Studies on thermal atomic layer deposition of silver thin films. *Chemistry of Materials*, 29(5):2040–2045, 2017.
- [227] Z. Mohammadpour, A. Safavi, and S. H. Abdollahi. Chlorine triggered de-alloying of AuAg@Carbon nanodots: Towards fabrication of a dual signalling assay combining the plasmonic property of bimetallic alloy nanoparticles and photoluminescence of carbon nanodots. *Analytica Chimica Acta*, 959:74–82, 2017.
- [228] J. S. Mohanty, P. L. Xavier, K. Chaudhari, M. S. Bootharaju, N. Goswami, S. K. Pal, and T. Pradeep. Luminescent, bimetallic AuAg alloy quantum clusters in protein templates. *Nanoscale*, 4(14):4255–62, 2012.
- [229] F. Monticone and A. Alù. Metamaterial, plasmonic and nanophotonic devices. *Reports on Progress in Physics*, 80(3):036401, 2017.
- [230] F. Monticone, D. Sounas, A. Krasnok, and A. Alù. Can a nonradiating mode be externally excited? nonscattering states versus embedded eigenstates. *ACS Photonics*, 6(12):3108–3114, 2019.
- [231] S. Mühlig, C. Menzel, C. Rockstuhl, and F. Lederer. Multipole analysis of meta-atoms. *Metamaterials*, 5(2):64 – 73, 2011.
- [232] S. Mühlig, C. Menzel, C. Rockstuhl, and F. Lederer. Multipole analysis of meta-atoms. *Metamaterials*, 5(2):64 – 73, 2011.
- [233] Y. Nagasaki, I. Hotta, M. Suzuki, and J. Takahara. Metal-masked mie-resonant full-color printing for achieving free-space resolution limit. *ACS Photonics*, 5(9):3849–3855, 2018.
- [234] G. V. Naik, V. M. Shalaev, and A. Boltasseva. Alternative plasmonic materials: Beyond gold and silver. *Advanced Materials*, 25(24):3264–3294, 2013.
- [235] A. A. Nastulyavichus, S. I. Kudryashov, N. A. Smirnov, A. A. Rudenko, A. Y. Kharin, N. I. Busleev, D. A. Zayarny, A. A. Ionin, D. A. Kirilenko, and P. N. Brunkov. Novel approach of controllable stoichiometric fabrication of alloyed Au/Ag nanoparticles by nanosecond laser ablation of thin bi-layered films in water. *Laser Physics Letters*, 16(9):096002, 2019.

Bibliography

- [236] S.-i. Naya, Y. Hayashido, R. Akashi, K. Kitazono, T. Soejima, M. Fujishima, H. Kobayashi, and H. Tada. Solid-phase photochemical growth of composition-variable Au–Ag alloy nanoparticles in agbr crystal. *The Journal of Physical Chemistry C*, 121(38):20763–20768, 2017.
- [237] Y. Negrín-Montecelo, M. Comesaña-Hermo, X.-T. Kong, B. Rodríguez-González, Z. Wang, M. Pérez-Lorenzo, A. O. Govorov, and M. A. Correa-Duarte. Traveling hot spots in plasmonic photocatalysis: Manipulating interparticle spacing for real-time control of electron injection. *ChemCatChem*, 10(7):1561–1565, 2018.
- [238] C. Ng, J. J. Cadusch, S. Dligatch, A. Roberts, T. J. Davis, P. Mulvaney, and D. E. Gómez. Hot carrier extraction with plasmonic broadband absorbers. *ACS Nano*, 10(4):4704–4711, 2016. PMID: 26982625.
- [239] M. T. Nguyen, T. Yonezawa, Y. Wang, and T. Tokunaga. Double target sputtering into liquid: A new approach for preparation of Ag–Au alloy nanoparticles. *Materials Letters*, 171:75–78, 2016.
- [240] Y. Ni, C. Kan, L. He, X. Zhu, M. Jiang, and D. Shi. Alloyed Au-Ag nanorods with desired plasmonic properties and stability in harsh environments. *Photonics Research*, 7(5):558–565, 2019.
- [241] B. Nie, Y. Luo, J. Shi, L. Gao, and G. Duan. Bowl-like pore array made of hollow Au/Ag alloy nanoparticles for SERS detection of melamine in solid milk powder. *Sensors and Actuators B: Chemical*, 301:127087, 2019.
- [242] R. G. Nikov, N. N. Nedyalkov, R. G. Nikov, and D. B. Karashanova. Nanosecond laser ablation of ag–au films in water for fabrication of nanostructures with tunable optical properties. *Applied Physics A*, 124(12):847, 2018.
- [243] H. Nishi and T. Tatsuma. Photoregulated nanopore formation via plasmon-induced dealloying of Au–Ag alloy nanoparticles. *The Journal of Physical Chemistry C*, 121(4):2473–2480, 2017.
- [244] H. Nishi, T. Torimoto, and T. Tatsuma. Wavelength- and efficiency-tunable plasmon-induced charge separation by the use of au–ag alloy nanoparticles. *Physical Chemistry Chemical Physics*, 17(6):4042–4046, 2015.
- [245] Y. Nishijima and S. Akiyama. Unusual optical properties of the Au/Ag alloy at the matching mole fraction. *Optical Materials Express*, 2(9):1226–1235, 2012.
- [246] P. N. Njoki, M. E. D. Roots, and M. M. Maye. The surface composition of Au/Ag core/alloy nanoparticles influences the methanol oxidation reaction. *ACS Applied Nano Materials*, 1(10):5640–5645, 2018.
- [247] F. A. A. Nugroho, B. Iandolo, J. B. Wagner, and C. Langhammer. Bottom-up nanofabrication of supported noble metal alloy nanoparticle arrays for plasmonics. *ACS Nano*, 10(2):2871–2879, 2016.

- [248] Y. Oh, J. Lee, and M. Lee. Fabrication of Ag-Au bimetallic nanoparticles by laser-induced dewetting of bilayer films. *Applied Surface Science*, 434:1293–1299, 2018.
- [249] S. A. Ojo, A. Lateef, M. A. Azeez, S. M. Oladejo, A. S. Akinwale, T. B. Asafa, T. A. Yekeen, A. Akinboro, I. C. Oladipo, E. B. Gueguim-Kana, and L. S. Beukes. Biomedical and catalytic applications of gold and silver-gold alloy nanoparticles biosynthesized using cell-free extract of *Bacillus safensis* lau 13: Antifungal, dye degradation, anti-coagulant and thrombolytic activities. *IEEE Transactions on NanoBioscience*, 15(5):433–442, 2016.
- [250] N. Okuya, H. Minami, H. Kurashige, S. Murahara, S. Suzuki, and T. Tanaka. Effects of metal primers on bonding of adhesive resin cement to noble alloys for porcelain fusing. *Dental Materials Journal*, 29(2):177–187, 2010.
- [251] S. J. Oldenburg, R. D. Averitt, S. L. Westcott, and N. J. Halas. Nanoengineering of optical resonances. *Chemical Physics Letters*, 288(2-4):243–247, 1998.
- [252] M. A. Otte, M.-C. Estévez, L. G. Carrascosa, A. B. González-Guerrero, L. M. Lechuga, and B. Sepúlveda. Improved biosensing capability with novel suspended nanodisks. *The Journal of Physical Chemistry C*, 115(13):5344–5351, 2011.
- [253] E. Panfilova, A. Shirokov, B. Khlebtsov, L. Matora, and N. Khlebtsov. Multiplexed dot immunoassay using Ag nanocubes, Au/Ag alloy nanoparticles, and Au/Ag nanocages. *Nano Research*, 5(2):124–134, 2012.
- [254] G. C. Papavassiliou. Surface plasmons in small Au-Ag alloy particles. *Journal of Physics F: Metal Physics*, 6(4):L103–L105, 1976.
- [255] B. Paramanik and A. Patra. Fluorescent AuAg alloy clusters: synthesis and SERS applications. *Journal of Materials Chemistry C*, 2(16):3005–3012, 2014.
- [256] M. Park, C. S. H. Hwang, and K.-H. Jeong. Nanoplasmonic alloy of Au/Ag nanocomposites on paper substrate for biosensing applications. *ACS Applied Materials & Interfaces*, 10(1):290–295, 2018.
- [257] J. Parra-Barranco, J. R. Sanchez-Valencia, A. Barranco, and A. R. González-Elipe. Silver and gold nanoparticles in nanometric confined templates: synthesis and alloying within the anisotropic pores of oblique angle deposited films. *Nanotechnology*, 28(48):485602, 2017.
- [258] E. R. Pashaki and C. Falamaki. A novel optical method for nondestructive determination of binary diffusion coefficients in metal nanoalloy films. *physica status solidi (a)*, 217(2):1900731, 2020.
- [259] K. Patel, S. Kapoor, D. P. Dave, and T. Mukherjee. Synthesis of Au, Au/Ag, Au/Pt and Au/Pd nanoparticles using the microwave-polyol method. *Research on Chemical Intermediates*, 32(2):103–113, 2006.

Bibliography

- [260] S. Patskovsky, E. Bergeron, D. Rioux, M. Simard, and M. Meunier. Hyperspectral reflected light microscopy of plasmonic Au/Ag alloy nanoparticles incubated as multiplex chromatic biomarkers with cancer cells. *Analyst*, 139(20):5247–5253, 2014.
- [261] O. Peña-Rodríguez, M. Caro, A. Rivera, J. Olivares, J. M. Perlado, and A. Caro. Optical properties of Au-Ag alloys: An ellipsometric study. *Optical Materials Express*, 4(2):403–410, 2014.
- [262] V. Pellas, D. Hu, Y. Mazouzi, Y. Mimoun, J. Blanchard, C. Guibert, M. Salmain, and S. Boujday. Gold nanorods for lspr biosensing: Synthesis, coating by silica, and bioanalytical applications. *Biosensors*, 10(10), 2020.
- [263] Z. Peng, B. Spliethoff, B. Tesche, T. Walther, and K. Kleinermanns. Laser-assisted synthesis of Au-Ag alloy nanoparticles in solution. *The Journal of Physical Chemistry B*, 110(6):2549–2554, 2006.
- [264] D. Philip. Biosynthesis of Au, Ag and Au–Ag nanoparticles using edible mushroom extract. *Spectrochimica Acta Part A: Molecular and Biomolecular Spectroscopy*, 73(2):374–381, 2009.
- [265] D. T. Pierce and W. E. Spicer. Electronic structure of amorphous si from photoemission and optical studies. *Phys. Rev. B*, 5:3017–3029, Apr 1972.
- [266] M. Piliarik and J. Homola. Surface plasmon resonance (spr) sensors: approaching their limits? *Optics Express*, 17(19):16505–16517, 2009.
- [267] S. Pramanik, S. Chattopadhyay, J. K. Das, U. Manju, and G. De. Extremely fast Au–Ag alloy–dealloy associated reversible plasmonic modifications in sio2 films. *Journal of Materials Chemistry C*, 4(16):3571–3580, 2016.
- [268] R. Praveen and R. Ramaraj. Gold/silver bimetal nanoparticles incorporated graphitic carbon nitride nanohybrid materials for oxygen reduction reaction. *Materials Chemistry and Physics*, 238:121915, 2019.
- [269] M. H. Putra, D. Djuhana, V. Fauzia, A. Harmoko, and C. Imawan. A numerical study of the sensitivity of surface plasmon resonance bimetallic silver-gold alloys using boundary element method. *IOP Conference Series: Materials Science and Engineering*, 188:012016, 2017.
- [270] H. Qian, M. Xu, X. Li, M. Ji, L. Cheng, A. Shoaib, J. Liu, L. Jiang, H. Zhu, and J. Zhang. Surface micro/nanostructure evolution of Au–Ag alloy nanoplates: Synthesis, simulation, plasmonic photothermal and surface-enhanced raman scattering applications. *Nano Research*, 9(3):876–885, 2016.
- [271] F. Qin, D. Zhang, Z. Liu, Q. Zhang, and J. Xiao. Designing metal-dielectric nanoantenna for unidirectional scattering via bayesian optimization. *Opt. Express*, 27(21):31075–31086, Oct 2019.

- [272] G. Qiu, S. P. Ng, and C.-M. L. Wu. Bimetallic Au-Ag alloy nanoislands for highly sensitive localized surface plasmon resonance biosensing. *Sensors and Actuators B: Chemical*, 265:459–467, 2018.
- [273] J. R. Daniel, L. A. McCarthy, S. Yazdi, M. Chagnot, E. Ringe, and D. Boudreau. Gold speciation and co-reduction control the morphology of agau nanoshells in formaldehyde-assisted galvanic replacement. *The Journal of Physical Chemistry C*, 122(31):18168–18176, 2018.
- [274] R. Ranjan, E. N. Esimbekova, M. A. Kirillova, and V. A. Kratasyuk. Metal-enhanced luminescence: Current trend and future perspectives- a review. *Analytica Chimica Acta*, 971:1–13, 2017.
- [275] D. C. Ratchford, A. D. Dunkelberger, I. Vurgaftman, J. C. Owrutsky, and P. E. Pehrsson. Quantification of efficient plasmonic hot-electron injection in gold nanoparticle–tio₂ films. *Nano Letters*, 17(10):6047–6055, 2017.
- [276] D. Ray, A. Kiselev, and O. J. F. Martin. Multipolar scattering analysis of hybrid metal-dielectric nanostructures. *arXiv*, 2105.00670, 2021.
- [277] D. Ray, A. Kiselev, and O. J. F. Martin. Refractive index data for 150 nm Ag measured with ellipsometry, Feb. 2021.
- [278] D. Ray and O. J. F. Martin. A review on auag alloys. *under preparation, passed initial stage of acceptance by Nature Reviews Materials*.
- [279] D. Ray, T. V. Raziman, C. Santschi, D. Etezadi, H. Altug, and O. J. F. Martin. Hybrid metal-dielectric metasurfaces for refractive index sensing. *Nano Letters*, 20(12):8752–8759, 2020.
- [280] D. Ray, H.-C. Wang, J. Kim, C. Santschi, and O. J. F. Martin. Low temperature annealing method for fabricating alloy nanostructures and metasurfaces: Unlocking a novel degree of freedom. *arXiv*, 2105.02461, 2021.
- [281] D. Ray, H.-C. Wang, J. Kim, C. Santschi, and O. J. F. Martin. Permittivity of AuAg alloys along with calculations and measurements of the alloyed Fano- resonant structures, May 2021.
- [282] T. V. Raziman, W. R. C. Somerville, O. J. F. Martin, and E. C. Le Ru. Accuracy of surface integral equation matrix elements in plasmonic calculations. *Journal of the Optical Society of America B*, 32(3):485–492, 2015.
- [283] M. Rebello Sousa Dias and M. S. Leite. Alloying: A platform for metallic materials with on-demand optical response. *Accounts of Chemical Research*, 52(10):2881–2891, 2019.

Bibliography

- [284] R. Regmi, J. Berthelot, P. M. Winkler, M. Mivelle, J. Proust, F. Bedu, I. Ozerov, T. Begou, J. Lumeau, H. Rigneault, M. F. García-Parajó, S. Bidault, J. Wenger, and N. Bonod. All-dielectric silicon nanogap antennas to enhance the fluorescence of single molecules. *Nano Letters*, 16(8):5143–5151, 2016.
- [285] S. M. Rehn and E. Ringe. Controllably hollow agau nanoparticles via nonaqueous, reduction agent-assisted galvanic replacement. *Particle & Particle Systems Characterization*, 35(5):1700381, 2018.
- [286] S. Reymond-Laruinaz, L. Saviot, V. Potin, C. Lopes, F. Vaz, and M. Marco de Lucas. Growth and size distribution of au nanoparticles in annealed au/tio₂ thin films. *Thin Solid Films*, 553:138–143, 2014. European Materials Research Society (E-MRS) Spring Meeting 2013 Symposium O: Synthesis, processing and characterization of nanoscale multi functional oxide films IV.
- [287] W.-Y. Rho, D. H. Song, H.-Y. Yang, H.-S. Kim, B. S. Son, J. S. Suh, and B.-H. Jun. Recent advances in plasmonic dye-sensitized solar cells. *Journal of Solid State Chemistry*, 258:271–282, 2018.
- [288] D. Rioux, S. Vallières, S. Besner, P. Muñoz, E. Mazur, and M. Meunier. An analytic model for the dielectric function of au, ag, and their alloys. *Advanced Optical Materials*, 2(2):176–182, 2014.
- [289] H. Robatjazi, S. M. Bahauddin, C. Doiron, and I. Thomann. Direct plasmon-driven photoelectrocatalysis. *Nano Letters*, 15(9):6155–6161, 2015.
- [290] H. Robatjazi, H. Zhao, D. F. Swearer, N. J. Hogan, L. Zhou, A. Alabastri, M. J. McClain, P. Nordlander, and N. J. Halas. Plasmon-induced selective carbon dioxide conversion on earth-abundant aluminum-cuprous oxide antenna-reactor nanoparticles. *Nature Communications*, 8(1):27, 2017.
- [291] W. Roberts-Austen. The colours of metals and alloys1. *Nature*, 35(892):106–111, 1886.
- [292] B. Rodríguez-González, A. Sánchez-Iglesias, M. Giersig, and L. M. Liz-Marzán. AuAg bimetallic nanoparticles: formation, silica-coating and selective etching. *Faraday Discuss*, 125:133–44; discussion 195–219, 2004.
- [293] E. Rusak, I. Staude, M. Decker, J. Sautter, A. E. Miroshnichenko, D. A. Powell, D. N. Neshev, and Y. S. Kivshar. Hybrid nanoantennas for directional emission enhancement. *Applied Physics Letters*, 105(22):221109, 2014.
- [294] V. Russo, N. Michieli, T. Cesca, C. Scian, D. Silvestri, M. Morpurgo, and G. Mattei. Gold–silver alloy semi-nanoshell arrays for label-free plasmonic biosensors. *Nanoscale*, 9(28):10117–10125, 2017.
- [295] M. Sahoo, S. Mansingh, and K. M. Parida. A bimetallic Au–Ag nanoalloy mounted ldh/rgo nanocomposite: a promising catalyst effective towards a coupled system for the

- photoredox reactions converting benzyl alcohol to benzaldehyde and nitrobenzene to aniline under visible light. *Journal of Materials Chemistry A*, 7(13):7614–7627, 2019.
- [296] N. Sakono, K. Omori, K. Yamamoto, N. Ishikuro, and M. Sakono. Vapor-phase synthesis of bimetallic plasmonic nanoparticles. *Analytical Sciences*, 36:61–65, 2019.
- [297] P. Sangpour, O. Akhavan, and A. Z. Moshfegh. rf reactive co-sputtered Au–Ag alloy nanoparticles in SiO₂ thin films. *Applied Surface Science*, 253(18):7438–7442, 2007.
- [298] Y. Sanguansap, K. Karn-orachai, and R. Laocharoensuk. Tailor-made porous striped gold-silver nanowires for surface enhanced raman scattering based trace detection of β -hydroxybutyric acid. *Applied Surface Science*, 500:144049, 2020.
- [299] M. A. Santiago-Cordoba, S. V. Boriskina, F. Vollmer, and M. C. Demirel. Nanoparticle-based protein detection by optical shift of a resonant microcavity. *Applied Physics Letters*, 99(7):073701, 2011.
- [300] D. Sarid and W. A. Challener. *Modern Introduction to Surface Plasmons: Theory, Mathematica Modeling, and Applications*. Cambridge University Press, 2010.
- [301] R. S. Savelev, O. N. Sergaeva, D. G. Baranov, A. E. Krasnok, and A. Alù. Dynamically reconfigurable metal-semiconductor yagi-uda nanoantenna. *Phys. Rev. B*, 95:235409, Jun 2017.
- [302] V. Savinov, N. Papasimakis, D. P. Tsai, and N. Zheludev. Optical anapoles. *Communications Physics*, 2:69, 06 2019.
- [303] A. J. Shaikh, M. Batool, M. A. Yameen, and A. Waseem. Plasmonic effects, size and biological activity relationship of Au–Ag alloy nanoparticles. *Journal of Nano Research*, 54:98–111, 2018.
- [304] A. Shaltout, J. Liu, A. Kildishev, and V. Shalaev. Photonic spin hall effect in gap–plasmon metasurfaces for on-chip chiroptical spectroscopy. *Optica*, 2(10):860–863, Oct 2015.
- [305] K. Shanmugaraj and M. Ilanchelian. Visual and optical detection of hypochlorite in water samples based on etching of gold/silver alloy nanoparticles. *New Journal of Chemistry*, 41(23):14130–14136, 2017.
- [306] A. Shayeghi, L. F. Pašteka, D. A. Götz, P. Schwerdtfeger, and R. Schäfer. Spin–orbit effects in optical spectra of gold–silver trimers. *Physical Chemistry Chemical Physics*, 20(14):9108–9114, 2018.
- [307] S. N. Sheikholeslami, A. Garcia-Etxarri, and J. A. Dionne. Controlling the interplay of electric and magnetic modes via fano-like plasmon resonances. *Nano Letters*, 11(9):3927–3934, 2011.

Bibliography

- [308] P.-T. Shen, Y. Sivan, C.-W. Lin, H.-L. Liu, C.-W. Chang, and S.-W. Chu. Temperature- and roughness-dependent permittivity of annealed/unannealed gold films. *Optics Express*, 24(17):19254–19263, 2016.
- [309] T. Shibanuma, G. Grinblat, P. Albella, and S. A. Maier. Efficient third harmonic generation from metal–dielectric hybrid nanoantennas. *Nano Letters*, 17(4):2647–2651, 2017.
- [310] H. Shim, Z. Kuang, and O. D. Miller. Optical materials for maximal nanophotonic response. *Optical Materials Express*, 10(7):1561–1585, 2020.
- [311] N. Shin-ichi, F. Musashi, and T. Hiroaki. Synthesis of Au–Ag alloy nanoparticle-incorporated agbr crystals. *Catalysts*, 9(9), 2019.
- [312] M. S. Shore, J. Wang, A. C. Johnston-Peck, A. L. Oldenburg, and J. B. Tracy. Synthesis of Au(Core)/Ag(Shell) nanoparticles and their conversion to AuAg alloy nanoparticles. *Small*, 7(2):230–234, 2011.
- [313] Y. Si, Y. Bai, X. Qin, J. Li, W. Zhong, Z. Xiao, J. Li, and Y. Yin. Alkyne–dna-functionalized alloyed Au/Ag nanospheres for ratiometric surface-enhanced raman scattering imaging assay of endonuclease activity in live cells. *Analytical Chemistry*, 90(6):3898–3905, 2018.
- [314] J. Simon, V. P. N. Nampoori, and M. Kailasnath. Facile synthesis of Au–Ag core shell and nanoalloy using femtosecond laser ablation and their optical characterization. *Optik*, 195:163168, 2019.
- [315] A. V. Singh, B. M. Bandgar, M. Kasture, B. L. V. Prasad, and M. Sastry. Synthesis of gold, silver and their alloy nanoparticles using bovine serum albumin as foaming and stabilizing agent. *Journal of Materials Chemistry*, 15(48):5115–5121, 2005.
- [316] Y. Sivan, I. W. Un, and Y. Dubi. Assistance of metal nanoparticles in photocatalysis – nothing more than a classical heat source. *Faraday Discussions*, 214(0):215–233, 2019.
- [317] A. V. Skidanenko, L. A. Avakyan, E. A. Kozinkina, and L. A. Bugaev. An effect of internal structure of bimetallic nanoparticles on optical properties for AuAg/Glass Material. *Physics of the Solid State*, 60(12):2571–2578, 2018.
- [318] J. Sánchez-Ramírez, U. Pal, L. Nolasco-Hernández, J. Mendoza-Alvarez, and J. Pescador-Rojas. Synthesis and optical properties of Au–Ag alloy nanoclusters with controlled composition. *J Nanomater*, 2008, 2008.
- [319] G. Song, L. Cheng, Y. Chao, K. Yang, and Z. Liu. Emerging nanotechnology and advanced materials for cancer radiation therapy. *Advanced Materials*, 29(32):1700996, 2017.
- [320] G. A. Sotiriou, G. D. Etterlin, A. Spyrogianni, F. Krumeich, J.-C. Leroux, and S. E. Pratsinis. Plasmonic biocompatible silver–gold alloyed nanoparticles. *Chemical Communications*, 50(88):13559–13562, 2014.

- [321] A. Sousa-Castillo, M. Comesaña-Hermo, B. Rodríguez-González, M. Pérez-Lorenzo, Z. Wang, X.-T. Kong, A. O. Govorov, and M. A. Correa-Duarte. Boosting hot electron-driven photocatalysis through anisotropic plasmonic nanoparticles with hot spots in Au-TiO_2 nanoarchitectures. *The Journal of Physical Chemistry C*, 120(21):11690–11699, 2016.
- [322] I. Staude, A. E. Miroshnichenko, M. Decker, N. T. Fofang, S. Liu, E. Gonzales, J. Dominguez, T. S. Luk, D. N. Neshev, I. Brener, and Y. Kivshar. Tailoring directional scattering through magnetic and electric resonances in subwavelength silicon nanodisks. *ACS Nano*, 7(9):7824–7832, 2013.
- [323] I. Staude and J. Schilling. Metamaterial-inspired silicon nanophotonics. *Nature Photonics*, 11:274–284, 04 2017.
- [324] P. Steglich, C. Villringer, S. Pulwer, F. Heinrich, J. Bauer, B. Dietzel, C. Mai, A. Mai, M. Casalboni, and S. Schrader. Hybrid-waveguide ring resonator for biochemical sensing. *IEEE Sensors Journal*, 17(15):4781–4790, 2017.
- [325] L. Sun, P. Lv, H. Li, F. Wang, W. Su, and L. Zhang. One-step synthesis of Au–Ag alloy nanoparticles using soluble starch and their photocatalytic performance for 4-nitrophenol degradation. *Journal of Materials Science*, 53(23):15895–15906, 2018.
- [326] L. Sun, Y. Yin, P. Lv, W. Su, and L. Zhang. Green controllable synthesis of Au–Ag alloy nanoparticles using chinese wolfberry fruit extract and their tunable photocatalytic activity. *RSC Advances*, 8(8):3964–3973, 2018.
- [327] S. Sun, M. Li, Q. Du, C. E. Png, and P. Bai. Metal–dielectric hybrid dimer nanoantenna: Coupling between surface plasmons and dielectric resonances for fluorescence enhancement. *The Journal of Physical Chemistry C*, 121(23):12871–12884, 2017.
- [328] S. Sun, R. Li, M. Li, Q. Du, C. E. Png, and P. Bai. Hybrid mushroom nanoantenna for fluorescence enhancement by matching the stokes shift of the emitter. *The Journal of Physical Chemistry C*, 122(26):14771–14780, 2018.
- [329] S. Sun, D. Wang, Z. Feng, and W. Tan. Highly efficient unidirectional forward scattering induced by resonant interference in a metal–dielectric heterodimer. *Nanoscale*, 12:22289–22297, 2020.
- [330] S. Sun, T. Zhang, Q. Liu, L. Ma, Q. Du, and H. Duan. Enhanced directional fluorescence emission of randomly oriented emitters via a metal–dielectric hybrid nanoantenna. *The Journal of Physical Chemistry C*, 123(34):21150–21160, 2019.
- [331] X. Sun and D. Qin. Co-titration of AgNO_3 and HAuCl_4 : a new route to the synthesis of Ag@Ag-Au core–frame nanocubes with enhanced plasmonic and catalytic properties. *Journal of Materials Chemistry C*, 3(45):11833–11841, 2015.

Bibliography

- [332] Y. Sun, B. Wiley, Z.-Y. Li, and Y. Xia. Synthesis and optical properties of nanorattles and multiple-walled nanoshells/nanotubes made of metal alloys. *Journal of the American Chemical Society*, 126(30):9399–9406, 2004.
- [333] Y. Sun and Y. Xia. Mechanistic study on the replacement reaction between silver nanostructures and chloroauric acid in aqueous medium. *Journal of the American Chemical Society*, 126(12):3892–3901, 2004.
- [334] Z. Sun, Y. Xiahou, T. Cao, K. Zhang, Z. Wang, P. Huang, K. Zhu, L. Yuan, Y. Zhou, B. Song, H. Xia, and N. Chen. Enhanced p-i-n type perovskite solar cells by doping AuAg@AuAg core-shell alloy nanocrystals into pedot:pss layer. *Organic Electronics*, 52:309–316, 2018.
- [335] M. Sundarapandi, P. Viswanathan, S. Sivakumar, and R. Ramaraj. Catalytic activities of mono- and bimetallic (gold/silver) nanoshell-coated gold nanocubes toward catalytic reduction of nitroaromatics. *Langmuir*, 34(46):13897–13904, 2018.
- [336] R. Sundararaman, P. Narang, A. S. Jermyn, W. A. Goddard Iii, and H. A. Atwater. Theoretical predictions for hot-carrier generation from surface plasmon decay. *Nature Communications*, 5(1):5788, 2014.
- [337] M. Tahir, B. Tahir, and N. A. S. Amin. Synergistic effect in plasmonic au/ag alloy nps co-coated tio2 nws toward visible-light enhanced co2 photoreduction to fuels. *Applied Catalysis B: Environmental*, 204:548–560, 2017.
- [338] M. Takenaka, Y. Hashimoto, T. Iwasa, T. Taketsugu, G. Seniutinas, A. Balčytis, S. Juodkazis, and Y. Nishijima. First principles calculations toward understanding SERS of 2,2'-bipyridyl adsorbed on Au, Ag, and Au-Ag nanoalloy. *Journal of Computational Chemistry*, 40(8):925–932, 2019.
- [339] H. Tao, T. Hu, J. Yan, and J. Di. A comparative study of different reagentless plasmon sensors based on Ag–Au alloy nanoparticles for detection of hg. *Sensors and Actuators B: Chemical*, 208:43–49, 2015.
- [340] K. Terakura, T. Oguchi, T. Mohri, and K. Watanabe. Electronic theory of the alloy phase stability of Cu-Ag, Cu-Au, and Ag-Au systems. *Phys Rev B Condens Matter*, 35(5):2169–2173, 1987.
- [341] M. Thangamuthu, D. Ray, P. Kumar, C. Santschi, and O. J. F. Martin. Engineered schottky junction for boosting hot electron extraction from plasmonic gold-silver alloy nanoparticles. *under preparation*.
- [342] M. Thangamuthu, C. Santschi, and O. J. Martin. Reliable langmuir blodgett colloidal masks for large area nanostructure realization. *Thin Solid Films*, 709:138195, 2020.
- [343] M. Thangamuthu, C. Santschi, and O. J. F. Martin. Photocatalytic ammonia production enhanced by a plasmonic near-field and hot electrons originating from aluminium nanostructures. *Faraday Discussions*, 214(0):399–415, 2019.

-
- [344] K. Thyagarajan, C. Santschi, P. Langlet, and O. J. F. Martin. Highly improved fabrication of ag and al nanostructures for uv and nonlinear plasmonics. *Advanced Optical Materials*, 4(6):871–876, 2016.
- [345] K. Thyagarajan, C. Santschi, P. Langlet, and O. J. F. Martin. Highly Improved Fabrication of Ag and Al Nanostructures for UV and Nonlinear Plasmonics. *Advanced Optical Materials*, 4(6):871–876, 2016.
- [346] S. Tian, O. Neumann, M. J. McClain, X. Yang, L. Zhou, C. Zhang, P. Nordlander, and N. J. Halas. Aluminum nanocrystals: A sustainable substrate for quantitative SERS-based DNA detection. *Nano Letters*, 17(8):5071–5077, 2017.
- [347] A. Tittl, A. Leitis, M. Liu, F. Yesilkoy, D.-Y. Choi, D. N. Neshev, Y. S. Kivshar, and H. Altug. Imaging-based molecular barcoding with pixelated dielectric metasurfaces. *Science*, 360(6393):1105, 2018.
- [348] L. Tong, T. Pakizeh, L. Feuz, and A. Dmitriev. Highly directional bottom-up 3d nanoantenna for visible light. *Scientific Reports*, 3(1):2311, 2013.
- [349] N. Toshima and T. Yonezawa. Bimetallic nanoparticles-novel materials for chemical and physical applications. *New Journal of Chemistry*, 22(11):1179–1201, 1998.
- [350] S.-Y. Tseng, S.-Y. Li, S.-Y. Yi, A. Y. Sun, D.-Y. Gao, and D. Wan. Food quality monitor: Paper-based plasmonic sensors prepared through reversal nanoimprinting for rapid detection of biogenic amine odorants. *ACS Applied Materials & Interfaces*, 9(20):17306–17316, 2017.
- [351] S. Tu, D. Rioux, J. Perreault, D. Brouard, and M. Meunier. Fluorescence and scattering dual-mode multiplexed imaging with gold–silver alloy core silica shell nanoparticles. *The Journal of Physical Chemistry C*, 121(16):8944–8951, 2017.
- [352] D. Tzarouchis and A. Sihvola. Light scattering by a dielectric sphere: Perspectives on the mie resonances. *Applied Sciences*, 8, 01 2018.
- [353] A. Unger and M. Kreiter. Analyzing the performance of plasmonic resonators for dielectric sensing. *The Journal of Physical Chemistry C*, 113(28):12243–12251, 2009.
- [354] A. Unger and M. Kreiter. Analyzing the performance of plasmonic resonators for dielectric sensing. *The Journal of Physical Chemistry C*, 113(28):12243–12251, 2009.
- [355] M. Vala, S. Etheridge, J. A. Roach, and J. Homola. Long-range surface plasmons for sensitive detection of bacterial analytes. *Sensors and Actuators B: Chemical*, 139(1):59–63, 2009.
- [356] M. Valenti, A. Venugopal, D. Tordera, M. P. Jonsson, G. Biskos, A. Schmidt-Ott, and W. A. Smith. Hot carrier generation and extraction of plasmonic alloy nanoparticles. *ACS Photonics*, 4(5):1146–1152, 2017.

- [357] J. van de Groep and A. Polman. Designing dielectric resonators on substrates: Combining magnetic and electric resonances. *Opt. Express*, 21(22):26285–26302, Nov 2013.
- [358] M. A. van de Haar, J. van de Groep, B. J. Brenny, and A. Polman. Controlling magnetic and electric dipole modes in hollow silicon nanocylinders. *Opt. Express*, 24(3):2047–2064, Feb 2016.
- [359] S. W. Verbruggen, M. Keulemans, M. Filippousi, D. Flahaut, G. Van Tendeloo, S. Lacombe, J. A. Martens, and S. Lenaerts. Plasmonic gold–silver alloy on tio2 photocatalysts with tunable visible light activity. *Applied Catalysis B: Environmental*, 156-157:116–121, 2014.
- [360] M. Verma, M. B. Newmai, and P. Senthil Kumar. Synergistic effect of au–ag nano-alloying: intense seira and enhanced catalysis. *Dalton Transactions*, 46(29):9664–9677, 2017.
- [361] S. Verma, B. T. Rao, V. Sathe, S. Bhartiya, H. S. Patel, R. Kaul, and B. Singh. Optical and surface enhanced raman scattering responses of densely packed ag–au alloy nanoparticle films of varied composition and thickness. *Journal of Alloys and Compounds*, 753:395–406, 2018.
- [362] F. Vollmer, S. Arnold, and D. Keng. Single virus detection from the reactive shift of a whispering-gallery mode. *Proceedings of the National Academy of Sciences*, 105(52):20701–20704, 2008.
- [363] B. Špačková, P. Wrobel, M. Bocková, and J. Homola. Optical biosensors based on plasmonic nanostructures: A review. *Proceedings of the IEEE*, 104(12):2380–2408, Dec 2016.
- [364] S. Wack, P. Lunca Popa, N. Adjeroud, J. Guillot, B. R. Pistillo, and R. Leturcq. Large-scale deposition and growth mechanism of silver nanoparticles by plasma-enhanced atomic layer deposition. *The Journal of Physical Chemistry C*, 123(44):27196–27206, 2019.
- [365] C. Wang, H. Yin, R. Chan, S. Peng, S. Dai, and S. Sun. One-pot synthesis of oleylamine coated AuAg alloy nps and their catalysis for co oxidation. *Chemistry of Materials*, 21(3):433–435, 2009.
- [366] D. Wang and Y. Li. Bimetallic nanocrystals: Liquid-phase synthesis and catalytic applications. *Advanced Materials*, 23(9):1044–1060, 2011.
- [367] H. Wang, P. Liu, Y. Ke, Y. Su, L. Zhang, N. Xu, S. Deng, and H. Chen. Janus magneto–electric nanosphere dimers exhibiting unidirectional visible light scattering and strong electromagnetic field enhancement. *ACS Nano*, 9(1):436–448, 2015. PMID: 25554917.
- [368] H.-C. Wang, C. H. Chu, P. C. Wu, H.-H. Hsiao, H. J. Wu, J.-W. Chen, W. H. Lee, Y.-C. Lai, Y.-W. Huang, M. L. Tseng, S.-W. Chang, and D. P. Tsai. Ultrathin planar cavity metasurfaces. *Small*, 14(17):1703920, 2018.
- [369] J. Wang and J. Du. Plasmonic and dielectric metasurfaces design, fabrication and applications. *Applied Sciences*, 6(9):239, 2016.

- [370] J. L. Wang, R. A. Ando, and P. H. C. Camargo. Investigating the plasmon-mediated catalytic activity of agau nanoparticles as a function of composition: Are two metals better than one? *ACS Catalysis*, 4(11):3815–3819, 2014.
- [371] P. Wang, Y. Bai, C. Yao, X. Li, L. Zhou, W. Wang, A. M. El-Toni, J. Zi, D. Zhao, L. Shi, and F. Zhang. Intracellular and in vivo cyanide mapping via surface plasmon spectroscopy of single au–ag nanoboxes. *Analytical Chemistry*, 89(4):2583–2591, 2017.
- [372] Q. Wang, H. Zhao, X. Du, W. Zhang, M. Qiu, and Q. Li. Hybrid photonic-plasmonic molecule based on metal/si disks. *Opt. Express*, 21(9):11037–11047, May 2013.
- [373] Q. H. Wang, K. Kalantar-Zadeh, A. Kis, J. N. Coleman, and M. S. Strano. Electronics and optoelectronics of two-dimensional transition metal dichalcogenides. *Nature Nanotechnology*, 7(11):699–712, 2012.
- [374] S. Wang, P. C. Wu, V.-C. Su, Y.-C. Lai, C. Hung Chu, J.-W. Chen, S.-H. Lu, J. Chen, B. Xu, C.-H. Kuan, T. Li, S. Zhu, and D. P. Tsai. Broadband achromatic optical metasurface devices. *Nature Communications*, 8(1):187, 2017.
- [375] X. Wang, G. Ma, A. Li, J. Yu, Z. Yang, J. Lin, A. Li, X. Han, and L. Guo. Composition-adjustable ag–au substitutional alloy microcages enabling tunable plasmon resonance for ultrasensitive SERS. *Chemical Science*, 9(16):4009–4015, 2018.
- [376] X. Wang, C. Santschi, and O. J. F. Martin. Strong improvement of long-term chemical and thermal stability of plasmonic silver nanoantennas and films. *Small*, 13(28):1700044, 2017.
- [377] Y. Wang, Z. Gao, B. Liu, and X. Xia. Peroxidase-agau hybrid nanocages as signal transducers for sensitive plasmonic colorimetric sensing. *Journal of Materials Chemistry C*, 7(48):15179–15187, 2019.
- [378] Y. Wang, J. Zhou, and J. Li. Construction of plasmonic nano-biosensor-based devices for point-of-care testing. *Small Methods*, 1(11):1700197, 2017.
- [379] Z. Wang, X. Huang, S. Jin, H. Wang, L. Yuan, and J. L. Brash. Rapid antibacterial effect of sunlight-exposed silicon nanowire arrays modified with au/ag alloy nanoparticles. *Journal of Materials Chemistry B*, 7(40):6202–6209, 2019.
- [380] S. C. Warren and E. Thimsen. Plasmonic solar water splitting. *Energy & Environmental Science*, 5(1):5133–5146, 2012.
- [381] J. Wei, Y. Guo, J. Li, M. Yuan, T. Long, and Z. Liu. Optically active ultrafine au–ag alloy nanoparticles used for colorimetric chiral recognition and circular dichroism sensing of enantiomers. *Analytical Chemistry*, 89(18):9781–9787, 2017.
- [382] X. Wei, Q. Fan, H. Liu, Y. Bai, L. Zhang, H. Zheng, Y. Yin, and C. Gao. Holey au–ag alloy nanoplates with built-in hotspots for surface-enhanced raman scattering. *Nanoscale*, 8(34):15689–15695, 2016.

Bibliography

- [383] J. Weiss, P. Takhistov, and D. J. McClements. Functional materials in food nanotechnology. *Journal of Food Science*, 71(9):R107–R116, 2006.
- [384] P. West, S. Ishii, G. Naik, N. Emani, V. Shalaev, and A. Boltasseva. Searching for better plasmonic materials. *Laser & Photonics Reviews*, 4(6):795–808, 2010.
- [385] K. Wu, J. Chen, J. R. McBride, and T. Lian. Efficient hot-electron transfer by a plasmon-induced interfacial charge-transfer transition. *Science*, 349(6248):632–635, 2015.
- [386] N. Wu. Plasmonic metal–semiconductor photocatalysts and photoelectrochemical cells: a review. *Nanoscale*, 10:2679–2696, 2018.
- [387] W. Wu and M. M. Maye. Discrete dipole approximation analysis of plasmonic core/alloy nanoparticles. *ChemPhysChem*, 15(12):2582–2587, 2014.
- [388] Y. Wu, G. Li, C. Cherqui, N. W. Bigelow, N. Thakkar, D. J. Masiello, J. P. Camden, and P. D. Rack. Electron energy loss spectroscopy study of the full plasmonic spectrum of self-assembled au–ag alloy nanoparticles: Unraveling size, composition, and substrate effects. *ACS Photonics*, 3(1):130–138, 2016.
- [389] X. Xia, Y. Wang, A. Ruditskiy, and Y. Xia. 25th anniversary article: Galvanic replacement: A simple and versatile route to hollow nanostructures with tunable and well-controlled properties. *Advanced Materials*, 25(44):6313–6333, 2013.
- [390] Y. Xie, Y. Ju, Y. Toku, and Y. Morita. Fabrication of fe₂o₃ nanowire arrays based on oxidation-assisted stress-induced atomic-diffusion and their photovoltaic properties for solar water splitting. *RSC Adv.*, 7:30548–30553, 2017.
- [391] C. Xu, K. Cheng, Q. Li, X. Shang, C. Wu, Z. Wei, X. Zhang, and H. Li. The dual-frequency zero-backward scattering realized in a hybrid metallo-dielectric nanoantenna. *AIP Advances*, 9(7):075121, 2019.
- [392] L. Xu, L. S. Tan, and M. H. Hong. Tuning of localized surface plasmon resonance of well-ordered ag/au bimetallic nanodot arrays by laser interference lithography and thermal annealing. *Applied Optics*, 50(31), 2011.
- [393] M. Xu, J. Feng, Y.-S. Liu, Y. Jin, H.-Y. Wang, and H.-B. Sun. Effective and tunable light trapping in bulk heterojunction organic solar cells by employing Au-Ag alloy nanoparticles. *Applied Physics Letters*, 105(15):153303, 2014.
- [394] Q. Xu, F. Liu, Y. Liu, K. Cui, X. Feng, W. Zhang, and Y. Huang. Broadband light absorption enhancement in dye-sensitized solar cells with Au-Ag alloy popcorn nanoparticles. *Scientific Reports*, 3(1):2112, 2013.
- [395] X. Xu, T. Isik, S. Kundu, and V. Ortalan. Investigation of laser-induced inter-welding between au and ag nanoparticles and the plasmonic properties of welded dimers. *Nanoscale*, 10(48):23050–23058, 2018.

-
- [396] C. Yan, X. Wang, T. V. Raziman, and O. J. F. Martin. Twisting fluorescence through extrinsic chiral antennas. *Nano Letters*, 17(4):2265–2272, 2017.
- [397] G. Yang, Y. Niu, H. Wei, B. Bai, and H.-B. Sun. Greatly amplified spontaneous emission of colloidal quantum dots mediated by a dielectric-plasmonic hybrid nanoantenna. *Nanophotonics*, 8(12):2313, 2019.
- [398] J.-H. Yang and K.-P. Chen. Hybridization of plasmonic and dielectric metasurfaces with asymmetric absorption enhancement. *Journal of Applied Physics*, 128(13):133101, 2020.
- [399] M. Yang, K. D. Gilroy, and Y. Xia. A general approach to the synthesis of m@au/ag (m = au, pd, and pt) nanorattles with ultrathin shells less than 2.5 nm thick. *Particle & Particle Systems Characterization*, 34(8):1600279, 2017.
- [400] W. Yang, K. Wu, W. Yang, H. Wang, X. Lv, L. Qian, T. Yu, Z. Li, X. Zhou, G. Okumu Barasa, S. Yuan, Y. Jiang, and Z. Yang. Nanoporous Au-Ag shell with fast kinetics: integrating chemical and plasmonic catalysis. *Nanotechnology*, 28(42):425704, 2017.
- [401] Y. Yang, I. I. Kravchenko, D. P. Briggs, and J. Valentine. All-dielectric metasurface analogue of electromagnetically induced transparency. *Nature Communications*, 5:5753, 2014.
- [402] Y. Yang, O. D. Miller, T. Christensen, J. D. Joannopoulos, and M. Soljačić. Low-loss plasmonic dielectric nanoresonators. *Nano Letters*, 17(5):3238–3245, 2017. PMID: 28441499.
- [403] Y. Yang, Q. Zhang, Z.-W. Fu, and D. Qin. Transformation of ag nanocubes into ag–au hollow nanostructures with enriched ag contents to improve SERS activity and chemical stability. *ACS Applied Materials & Interfaces*, 6(5):3750–3757, 2014.
- [404] O. Yavas, M. Svedendahl, P. Dobosz, V. Sanz, and R. Quidant. On-a-chip biosensing based on all-dielectric nanoresonators. *Nano Letters*, 17(7):4421–4426, 2017.
- [405] R.-m. Yi, Z. Zhang, C.-x. Liu, and Z.-m. Qi. Gold-silver alloy film based surface plasmon resonance sensor for biomarker detection. *Materials Science and Engineering: C*, 116:111126, 2020.
- [406] H. You, S. Yang, B. Ding, and H. Yang. Synthesis of colloidal metal and metal alloy nanoparticles for electrochemical energy applications. *Chemical Society Reviews*, 42(7):2880–2904, 2013.
- [407] K. Yu, X. Sun, L. Pan, T. Liu, A. Liu, G. Chen, and Y. Huang. Hollow Au-Ag alloy nanorices and their optical properties. *Nanomaterials (Basel, Switzerland)*, 7(9):255, 2017.
- [408] W. Yue, G. Song, L. Sang-Shin, K. Eun-Soo, and C. Duk-Yong. Subtractive color filters based on a silicon-aluminum hybrid-nanodisk metasurface enabling enhanced color purity. *Scientific Reports*, 6:29756, Jun 2016.

Bibliography

- [409] X. Zeng, W. Yu, P. Yao, Z. Xi, Y. Lu, and P. Wang. Metallo-dielectric hybrid antenna for high purcell factor and radiation efficiency. *Optics Express*, 22(12):14517–14523, Jun 2014.
- [410] C. Zhang, T. Zhang, Z. Zhang, and H. Zheng. Plasmon enhanced fluorescence and raman scattering by [Au-Ag Alloy NP Cluster]@SiO₂ core-shell nanostructure. *Frontiers in Chemistry*, 7(647), 2019.
- [411] H. Zhang, J. Cadusch, C. Kinnear, T. James, A. Roberts, and P. Mulvaney. Direct assembly of large area nanoparticle arrays. *ACS Nano*, 12(8):7529–7537, 2018. PMID: 30004661.
- [412] H. Zhang and A. O. Govorov. Optical generation of hot plasmonic carriers in metal nanocrystals: The effects of shape and field enhancement. *The Journal of Physical Chemistry C*, 118(14):7606–7614, 2014.
- [413] H. Zhang, C. Wang, H. Li, L. Jiang, D. Men, J. Wang, and J. Xiang. Physical process-aided fabrication of periodic au-m (m = ag, cu, ag-cu) alloyed nanoparticle arrays with tunable localized surface plasmon resonance and diffraction peaks. *RSC Advances*, 8(17):9134–9140, 2018.
- [414] J. Zhang, J. Claverie, M. Chaker, and D. Ma. Colloidal metal nanoparticles prepared by laser ablation and their applications. *ChemPhysChem*, 18(9):986–1006, 2017.
- [415] J. Zhang, Y. Tang, K. Lee, and M. Ouyang. Tailoring light-matter-spin interactions in colloidal hetero-nanostructures. *Nature*, 466(7302):91–95, 2010.
- [416] T. Zhang, Y. Sun, L. Hang, H. Li, G. Liu, X. Zhang, X. Lyu, W. Cai, and Y. Li. Periodic porous alloyed au-ag nanosphere arrays and their highly sensitive SERS performance with good reproducibility and high density of hotspots. *ACS Applied Materials & Interfaces*, 10(11):9792–9801, 2018.
- [417] T. Zhang, F. Zhou, L. Hang, Y. Sun, D. Liu, H. Li, G. Liu, X. Lyu, C. Li, W. Cai, and Y. Li. Controlled synthesis of sponge-like porous au-ag alloy nanocubes for surface-enhanced raman scattering properties. *Journal of Materials Chemistry C*, 5(42):11039–11045, 2017.
- [418] W. Zhang and O. J. F. Martin. A universal law for plasmon resonance shift in biosensing. *ACS Photonics*, 2(1):144–150, 2015.
- [419] X.-D. Zhang, M.-L. Guo, D. Wu, P.-X. Liu, Y.-M. Sun, L.-A. Zhang, Y. She, Q.-F. Liu, and F.-Y. Fan. First-principles investigation of ag-doped gold nanoclusters. *International journal of molecular sciences*, 12(5):2972–2981, 2011.
- [420] Y. Zhang, H. Sun, S. Zhang, S. Li, X. Wang, X. Zhang, T. Liu, and Z. Guo. Enhancing luminescence in all-inorganic perovskite surface plasmon light-emitting diode by incorporating Au-Ag alloy nanoparticle. *Optical Materials*, 89:563–567, 2019.

-
- [421] Y. Zhang, P. Yue, J.-Y. Liu, W. Geng, Y.-T. Bai, and S.-D. Liu. Ideal magnetic dipole resonances with metal-dielectric-metal hybridized nanodisks. *Opt. Express*, 27(11):16143–16155, May 2019.
- [422] L.-B. Zhao, X.-X. Liu, and D.-Y. Wu. Oxidative coupling or reductive coupling? effect of surroundings on the reaction route of the plasmonic photocatalysis of nitroaniline. *The Journal of Physical Chemistry C*, 120(3):1570–1579, 2016.
- [423] X. Zhou, G. Liu, H. Zhang, Y. Li, and W. Cai. Porous zeolite imidazole framework-wrapped urchin-like Au-Ag nanocrystals for SERS detection of trace hexachlorocyclohexane pesticides via efficient enrichment. *Journal of Hazardous Materials*, 368:429–435, 2019.
- [424] C. Zhu, D. Du, A. Eychmüller, and Y. Lin. Engineering ordered and nonordered porous noble metal nanostructures: Synthesis, assembly, and their applications in electrochemistry. *Chemical Reviews*, 115(16):8896–8943, 2015.
- [425] G. Zhu, L. Wang, N. Bing, H. Xie, and W. Yu. Enhancement of photothermal conversion performance using nanofluids based on bimetallic ag-au alloys in nitrogen-doped graphitic polyhedrons. *Energy*, 183:747–755, 2019.
- [426] G. Zhu, L. Wang, Y. Zhang, W. Yu, and H. Xie. Au–ag alloy nanoparticles supported on ordered mesoporous carbon (cmk-3) with remarkable solar thermal conversion efficiency. *Applied Physics A*, 125(2):151, 2019.
- [427] A. E. Zweber, T. Komizo, J. Levin, and Z. Benes. Criteria for success in e-beam resists. In C. L. Henderson, editor, *Advances in Resist Materials and Processing Technology XXVI*, volume 7273, pages 163 – 171. International Society for Optics and Photonics, SPIE, 2009.



DEBDATTA RAY

Doctoral Student, EPFL, Switzerland

CONTACT

PHONE:
+41786861524
Researchgate:
https://www.researchgate.net/profile/Debdatta_Ray
Google scholar
[Link](#)
EMAIL:
debdattaray.ece@gmail.com

TECHNICAL SKILLS

Nanofabrication

1. **Lithography**
 - Electron beam lithography
2. **Etching**
 - Dry etching (Plasma etching-reactive and non-reactive)
 - Wet etching
3. **Deposition**
 - Sputtering
 - E-beam evaporation
 - ALD
4. **Metrology**
 - Focussed Ion beam
 - Scanning electron microscopy
 - Ellipsometry
 - Atomic force microscopy

Numerical simulation

- Surface Integral Equation
- Multipolar analysis

SCHOLARSHIPS

- Awarded **Swiss Government Excellence Scholarship** for pursuing PhD in EPFL
- Awarded **IIT Master Sandwich Scholarship by DAAD, Germany**
- Government of India (MHRD) **GATE** Scholarship for pursuing Master's in engineering in IIT Madras
- Awarded **National Scholarship** by Govt. Of India for pursuing BTech

RESEARCH INTEREST

- Nanophotonics
- Plasmonics (including metasurfaces)
- Nanofabrication

EDUCATION

PhD, 01/09/2016 - Present
École polytechnique fédérale de Lausanne,, (EPFL) Switzerland

Nanophotonics and Metrology Laboratory

Thesis advisor: Prof. Olivier J.F. Martin

Dissertation topic: Fabrication of metasurfaces using hybrid metal-dielectric nanoantennas and alloy nanostructures

MS by Research, 01/07/2012 – 30/06/2016
Indian Institute of Technology, Madras, India (IIT Madras)

Photonics, Electrical Engineering Department

Thesis Advisor: Prof. Anil Prabhakar (IITM),
Prof. Habil Jorg. Schulze (Germany)

(Spent 7 months in **Institute of Halbleitertechnik, the University of Stuttgart** (as a part of a sandwich programme funded by **DAAD** (German Academic Exchange Service))

Thesis topic: Simulation, fabrication and characterization of plasmonic gratings in Ge pin diodes

Course CGPA: 9/10

Bachelor of Technology (B.Tech), 01/07/2008-30/06/2012
Heritage Institute of Technology, West Bengal University of Technology, Kolkata, India

Electronics and communication engineering
CGPA: 9.09/10

RESEARCH EXPERIENCE

• PhD

My PhD thesis work is based on the fabrication of unconventional metasurfaces, where we use hybrid metal-dielectric nanoantennas or alloy nanostructures as the unit cell. The hybrid nanoantenna was used as a bulk refractive index sensor with a bulk sensitivity of 250 nm/RIU. The alloy Fano-resonant structures and holograms with $\text{Au}_{0.2}\text{Ag}_{0.8}$ and $\text{Au}_{0.8}\text{Ag}_{0.2}$ were fabricated with a novel low-temperature annealing technique, developed by me, where we annealed a bilayer of the metal where the shape of the nanostructures were retained after annealing. This method eliminates the need to buy different alloy targets. I have also fabricated large area samples with AuAg alloy by dewetting on TiO_2 , to measure photocurrent generated by hot electrons.

• Masters

My master's thesis comprised of computation of band diagram of bull's eye structure using plane wave method. The structures were fabricated on the Al metallic layer on the Ge pin diode using E-beam lithography. The photocurrent of these diodes were measured using a 'home-made' characterization setup.

PUBLICATIONS

Journals:

- **Hybrid metal-dielectric metasurfaces for refractive index sensing**, Debdatta Ray et. al, *Nano Letters* **2020** 20 (12), 8752-8759, DOI: [10.1021/acs.nanolett.0c03613](https://doi.org/10.1021/acs.nanolett.0c03613) (Link)
- **Review on AuAg alloys** (has passed the first stage of acceptance in Nature Material Reviews, writing in progress)
- **Low temperature annealing method for fabricating alloy nanostructures and metasurfaces: Unlocking a novel degree of freedom** (arxiv, 2105.02461, 2021)
- **Generation of a hot electron with alloys** (in preparation)
- **Multipolar scattering analysis of metal-dielectric nanostructures** (submitted, under peer-review)

Summit

- **Global Young Scientists Summit (GYSS 2020)**, Singapore, Jan 14th -17th, 2020, (organized by National Research Foundation, Prime Minister's Office, Singapore; I am among the 5 doctoral student chosen by EPFL to attend the summit)
- **"Extending the limits of plasmonics with unconventional metasurfaces"**, Debdatta Ray et al, (POSTER)

Conferences:

- **"Extending the limits of conventional plasmonics with low-temperature alloying of noble metal"**, Debdatta Ray et.al, **9th International Conference on Surface Plasmon Photonics (SPP9)**, Copenhagen, Denmark, May 26th-31st, 2019, (2019), (ORAL)
- **"Plasmonic nanostructures made of Au/Ag alloyed at low temperature: Unlocking an additional degree of freedom"**, Debdatta Ray et.al, **Material Research Society Spring Meeting and Exhibit (MRS Spring)**, Arizona, USA, April 22nd-26th, 2019, (ORAL)
- **"Fabrication of alloyed plasmonic nanostructures"**, D. Ray et.al, **Conference on Optical MEMS and Nanophotonics (OMN)**, Lausanne, Switzerland, July 29th- August 2nd, 2018, DOI: [10.1109/OMN.2018.8454538](https://doi.org/10.1109/OMN.2018.8454538) (Link) (POSTER)
- **"Hybrid metal-dielectric metasurfaces for refractive index sensing"**, Debdatta Ray et.al, **International Conference on Lasers and Electro-optics (CLEO 2018)**, May 2018 at San Jose, CA, USA, DOI: [10.1364/CLEO_AT.2018.JTh2A.74](https://doi.org/10.1364/CLEO_AT.2018.JTh2A.74) (Link) (POSTER)
- **"Hybrid metal-dielectric nanoantennas for refractive index sensing"**, Debdatta Ray et.al, **8th International Conference on Surface Plasmon Photonics (SPP8)**, May 2017, Taipei, Taiwan, (POSTER)
- **"Plane-wave analysis of bull's eye gratings"**, Debdatta Ray et.al, **International Conference on Numerical Simulation of Optoelectronic Devices (NUSOD16)**, July 2016, at Sydney, Australia, (POSTER)
- **"Numerical Simulation Of Bull's Eye Grating Using 2D Axisymmetric Model"**, Debdatta Ray et.al, **COMSOL Conference 2016**, Bangalore, Oct 2016 (ORAL)
- **"Plasmonic Waveguiding and Detection Structures integrated with Ge PIN diodes"**, I. A. Fischer, L. Augel, D. Ray, H.J. Schulze, **International SiGe Technology and Device Meeting (ISTDM)**, 2014, Singapore (Sponsored by IEEE), DOI: [10.1109/ISTDM.2014.6874648](https://doi.org/10.1109/ISTDM.2014.6874648) (Link) (POSTER)

INVITED TALKS

- **"Transcending conventional plasmonics with metal alloys"** **EPFL Photonics Day**, EPFL, Switzerland, 2019
- **"Transcending conventional plasmonics using dielectric and metal alloys"** **EPFL Core to Core workshop**, EPFL, Switzerland, 2018
- **"Plasmonic Bull's eye structures for enhanced detector efficiency"**, **Collaborative workshop on emerging semiconductor technologies**, IIT Mandi., 2014, India

NUMERICAL SOFTWARES USED

- MATLAB
- VISUAL C
- LabVIEW
- COMSOL

AWARDS

- Ranked **1st** in EPFL Photonics Day competition **'Present your thesis in 180 secs'** in Sept. 2017.
- Ranked **1st** in India and **participated as finalist** in **Falling Walls Lab** and conference, Berlin, 2014 with the topic "Breaking the wall of scaling devices with plasmonics" - <https://www.youtube.com/watch?v=gLOZkqTqo9U>

COURSES TAKEN IN PHD

- Advances in Nanophotonics
- Nanophotonics and Plasmonics
- Introduction to nanomaterials
- Materials and technology of microfabrication
- Scanning electron microscopy
- Selected topics in advanced optics
- Transmission electron microscopy and diffraction (basics)

COURSES TAKEN IN MASTER'S

- Integrated optoelectronic devices
- Optical engineering
- Laser Physics
- Wave propagation for communication
- DSP application laboratory
- Introduction to Photonics

POSITIONS OF RESPONSIBILITY

- **Reviewed** for Optical Materials Society
- **Designed experiments** for Advanced Photonics lab, IIT Madras
- **Head of the outreach committee** in IIT Madras, India, **OSA** Student Chapter
<https://www.youtube.com/watch?v=SsIR25YicI4>

CO-CURRICULAR ACTIVITIES

- Stood **1st** in **All India Elocution Competition** conducted by Ramakrishna Institute of culture

AFFILIATIONS

- OSA

EXAMS PASSED

- GRE 320/340
- TOEFL 112/120

LANGUAGES KNOWN

- ENGLISH
- GERMAN (A1)
- FRENCH (A1)

TEACHING EXPERIENCE

- Selected Topics in Advanced Optics (2 semesters, 2018-2019, EPFL)
- Optical Engineering (1 semester, 2018, EPFL)
- Electromagnetic field (2 semesters, 2014-2015, IITM)
- Semiconductor devices (1 semester, 2015, IITM)

REFERENCES

- Prof. Olivier J.F Martin olivier.martin@epfl.ch
- Dr. Christian Santschi christian.santschi@epfl.ch
- Dr. Xialong Wang wangrains@gmail.com